

# Aggravating matters: Accounting for baryons in cosmological analyses

Stijn Nicole Bart Debackere

**Cover design:**

The front cover shows a three-dimensional capital Omega, the usual symbol for the cosmological density parameters, filled in with the cosmic web measured in the cosmological Millennium simulation. A two-dimensional capital Alpha, filled in with observations of clusters of galaxies, completes the back cover. The Alpha and Omega, the first and last letters of the Greek alphabet, indicate the importance of observations and simulations in understanding the cosmological evolution of our Universe.

# Aggravating matters: Accounting for baryons in cosmological analyses

## Proefschrift

ter verkrijging van  
de graad van doctor aan de Universiteit Leiden,  
op gezag van rector magnificus prof. dr. ir. H. Bijl,  
volgens besluit van het college voor promoties  
te verdedigen op donderdag 22 september 2022  
klokke 10.00 uur

door

Stijn Nicole Bart Debackere

geboren te Gent, België  
in 1993

Promotores: Prof. dr. J. Schaye  
Prof. dr. H. Hoekstra

Promotiecommissie: Prof. dr. S. Borgani (University of Trieste)  
Prof. dr. E. Krause (University of Arizona)  
Prof. dr. K. Kuijken  
Prof. dr. H. J. A. Röttgering  
Prof. dr. A. Silvestri

Printed by: Gildeprint

ISBN: 978-94-6419-591-0

An electronic copy of this thesis can be found at <https://openaccess.leidenuniv.nl>.

© Stijn Debackere, 2022

*To Tom,  
the first explorer*



# Contents

<b>1</b>	<b>Introduction</b>	<b>1</b>
1.1	The challenges of future surveys . . . . .	2
1.2	A brief history of our Universe . . . . .	4
1.3	The basics of cosmology . . . . .	8
1.3.1	Smooth background evolution . . . . .	8
1.3.2	Growth of structure . . . . .	13
1.3.3	Galaxy formation . . . . .	17
1.4	Weak gravitational lensing . . . . .	19
1.4.1	The basics . . . . .	19
1.4.2	Cosmic shear . . . . .	23
1.5	Galaxy clusters . . . . .	26
1.6	This thesis . . . . .	27
	References . . . . .	29
<b>2</b>	<b>The impact of the observed baryon distribution in haloes on the total matter power spectrum</b>	<b>35</b>
2.1	Introduction . . . . .	36
2.2	Halo Model . . . . .	39
2.2.1	Theory . . . . .	39
2.2.2	Linking observed halo masses to abundances . . . . .	41
2.2.3	Matter density profiles . . . . .	44
2.3	X-ray observations . . . . .	48
2.4	Model density components . . . . .	54
2.5	Results . . . . .	58
2.5.1	Influence of the unobserved baryon distribution . . . . .	58
2.5.2	Influence of halo mass correction due to baryonic processes . . . . .	65
2.5.3	Contribution of different halo masses . . . . .	69
2.5.4	Influence of density profile fitting parameters . . . . .	69
2.5.5	Influence of hydrostatic bias . . . . .	71
2.6	Discussion . . . . .	75
2.7	Summary and conclusions . . . . .	77
2.A	Influence of the halo mass range . . . . .	79
2.B	Influence of concentration–mass relation . . . . .	79
	References . . . . .	80

<b>3 How baryons can significantly bias cluster count cosmology</b>	<b>85</b>
3.1 Introduction . . . . .	86
3.2 Halo mass model . . . . .	88
3.2.1 Linking observed and DMO haloes . . . . .	88
3.2.2 Including observations of baryons . . . . .	89
3.2.3 Fitting the gas density profiles . . . . .	90
3.3 Mock observational analysis . . . . .	95
3.4 Influence on cosmological parameter estimation . . . . .	102
3.4.1 Mock cluster sample generation . . . . .	102
3.4.2 Stage III-like survey . . . . .	104
3.4.3 Stage IV-like survey . . . . .	106
3.5 Aperture masses . . . . .	113
3.6 Discussion . . . . .	115
3.7 Conclusions . . . . .	118
3.A Model fits . . . . .	121
3.B Mixed likelihood . . . . .	122
References . . . . .	124
<b>4 Why are we still using 3D masses for cluster cosmology?</b>	<b>127</b>
4.1 Introduction . . . . .	128
4.2 Simulations . . . . .	131
4.3 Aperture mass–observable relation . . . . .	133
4.3.1 Extraction from the simulations . . . . .	133
4.3.2 Aperture mass behaviour . . . . .	138
4.3.3 Uncertainties . . . . .	142
4.4 Halo aperture mass function . . . . .	145
4.4.1 Aperture mass function behaviour . . . . .	145
4.4.2 Emulating the aperture mass function . . . . .	150
4.4.3 Cosmology dependence of the aperture mass function . . . . .	151
4.5 Discussion . . . . .	158
4.5.1 Impact of the selection function . . . . .	159
4.5.2 Impact of systematic uncertainties . . . . .	160
4.5.3 Comparison to previous work . . . . .	161
4.6 Conclusions . . . . .	162
4.A Weak lensing measurements of the aperture mass . . . . .	165
4.B Scalable Gaussian processes for non-Gaussian likelihoods . . . . .	167
4.C Emulator performance . . . . .	170
References . . . . .	174

<b>5 Galaxy cluster aperture masses are more robust to baryonic effects than 3D halo masses</b>	<b>177</b>
5.1 Introduction . . . . .	178
5.2 Simulations . . . . .	181
5.2.1 Simulation set . . . . .	181
5.2.2 Aperture mass measurement . . . . .	183
5.2.3 Matching haloes to their DMO counterparts . . . . .	183
5.3 The relation between aperture mass and 3D halo mass . . . . .	184
5.4 Aperture mass correction due to baryonic effects . . . . .	186
5.4.1 Binned by 3D halo mass . . . . .	186
5.4.2 Binned by aperture mass . . . . .	188
5.4.3 Scatter in the baryonic correction . . . . .	190
5.4.4 Redshift evolution . . . . .	190
5.4.5 Dependence on feedback strength . . . . .	193
5.5 Conclusions . . . . .	193
References . . . . .	197
<b>Nederlandstalige samenvatting</b>	<b>199</b>
<b>List of publications</b>	<b>205</b>
<b>Curriculum vitae</b>	<b>207</b>
<b>Acknowledgments</b>	<b>209</b>



# 1 | Introduction

In Greek mythology, the cosmos (*χόσμος*) is an ordered state that came from chaos (*χάος*), the void<sup>1</sup>. In a similar vein, the field of cosmology attempts to fill up the metaphorical void in our understanding of the Universe: where did it come from and how does it evolve? While some form of cosmology has been practised for millennia, only in the last century has it evolved from a philosophical pastime into a fully fledged scientific subject. All it took was the development of large and powerful telescopes that allowed us to study the spectra of fuzzy nebulae—the nearest of which are visible with the naked eye in unpolluted skies—to come to the realization that these are actually conglomerations of stars, some of which are receding away from us at “unparalleled velocities” (Curtis, 1915; Wilson, 1915; Slipher, 1921, 1922; Stromberg, 1925). While this conclusion proved controversial initially as evidenced by the “Great Debate” between Shapley & Curtis (1921), the discovery of individual Cepheid variable stars in Andromeda and the Triangulum galaxy by Hubble (1925) provided a definitive proof for the immense distance and the extra-galactic nature of these and similar spiral nebulae. Lemaître (1927) was the first to interpret the high recession velocities to these galaxies as proof for an expanding Universe as predicted by general relativity. Hubble (1929) later explicitly showed that galaxies at larger distances recede away at higher velocities, as required for an expanding Universe. This breakthrough heralded the start of *observational cosmology*.

In the past almost century since this initial discovery of the increasing recession velocity of more distant galaxies, a wealth of disparate observations have elucidated the distribution of matter on cosmological scales, spanning millions to billions of lightyears. The picture emerged of an expanding Universe containing structure on different scales: galaxies bunch together inside groups and clusters, which form the filaments and nodes of an extensive network of overdensities, known as the cosmic web. Dark matter, which only feels gravity, forms the backbone of the cosmic web, constituting about 25 % of the total energy density of the Universe, whereas the ordinary matter that we are all familiar with, present in gas clouds, stars, planets and their inhabitants, only accounts for 5 %. The final 70 % is contributed by the mysterious and unknown dark energy, which counteracts gravity and forces the Universe into a seemingly never-ending phase of accelerated expansion.

To shed light on the properties of dark energy, a slew of telescopes will see their first light in the coming decade. Their aim? To observe over a billion galaxies and use them to map the evolution of the total matter distribution—both dark and ordinary—over the past 10 billion years. The real breakthrough expected from these surveys is their ability to directly probe the era in which dark energy starts dominating the energy content of the Universe, about 3.6 billion years ago. The accelerating expansion of space counteracts the gravitational attraction of matter, slowing down the formation of new structures, leaving a clear mark on the distribution of galaxies. However, inferring the distribution of the total matter while only observing the galaxies is a challenge.

---

<sup>1</sup>Hesiod, Theogony, 110

Using weak gravitational lensing, a statistical method that measures the tiny but coherent distortion of galaxy shapes due to the curvature of space-time caused by intervening matter, it is possible to probe the full cosmologically evolving matter distribution. From these distortions, the total mass between us, the observers, and those galaxies can be inferred. When used to directly study the large-scale distribution of matter, these distortions are called cosmic shear, as the cosmic matter is shearing the images of galaxies. Weak lensing can also measure the total mass, including dark and ordinary matter, of individual objects, such as clusters of galaxies. Clusters are rare objects: they take a long time to form and they contain enormous amounts of matter. The change in the cluster abundance over time strongly constrains the evolution of the matter content and dark energy.

The problem this thesis focusses on, is interpreting these weak lensing observations to obtain the correct mass. A complex issue, since we need to know how the ordinary matter, known as baryons to cosmologists, traces the dominant dark matter. Only normal matter feels the electromagnetic force which substantially changes its behaviour on the smaller scales, cosmologically speaking, of galaxies—as a matter of fact, galaxies can only exist because of this fundamentally different behaviour. Paradoxically, however, not all of this *normal* matter is visible to us as a significant fraction of the total normal matter in the Universe resides in hot, low-density gas, which we are unable to observe directly with our current X-ray telescopes. Hence, we need to find a way to disentangle the unknown contribution of the normal matter from the measured weak lensing signal. Our suggested solutions combine the predictions of computer-simulated universes, evolving billions of particles in time, with simplified models that reproduce the observed distribution of hot gas inside clusters of galaxies, but that freely vary the amount of matter where no observations are available, to quantify how strongly our ignorance of the relation between ordinary and dark matter will affect the analysis of the aforementioned planned surveys. Additionally, we study how baryons affect cluster mass determinations and we suggest a new analysis method for cluster abundance studies that is less sensitive to our lack of knowledge of the exact distribution of normal matter in the outskirts of galaxy clusters.

## 1.1 The challenges of future surveys

Three major missions are planned for the next decade: the Euclid space telescope<sup>2</sup> (Laureijs et al., 2011), the Vera C. Rubin Observatory<sup>3</sup> in Chile (LSST Science Collaboration et al., 2009), and the Nancy Grace Roman Space Telescope<sup>4</sup> (Spergel et al., 2015). Collectively, they are called stage IV surveys by the community. Peaking back in time, these surveys aim to detect over 1 billion galaxies over the area of the sky not blocked by our own Milky Way. Different from the Hubble Space Telescope and large, ground-based telescopes such as the Very Large Telescope (VLT) or the Keck telescopes, these planned observatories are designed to have large fields-of-view to image huge swathes of the sky in a short amount of time.

---

<sup>2</sup><https://www.euclid-ec.org>

<sup>3</sup><https://www.lsst.org/>

<sup>4</sup><https://roman.gsfc.nasa.gov/>

The Euclid space telescope has a 1.2 m primary mirror with a field-of-view of  $0.5 \text{ deg}^2$  (approximately twice the area of the Sun on the sky). To compare, the Wide Field Camera 3 on the Hubble Space Telescope covers a mere  $0.002 \text{ deg}^2$  of the sky. The planned Euclid survey will cover an area  $> 15\,000 \text{ deg}^2$ —more than a third of the entire celestial sphere—probing back in time over the past 10 billion years. It will yield a sample of more than 1.5 billion galaxies whose distorted shapes will constrain the intervening matter. Additionally, the observations will generate a sample of  $> 100\,000$  galaxy clusters whose abundance will constrain the late-time evolution of matter and dark energy. The survey will reach limiting magnitudes of  $\approx 24.5$  in a single, wide visual band, with a small point-spread function (PSF)  $< 0.2 \text{ arcsec}$  for optimal galaxy shape measurements. Similar limiting magnitudes are expected in the three near-infrared filters within the wavelength range of  $1.1 - 2.0 \mu\text{m}$ , which will be used to photometrically measure the distance to the observed galaxies. With these properties, an average number density of  $n_{\text{gal}} \approx 30 \text{ arcmin}^{-2}$  background galaxies is expected in each Euclid image, approximately 54 000 galaxies in total. To improve its distance calibrations, Euclid will rely on large, ground-based surveys to supplement its visual band observations.

The Earth-based Rubin observatory, on the other hand, boasts an 8.4 m primary mirror with an impressive  $9.6 \text{ deg}^2$  field-of-view, allowing it to—theoretically—image its entire  $20\,000 \text{ deg}^2$  survey area in only  $\approx 2000$  exposures of less than 1 min each. The more familiar name of this survey is the Legacy Survey of Space and Time (LSST). Similarly to Euclid, the Rubin observatory is expected to reach limiting magnitudes of  $\approx 24.5$  in a single exposure resulting in  $n_{\text{gal}} \approx 30 \text{ arcmin}^{-2}$ . The fast turnover time of the observations means that the LSST will be able to probe its full area more than a hundred times, allowing it detect galaxies to very high depths, yielding a baffling sample of 10 billion galaxies, out of which approximately 3 billion are expected to be useful for weak lensing. We will undoubtedly discover many unknown transient phenomena thanks to the high-cadence observations enabled by the massive field-of-view. Since the survey is ground-based, however, it will face varying observing conditions and seeing, significantly affecting its angular resolution and resulting in the blending of galaxies. Due to the large overlap between LSST and the Euclid survey, a close collaboration will benefit both surveys ([Rhodes et al., 2017, 2019](#)).

Finally, the Nancy Grace Roman Space Telescope consists of a 2.4 m primary mirror, just like Hubble, but with a significantly wider field-of-view of  $0.28 \text{ deg}^2$ . The telescope housing and mirrors were a gift from the National Reconnaissance Office to NASA—the original mission was planned to house a 1.3 m primary mirror ([Hand, 2012](#)). While the final mission became more expensive, the large diameter will allow high-resolution observations of fainter objects in its four near-infrared bands down to magnitudes of  $\approx 26.5$ . The expected number of detected background galaxies is impressive at  $n_{\text{gal}} \approx 45 \text{ arcmin}^{-2}$ . However, the planned survey area for large-scale structure studies will only cover  $2200 \text{ deg}^2$  on the sky, yielding an expected 380 million galaxies to measure the cosmic shear and 40 000 galaxy clusters to constrain the abundance. The overlapping area with Euclid and LSST will boost the performance of those missions significantly, as it can be used as a powerful calibration tool.

These surveys will revolutionize our understanding of the evolution of the late-time matter distribution due to the immense size of their detected galaxy samples, their high

spatial resolution and the depth to which they can detect galaxies. No current survey comes close: the completed Kilo-Degree Survey (KiDS), carried out by the 2.6 m VLT Survey Telescope covers an area of  $1000 \text{ deg}^2$ , but at a lower angular resolution limited by the seeing to  $\approx 0.7 \text{ arcsec}$  and a limiting magnitude between 23.5 in the  $i$  filter to 25 in the  $ugr$  filters (Kuijken et al., 2019). Importantly, the whole survey area is additionally covered by five band near-infrared bands using the 4.1 m Visible and Infrared Survey Telescope for Astronomy (VISTA), which significantly improves the distance measurements to galaxies. The final KiDS sample contains about 21 million of galaxies with accurate distance measurements with  $n_{\text{gal}} \approx 6 \text{ arcmin}^{-2}$  (Giblin et al., 2021). The Dark Energy Survey (DES), using the 4 m Blanco telescope in Chile, probes a larger area of  $5000 \text{ deg}^2$ , but to a lower depth than the KiDS data (Abbott et al., 2021). The DES sample contains about 390 million galaxies (Sevilla-Noarbe et al., 2021). Finally, the Hyper Suprime-Cam Survey (HSC) has the largest mirror size, observing with the 8.2 m Subaru telescope, probing an area of  $1400 \text{ deg}^2$  down to a deeper limiting magnitude of  $\approx 26$  (Aihara et al., 2018). Due to the large collecting area of the telescope, a number of background galaxies  $n_{\text{gal}} \approx 20 \text{ arcmin}^{-2}$  can be reached (Mandelbaum et al., 2018). The whole area has not yet been observed, so a final sample size is not available for the HSC survey.

The ambitious goal of future stage IV surveys is to constrain the statistical distribution of matter, quantified by the matter power spectrum, to 1% precision, and to pin down the evolving behaviour of dark energy, specifically, the constant and the time-varying equation of state parameters to 2% and 10%, respectively. The gargantuan galaxy samples will provide sufficient statistical power to reach such high precision. However, biases in the analysis can arise if we do not control the systematic uncertainties in the theoretical models we use to analyse the observations to the same level of accuracy (e.g. Hearin et al., 2012; Taylor et al., 2018). Hence, we need to scrutinize our models to identify all possible sources of uncertainty that would bias the data analysis and the inferred cosmological model. In this thesis we will consider the impact of uncertainties in the normal matter distribution for both cosmic shear analyses and galaxy cluster abundance studies.

## 1.2 A brief history of our Universe

Before diving into the cosmologist's mathematical toolkit that allows them to model the evolution of the Universe, a brief status overview of our knowledge of the Universe is in order.

The current standard model, the Lambda Cold Dark Matter ( $\Lambda$ CDM) cosmology, is an immense achievement both theoretically and observationally: a theory tweaked and polished over the past century. Einstein's theory of general relativity provides the framework to model the evolution of an expanding, isotropic and homogeneous universe composed of ordinary matter contributing a mere 5 % of the total energy content of the Universe, dark matter ( $\approx 25 \%$ ), and dark energy ( $\approx 70 \%$ ), lending its name to the model through the cosmological constant,  $\Lambda$  (Planck Collaboration et al., 2020b). Radiation, in terms of photons emitted by gas and stars, and neutrinos generated in radioactive decays, amounts to a negligible fraction of  $\approx 0.01 \%$  of the total energy density of our Universe. Against

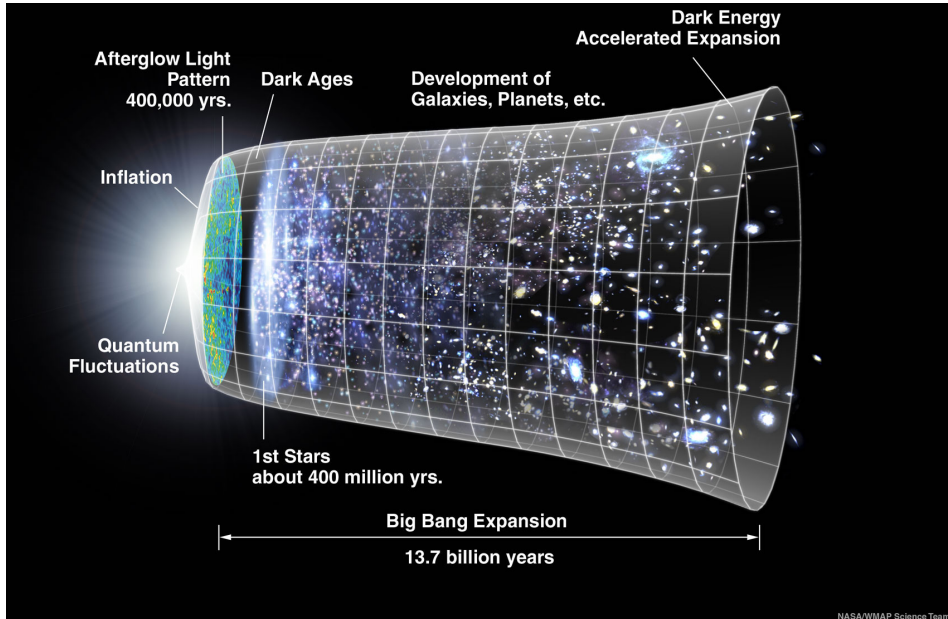


Figure 1.1: Timeline of the Universe from the beginning, on the left, to today, on the right. The vertical size represents the spatial expansion (not to scale). Inflation generates macroscopic density perturbations from the quantum fluctuations present in the beginning of the Universe. The dark matter fluctuations grow as soon as matter dominates the energy content, eventually attracting ordinary matter when it decouples from radiation around 400 000 years after the Big Bang. The ordinary matter collapses, forming stars that make up the galaxies that we see. Over time, these galaxies coalesce into more massive groups and clusters, forming the cosmic web. In the past 3.6 billion years, dark energy has started to dominate the expansion of the Universe, inaugurating a phase of accelerated expansion.

*Figure by the NASA/WMAP Science Team.*

this smooth backdrop, tiny density perturbations generated during the early inflationary phase of exponentially fast expansion, will coalesce into ever more massive dark matter overdensities under the influence of gravity, eventually drawing in the ordinary matter, sparking star formation about 400 million years after the Big Bang and forming galaxies. After about 10 billion years, the expansion of the Universe has sufficiently diluted the matter density for dark energy to become the dominant energy density component, toppling the Universe into a supposedly everlasting accelerated expansion. This is where we are now, about 13.8 billion years after the Big Bang. Fig. 1.1 shows an illustration of the expansion history of the Universe with several milestones in the development of structure.

The standard cosmological model has been immensely successful in simultaneously explaining an eclectic range of observations, including the typical size of pressure waves propagating in the primordial plasma imprinted as fluctuations in both the cosmic mi-

crowave background (CMB), approximately 380 000 years after the Big Bang (e.g. Spergel et al., 2003) and the late-time distribution of luminous red galaxies, about 10 billion years after the Big Bang, known as baryon acoustic oscillations (BAO, e.g. Cole et al., 2005; Eisenstein et al., 2005), the absence of a decrease in the velocity with which galaxies encircle massive agglomerations known as galaxy clusters (Zwicky, 1933), and also of stars in the outskirts of galaxies (Rubin et al., 1980) due to an additional mass contribution of a non-directly observable, “dark” matter, the accelerating expansion of the Universe as probed by supernovae at cosmological distances (e.g. Riess et al., 1998; Perlmutter et al., 1999), the clustering of galaxies (e.g. Peacock et al., 2001; Percival et al., 2001), the statistical distortion of observed galaxy shapes due to the weak lensing effect of intervening matter (e.g. Wittman et al., 2000; Van Waerbeke et al., 2000; Bacon et al., 2000; Hoekstra et al., 2002), the abundance of massive clusters of galaxies (e.g. Bahcall & Cen, 1993) and more.

There are two hidden elephants in the room, however. Neither dark matter nor dark energy fit comfortably within the standard model of particle physics. While there are many smoking guns pointing to a consistent dark matter component, dark energy still remains a mystery. The inferred amount of dark matter is required to explain a range of different observations. Peebles (2017) provides an interesting personal and historical overview of how the evidence and the acceptance of cold dark matter has grown over the past century—another fascinating account on the history of cosmology in general is given in Peebles (2012). We provide a small summary: Firstly, the ratio of the acoustic peaks in the statistical distribution of CMB anisotropies indicate an extra gravitational forcing due to a non-baryonic component (e.g. Hu & Dodelson, 2002; Planck Collaboration et al., 2020b)<sup>5</sup>. Ubiquitous already established dark matter structures are also required at the time of the CMB to explain how the tiny observed ordinary matter perturbations were able to quickly collapse and form galaxies by the current time. Additionally, the flat rotation curves of stars in galaxies (e.g. Rubin & Ford, 1970; Rubin et al., 1980) and the lack of decreasing velocity of galaxies toward the outskirts of clusters indicate the need for an additional invisible mass (e.g. Zwicky, 1933). Finally, gravitational lensing observations of colliding clusters indicate that most of the (dark) mass stays confined to the cluster while the hot gas is left behind in the collision, as observed in the Bullet Cluster (Clowe et al., 2006). However, so far no dark matter particle candidates have been found in any direct searches (e.g. Undagoitia & Rauch, 2016).

Dark energy, on the other hand, remains elusive. From quantum field theory, we expect the vacuum of space to have an associated energy, but the measured cosmological constant comes out about 120 orders of magnitude lower than the predicted value (Weinberg, 1989). However, the energy density of the cosmological constant inferred from observations simultaneously explains both the flatness of the Universe and the late-time accelerating expansion (for a review, see Frieman et al., 2008). Many different theoretical dark energy models exist, ranging from scalar fields with negative pressure to modifications to the laws of gravity (e.g. Joyce et al., 2016). So far, however, the data do not show a preference for more complicated models over a standard cosmological constant (e.g. Chiba et al., 2013; Wang et al., 2018; Gerardi et al., 2019).

---

<sup>5</sup>Clear animated plots can be found on Wayne Hu’s personal website

Now that late-time observational probes of the cosmological expansion history and the matter distribution are gaining statistical power, another potential problem is appearing for  $\Lambda$ CDM in the guise of tensions between cosmological parameters inferred from the CMB and late-time probes (for a recent overview, see [Abdalla et al., 2022](#)). Most famously, the current value of the Hubble parameter inferred from distances to supernovae in galaxies flowing along with the expanding Universe, is larger and in a  $5\sigma$  tension with that extrapolated from the CMB—a discrepancy known as the Hubble tension ([Planck Collaboration et al., 2020b](#); [Riess et al., 2021](#)). Additionally, late-time probes of the matter distribution consistently find values of the matter clustering between  $2-3\sigma$  lower than predicted by the CMB—dubbed the  $S_8$  tension (e.g. [Bocquet et al., 2019](#); [Heymans et al., 2021](#)). There are two possible ways to solve these problems: either there are unidentified sources of systematic error in at least one of the analysis methods or there are unaccounted for physical effects present in the data—colloquially, we speak of “new physics”.

For Planck, there seem to be inconsistencies in the data between measurements when using only small or large scales (e.g. [Addison et al., 2016](#)), partially manifesting as a smoothing of the small scale peaks, similar to the signal expected from a stronger lensing of the CMB ([Planck Collaboration et al., 2017](#)). However, these features are stronger than expected from direct constraints inferred from the higher-order correlations that the lensing induces in the anisotropies of the CMB (e.g. [Obied et al., 2017](#); [Motloch & Hu, 2018, 2020](#)). Tantalizingly, excluding the small-scale information shifts the best-fitting values of both the Hubble parameter and the matter clustering closer to the late-time measurements ([Planck Collaboration et al., 2017](#)). However, given the high dimensionality of the parameter space, [Planck Collaboration et al. \(2017\)](#) finds shifts in the cosmological parameters with a similar significance in about 10 % of their simulated data, consistent with statistical fluctuations. The inconsistencies could also point to some unknown systematic effects in the Planck analysis, or to unaccounted for physical processes.

The supernovae analyses calibrate distances to nearby galaxies that have hosted a supernova explosion, using a standard candle, such as Cepheid variable stars (e.g. [Riess et al., 2021](#)). This method has several requirements. Firstly, it requires an accurate calibration of the standard candle, for example, the Cepheid period–luminosity relation, extrapolated to more distant, SN-hosting galaxies. Additionally, geometric distance calibrations to local galaxies are needed. Finally, the decay in the supernova brightness must follow a universal, redshift-independent relation. [Riess et al. \(2021\)](#) carefully investigate and dispel most currently hypothesized sources of systematic error for Cepheid distance calibrations, such as biases induced by crowding of background stars in the Cepheid photometry, inconsistencies in the period–luminosity relation for different galaxies, or the impact of using different nearby anchors for the distance ladder (as detailed in the responses to [Efstathiou 2020](#), and also in the discussion of [Riess et al. 2021](#)). However, the complex analysis, the possible astrophysical sources of systematic uncertainty and the fact that different distance calibrations, using, for example, the tip of the red giant branch (e.g. [Freedman et al., 2019](#); [Freedman, 2021](#); [Anand et al., 2022](#)), or lensing time delays (e.g. [Birrer et al., 2020](#)), result in parameter determinations consistent with the CMB prediction, should serve as a caution before concluding that a modification to  $\Lambda$ CDM is needed. In a few years, a completely independent measurement using standard gravitational sirens will be able to shed light on this issue (e.g. [The LIGO Scientific Collaboration and The](#)

[Virgo Collaboration et al., 2017](#); [Feeney et al., 2019](#); [Soares-Santos et al., 2019](#)).

Finally, the most significant discrepancy in the inferred matter clustering compared to the CMB data is found in cosmic shear analyses (e.g. [Asgari et al., 2021](#); [Amon et al., 2022b,a](#)). Inferring cosmological parameters from measuring the statistical shape distortion of galaxies caused by the intervening matter is a complicated problem beset by possible systematic uncertainties. First of all, for a fixed lensing signal over or underestimating the distance to the source galaxies results in higher or lower values for the inferred clustering of matter, respectively ([Joudaki et al., 2020](#)). Additionally, intrinsic alignments of galaxies in each other’s neighbourhood can masquerade as a cosmological signal (e.g. [Croft & Metzler, 2000](#); [Heavens et al., 2000](#); [Hirata & Seljak, 2004](#)). The details of this alignment signal will depend on galaxy formation processes and the galaxy population, but current models are likely too simplistic to capture the full behaviour (e.g. [Joachimi et al., 2015](#)). Different analysis methods and different surveys find significantly different values for the strength of the intrinsic alignment signal (e.g. [Efstathiou & Lemos, 2018](#); [Asgari et al., 2021](#)), which could indicate that the parameter is accounting for another systematic uncertainty in the data. Calibrating the intrinsic alignment signal observationally, as suggested by [Fortuna et al. \(2021\)](#), could reduce this effect. However, tests of the internal consistency of the observations and variations in the systematic uncertainty modelling have not identified any significant possible reductions in the tension which could point to the need for modifications to the cosmological model (e.g. [Asgari et al., 2021](#); [Joachimi et al., 2021](#); [Amon et al., 2022b](#)).

As the saying goes: “May you live in interesting times”, and we certainly do. The advent of future surveys aims to constrain the expansion history and the matter content of the Universe with revolutionary precision. Any inconsistencies in the standard model of cosmology will be tremendously magnified with the future data, that is, if we are able to adequately control the systematic uncertainties in the challenging data analysis.

## 1.3 The basics of cosmology

To understand how weak lensing can probe the matter distribution of the Universe, we first need to introduce the tools of modern cosmology. We start by introducing how we can model the smooth background evolution of the average density of the Universe in Section 1.3.1, then, we will detail in Section 1.3.2 how small density fluctuations generate structure on top of this smooth background, providing the seed locations to form galaxies. Finally, we will describe how baryons condense into the galaxies that we observe in Section 1.3.3.

### 1.3.1 Smooth background evolution

The current cosmological framework rests on the foundational assumption that our Universe is homogeneous and isotropic when averaged over sufficiently large length scales, also known as the cosmological principle. The distribution of galaxies and quasars on scales  $\gtrsim 100$  Mpc (about 330 million lightyears) provides evidence for homogeneity (e.g. [Hogg et al., 2005](#); [Laurent et al., 2016](#); [Ntelis et al., 2017](#)), and the remarkable isotropy of

the cosmic microwave background is taken as strong evidence for the latter. The maturing of cosmology as a scientific subject started with the development of Einstein's theory of general relativity ([Einstein, 1916](#)). In its full glory, the theory of general relativity involves solving the highly non-linear set of Einstein field equations relating the local curvature of four dimensional space-time to the matter and energy density. In compact index notation, the field equations can be written as

$$R_{\mu\nu} + \left( \Lambda - \frac{1}{2}R \right) g_{\mu\nu} = \frac{8\pi G}{c^4} T_{\mu\nu}, \quad (1.1)$$

where  $R_{\mu\nu}$  is the Ricci curvature tensor,  $R$  is the scalar curvature, i.e. the trace of the Ricci tensor,  $\Lambda$  is the cosmological constant,  $g_{\mu\nu}$  is the metric tensor,  $G$  is Newton's gravitational constant,  $c$  is the speed of light, and, finally,  $T_{\mu\nu}$  is the stress-energy tensor. The different Greek subscript letters can be any of either the three spatial dimensions or the single time dimension, resulting in a set of  $4 \times 4 = 16$  equations. The fundamental geometric quantity in general relativity is the metric,  $g_{\mu\nu}$ , since the Ricci tensor can be derived from it. The metric acts as a ruler, allowing distances in a curved space to be uniquely defined, independently of the assumed coordinate system, in accordance with the relativity principle promoted by Einstein. Physical properties of the matter enter through the stress-energy tensor.

The cosmological principle greatly simplifies the Einstein field equations. Under the assumption of homogeneity and isotropy, the space-time line element, defined by the Friedmann-Lemaître-Robertson-Walker (FLRW) metric, can be written as

$$\begin{aligned} ds^2 &= g_{\mu\nu} dx^\mu dx^\nu \\ &= -c^2 dt^2 + a^2(t) d\chi^2 \\ &= -c^2 dt^2 + a^2(t) (d\chi^2 + f_K(\chi)(d\theta^2 + \sin^2 \theta d\phi^2)) , \end{aligned} \quad (1.2)$$

where we have introduced standard spherical coordinates,  $(\chi, \theta, \phi)$ , the scale factor,  $a(t)$ , and

$$f_K(\chi) = \begin{cases} 1/\sqrt{K} \sin(\sqrt{K}\chi) & K > 0 \\ \chi & K = 0 \\ 1/\sqrt{-K} \sinh(\sqrt{-K}\chi) & K < 0 \end{cases} \quad (1.3)$$

introduces the dependence on the spatial curvature,  $K$ , which is measured to be indistinguishable from 0 ([Planck Collaboration et al., 2020b](#)). The FLRW metric implies a Universe consisting of flat, three-dimensional hypersurfaces with an increasing physical distance  $dl = a(t)d\chi$  between observers that move along with its expansion. The comoving distance,  $\chi$ , provides a spatial distance measure that is unaffected by the expansion, and the scale factor,  $a(t)$ , which can be freely set to be 1 at our current time, functions as a clock, measuring time in terms of how much the Universe has expanded. In the beginning,  $t = 0$ , the FLRW metric implies a singularity,  $a = 0$ , where all matter was packed together so densely that our known laws of physics no longer hold. This initial hot and dense state of the Universe is known as the Big Bang. Since the expansion of space also stretches the wavelength of individual photons, another way of measuring time is by

identifying the observed wavelength,  $\lambda_{\text{obs}}$ , of a known atomic emission line at wavelength  $\lambda_{\text{em}}$ . The redshift,  $z$ , of the emission lines tells us how much smaller the Universe was at the time of emission from the relation

$$\frac{\lambda_{\text{obs}}}{\lambda_{\text{em}}} = 1 + z = \frac{a(t_{\text{obs}})}{a(t_{\text{em}})}. \quad (1.4)$$

Since practically all the information from the distant Universe reaches us through photons (neglecting gravitational waves and neutrinos), the redshift is the best tool to correctly situate observed objects or events in the history of the Universe.

The finite speed of light allows us to look back in time, with photons leaving galaxies in the very early Universe travelling for billions of years before finally reaching our detectors. The finite speed of photons also results in a cosmological “horizon”, the region from which light is able to reach us in the age of the Universe. Since photons travel along null geodesics,  $ds^2 = 0$ , the metric in Eq. (1.2) gives the comoving horizon size,

$$\chi_h(t) = c \int_0^t \frac{dt'}{a(t')}, \quad (1.5)$$

which at the current time equals about 14 Gpc.

Now, we only need Einstein’s field equations to solve for the scale factor and to capture the expansion history of the Universe (e.g. [Weinberg, 1972](#)). [Friedmann \(1922\)](#) was the first to show that the scale factor in the FLRW metric must obey the relation

$$H^2(t) \equiv \left( \frac{\dot{a}(t)}{a(t)} \right)^2 = \frac{8\pi G}{3} \rho(t) - \frac{Kc^2}{a^2(t)} \quad (1.6)$$

also known as the Friedmann equation, which follows from the space-space and time-time components of Einstein’s equations. We have introduced the common notation  $d/dt \equiv \cdot$  and the density,

$$\rho(t) = \rho_m(t) + \rho_\gamma(t) + \rho_\Lambda, \quad (1.7)$$

consisting of a matter (m), radiation ( $\gamma$ ), and cosmological constant ( $\Lambda$ ) contribution. Additionally, the time-time component of Einstein’s equations gives

$$\frac{\ddot{a}(t)}{a(t)} = -\frac{4\pi G}{3} \left( \rho(t) + \frac{3p(t)}{c^2} \right), \quad (1.8)$$

where the pressure,

$$p(t) = \sum_i w_i \rho_i(t), \quad (1.9)$$

depends on the equation of state parameter,  $w_i$ , of each density component. Eqs. (1.6) and (1.8) explicitly show how the expansion of the Universe depends on the physical properties, that is the density and the pressure, of its constituent matter and energy components. Defining Eq. (1.6) in terms of the critical density for which the Universe is flat, that is, for which space is Euclidean,

$$\rho_{\text{crit}}(t) = \frac{3H^2(t)}{8\pi G}, \quad (1.10)$$

we obtain the most-widely used form for a flat universe,

$$H^2(z) = H_0^2(\Omega_{m,0}(1+z)^3 + \Omega_{\gamma,0}(1+z)^4 + \Omega_{\Lambda,0}), \quad (1.11)$$

where  $\Omega_i \equiv \rho_i/\rho_{\text{crit}}$  and the subscript 0 indicates that the quantity is measured at the current time  $t_0$ , or, identically,  $a = 1$  and  $z = 0$ . Observationally, the parameters are constrained to  $H_0 = 67.44 \pm 0.42 \text{ km s}^{-1} \text{ Mpc}$  and  $(\Omega_{m,0}, \Omega_{\Lambda,0}) = (0.311, 0.689) \pm 0.006$ , with  $\Omega_{\gamma,0} < 10^{-4}$  (Planck Collaboration et al., 2020b). Here, we have used Eq. (1.8) with the equation of state parameters for a photon gas,  $w_\gamma = 1/3$ , pressureless dark and ordinary matter,  $w_m = 0$ , and dark energy in the form of a cosmological constant,  $w_\Lambda = -1$ . The radiation density decreases strongly with time since the spatial expansion decreases the number density of photons and additionally stretches their wavelength, reducing the total energy density. Matter, on the other hand, is only affected by the decreasing number density. Finally, the cosmological constant permeates space with a fixed background density, unaffected by the expansion of the Universe.

According to the most recent Planck Collaboration et al. (2020b) measurements of the temperature fluctuations imprinted in the cosmic microwave background (CMB), the Universe is currently approximately 13.8 billion years old. It has passed through different epochs in which different density components dominate its expansion history. The early Universe was dominated by radiation, until about 20 000 years after the Big Bang (or  $z \approx 5700$ ) when matter took over. Interestingly, about 3.6 billion years ago (or  $z \approx 0.3$ )—recent history, cosmologically speaking—dark energy started dominating over matter, initiating a phase of seemingly never-ending, accelerated expansion. However, until we fully understand what causes the observed acceleration, that is, until we have a satisfactory model of dark energy or modified gravity that is observationally preferred, reports about the final fate of the Universe are greatly exaggerated.

A final important consequence of our expanding Universe for observational cosmologists is that measuring distances to objects is more complex. In the neighbourhood of our own galaxy, we can infer distances,  $D$ , to objects from their flux,  $F_{\text{tot}}$ , if we know their total bolometric luminosity,  $L_{\text{tot}}$ , using the fact that

$$D_L = \sqrt{\frac{L_{\text{tot}}}{4\pi F_{\text{tot}}}}. \quad (1.12)$$

Alternatively, if we know some physical size,  $\delta l$ , we can infer the distance from the angle,  $\delta\theta$ , it subtends on the sky since

$$D_\theta = \frac{\delta l}{\delta\theta}. \quad (1.13)$$

In a flat, expanding Universe, the expansion of space need to be taken into account when inferring distances in a similar way. It is useful to first define the line-of-sight comoving distance,  $\chi$ , between us, the observers, and a point located at a particular redshift,  $z$ , as

$$\chi(z) = \int_0^z dz \frac{c}{H(z)}, \quad (1.14)$$

which follows from the metric in Eq. (1.2). This comoving distance defines the spherical surface over which photons emitted at redshift  $z$  will be spread out by  $z = 0$ . Additionally,

photons are redshifted by the time they reach the detector, decreasing the energy and increasing the arrival time interval, resulting in a measured flux

$$F_{\text{tot,obs}} = \frac{L_{\text{tot}}}{4\pi\chi^2(z)(1+z)^2} \quad (1.15)$$

## 1

from which we get the luminosity distance

$$D_L = (1+z)\chi(z). \quad (1.16)$$

The angular diameter distance, which is the generalization of Eq. (1.13), is easily derived from the metric, Eq. (1.2). The proper size,  $\delta l$ , of an object or feature at redshift  $z$ , a comoving distance  $\chi$  from an observer at the origin, fixes the angular size,  $\delta\theta$ , seen by the observer to

$$\delta l^2 = a^2(t_{\text{em}})f_K^2(\chi)\delta\theta^2, \quad (1.17)$$

giving

$$D_A = \frac{f_K(\chi)}{1+z}. \quad (1.18)$$

A fascinating property of our expanding Universe is that objects of fixed physical size,  $\delta l$ , will reach a minimum angular size between  $z \simeq 1 - 2$ , but for higher redshifts their angular sizes actually become larger because the physical distance to the observer was significantly smaller at the time of emission, resulting in a larger angular size.

Being able to convert angles on the sky or luminosities on a detector into distances, requires so-called standard rulers or standard candles. With a ruler or a candle in hand, observational cosmologists are able to constrain the expansion history and the geometry of the Universe through the inferred comoving distance,  $\chi(z)$ , to said ruler or candle, which depends on the Hubble parameter,  $H(z)$ . Some of the strongest current constraints on the properties of our Universe were derived this way. Anisotropies in the cosmic microwave background provide a fossil record of the sound horizon, the maximum distance that pressure waves were able to travel since the start of the Universe, at the time of recombination of protons and electrons around 380 000 years ( $z \approx 1100$ ) after the Big Bang. The physical size of the sound horizon depends on the matter-to-photon ratio, due to the balance between gravitational collapse and radiation pressure that generate the oscillation responsible for the pressure waves (e.g. Peebles & Yu, 1970; Hu et al., 1997). The angular scale of these perturbations has been measured to be 0.59643 deg (about the angular size of the Sun on the sky) with an exquisite accuracy of 0.05 % by the Planck satellite (Planck Collaboration et al., 2020b). The angular size additionally depends on the expansion history of the Universe through  $\chi(z)$ , as can be seen from Eq. (1.17), making the CMB a powerful cosmological probe. Since these perturbations are also imprinted—although strongly damped—in the baryons which collapse under gravity to form galaxies, another standard ruler can be found in the statistical distribution of galaxies at much later times. This baryon acoustic oscillation (BAO) feature was first detected by Eisenstein et al. (2005) and Cole et al. (2005). Finally, type Ia supernova explosions can function as standard candles, since they are generated when a white dwarf reaches the Chandrasekhar limit of  $\approx 1.44 M_\odot$  through mass accretion from a companion, which results in a fixed

luminosity explosion event. These standard candles have been used by [Riess et al. \(1998\)](#) and [Perlmutter et al. \(1999\)](#) to constrain the distance–redshift relation out to  $z \approx 1$  and show that the Universe is entering a phase of accelerated expansion.

### 1.3.2 Growth of structure

Even though the modelling of the evolution of the average density of the entire Universe is an impressive feat, it does not bring us closer to understanding how the observed galaxies form and cluster together in the cosmic web and how we can predict the lensing signal that this matter distribution generates. For that, we need to know the initial distribution of density perturbations and their evolution in time.

The stage for galaxy formation is set extremely early when quantum fluctuations get inflated to scales orders of magnitude larger than the causal horizon—the region where particles have been able to communicate—in a phase of exponential expansion, known as inflation ([Guth, 1981](#); [Linde, 1982](#)). Inflation ends in a reheating period that spawns the standard model particles and initiates the radiation-dominated period of our Universe. The inflationary scenario provides an explanation for the counter-intuitive observed isotropy of the CMB: patches on opposite parts of the sky that cannot possibly be in thermal equilibrium, are observed to have the same temperature to within a fractional difference of  $\Delta T/T \approx 10^{-5}$ . Inflation explains this isotropy since these regions were actually in causal contact before they were stretched outside of each other’s horizons, meaning they were in thermal equilibrium before inflation. Additionally, inflation also smooths out any initial curvature present in the early Universe, explaining why the current Universe is observed to be flat even though any tiny deviation from flatness exacerbates with time.

Due to the stochastic nature of the initial quantum fluctuations, we can only ever describe the spatial distribution of density perturbations in a statistical sense. Standard inflationary models predict that the initial density perturbation compared to the mean density,  $\bar{\rho}$ ,

$$\delta(\mathbf{x}, t) = \frac{\rho(\mathbf{x}, t)}{\bar{\rho}(t)} - 1, \quad (1.19)$$

is a zero-mean Gaussian random field with correlations on length scales  $\lambda = 2\pi/k$  described by a power spectrum,

$$P(k) = \langle |\delta_k|^2 \rangle \propto k^{n_s}, \quad (1.20)$$

that is almost scale-free, i.e.  $n_s \approx 1$ . Here, scale-free means that all density perturbations have the same amplitude when they re-enter the horizon after inflation has ended and radiation dominates the energy density (e.g. [Bardeen et al., 1983](#)). As a zero-mean Gaussian random field, the initial density perturbations are fully specified by the power spectrum since all even, non-zero higher-order moments can be derived from it.

The initial growth of density perturbations depends on the dominant energy component of the Universe. Perturbations that re-enter the horizon during the radiation-dominated epoch will stall their growth until matter becomes the dominant component and dark matter perturbations start to collapse and establish the potential wells in which galaxies will eventually form. This stalled growth imprints the comoving horizon size at

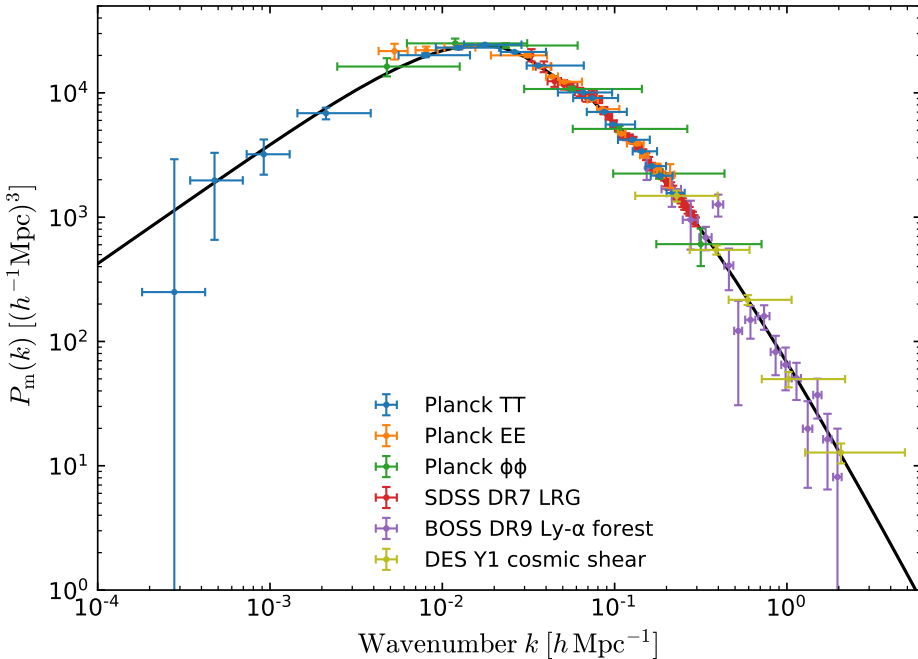


Figure 1.2: The linear matter power spectrum at  $z = 0$  inferred from different observational probes. The Planck satellite measures the temperature fluctuations (TT) and the polarization (EE) of the cosmic microwave background at  $z \approx 1100$ , but also how it is lensed by the intermediate large-scale structure around  $z \simeq 0.5 - 1$  ( $\phi\phi$ ). The Sloan Digital Sky Survey (SDSS) measures the clustering of luminous red galaxies (LRGs) with  $z < 0.5$ . The Baryon Acoustic Oscillatory Spectroscopic Survey (BOSS) Ly- $\alpha$  forest probes Ly- $\alpha$  absorption features in spectra of quasars that closely trace the underlying matter distribution. Finally, cosmic shear uses the weak gravitational lensing shape distortion of large samples of galaxies to constrain the statistical matter distribution between the observer and the galaxies. *Figure taken from Planck Collaboration et al. (2020a).*

matter–radiation equality,  $d_{H,\text{eq}} \approx 100 \text{ Mpc}$  or  $k_{\text{eq}} \approx 0.01 \text{ Mpc}^{-1}$ , as a characteristic scale in the power spectrum of small fluctuations,  $\delta < 1$ , also known as the linear power spectrum. Fig. 1.2 shows observational constraints on the linear matter power spectrum inferred from the CMB, galaxy clustering, the Ly- $\alpha$  forest absorption feature in quasar spectra, and cosmic shear, together with the linear power spectrum predicted from the best-fit Planck Collaboration et al. (2020b) constraints. On large scales ( $k < k_{\text{eq}}$ ), the power spectrum retains its initial  $\propto k$  dependence, whereas on small scales ( $k > k_{\text{eq}}$ ), the scaling changes to a  $\propto k^{-3}$  dependence since smaller scales entered the horizon earlier and have been stalled for longer.

The seed locations of structure formation can be determined by following the growth of small, linear dark matter perturbations on top of the smooth background density of

the Universe. The growth of subhorizon dark matter perturbations in a matter-dominated Universe is captured by the simplified, Newtonian fluid equation

$$\ddot{\delta} + 2H\dot{\delta} = 4\pi G\bar{\rho}\delta, \quad (1.21)$$

with  $\delta \ll 1$ . Here, the right-hand side exerts a gravitational pull, increasing the over-density, whereas the expansion of the Universe, represented by the Hubble parameter term on the left-hand side, opposes this growth, decreasing the perturbation growth rate from an exponential, in the case of no expansion ( $H = 0$ ), to a power-law,  $\delta \propto a$ , in the matter-dominated regime. Hence, even in the presence of the expansion of the Universe, dark matter perturbations will grow, eventually reaching  $\delta \approx 1$ , where the linear approximation no longer holds and higher-order terms in  $\delta$  need to be included in Eq. (1.21).

The evolution of non-linear overdensities can be modelled with a simplified spherical collapse model, treating spherical overdensities as their own separate universes with higher density (e.g. Peebles, 1965, 1967). This calculation shows that overdensities first decouple from the Hubble flow and start to collapse when they are about 4 times denser than the average density of the Universe. The resulting haloes are about 200 times more dense than the average background density at their formation time. From these models, we know that this collapse occurs when the linear density perturbations in Eq. (1.21) reach a critical value of  $\delta_c \approx 1.686$ . Non-linearities become important on scales  $\lambda \lesssim 10$  Mpc, or, equivalently,  $k \gtrsim 0.1$  Mpc $^{-1}$ , where the total matter power spectrum will start deviating from the linear matter power spectrum shown in Fig. 1.2.

Press & Schechter (1974) used similar analytic arguments to predict the distribution of collapsed objects consisting of cold gas—dark matter was not yet considered in the cosmological models back then—as a function of their mass. They argued, following the spherical collapse model, that when linear perturbations on a scale  $R$  reach the threshold for collapse, they will form a structure of mass  $m \propto \bar{\rho}R^3$ . Assuming that the probability  $P(\delta_R > \delta_{\text{crit}})$  determines the fraction of the mass of the Universe present in objects of mass  $> m$ , the resulting halo distribution is fully determined by the possible cosmology dependence of the critical density for collapse,  $\delta_{\text{crit}}$ , and the variance of the overdensity field. Impressively, their prediction based on linear theory was later shown to qualitatively reproduce the mass-dependent abundance of haloes in simulations (e.g. Efstathiou et al., 1988).

Our understanding of how structure forms was furthered by studying the clustering of the most significant peaks in the density field: clusters of galaxies. Kaiser (1984) noted that the larger correlation lengths observed for clusters compared to lower-mass galaxies could be explained if clusters are a biased tracer of the underlying density field. That is, clusters only form when the local density field is coherently boosted by a large-wavelength perturbation allowing large-scale overdensities to become significant and form massive haloes with correlations on the lengthscale of the wavelength. Smaller fluctuations behave more like noise and small patches can reach significant overdensities, resulting in the formation of low-mass haloes with smaller coherence lengths. The analytic population properties of the peaks of random Gaussian fields have been worked out meticulously by Bardeen et al. (1986).

Studying the details of halo formation requires N-body simulations that model the gravitational evolution of collisionless matter particles in an expanding Universe. The

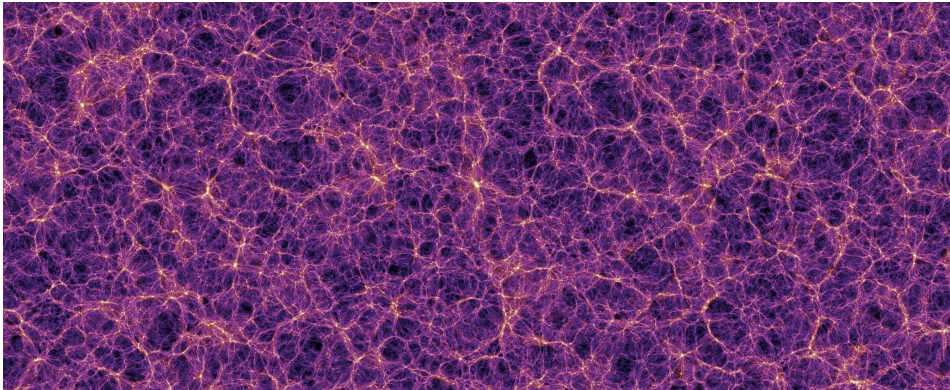


Figure 1.3: The cosmic dark matter distribution at  $z = 0$  predicted by the Millennium simulation of [Springel et al. \(2005\)](#) in a  $15 h^{-1}$  Mpc thick slice of the simulated volume. The cosmic web with dense, yellow nodes and connective filamentary structures surrounding empty voids is clearly visible. Galaxies predominantly form in haloes along the filaments, clustering in groups and clusters, which are located at the nodes of the cosmic web. *Figure by the Virgo consortium.*

first computer simulations in a cosmological context, carried out by [Aarseth \(1963\)](#), only followed the gravitational evolution of 100 collisionless particles, limited by the available computational power and the  $N^2$  scaling of the direct force calculation between all the particles. In the early 80s, [Efstatiou & Eastwood \(1981\)](#) carried out the first cosmological simulation with 20 000 particles, using the more advanced particle-particle/particle-mesh (abbreviated as P<sup>3</sup>M) method, introduced by [Eastwood \(1975\)](#). The P<sup>3</sup>M method reduces the computational expense of N-body simulations by introducing a mesh with  $M^3$  cells over which the average gravitational potential is calculated. Forces on individual particles receive a large-scale contribution from the mesh and a short-range particle-particle contribution that only includes particles within a fixed, smaller distance from each other, saving a significant amount of computation and enabling much larger ensembles of particles to be modelled. Current simulation codes have upgraded their gravity calculations to a TreePM method that calculates short-range forces more efficiently using a tree structure while keeping the mesh for large scales (e.g. [Barnes & Hut, 1986](#); [Xu, 1995](#)).

In the 90s, [Navarro et al. \(1996, 1997\)](#) showed that haloes in simulations modelling solely the evolution of dark matter in universes with different initial power spectra follow a universal density profile, now known as the Navarro-Frenk-White (NFW) profile, characterized by

$$\rho_{\text{NFW}}(r) \propto \left(\frac{r}{r_s}\right)^{-1} \left(1 + \frac{r}{r_s}\right)^{-2}, \quad (1.22)$$

where  $r_s$  is the scale radius where the power-law slope  $d \ln \rho_{\text{NFW}} / d \ln r = -2$ , transitioning between the  $r^{-1}$  and  $r^{-3}$  scaling of the inner and outer halo, respectively.

From the early 2000s to now, an increase in the computational power of supercomput-

ers has lead to ever larger simulations being run with increasing numbers of particles and for many different cosmological models. [Springel et al. \(2005\)](#) introduced the Millennium simulation, evolving over 10 billion dark matter particles, each weighing  $\approx 10^9 h^{-1} M_\odot$ , in a comoving volume of  $500 h^{-1} \text{Mpc}$ , where  $h = H_0/100 \text{ km s}^{-1} \text{Mpc}^{-1}$ . Such simulations aim to self-consistently model the full cosmological evolution of a large, representative patch of the Universe. They start at high redshift, well before the first galaxies formed, usually  $z > 100$ —less than  $\approx 15$  million years after the Big Bang—with a particle distribution that follows the statistical distribution predicted for a chosen cosmology. Evolving these particles through time, including the effects of gravity and the expansion of the Universe, we end up with accurate predictions for the structure of the Universe, including the cosmic web and highly non-linear haloes, as shown in Fig. 1.3. Many features of the large-scale clustering of matter can be accurately inferred from such simulations since the ordinary matter—which is *not* included in these dark matter-only simulations—approximately follows the dark matter.

To predict the cosmology-dependence of quantities such as the halo abundance or matter clustering from simulations, we need a sample of simulations that vary the cosmological parameters and the resulting matter distribution and evolution. [Heitmann et al. \(2006\)](#) and [Habib et al. \(2007\)](#) suggested to run a set of simulations with cosmological parameters sampled on a grid that maximizes the minimum distance between all the parameter vectors. This enables an efficient interpolation between the results with sufficient accuracy while also minimizing the computational expense since the sampling can be relatively sparse. Such *emulator* approaches are gaining popularity owing to the stringent theoretical accuracy requirements of future galaxy surveys. Emulators have been developed for the halo abundance (e.g. [McClintock et al., 2019](#); [Nishimichi et al., 2019](#); [Bocquet et al., 2020](#)) and the matter power spectrum (e.g. [Heitmann et al., 2009](#); [Euclid Collaboration et al., 2018](#)), both quantities of interest for this thesis. However, simulations can only be fully representative of our actual Universe with its stars, gas and galaxies, when they also include baryons and their associated physical processes, as we will discuss next.

### 1.3.3 Galaxy formation

The formation of galaxies is the next step after dark matter structures have collapsed. Dark matter has an approximately 350 000 year head start, being able to collapse as soon as matter dominates the energy budget of the Universe. Normal matter, on the other hand, only decouples from radiation when the Universe has cooled down to  $T_{\text{dec}} \approx 3000 \text{ K}$  (at  $z_{\text{dec}} \approx 1100$ ) and photon collisions can no longer keep the primordial gas ionized. At this stage, the gas becomes neutral and can collapse into the already established dark matter potential wells.

The crucial difference between ordinary and dark matter is that ordinary matter takes part in electromagnetic interactions. As a result, gas particles can collide with each other, exerting a pressure that can balance gravitational collapse. Hence, collapsed dark matter haloes form a gaseous halo with an equilibrium, virial temperature and density profile set by the mass of the halo. This is not the full story, however: if the density and temperature are sufficiently high, the gas becomes ionized and collisions between electrons and atoms can excite electronic transitions or even ionize more atoms, resulting in radiative

cooling (which is more efficient for higher-metallicity gas due to the availability of more electrons). Gas at temperatures comparable to the ionization energy of the atomic lines, mostly between  $10^4 - 10^6$  K, will be able to cool efficiently through these processes, fragmenting to form stars in low-mass haloes (e.g. [Rees & Ostriker, 1977](#); [Silk, 1977](#); [White & Rees, 1978](#)). The small initial angular momentum of the gas clouds, imparted by gravitational tidal torques from the surrounding large-scale structure, gets amplified in the collapse, resulting in the formation of a disk (e.g. [Fall & Efstathiou, 1980](#)). Subsequent halo mergers grow the total halo and stellar mass, possibly disturbing the disk, resulting in the formation of elliptical galaxies. The emerging picture is one of hierarchical growth of haloes, with the central galaxy mass increasing due to continuous accretion and mergers, and with large haloes accreting smaller haloes and their galaxies as a satellite population.

A successful galaxy formation model should be able to reproduce the observed abundance of galaxies as a function of properties such as their mass, colours, sizes, and their observed clustering. To self-consistently model the growth of dark matter haloes from their initial perturbations as well as the formation of galaxies, we need to resort to cosmological hydrodynamical simulations that simultaneously evolve dark matter and gas while accounting for the formation of stars and their associated feedback such as stellar winds and supernovae explosions (for a review, see [Somerville & Davé, 2015](#)). The immense dynamic range of galaxy formation requires a trade-off to be made between the mass resolution and the volume of the simulation. Processes that cannot be resolved due to the limited resolution of the simulations are included as subgrid physics recipes.

First of all, gas in the simulations needs to be able to cool. Hence, gas particles in cosmological hydrodynamical simulations typically track the abundance of the 11 dominant atomic species for cooling and interpolate the pre-calculated cooling and heating rates tabulated as a function of the density, temperature, metallicity and redshift of the gas (e.g. [Wiersma et al., 2009a](#)). When the gas becomes dense enough, it should be able to form stars. Gas particles are stochastically converted into stellar particles, representing stellar populations of thousands of stars, when their density exceeds the critical density for gravitational collapse (e.g. [Schaye, 2004](#); [Schaye & Dalla Vecchia, 2008](#)). The stellar populations evolve, generating type II supernovae and stellar winds that enrich the surrounding gas (e.g. [Wiersma et al., 2009b](#)). The supernovae additionally kick or heat their neighbours, simulating the violent explosions that can shut down the star formation in low-mass galaxies by heating and dispersing the high-density star-forming gas (e.g. [Dalla Vecchia & Schaye, 2008, 2012](#)). This stellar feedback is important since it allows simulations to reproduce the observed low-mass slope of the galaxy stellar mass function (e.g. [Puchwein & Springel, 2013](#)).

Finally, most massive galaxies are observed to host central supermassive black holes (SMBHs) and hot haloes (e.g. [Faber et al., 1997](#); [Magorrian et al., 1998](#)). The supermassive black holes are expected to form early on from the coherent collapse of massive gas clouds and grow through continuous gas accretion and mergers. Gas is funnelled onto the SMBH accretion disk, growing the black hole and fuelling powerful galactic-scale winds and jets that heat the surrounding gas, eventually unbinding it and ejecting metal-enriched gas into the hot halo while suppressing star formation (e.g. [Silk & Rees, 1998](#); [Blandford, 1999](#); [Fabian, 1999](#)). This AGN feedback is important to reproduce the high-mass end of the galaxy stellar mass function and also the observed baryon fractions in groups and

clusters of galaxies (e.g. [Fabjan et al., 2010](#); [McCarthy et al., 2010](#); [Puchwein & Springel, 2013](#)). In simulations, black hole particles can save up energy that they will eventually redistribute among their neighbours, heating them and suppressing star formation (e.g. [Booth & Schaye, 2009](#)).

To ensure that these physically inspired subgrid prescriptions result in realistic galaxy populations, their free parameters need to be calibrated to reproduce a chosen set of observations (see the discussion in Section 2.1 of [Schaye et al., 2015](#)). This necessary step does not detract from the predictive power of cosmological, hydrodynamical simulations: the highly non-linear relation between the subgrid model parameters and the simulated galaxy properties means that reproducing one observable does not imply that the simulation correctly predicts non-calibrated galaxy properties—if only. Hence, simulations should always be judged based on how well they can reproduce a wide range of observations. In this thesis, we mainly work with the BAHAMAS simulations, since they have been calibrated to reproduce the large-scale distribution of matter by fitting both the galaxy stellar mass function, ensuring that the abundance of galaxies as a function of mass is accurately reproduced, and the hot gas mass fraction of clusters, meaning that clusters contain the correct amount of baryons ([McCarthy et al., 2017](#)).

## 1.4 Weak gravitational lensing

One of the first confirmations of Einstein’s theory of general relativity came from the stronger predicted lensing effect of massive objects compared to Newton’s theory observed in the 1919 solar eclipse (e.g. [Eddington, 1919](#); [Dyson et al., 1920](#)). In the 80s, [Tyson et al. \(1984\)](#) suggested to use this lensing effect to measure the mass of galaxies through the coherent statistical distortion that their mass will induce in the shape of randomly oriented background galaxies.

### 1.4.1 The basics

Weak gravitational lensing relies on the fact that a point mass,  $M$ , will deflect the path of photons travelling within a closest distance  $\xi$ , by an angle

$$\begin{aligned}\hat{\alpha} &= \frac{4GM}{c^2} \frac{\xi}{|\xi|^2} \\ &= 12.5 \left( \frac{M}{10^{14.5} M_\odot} \right) \left( \frac{1 \text{ Mpc}}{\xi} \right) \text{ arcsec},\end{aligned}\tag{1.23}$$

where  $G$  is the gravitational constant and  $c$  the speed of light. The geometry of this deflection is illustrated in Fig. 1.4. This relation holds in the region where the gravitational field is weak, that is,  $\xi$  is much larger than the Schwarzschild radius,  $r_S = 2GM/c^2$ , of the point mass, and  $\hat{\alpha} \ll 1$ . In this regime, the apparent change in the source position in the source plane,  $\delta\alpha$ , for the observer can be written as

$$\delta\alpha = \theta - \beta = \frac{D_{\text{ds}}}{D_s} \hat{\alpha},\tag{1.24}$$

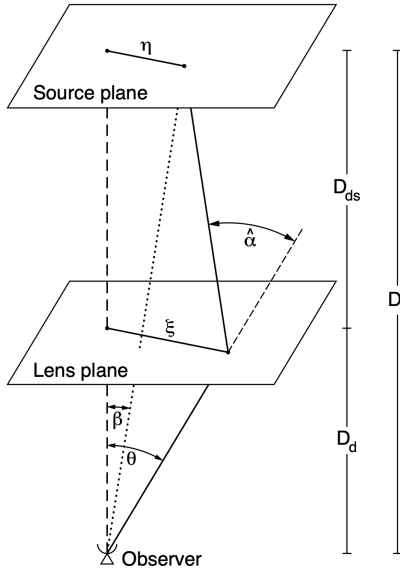


Figure 1.4: The geometry of the deflection of a ray of light by a point mass. The mass,  $M$ , bends a light ray emitted in the source plane at physical position  $\eta$ , or angular position  $\beta$ , by an angle  $\dot{\alpha}(\xi, M)$ , resulting in an apparent angular position  $\theta$  for the observer. In a curved Universe, the angular and physical positions can be related using the angular diameter distances  $D_i$ , with  $i = d$  indicating the deflector and  $i = s$  the source. *Figure taken from Bartelmann & Schneider (2001).*

where  $D_{ds}$  is the angular diameter distance to the source as seen from the deflector, and  $D_s$  is the angular diameter distance from the observer to the source plane.

This principle also holds for mass distributions, such as galaxies or clusters of galaxies, that are located at a fixed redshift, but with a density profile that varies along the line-of-sight. As long as the total deflection along the mass distribution is small,  $\sum_i \delta\alpha_i \ll 1$ , photons will travel in approximately straight lines and their total deflection is simply the sum of all the thin lens contributions along a fixed line-of-sight,  $l$ , through the matter distribution

$$\alpha(\theta) = \frac{4G}{c^2} \int d^2\theta' dl \frac{D_{ds}D_d}{D_s} \rho(\theta', l) \frac{\theta - \theta'}{|\theta - \theta'|^2} \quad (1.25)$$

$$= \frac{1}{\pi} \int d^2\theta' \kappa(\theta') \frac{\theta - \theta'}{|\theta - \theta'|^2}, \quad (1.26)$$

where we have changed to angular coordinates, using  $\theta = \xi/D_d$ , we have assumed  $\delta l \ll D_d$ , and we have introduced the convergence,

$$\kappa(\theta) = \frac{\Sigma(\theta)}{\Sigma_{\text{crit}}}, \quad (1.27)$$

where  $\Sigma$  is the surface mass density of the mass distribution along the line-of-sight and

$$\Sigma_{\text{crit}} = \frac{c^2}{4\pi G} \frac{D_s}{D_{\text{ds}} D_{\text{d}}} \quad (1.28)$$

is the critical surface mass density. The deflection in Eq. (1.26) can be written as a force sourced by a two-dimensional potential given by the Poisson equation,

$$\nabla_{\boldsymbol{\theta}}^2 \psi(\boldsymbol{\theta}) = 2\kappa(\boldsymbol{\theta}), \quad (1.29)$$

with

$$\psi(\boldsymbol{\theta}) = \frac{1}{\pi} \int d^2\boldsymbol{\theta}' \kappa(\boldsymbol{\theta}') \ln |\boldsymbol{\theta} - \boldsymbol{\theta}'|, \quad (1.30)$$

from which it is easy to see that

$$\boldsymbol{\alpha}(\boldsymbol{\theta}) = \nabla_{\boldsymbol{\theta}} \psi(\boldsymbol{\theta}). \quad (1.31)$$

For strong gravitational lensing, which occurs when  $\kappa > 1$ , background galaxies can generate multiple images and these images can get spectacularly distorted, as shown for the galaxy cluster Abell 370 in Fig. 1.5. Abell 370 was one of the first clusters for which these arcs have been detected (Paczynski, 1987). In the weak lensing regime, on the other hand, this deformation is not so obvious: it can only be measured statistically by looking at the coherent distortion of background galaxy shapes equidistant from the cluster centre. The weak lensing distortion can be calculated by considering how much the emitted light ray position changes in the source plane for small changes in the lens plane, that is,

$$\mathcal{A}_{ij} = \frac{\partial \beta_i}{\partial \theta_j} = \delta_{ij} - \psi_{,ij}(\boldsymbol{\theta}) = \begin{pmatrix} 1 - \kappa - \gamma_1 & -\gamma_2 \\ -\gamma_2 & 1 - \kappa + \gamma_1 \end{pmatrix}_{ij}, \quad (1.32)$$

where we identify the  $i$ th component of the vector  $\boldsymbol{x}$  as  $x_i$ , we have defined  $\psi_{,i} \equiv \partial \psi / \partial \theta_i$ ,  $\kappa$  is the convergence from Eq. (1.29), and we have introduced the components of the shear

$$\gamma_1(\boldsymbol{\theta}) = \frac{1}{2}(\psi_{,11}(\boldsymbol{\theta}) - \psi_{,22}(\boldsymbol{\theta})) \quad (1.33)$$

$$\gamma_2(\boldsymbol{\theta}) = \psi_{,12}(\boldsymbol{\theta}). \quad (1.34)$$

By diagonalizing the matrix  $\mathcal{A}$ , it is easy to see that the distortion matrix,  $\mathcal{A}^{-1}$ , has eigenvalues  $\lambda_{\pm} = (1 - \kappa \mp |\gamma|)^{-1}$ , where  $|\gamma| = \sqrt{\gamma_1^2 + \gamma_2^2}$ , showing that the convergence magnifies source images in the lens plane, whereas the shear distorts images, magnifying and compressing them along the eigenvectors located at an angle  $\phi_+$  and  $\phi_-$  from the  $\theta_1$ -axis, respectively, with  $\phi_{\pm} = \gamma_1/\gamma_2 \mp \sqrt{1 + (\gamma_1/\gamma_2)^2}$ .

Weak lensing observations are unable to probe the shear and the convergence directly, instead they can only measure galaxy shapes. The coherent shape distortion caused by the intervening mass distribution can be measured under the assumption that the background galaxies are intrinsically randomly oriented following a specific ellipticity distribution. We show an illustration of this effect in Fig. 1.6. Observers measure galaxy ellipticities from the moments of the light distribution (e.g. Blandford et al., 1991; Bartelmann &

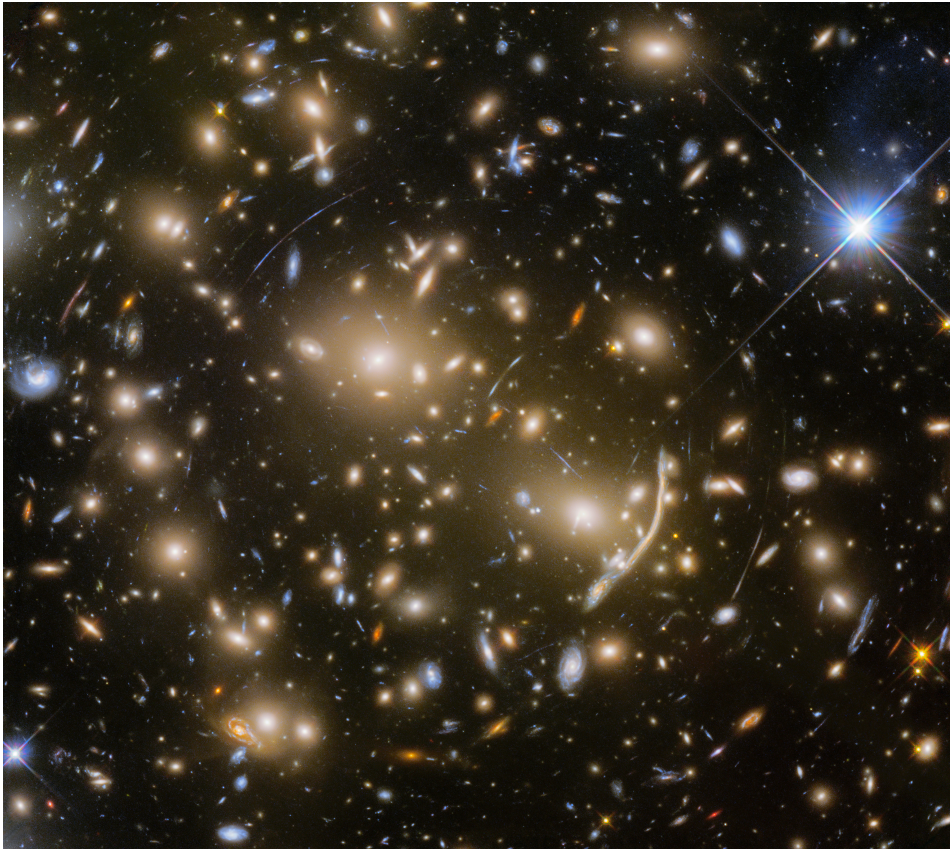


Figure 1.5: The galaxy cluster Abell 370, imaged with the Hubble Space Telescope by the Frontier Fields team. Circular arcs are clearly visible around the cluster centre: these are background galaxies that are strongly lensed and distorted by the mass of the cluster. Towards the cluster outskirts, this effect diminishes and it can only be detected statistically in the coherent distortion of large samples of background galaxies. *Picture from ESA/Hubble.*

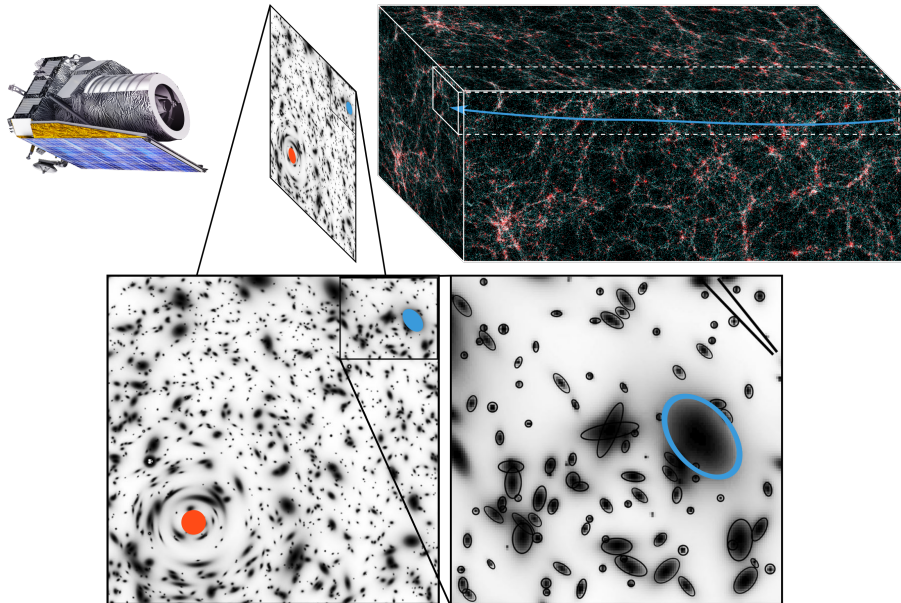
[Schneider, 2001](#)). In the weak lensing regime, the intrinsic complex ellipticity of the source,  $\epsilon^s$ , is related to the measured ellipticity after lensing,  $\epsilon$ , through a transformation that only depends on the reduced shear,  $g$ ,

$$\epsilon \approx \epsilon^s + g \quad (1.35)$$

with

$$g(\boldsymbol{\theta}) = \frac{\gamma(\boldsymbol{\theta})}{1 - \kappa(\boldsymbol{\theta})}, \quad (1.36)$$

and  $\gamma = \gamma_1 + i\gamma_2$ . Since the sources are assumed to be randomly oriented, we expect  $\langle \epsilon^s \rangle = 0$  for small local patches containing sufficient galaxies. This means that the mea-



1

Figure 1.6: The differential bending of photon paths due to an intervening mass distribution, as illustrated in the top-right slice through the density field of the Euclid Flagship simulation, distorts the observed galaxy shapes (bottom panels). A massive cluster, indicated by the red circle, strongly lenses background galaxies close to the cluster centre, distorting them into clearly visible arcs (bottom-left image). Further out, the effect is smaller and the distortion can only be inferred by averaging over the shape of a large sample of galaxies (bottom-right inset). The thick bars in the top-right corner show the true shear signal (bottom bar) and the signal inferred from averaging the observed galaxy shapes (top bar). *Figure created by combining Euclid flagship mock data and illustrations by Mellier (1999).*

sured ellipticity directly probes the reduced shear,

$$\langle \epsilon \rangle \approx g \approx \gamma. \quad (1.37)$$

Since weak lensing is by definition a small effect, a sufficient number of galaxies is needed to obtain a statistically significant measurement of the reduced shear.

#### 1.4.2 Cosmic shear

Blandford et al. (1991) extrapolated the weak lensing idea of galaxies and clusters to measure the mass fluctuations over large regions of the sky to constrain the typical clustering of matter between us and samples of background galaxies. This effect is known as “cosmic shear”.

The power spectrum of the cosmic shear can be derived heuristically from the convergence defined in Eq. (1.27). First, we can define the convergence for a source at redshift  $z_s$  being lensed by an overdense thin matter slice at redshift  $z_d$  as follows

$$\delta\kappa(\boldsymbol{\theta}, z_s, z_d) = \frac{4\pi G}{c^2} \frac{D_{ds} D_d}{D_s} (\rho(\boldsymbol{\theta}, z_d) - \bar{\rho}(z_d)) \delta l. \quad (1.38)$$

We can integrate this expression along the line-of-sight to the source while switching to comoving coordinates and using the fact that  $\rho(\boldsymbol{\theta}, z) - \bar{\rho} = \delta(\boldsymbol{\theta}, z)\bar{\rho}$  and

$$\bar{\rho} = \frac{3H_0^2 \Omega_{m,0}}{8\pi G}, \quad (1.39)$$

giving the effective convergence

$$\kappa_{\text{eff}}(\boldsymbol{\theta}, \chi_s) = \frac{3H_0^2 \Omega_{m,0}}{2c^2} \int_0^{\chi_s} d\chi \frac{f_K(\chi_s - \chi) f_K(\chi)}{f_K(\chi_s)} \frac{\delta(f_K(\chi)\boldsymbol{\theta}, \chi)}{a(\chi)}, \quad (1.40)$$

where  $f_K(\chi)$ , defined in Eq. (1.3), enters through the comoving angular diameter distance as can be seen from Eq. (1.18). Realistically, the shapes of many source galaxies over a range of redshifts, or comoving distances, will be measured. Assuming a source redshift distribution,  $n(z)$ , with  $n(z)dz = n(\chi)d\chi$ , a selection limit,  $\chi_{\text{lim}}$ , and accounting for the fact that only galaxies behind the matter overdensity will be lensed, we find

$$\kappa_{\text{eff}}(\boldsymbol{\theta}) = \frac{3H_0^2 \Omega_{m,0}}{2c^2} \int_0^{\chi_{\text{lim}}} d\chi W(\chi) f_K(\chi) \frac{\delta(f_K(\chi)\boldsymbol{\theta}, \chi)}{a(\chi)}, \quad (1.41)$$

with the lensing efficiency for the source distribution given by

$$W(\chi) = \int_\chi^{\chi_{\text{lim}}} d\chi_s n(\chi_s) \frac{f_K(\chi_s - \chi)}{f_K(\chi_s)}. \quad (1.42)$$

This simple argument gives the same result as a full general relativistic calculation of the deviation between neighbouring photons that reach the observer from minutely different angular positions after travelling through a perturbed homogeneous and isotropic universe (e.g. [Bartelmann & Schneider, 2001](#)).

The cosmic shear power spectrum,  $P_\gamma(\ell)$ , is then given by the correlations between galaxy shape distortions on different scales,  $\ell$ , in the plane of the sky. This power spectrum can be calculated from the convergence power spectrum, since the Fourier components of the shear,  $\gamma$ , and the convergence,  $\kappa$ , only differ by a phase—which can easily be derived from Eqs. (1.29), (1.33), and (1.34), and the fact that  $\gamma = \sqrt{\gamma_1^2 + \gamma_2^2} e^{2i\phi}$ . Using the Limber approximation (full details can be found in Section 2.4 of [Bartelmann & Schneider, 2001](#)), the projected correlations on the sky can be related to the 3D power spectrum of density fluctuations,  $P_m$ , as follows

$$P_\kappa(\ell) = \frac{9H_0^4 \Omega_{m,0}^2}{4c^2} \int_0^{\chi_{\text{lim}}} d\chi \frac{W^2(\chi)}{a^2(\chi)} P_m(\ell/f_K(\chi), \chi), \quad (1.43)$$

where  $\ell = f_K(\chi)\mathbf{k}_\perp$  and  $\mathbf{k}_\perp$  is the wavevector in the plane of the sky. This result has some noteworthy implications: a fixed lengthscale,  $\ell$ , on the sky receives contributions from many different physical scales along the line-of-sight, since it corresponds to larger scales at higher redshifts. Interestingly, however, fluctuations *along* the line-of-sight do not contribute to the cosmic shear, which implies that we can limit the impact of small-scale non-linearities by choosing an appropriate cutoff  $\ell_{\max}$ .

In conclusion, in cosmic shear analyses, the statistical shape distortion of galaxies at different distances from us, constrains the typical clustering of matter between us and those galaxies (e.g. [Tyson et al., 1984](#); [Blandford et al., 1991](#)). A successful weak lensing analysis is observationally challenging since it needs to be able to accurately measure the galaxy shapes, which requires a small and well-characterized point-spread function, a good understanding of the image noise, the blending of sources, and the impact of undetected background galaxies (e.g. [Hoekstra et al., 2017, 2021](#)). Another difficulty arises in the distance measurement to galaxies: due to the massive size of the survey, not all galaxies will have reliable spectroscopic measurements to determine distances from their spectra. Instead, their distance will have to be inferred photometrically with the information available from broadband filters, which results in significantly larger uncertainties (for a recent review, see [Salvato et al., 2019](#)).

Additionally, background galaxies that are part of coherent large-scale structures along the line-of-sight can have intrinsic correlations in their shape which are not of cosmological origin, but that depend on galaxy formation processes (e.g. [Croft & Metzler, 2000](#); [Heavens et al., 2000](#)). [Hirata & Seljak \(2004\)](#) identified that lensing structures additionally generate anti-correlated shape distortions between galaxies local to the lens that are stretched along the tidal field towards overdensities, and background galaxies that will be distorted tangentially to the tidal field generated by the overdensity. These intrinsic galaxy alignments pose a significant challenge for weak lensing surveys with different surveys finding different values for the strength of this signal (e.g. [Efstathiou & Lemos, 2018](#)). Fortunately, [Fortuna et al. \(2021\)](#) found that it is possible to constrain the strength of the intrinsic alignment of galaxies observationally, which can prevent the parameter being high-jacked to hide non-related systematic uncertainties in the analysis.

On the theoretical side, we also need accurate predictions of the average non-linear matter clustering,  $P_m(k)$  and its time evolution in order to correctly interpret the observed signal and infer the cosmological matter distribution (e.g. [Jain & Seljak, 1997](#); [Schneider et al., 1998](#)). The non-linear behaviour can be predicted accurately by dark matter-only (DMO) simulations. However, cosmological hydrodynamical simulations that evolve the ordinary and dark matter distribution jointly in an expanding universe, have shown that violent AGN feedback processes significantly alter the large-scale structure compared to universes that only contain dark matter (e.g. [Rudd et al., 2008](#); [Semboloni et al., 2011](#); [van Daalen et al., 2011, 2020](#)). While these effects can be mitigated by only considering large scales (as is done by the Dark Energy Survey, e.g. [Amon et al., 2022b](#)), future surveys would be throwing away a considerable amount of useful information by neglecting small scales (e.g. [Taylor et al., 2018](#)).

In the absence of observational data that can fully constrain the normal matter distribution, including small-scale baryonic effects in the matter power spectrum necessarily relies on cosmological, hydrodynamical simulations to predict the expected effect. As

[McCarthy et al. \(2017\)](#) stresses, it is important that the simulations correctly reproduce the observed properties of the large scale matter distribution. The main idea is to come up with an analysis method that can either add the baryonic contribution to the matter power spectrum predicted from suites of dark matter-only simulations, or remove the baryonic signal from the data. [Eifler et al. \(2015\)](#) and [Huang et al. \(2019\)](#) perform a principal component analysis of the matter power spectrum including baryonic effects which results in a flexible model for the expected signal that can be marginalized over in the cosmological analysis. [Mead et al. \(2015\)](#) use hydrodynamical simulations to calibrate a halo model with additional freedom in the halo density profiles to flexibly capture the total matter power spectrum, including baryons. [Schneider et al. \(2019\)](#) phenomenologically modify the matter distribution in DMO simulations by shifting particles in haloes such that the density profiles more closely match those in observations.

The need to account for all the aforementioned effects makes cosmic shear a complex cosmological observable. However, the potential gain in information about the Universe from directly probing the total matter distribution is enormous.

## 1.5 Galaxy clusters

The final cosmological probe of interest to this thesis, is the abundance of massive galaxy clusters. Clusters are located at the nodes of the intricate cosmic web, resulting in a continuous accretion of smaller galaxy groups, gas, and an occasional merger with another massive cluster. The cluster mass growth depends strongly on the amount of matter in the Universe and how clustered it is. The late-time accelerating expansion due to dark energy suppresses their growth and leaves a clear imprint in the cluster abundance as a function of mass and redshift, making clusters powerful probes of the matter distribution of the Universe and also of the history of dark energy (e.g. [Allen et al., 2011](#)). However, since the cluster abundance decreases exponentially with increasing mass, any error in the cluster mass calibration will result in highly biased estimates of the cosmology.

Clusters are fascinating laboratories: they contain hundreds to thousands of galaxies within a radius of a few million lightyears, making them easy to detect as localized overdensities of galaxies in large optical surveys. In the 50s and 60s, [Abell \(1958\)](#) and [Zwicky et al. \(1961, 1963, 1966\)](#) released large catalogues of clusters identified exactly this way. The launch of the first X-ray telescopes in the 70s, opened up a whole new view (e.g. [Sarazin, 1986](#)). It became clear that clusters are filled with hot, metal-enriched gas that is supported in a state of quasi-equilibrium with the gas pressure opposing full gravitational collapse. The hot gas is a shining beacon in X-rays. Additionally, the hot cluster electrons can boost the photons of the CMB through inverse Compton scattering, leaving behind a clear hole in the temperature fluctuations of the CMB below a frequency of  $\approx 200$  GHz, known as the Sunyaev–Zel’dovich effect ([Sunyaev & Zeldovich, 1972](#)). There are thus many different ways to observationally identify clusters.

On the theoretical side, we can use large-volume, dark matter-only simulations to accurately predict the abundance of clusters for varying cosmologies (e.g. [McClintock et al., 2019](#); [Nishimichi et al., 2019](#); [Bocquet et al., 2020](#)). The problem that we face, however, is that a significant fraction of the total mass of actual clusters consists of hot

gas that behaves differently from the dark matter. [Velliscig et al. \(2014\)](#) showed that AGN feedback redistributes the hot cluster gas component to large scales, resulting in lower masses closer to the cluster centre when comparing to clusters consisting purely of collisionless dark matter. Since galaxy clusters dominate the total matter along their line-of-sight, their total mass, including dark and ordinary matter, can be measured from the weak lensing signal that they generate in the shapes of the background galaxies, as described in Section 1.4.1. This effect was first detected by [Tyson et al. \(1990\)](#). The only remaining problem is then linking the inferred mass from observations to the theoretical, DMO cluster mass.

The mass change is small for the most massive clusters ( $m_{500c} > 10^{14.5} M_\odot$ )<sup>6</sup> since they are able to retain practically all their baryons within the radius  $r_{500c}$  where weak lensing observations are able to infer the total mass. Hence, the differing distribution of the baryons is not a big problem for current cluster surveys whose detection limit is  $m_{500c,\text{lim}} \approx 10^{14.5} M_\odot$  (e.g. [Bocquet et al., 2016](#)). However, future surveys will be able to detect clusters down to masses  $m_{500c,\text{lim}} \approx 10^{14} M_\odot$  (e.g. [Sartoris et al., 2016](#)), where the mass change compared to the DMO halo is predicted to significantly exceed the sub-percent statistical uncertainty of the cluster mass determination afforded by the massive cluster sample (e.g. [Köhlinger et al., 2015](#)). Our only options are then to either link the observed cluster mass to the theoretical mass that the same cluster would have in a universe consisting only of dark matter (e.g. [Balaguera-Antolínez & Porciani, 2013](#); [Cusworth et al., 2014](#)), or to predict the cosmology dependence of the cluster abundance in large-volume cosmological hydrodynamical simulations. Unfortunately, the computational cost of the latter option has so far been a barrier to its realization.

## 1.6 This thesis

In this thesis, we study how our imperfect knowledge of galaxy formation processes and their impact on the total matter distribution impacts the cosmological analysis of future all-sky galaxy surveys. Galactic winds generated by supernova explosions or buoyant bubbles lifted by the powerful supermassive black holes at the centres of galaxies significantly alter the matter distribution compared to what it would be if we only accounted for gravitational collapse. This poses a challenging problem for future surveys, since these processes are still not well-understood theoretically.

In [Chapter 2](#), we shed light on the issue of the total matter distribution uncertainty for cosmic shear surveys. We resort to a phenomenological halo model that can incorporate observational information to constrain the total matter distribution, while including enough freedom to quantify how the unobserved baryonic matter can impact the final answer. We show that it is crucially important to constrain the amount of hot gas in groups and clusters of galaxies, since these objects dominate the total matter clustering signal on intermediate scales that dominate the cosmic shear signal. We also reiterate the important point that the dominant baryonic effect is not changing the clustering properties of

---

<sup>6</sup>The mass  $m_{500c}$  is the total mass within the region  $r_{500c}$  where the average density of the cluster is  $\langle \rho \rangle (< r_{500c}) = 500 \rho_{\text{crit}}(z)$ .

haloes, but rather the redistribution and systematic lowering of the halo mass compared to a universe that only includes dark matter.

We switch our focus to cluster abundance studies in **Chapter 3**, instigated by how successfully the halo model of Chapter 2 reproduces the impact of baryons on the matter distribution seen in simulations, while only using observational data for the baryon distribution. We use X-ray observations of the hot gas in clusters to constrain the total galaxy cluster density profile and we establish a link between observed haloes and the theoretical haloes in a universe containing only dark matter whose abundance we can predict with simulations. Inferring the cluster mass from mock weak lensing observations then allows us to quantify the mass bias incurred when not properly accounting for the differing density profiles between the ordinary and the dark matter. We show that future surveys with such inaccurate mass calibrations will infer significantly biased values for the amount of matter, its clustering, and the dark energy equation of state.

In **Chapter 4**, we tackle the mass calibration of galaxy clusters in a different way. We suggest that, currently, there is an unfair onus on weak lensing mass calibrations to constrain 3D cluster masses that are easy to measure in simulations but difficult to infer observationally. We propose to calibrate the cluster abundance as a function of the excess projected mass of a cluster: a quantity that is directly probed observationally and easily measured in simulations. We show that these projected masses have a significantly lower observational uncertainty than 3D cluster masses. Moreover, using a large suite of dark matter-only simulations, we find that the cluster abundance as a function of the projected mass is at least as sensitive to changes in cosmology as the abundance measured for 3D masses. As a result, this projected mass determination can significantly reduce the systematic uncertainty in the mass calibration for cluster abundance studies.

Finally, in **Chapter 5**, we use cosmological hydrodynamical simulations to quantify the impact of baryons on the excess projected mass measurements proposed in Chapter 4 by comparing the change in mass between the same haloes in universes with and without baryons. We find that the projected masses are slightly less affected by feedback processes than 3D halo masses, since the projected mass receives contributions from the halo outskirts along the line-of-sight where the baryons eventually trace the dark matter. While the reduction is not dramatic, together with the decreased systematic uncertainty in the mass calibration it provides another benefit to projected mass calibrations.

## Bibliography

- Aarseth S. J., 1963, *Monthly Notices of the Royal Astronomical Society*, 126, 223 → p. 16
- Abbott T. M. C., et al., 2021, *ApJS*, 255, 20 → p. 4
- Abdalla E., et al., 2022, *Journal of High Energy Astrophysics*, 34, 49 → p. 7
- Abell G. O., 1958, *The Astrophysical Journal Supplement Series*, 3, 211 → p. 26
- Addison G. E., Huang Y., Watts D. J., Bennett C. L., Halpern M., Hinshaw G., Weiland J. L., 2016, *ApJ*, 818, 132 → p. 7
- Aihara H., et al., 2018, *Publ. Astron. Soc. Japan*, 70, 1 → p. 4
- Allen S. W., Evrard A. E., Mantz A. B., 2011, *Annu. Rev. Astron. Astrophys.*, 49, 409 → p. 26
- Amon A., et al., 2022a, arXiv:2202.07440 [astro-ph] → p. 8
- Amon A., et al., 2022b, *Phys. Rev. D*, 105, 023514 → p. 8, 25
- Anand G. S., Tully R. B., Rizzi L., Riess A. G., Yuan W., 2022, Comparing Tip of the Red Giant Branch Distance Scales: An Independent Reduction of the Carnegie-Chicago Hubble Program and the Value of the Hubble Constant ([arXiv:2108.00007](https://arxiv.org/abs/2108.00007)), doi:10.48550/arXiv.2108.00007 → p. 7
- Asgari M., et al., 2021, *A&A*, 645, A104 → p. 8
- Bacon D. J., Refregier A. R., Ellis R. S., 2000, *Monthly Notices of the Royal Astronomical Society*, 318, 625 → p. 6
- Bahcall N. A., Cen R., 1993, *The Astrophysical Journal*, 407, L49 → p. 6
- Balaguera-Antolínez A., Porciani C., 2013, *J. Cosmol. Astropart. Phys.*, 2013 → p. 27
- Bardeen J. M., Steinhardt P. J., Turner M. S., 1983, *Phys. Rev. D*, 28, 679 → p. 13
- Bardeen J. M., Bond J. R., Kaiser N., Szalay A. S., 1986, *Astrophys. J.*, 304, 15 → p. 15
- Barnes J., Hut P., 1986, *Nature*, 324, 446 → p. 16
- Bartelmann M., Schneider P., 2001, *Physics Reports*, 340, 291 → p. 20, 21, 24
- Birrer S., et al., 2020, *A&A*, 643, A165 → p. 7
- Blandford R. D., 1999, 182, 87 → p. 18
- Blandford R. D., Saust A. B., Brainerd T. G., Villumsen J. V., 1991, *Monthly Notices of the Royal Astronomical Society*, 251, 600 → p. 21, 23, 25
- Bocquet S., Saro A., Dolag K., Mohr J. J., 2016, *Mon. Not. R. Astron. Soc.*, 456, 2361 → p. 27
- Bocquet S., et al., 2019, *Astrophys. J.*, 878, 55 → p. 7
- Bocquet S., Heitmann K., Habib S., Lawrence E., Uram T., Frontiere N., Pope A., Finkel H., 2020, *Astrophys. J.*, 901, 5 → p. 17, 26
- Booth C. M., Schaye J., 2009, *Mon. Not. R. Astron. Soc.*, 398, 53 → p. 19
- Chiba T., De Felice A., Tsujikawa S., 2013, *Phys. Rev. D*, 87, 083505 → p. 6
- Clowe D., Bradač M., Gonzalez A. H., Markevitch M., Randall S. W., Jones C., Zaritsky D., 2006, *The Astrophysical Journal*, 648, L109 → p. 6
- Cole S., et al., 2005, *Monthly Notices of the Royal Astronomical Society*, 362, 505 → p. 6, 12
- Croft R. A. C., Metzler C. A., 2000, *The Astrophysical Journal*, 545, 561 → p. 8, 25
- Curtis H. D., 1915, *Publications of the Astronomical Society of the Pacific*, 27, 214 → p. 1
- Cusworth S. J., Kay S. T., Battye R. A., Thomas P. A., 2014, *Mon. Not. R. Astron. Soc.*, 439, 2485 → p. 27
- Dalla Vecchia C., Schaye J., 2008, *Mon. Not. R. Astron. Soc.*, 387, 1431 → p. 18
- Dalla Vecchia C., Schaye J., 2012, *Mon. Not. R. Astron. Soc.*, 426, 140 → p. 18
- Dyson F. W., Eddington A. S., Davidson C., 1920, *Philosophical Transactions of the Royal Society of London*, 220, 291 → p. 19
- Eastwood J. W., 1975, *Journal of Computational Physics*, 18, 1 → p. 16
- Eddington A. S., 1919, *The Observatory*, 42, 119 → p. 19

- Efstathiou G., 2020, A Lockdown Perspective on the Hubble Tension (with Comments from the SH0ES Team) ([arXiv:2007.10716](https://arxiv.org/abs/2007.10716)) → p. 7
- Efstathiou G., Eastwood J. W., 1981, *Monthly Notices of the Royal Astronomical Society*, 194, 503 → p. 16
- Efstathiou G., Lemos P., 2018, *Mon. Not. R. Astron. Soc.* → p. 8, 25
- Efstathiou G., Frenk C. S., White S. D. M., Davis M., 1988, *Mon. Not. R. Astron. Soc.*, 235, 715 → p. 15
- Eifler T., Krause E., Dodelson S., Zentner A. R., Hearin A. P., Gnedin N. Y., 2015, *Mon. Not. R. Astron. Soc.*, 454, 2451 → p. 26
- Einstein A., 1916, *Annalen der Physik*, 354, 769 → p. 9
- Eisenstein D. J., et al., 2005, *The Astrophysical Journal*, 633, 560 → p. 6, 12
- Euclid Collaboration et al., 2018, 000 → p. 17
- Faber S. M., et al., 1997, *The Astronomical Journal*, 114, 1771 → p. 18
- Fabian A. C., 1999, *Monthly Notices of the Royal Astronomical Society*, 308, L39 → p. 18
- Fabjan D., Borgani S., Tornatore L., Saro A., Murante G., Dolag K., 2010, *Monthly Notices of the Royal Astronomical Society*, 401, 1670 → p. 19
- Fall S. M., Efstathiou G., 1980, *Monthly Notices of the Royal Astronomical Society*, 193, 189 → p. 18
- Feeley S. M., Peiris H. V., Williamson A. R., Nissanke S. M., Mortlock D. J., Alsing J., Scolnic D., 2019, *Phys. Rev. Lett.*, 122, 061105 → p. 8
- Fortuna M. C., et al., 2021, *A&A*, 654, A76 → p. 8, 25
- Freedman W. L., 2021, *ApJ*, 919, 16 → p. 7
- Freedman W. L., et al., 2019, *The Astrophysical Journal*, 882, 34 → p. 7
- Friedmann A., 1922, *Zeitschrift fur Physik*, 10, 377 → p. 10
- Frieman J. A., Turner M. S., Huterer D., 2008, *Annu. Rev. Astron. Astrophys.*, 46, 385 → p. 6
- Gerardi F., Martinelli M., Silvestri A., 2019, *J. Cosmol. Astropart. Phys.*, 2019, 042 → p. 6
- Giblin B., et al., 2021, *Astronomy and Astrophysics*, 645, A105 → p. 4
- Guth A. H., 1981, *Phys. Rev. D*, 23, 347 → p. 13
- Habib S., Heitmann K., Higdon D., Nakhleh C., Williams B., 2007, *Physical Review D*, 76, 083503 → p. 17
- Hand E., 2012, *Nature*, 490, 16 → p. 3
- Hearin A. P., Zentner A. R., Ma Z., 2012, *J. Cosmol. Astropart. Phys.*, 2012, 034 → p. 4
- Heavens A., Refregier A., Heymans C., 2000, *Monthly Notices of the Royal Astronomical Society*, 319, 649 → p. 8, 25
- Heitmann K., Higdon D., Nakhleh C., Habib S., 2006, *The Astrophysical Journal*, 646, L1 → p. 17
- Heitmann K., Higdon D., White M., Habib S., Williams B. J., Lawrence E., Wagner C., 2009, *Astrophys. J.*, 705, 156 → p. 17
- Heymans C., et al., 2021, *Astronomy and Astrophysics*, 646, A140 → p. 7
- Hirata C. M., Seljak U., 2004, *Phys. Rev. D - Part. Fields, Gravit. Cosmol.*, 70, 1 → p. 8, 25
- Hoekstra H., Yee H. K. C., Gladders M. D., 2002, *The Astrophysical Journal*, 577, 595 → p. 6
- Hoekstra H., Viola M., Herbonnet R., 2017, *Mon. Not. R. Astron. Soc.*, 468, 3295 → p. 25
- Hoekstra H., Kannawadi A., Kitching T. D., 2021, *Astronomy and Astrophysics*, 646, A124 → p. 25
- Hogg D. W., Eisenstein D. J., Blanton M. R., Bahcall N. A., Brinkmann J., Gunn J. E., Schneider D. P., 2005, *The Astrophysical Journal*, Volume 624, Issue 1, pp. 54-58., 624, 54 → p. 8
- Hu W., Dodelson S., 2002, *Annu. Rev. Astron. Astrophys.*, 40, 171 → p. 6
- Hu W., Sugiyama N., Silk J., 1997, *Nature*, 386, 37 → p. 12
- Huang H.-j., Eifler T., Mandelbaum R., Dodelson S., 2019, *Mon. Not. R. Astron. Soc.*, 488, 1652 → p. 26

- Hubble E. P., 1925, *The Observatory*, 48, 139 → p. 1
- Hubble E., 1929, *Proceedings of the National Academy of Sciences*, 15, 168 → p. 1
- Jain B., Seljak U., 1997, *Astrophys. J.*, 484, 560 → p. 25
- Joachimi B., et al., 2015, *Space Sci Rev*, 193, 1 → p. 8
- Joachimi B., et al., 2021, *A&A*, 646, A129 → p. 8
- Joudaki S., et al., 2020, *A&A*, 638, L1 → p. 8
- Joyce A., Lombriser L., Schmidt F., 2016, *Annu. Rev. Nucl. Part. Sci.*, 66, 95 → p. 6
- Kaiser N., 1984, *Astrophys. J.*, 284, L9 → p. 15
- Köhlinger F., Hoekstra H., Eriksen M., 2015, *Mon. Not. R. Astron. Soc.*, 453, 3107 → p. 27
- Kuijken K., et al., 2019, *A&A*, 625, A2 → p. 4
- LSST Science Collaboration et al., 2009, arXiv e-prints, p. arXiv:0912.0201 → p. 2
- Laureijs R., et al., 2011, preprint → p. 2
- Laurent P., et al., 2016, *J. Cosmol. Astropart. Phys.*, 2016, 060 → p. 8
- Lemaître G., 1927, *Annales de la Société Scientifique de Bruxelles*, 47, 49 → p. 1
- Linde A. D., 1982, *PHYSICS LETTERS*, 108, 5 → p. 13
- Magorrian J., et al., 1998, *Astron. J.*, 115, 2285 → p. 18
- Mandelbaum R., et al., 2018, *Publ. Astron. Soc. Japan*, 70, 1 → p. 4
- McCarthy I. G., et al., 2010, *Monthly Notices of the Royal Astronomical Society*, pp 822–839 → p. 19
- McCarthy I. G., Schaye J., Bird S., Le Brun A. M., 2017, *Mon. Not. R. Astron. Soc.*, 465, 2936 → p. 19, 26
- McClintock T., et al., 2019, *Astrophys. J.*, 872, 53 → p. 17, 26
- Mead A. J., Peacock J. A., Heymans C., Joudaki S., Heavens A. F., 2015, *Mon. Not. R. Astron. Soc.*, 454, 1958 → p. 26
- Mellier Y., 1999, *Annu. Rev. Astron. Astrophys.*, 37, 127 → p. 23
- Motloch P., Hu W., 2018, *Phys. Rev. D*, 97, 103536 → p. 7
- Motloch P., Hu W., 2020, *Phys. Rev. D*, 101, 083515 → p. 7
- Navarro J. F., Frenk C. S., White S. D. M., 1996, *The Astrophysical Journal*, 462, 563 → p. 16
- Navarro J. F., Frenk C. S., White S. D. M., 1997, *Astrophys. J.*, 490, 493 → p. 16
- Nishimichi T., et al., 2019, *Astrophys. J.*, 884, 29 → p. 17, 26
- Ntelis P., et al., 2017, *J. Cosmol. Astropart. Phys.*, 2017, 019 → p. 8
- Obied G., Dvorkin C., Heinrich C., Hu W., Miranda V., 2017, *Phys. Rev. D*, 96, 083526 → p. 7
- Paczynski B., 1987, *Nature*, 325, 572 → p. 21
- Peacock J. A., et al., 2001, *Nature*, 410, 169 → p. 6
- Peebles P. J. E., 1965, *ApJ*, 142, 1317 → p. 15
- Peebles P. J. E., 1967, *The Astrophysical Journal*, 147, 859 → p. 15
- Peebles P. J., 2012, *Annu. Rev. Astron. Astrophys.*, 50, 1 → p. 6
- Peebles P. J. E., 2017, *Nat Astron*, 1, 0057 → p. 6
- Peebles P. J. E., Yu J. T., 1970, *Astrophys. J.*, 162, 815 → p. 12
- Percival W. J., et al., 2001, *Monthly Notices of the Royal Astronomical Society*, 327, 1297 → p. 6
- Perlmutter S., et al., 1999, *Astrophys. J.*, 517, 565 → p. 6, 13
- Planck Collaboration et al., 2017, *A&A*, 607, A95 → p. 7
- Planck Collaboration et al., 2020a, *A&A*, 641, A1 → p. 14
- Planck Collaboration et al., 2020b, *Astron. Astrophys.*, 641, A6 → p. 4, 6, 7, 9, 11, 12, 14
- Press W. H., Schechter P., 1974, *Astrophys. J.*, 187, 425 → p. 15
- Puchwein E., Springel V., 2013, *Monthly Notices of the Royal Astronomical Society*, 428, 2966 → p. 18, 19
- Rees M. J., Ostriker J. P., 1977, *Monthly Notices of the Royal Astronomical Society*, 179, 541 → p. 18

- Rhodes J., et al., 2017, *ApJS*, 233, 21 → p. 3
- Rhodes J., et al., 2019, Bulletin of the American Astronomical Society, 51, 201 → p. 3
- Riess A. G., et al., 1998, *Astron. J.*, 116, 1009 → p. 6, 13
- Riess A. G., et al., 2021, A Comprehensive Measurement of the Local Value of the Hubble Constant with 1 Km/s/Mpc Uncertainty from the Hubble Space Telescope and the SH0ES Team → p. 7
- 1**
- Rubin V. C., Ford Jr. W. K., 1970, *The Astrophysical Journal*, 159, 379 → p. 6
- Rubin V. C., Thonnard N., Ford Jr. W. K., 1980, *ApJ*, 238, 471 → p. 6
- Rudd D. H., Zentner A. R., Kravtsov A. V., 2008, *Astrophys. J.*, 672, 19 → p. 25
- Salvato M., Ilbert O., Hoyle B., 2019, *Nat Astron*, 3, 212 → p. 25
- Sarazin C. L., 1986, *Rev. Mod. Phys.*, 58, 1 → p. 26
- Sartoris B., et al., 2016, *Mon. Not. R. Astron. Soc.*, 459, 1764 → p. 27
- Schaye J., 2004, *Astrophys. J.*, 609, 667 → p. 18
- Schaye J., Dalla Vecchia C., 2008, *Mon. Not. R. Astron. Soc.*, 383, 1210 → p. 18
- Schaye J., et al., 2015, *Mon. Not. R. Astron. Soc.*, 446, 521 → p. 19
- Schneider P., Van Waerbeke L., Jain B., Kruse G., 1998, *Mon. Not. R. Astron. Soc.*, 296, 873 → p. 25
- Schneider A., Teyssier R., Stadel J., Chisari N. E., Brun A. M. L., Amara A., Refregier A., 2019, *J. Cosmol. Astropart. Phys.*, 2019, 020 → p. 26
- Semboloni E., Hoekstra H., Schaye J., Van Daalen M. P., McCarthy I. G., 2011, *Mon. Not. R. Astron. Soc.*, 417, 2020 → p. 25
- Sevilla-Noarbe I., et al., 2021, *ApJS*, 254, 24 → p. 4
- Shapley H., Curtis H. D., 1921, The Scale of the Universe. Washington, D.C., Published by the National research council of the National academy of sciences → p. 1
- Silk J., 1977, *The Astrophysical Journal*, 211, 638 → p. 18
- Silk J., Rees M. J., 1998, *Astron. Astrophys.*, 331, L1 → p. 18
- Slipher V. M., 1921, *Popular Astronomy*, 29, 128 → p. 1
- Slipher V. M., 1922, 4, 284 → p. 1
- Soares-Santos M., et al., 2019, *ApJ*, 876, L7 → p. 8
- Somerville R. S., Davé R., 2015, *Annu. Rev. Astron. Astrophys.*, 53, 51 → p. 18
- Spergel D. N., et al., 2003, *Astrophys. J. Suppl. Ser.*, 148, 175 → p. 6
- Spergel D., et al., 2015, Wide-Field InfrarRed Survey Telescope-Astrophysics Focused Telescope Assets WFIRST-AFTA 2015 Report ([arXiv:1503.03757](https://arxiv.org/abs/1503.03757)) → p. 2
- Springel V., et al., 2005, *Nature*, 435, 629 → p. 16, 17
- Stromberg G., 1925, *The Astrophysical Journal*, 61, 353 → p. 1
- Sunyaev R. A., Zeldovich Y. B., 1972, The Observation of Relic Radiation as a Test of the Nature of X-Ray Radiation from the Clusters of Galaxies. Vol. 4 → p. 26
- Taylor P. L., Kitching T. D., McEwen J. D., 2018, *Phys. Rev. D*, 98, 043532 → p. 4, 25
- The LIGO Scientific Collaboration and The Virgo Collaboration et al., 2017, *Nature*, 551, 85 → p. 7
- Tyson J. A., Valdes F., Jarvis J. F., Mills Jr. A. P., 1984, *The Astrophysical Journal*, 281, L59 → p. 19, 25
- Tyson J. A., Valdes F., Wenk R. A., 1990, *The Astrophysical Journal*, 349, L1 → p. 27
- Undagoitia T. M., Rauch L., 2016, *J. Phys. G: Nucl. Part. Phys.*, 43, 013001 → p. 6
- Van Waerbeke L., et al., 2000, *Astronomy and Astrophysics*, v.358, p.30-44 (2000), 358, 30 → p. 6
- Velliscig M., van Daalen M. P., Schaye J., McCarthy I. G., Cacciato M., Le Brun A. M., Vecchia C. D., 2014, *Mon. Not. R. Astron. Soc.*, 442, 2641 → p. 27
- Wang Y., Pogosian L., Zhao G.-B., Zucca A., 2018, *ApJ*, 869, L8 → p. 6
- Weinberg S., 1972, Gravitation And Cosmology: Principles And Applications Of The General Theory Of Relativity. John Wiley & Sons, Inc. → p. 10

- Weinberg S., 1989, *Rev. Mod. Phys.*, 61, 1 → p. 6
- White S. D. M., Rees M. J., 1978, *Mon. Not. R. Astron. Soc.*, 183, 341 → p. 18
- Wiersma R. P. C., Schaye J., Smith B. D., 2009a, *Mon. Not. R. Astron. Soc.*, 393, 99 → p. 18
- Wiersma R. P. C., Schaye J., Theuns T., Dalla Vecchia C., Tornatore L., 2009b, *Mon. Not. R. Astron. Soc.*, 399, 574 → p. 18
- Wilson R. E., 1915, *Popular Astronomy*, 23, 553 → p. 1
- Wittman D. M., Tyson J. A., Kirkman D., Dell'Antonio I., Bernstein G., 2000, *Nature*, 405, 143 → p. 6
- Xu G., 1995, *The Astrophysical Journal Supplement Series*, 98, 355 → p. 16
- Zwicky F., 1933, *Helvetica Physica Acta*, 6, 110 → p. 6
- Zwicky F., Herzog E., Wild P., Karpowicz M., Kowal C. T., 1961, Catalogue of Galaxies and of Clusters of Galaxies, Vol. I → p. 26
- Zwicky F., Herzog E., Wild P., 1963, Catalogue of Galaxies and of Clusters of Galaxies, Vol. 2 → p. 26
- Zwicky F., Herzog E., Wild P., 1966, Catalogue of Galaxies and of Clusters of Galaxies, Vol. 3 → p. 26
- van Daalen M. P., Schaye J., Booth C. M., Dalla Vecchia C., 2011, *Monthly Notices of the Royal Astronomical Society*, 415, 3649 → p. 25
- van Daalen M. P., McCarthy I. G., Schaye J., 2020, *Mon. Not. R. Astron. Soc.*, 491, 2424 → p. 25



## 2 | The impact of the observed baryon distribution in haloes on the total matter power spectrum

Based on

Stijn N. B. Debackere, Joop Schaye, Henk Hoekstra

*Monthly Notices of the Royal Astronomical Society, Volume 492, Issue 2,  
p. 2285-2307 (2020)*

2

The interpretation of upcoming weak gravitational lensing surveys depends critically on our understanding of the matter power spectrum on scales  $k < 10 h \text{ Mpc}^{-1}$ , where baryonic processes are important. We study the impact of galaxy formation processes on the matter power spectrum using a halo model that treats the stars and gas separately from the dark matter distribution. We use empirical constraints from X-ray observations (hot gas) and halo occupation distribution modelling (stars) for the baryons. Since X-ray observations cannot generally measure the hot gas content outside  $r_{500c}$ , we vary the gas density profiles beyond this radius. Compared with dark matter only models, we find a total power suppression of 1 per cent (5 per cent) on scales 0.2 to  $1 h \text{ Mpc}^{-1}$  ( $0.5$  to  $2 h \text{ Mpc}^{-1}$ ), where lower baryon fractions result in stronger suppression. We show that groups of galaxies ( $10^{13} < m_{500c}/(h^{-1} M_\odot) < 10^{14}$ ) dominate the total power at all scales  $k \lesssim 10 h \text{ Mpc}^{-1}$ . We find that a halo mass bias of 30 per cent (similar to what is expected from the hydrostatic equilibrium assumption) results in an underestimation of the power suppression of up to 4 per cent at  $k = 1 h \text{ Mpc}^{-1}$ , illustrating the importance of measuring accurate halo masses. Contrary to work based on hydrodynamical simulations, our conclusion that baryonic effects can no longer be neglected is not subject to uncertainties associated with our poor understanding of feedback processes. Observationally, probing the outskirts of groups and clusters will provide the tightest constraints on the power suppression for  $k \lesssim 1 h \text{ Mpc}^{-1}$ .

## 2.1 Introduction

Since the discovery of the Cosmic Microwave Background (CMB) (Penzias & Wilson, 1965; Dicke et al., 1965), cosmologists have continuously refined the values of the cosmological parameters. This resulted in the discovery of the accelerated expansion of the Universe (Riess et al., 1998; Perlmutter et al., 1999) and the concordance Lambda cold dark matter ( $\Lambda$ CDM) model. Future surveys such as Euclid<sup>1</sup>, the Large Synoptic Survey Telescope (LSST)<sup>2</sup>, and the Wide Field Infra-Red Survey Telescope (WFIRST)<sup>3</sup> aim to constrain the nature of this mysterious acceleration to establish whether it is caused by a cosmological constant or dark energy. This is one of the largest gaps in our current understanding of the Universe.

To probe the physical cause of the accelerated expansion, and to discern between different models for dark energy or even a modified theory of gravity, we require precise measurements of the growth of structure and the expansion history over a range of redshifts. This is exactly what future galaxy surveys aim to do, e.g. using a combination of weak gravitational lensing and galaxy clustering. Weak lensing measures the correlation in the distortion of galaxy shapes for different redshift bins, which depends on the matter distribution in the Universe, and thus on the matter power spectrum (for reviews, see e.g. Hoekstra & Jain, 2008; Kilbinger, 2015; Mandelbaum, 2018). The theoretical matter power spectrum is thus an essential ingredient for a correct interpretation of weak lensing observations.

The matter power spectrum can still not be predicted well at small scales ( $k \gtrsim 0.3 h \text{ Mpc}^{-1}$ ) because of the uncertainty introduced by astrophysical processes related to galaxy formation (Rudd et al., 2008; van Daalen et al., 2011; Semboloni et al., 2011). In order to provide stringent cosmological constraints with future surveys, the prediction of the matter power spectrum needs to be accurate at the sub-percent level (Hearin et al., 2012).

Collisionless N-body simulations, i.e. dark matter only (DMO) simulations, can provide accurate estimates of the non-linear effects of gravitational collapse on the matter power spectrum. They can be performed using a large number of particles, and in big cosmological boxes for many different cosmologies (e.g. Heitmann et al., 2009, 2010; Lawrence et al., 2010; Angulo et al., 2012). The distribution of baryons, however, does not perfectly trace that of the dark matter: baryons can cool and collapse to high densities, sparking the formation of galaxies. Galaxy formation results in violent feedback that can redistribute gas to large scales. Furthermore, these processes induce a back-reaction on the distribution of dark matter (e.g. van Daalen et al., 2011, 2019; Velliscig et al., 2014). Hence, the redistribution of baryons and dark matter modifies the power spectrum relative to that from DMO simulations.

Weak lensing measurements obtain their highest signal-to-noise ratio on scales  $k \approx 1 h \text{ Mpc}^{-1}$  (see Section 1.8.5 in Amendola et al., 2018). van Daalen et al. (2011) used the OWLS suite of cosmological simulations (Schaye et al., 2010) to show that the inclusion

---

<sup>1</sup><http://www.euclid-ec.org>

<sup>2</sup><http://www.lsst.org/>

<sup>3</sup><http://wfirst.gsfc.nasa.gov>

of baryon physics, particularly feedback from Active Galactic Nuclei (AGN), influences the matter power spectrum at the 1 to 10 per cent level between  $0.3 < k/(h \text{ Mpc}^{-1}) < 1$  in their most realistic simulation that reproduced the hot gas properties of clusters of galaxies. Further studies (e.g. [Vogelsberger et al., 2014b](#); [Hellwing et al., 2016](#); [Springel et al., 2017](#); [Chisari et al., 2018](#); [Peters et al., 2018](#); [van Daalen et al., 2019](#)) have found similar results. [Sembolini et al. \(2011\)](#) have shown, also using the OWLS simulations, that ignoring baryon physics in the matter power spectrum results in biased weak lensing results, reaching a bias of up to 40 per cent in the dark energy equation of state parameter  $w_0$  for a Euclid-like survey.

Current state-of-the-art hydrodynamical simulations allow us to study the influence of baryons on the matter power spectrum, but cannot predict it from first principles. Due to their computational cost, these simulations need to include baryon processes such as star formation and AGN feedback as “subgrid” recipes, as they cannot be directly resolved. The accuracy of the subgrid recipes can be tested by calibrating simulations to a fixed set of observed cosmological scaling relations, and subsequently checking whether other scaling relations are also reproduced (see e.g. [Schaye et al., 2015](#); [McCarthy et al., 2017](#); [Pillepich et al., 2017](#)). However, this calibration strategy may not result in a unique solution, since other subgrid implementations or different parameter values can provide similar predictions for the calibrated relation but may differ in some other observable. Thus, the calibrated relations need to be chosen carefully depending on what we want to study.

A better option is to calibrate hydrodynamical simulations using the observations that are most relevant for the power spectrum, such as cluster gas fractions and the galaxy mass function ([McCarthy et al., 2017](#)) and to include simulations that span the observational uncertainties ([McCarthy et al., 2018](#)). The calibration against cluster gas fractions is currently only implemented in the BAHAMAS suite of simulations ([McCarthy et al., 2017](#)). Current high-resolution hydrodynamical simulations, such as e.g. EAGLE ([Schaye et al., 2015](#)), Horizon-AGN ([Chisari et al., 2018](#)) and IllustrisTNG ([Springel et al., 2017](#)), do not calibrate against this observable. Moreover, the calibrated subgrid parameters required to reproduce their chosen observations result in gas fractions that are too high in their most massive haloes ([Schaye et al., 2015](#); [Barnes et al., 2017](#); [Chisari et al., 2018](#)). This is a problem, because both halo models ([Sembolini et al., 2013](#)) and hydrodynamical simulations ([van Daalen et al., 2019](#)) have been used to demonstrate the existence of a strong link between the suppression of the total matter power spectrum on large scales and cluster gas fractions. As a result, these state-of-the-art simulations of galaxy formation are not ideal to study the baryonic effects on the matter power spectrum.

Focussing purely on simulation predictions risks underestimating the possible range of power suppression due to baryons, since the simulations generally do not cover the full range of possible physical models. Hence, given our limited understanding of the astrophysics of galaxy formation and the computational expense of hydrodynamical simulations, it is important to develop other ways to account for baryonic effects and observational constraints upon them.

One possibility is to make use of phenomenological models that take the matter distribution as input without making assumptions about the underlying physics. Splitting the matter into its dark matter and baryonic components allows observations to be used as the

input for the baryonic component of the model. This bypasses the need for any model calibrations but may require extrapolating the baryonic component outside of the observed range. Such models can be implemented in different ways. For instance, Schneider & Teyssier (2015) and Schneider et al. (2019) use a “baryon correction model” to shift the particles in DMO simulations under the influence of hydrodynamic processes which are subsumed in a combined density profile including dark matter, gas and stars with phenomenological parameters for the baryon distribution that are fit to observations. Consequently, the influence of a change in these parameters on the power spectrum can be investigated. Since this model relies only on DMO simulations, it is less computationally expensive while still providing important information on the matter distribution.

## 2

We will take a different phenomenological approach and use a modified version of the halo model to predict how baryons modify the matter power spectrum. We opt for this approach because it gives us freedom in varying the baryon distribution at little computational expense. We do not aim to make the most accurate predictor for baryonic effects on the power spectrum, but our goal is to systematically study the influence of changing the baryonic density profiles on the matter power spectrum and to quantify the uncertainty of the baryonic effects on the power spectrum allowed by current observational constraints.

The halo model describes the clustering of matter in the Universe starting from the matter distribution of individual haloes. We split the halo density profiles into a dark matter component and baryonic components for the gas and the stars. We assume that the abundance and clustering of haloes can be modelled using DMO simulations, but that their density profiles, and hence masses, change due to baryonic effects. This assumption is supported by the findings of van Daalen et al. (2014), who used OWLS to show that matched sets of subhaloes cluster identically on scales larger than the virial radii in DMO and hydrodynamical simulations. We constrain the gas component with X-ray observations of groups and clusters of galaxies. These observations are particularly relevant since the matter power spectrum is dominated by groups and clusters on the scales affected by baryonic physics and probed by upcoming surveys  $0.3 \lesssim k/(h \text{ Mpc}^{-1}) \lesssim 10$ , (e.g. van Daalen & Schaye, 2015). For the stellar component, we assume the distribution from Halo Occupation Distribution (HOD) modelling.

Earlier studies have used extensions to the halo model to include baryon effects, either by adding individual matter components from simulations (e.g. White, 2004; Zhan & Knox, 2004; Rudd et al., 2008; Guillet et al., 2010; Semboloni et al., 2011, 2013; Fedeli, 2014; Fedeli et al., 2014), or by introducing empirical parameters inspired by the predicted physical effects of galaxy formation (see Mead et al., 2015, 2016). However, these studies were based entirely on data from cosmological simulations, whereas we stay as close as possible to the observations and thus do not depend on the uncertain assumptions associated with subgrid models for feedback processes.

There is still freedom in our model because the gas content of low-mass haloes and the outskirts of clusters cannot currently be measured. We thus study the range of baryonic corrections to the dark matter only power spectrum by assuming different density profiles for the unobserved regions. Our model gives us a handle on the uncertainty in the matter power spectrum and allows us to quantify how different mass profiles of different mass haloes contribute to the total power for different wavenumbers, whilst simultaneously

matching observations of the matter distribution. Moreover, we can study the impact of observational uncertainties and biases on the resulting power spectrum.

We start off by describing our modified halo model in Section 2.2. We describe the observations and the relevant halo model parameters in Section 2.3. We show our resulting model density components in Section 2.4 and report our results in Section 2.5. We discuss our model and compare it to the literature in Section 2.6. Finally, we conclude and provide some directions for future research in Section 2.7. This work assumes the *WMAP* 9 year (Hinshaw et al., 2013) cosmological parameters  $\{\Omega_m, \Omega_b, \Omega_\Lambda, \sigma_8, n_s, h\} = \{0.2793, 0.0463, 0.7207, 0.821, 0.972, 0.7\}$  and all of our results are computed for  $z = 0$ . All of the observations that we compare to assumed  $h = 0.7$ , so we quote their results in units of  $H_0 = 70 h_{70} \text{ km s}^{-1} \text{ Mpc}^{-1}$  with  $h_{70} = 1$ . Whenever we quote units without any  $h$  or  $h_{70}$  scaling, we assume  $h = 0.7$  or, equivalently,  $h_{70} = 1$  (for a good reference and arguments on making definitions explicit, see Croton, 2013). When fitting our model to observations, we always use  $h = 0.7$  to ensure a fair comparison between model and observations.

## 2.2 Halo Model

### 2.2.1 Theory

The halo model (e.g. Peacock & Smith, 2000; Seljak, 2000; but the basis was already worked out in McClelland & Silk, 1977 and Scherrer & Bertschinger, 1991; review in Cooray & Sheth, 2002) is an analytic prescription to model the clustering properties of matter for a given cosmology through the power spectrum (for a clear pedagogical exposition, see van den Bosch et al., 2013). It gives insight into non-linear structure formation starting from the linear power spectrum and a few simplifying assumptions.

The spherical collapse model of non-linear structure formation tells us that any overdense, spherical region will collapse into a virialized dark matter halo, with a final average density  $\langle \rho_f \rangle = \Delta_{\text{vir}} \rho_c(z_{\text{vir}})$ , where  $\Delta_{\text{vir}}$  in general depends on cosmology, but is usually taken as  $\Delta_{200} = 200$ , rounded from the Einstein-de Sitter value of  $\Delta_{\text{vir}} = 18\pi^2$ , with  $\rho_c(z_{\text{vir}})$  the critical density of the Universe at the redshift of virialization. The fundamental assumption of the halo model is that all matter in the Universe has collapsed into virialized dark matter haloes that grow hierarchically in time through mergers. Throughout the paper we will adhere to the notation  $m_{500c}$  and  $m_{200m}$  to indicate regions enclosing an average density  $\langle \rho \rangle_{500c} = 500\rho_c(z)$  and  $\langle \rho \rangle_{200m} = 200\bar{\rho}_m(z)$ , with  $\bar{\rho}_m(z) = \Omega_m \rho_c(z=0)(1+z)^3$ , respectively.

At a given time, the halo mass function  $n(m_h, z)$  determines the co-moving number density of dark matter haloes in a given halo mass bin centered on  $m_h$ . This function can be derived from analytic arguments, like for instance the Press-Schechter and Extended Press-Schechter (EPS) theories (e.g. Press & Schechter, 1974; Bond et al., 1991; Lacey & Cole, 1993), or by using DMO simulations (e.g. Sheth & Tormen, 1999; Jenkins et al., 2001; Tinker et al., 2008). Furthermore, assuming that the density profile of a halo is completely determined by its mass and redshift, i.e.  $\rho(r) = \rho(r|m_h, z)$ , we can then calculate the statistics of the matter distribution in the Universe, captured by the power

spectrum, by looking at the correlations between matter in different haloes (the two-halo or 2h term which probes large scales) and between matter within the same halo (the one-halo or 1h term which probes small scales).

Splitting the contributions to the power spectrum up into the 1h and 2h terms, we can rewrite

$$P(k, z) = V_u \langle |\hat{\delta}_m(k, z)|^2 \rangle \quad (2.1)$$

$$= P_{1h}(k, z) + P_{2h}(k, z). \quad (2.2)$$

Here  $V_u$  is the volume under consideration and  $\hat{\delta}_m(k, z)$  is the Fourier transform of the matter overdensity field  $\delta_m(\mathbf{x}, z) \equiv \rho(\mathbf{x}, z)/\bar{\rho}_m(z) - 1$ , with  $\bar{\rho}_m(z)$  the mean matter background density at redshift  $z$ . We define the Fourier transform of a halo as

$$\hat{\rho}(k|m_h, z) = 4\pi \int_0^{r_h} dr \rho(r|m_h, z) r^2 \frac{\sin(kr)}{kr}. \quad (2.3)$$

The 1h and 2h terms are given by (for detailed derivations, see [Cooray & Sheth, 2002](#); [Mo et al., 2010](#))

$$P_{1h}(k, z) = \int dm_{h,dmo} n(m_{h,dmo}(z), z) \frac{|\hat{\rho}(k|m_h(m_{h,dmo}), z)|^2}{\bar{\rho}_m^2(z)} \quad (2.4)$$

$$\begin{aligned} P_{2h}(k, z) &= P_{lin}(k, z) \int dm_{h,dmo} n(m_{h,dmo}(z), z) b(m_{h,dmo}(z), z) \\ &\quad \times \frac{\hat{\rho}(k|m_h(m_{h,dmo}), z)}{\bar{\rho}_m(z)} \\ &\simeq P_{lin}(k, z). \end{aligned} \quad (2.5)$$

Our notation makes explicit that because our predictions rely on the halo mass function and the bias obtained from DMO simulations, we need to correct the true halo mass  $m_h$  to the DMO equivalent mass  $m_{h,dmo}$ , as we will explain further in Section 2.2.2. The 2h term contains the bias  $b(m_{h,dmo}, z)$  between haloes and the underlying density field. For the 2h term, we simply use the linear power spectrum, which we get from CAMB<sup>4</sup> for our cosmological parameters. For the halo mass function, we assume the functional form given by [Tinker et al. \(2008\)](#), which is calibrated for the spherical overdensity halo mass  $m_{200m,dmo}$ .

We assume  $P_{2h} \approx P_{lin}$  since not all of our haloes will be baryonically closed. This would result in Eq. 2.5 not returning to the linear power spectrum at large scales for models that have missing baryons within the halo radius. Assuming that the 2h term follows the linear power spectrum is equivalent to assuming that all of the missing baryons will be accounted for in the cosmic web, which we cannot accurately capture with our simple halo model.

We will use our model to predict the quantity

$$R_i(k, z) \equiv \frac{P_i(k, z)}{P_{i,dmo}(k, z)}, \quad (2.6)$$

---

<sup>4</sup><http://camb.info/>

the ratio between the power spectrum of baryonic model  $i$  and the corresponding DMO power spectrum assuming the same cosmological parameters. This ratio has been given various names in the literature, e.g. the “response” (Mead et al., 2016), the “reaction” (Cataneo et al., 2019), or just the “suppression” (Schneider et al., 2019). We will refer to it as the power spectrum response to the presence of baryons. It quantifies the suppression or increase of the matter power spectrum due to baryons. If non-linear gravitational collapse and galaxy formation effects were separable, and baryonic effects were insensitive to the underlying cosmology, knowledge of this ratio would allow us to reconstruct a matter power spectrum from any DMO prediction. These last two assumptions can only be tested by comparing large suites of cosmological N-body and hydrodynamical simulations. We do not attempt to address them in this paper. However, van Daalen et al. (2011, 2019), Mummery et al. (2017), McCarthy et al. (2018), and Stafford et al. (2019) have investigated the cosmology dependence of the baryonic suppression. Mummery et al. (2017) find that a separation of the cosmology and baryon effects on the power spectrum is accurate at the 3 per cent level between  $1 \text{ } h \text{ Mpc}^{-1} \lesssim k \lesssim 10 \text{ } h \text{ Mpc}^{-1}$  for cosmologies varying the neutrino masses between  $0 < M_\nu/\text{eV} < 0.48$ . Similarly, van Daalen et al. (2019) find that varying the cosmology between WMAP 9 and Planck 2013 results in at most a 4 per cent difference for  $k < 10 \text{ } h \text{ Mpc}^{-1}$ .

Our model does not include any correction to the power spectrum due to halo exclusion. Halo exclusion accounts for the fact that haloes cannot overlap by canceling the 2h term at small scales (Smith et al., 2011). It also cancels the shot-noise contribution from the 1h term at large scales. In our model, the important effect occurs at scales where the 1h and 2h terms are of similar magnitude, since the halo exclusion would suppress the 2h term. However, since we look at the power spectrum response to baryons  $R_i(k)$ , which is the ratio of the power spectrum including baryons to the power spectrum in the DMO case, our model should not be significantly affected, since the halo exclusion term modifies both of these terms in a similar way. We have checked that subtracting a halo exclusion term that interpolates between the 1h term at large scales and the 2h term at small scales only affects our predictions for  $R_i(k)$  by at most 1 per cent at  $k \approx 3 \text{ } h \text{ Mpc}^{-1}$ .

### 2.2.2 Linking observed halo masses to abundances

Our model is similar to the traditional halo model as described by Cooray & Sheth (2002). We make two important changes, however. Firstly, we split up the density profile into a dark matter, a hot gas, and a stellar component

$$\rho(r|m_h, z) = \rho_{\text{dm}}(r|m_h, z) + \rho_{\text{gas}}(r|m_h, z) + \rho_{\star}(r|m_h, z). \quad (2.7)$$

We will detail our specific profile assumptions in Section 2.2.3. Secondly, we include a mapping from the observed halo mass  $m_h$  to the dark matter only equivalent halo mass  $m_{200m, \text{dmo}}$ , as shown in Eqs. 2.4 and 2.5.

This second step is necessary for two reasons. First, the masses of haloes change in hydrodynamical simulations. In simulations with the same initial total density field, haloes can be linked between the collisionless and hydrodynamical simulations, thus enabling the study of the impact of baryon physics on individual haloes. Sawala et al.

(2013), Velliscig et al. (2014) and Cui et al. (2014) found that even though the abundance of individual haloes does not change, their mass does, especially for low-mass haloes (see Fig. 10 in Velliscig et al., 2014). Feedback processes eject gas from haloes, lowering their mass at fixed radius. However, once this mass change is accounted for, the clustering of the matched haloes is nearly identical in the DMO and hydrodynamical simulations (van Daalen et al., 2014). Since the halo model relies on prescriptions for the halo mass function that are calibrated on dark matter only simulations, we need to correct our observed halo masses to predict their abundance.

Second, observed halo masses are not equivalent to the underlying true halo mass. Every observational determination of the halo mass carries its own intrinsic biases. Masses from X-ray measurements are generally obtained under the assumption of spherical symmetry and hydrostatic equilibrium, for example. However, due to the recent assembly of clusters of galaxies, sphericity and equilibrium assumptions break down in the halo outskirts (see Pratt et al., 2019, and references therein). In most weak lensing measurements, the halo is modeled assuming a Navarro-Frenk-White (NFW) profile (Navarro et al., 1996) with a concentration–mass relation  $c(m)$  from simulations. This profile does not necessarily accurately describe the density profile of individual haloes due to asphericity and the large scatter in the concentration–mass relation at fixed halo mass.

In our model, each halo will be labeled with four different halo masses. We indicate the cumulative mass profile of the observed and DMO equivalent halo with  $m_{\text{obs}}(\leq r)$  and  $m_{\text{dmo}}(\leq r)$ , respectively. Firstly, we define the total mass inside  $r_{500c,\text{obs}}$  inferred from observations

$$m_{500c,\text{obs}} \equiv m_{\text{obs}}(\leq r_{500c,\text{obs}}). \quad (2.8)$$

This mass will provide the link between our model and the observations. We work with  $r_{500c,\text{obs}}$  in this paper because it is similar to the radius up to which X-ray observations are able to measure the halo mass. However, any other radius can readily be used in all of the following definitions. Secondly, we have the true total mass inside the halo radius  $r_h$  for our extrapolated profiles

$$m_h \equiv m_{\text{obs}}(\leq r_h). \quad (2.9)$$

Thirdly, we define the total mass in our extrapolated profiles such that the mean enclosed density is  $\langle \rho \rangle_{200m}$

$$m_{200m,\text{obs}} \equiv m_{\text{obs}}(\leq r_{200m,\text{obs}}). \quad (2.10)$$

We differentiate between  $r_h$  and  $r_{200m,\text{obs}}$  because for some of our models we will extrapolate the density profile further than  $r_{200m,\text{obs}}$ . Fourthly, we define the dark matter only equivalent mass for the halo

$$m_{200m,\text{dmo}} \equiv m_{\text{dmo}}(\leq r_{200m,\text{dmo}}(m_{500c,\text{obs}}, c_{\text{dmo}}(m_{200m,\text{dmo}}))), \quad (2.11)$$

which depends on the observed halo mass  $m_{500c,\text{obs}}$  and the assumed DMO concentration–mass relation  $c_{\text{dmo}}(m_{200m,\text{dmo}})$ , as we will discuss below. In each of our models for the baryonic matter distribution there is a unique monotonic mapping between all four of

these halo masses. In the rest of the paper we will thus express all dependencies as a function of  $m_h$ , unless our calculation explicitly depends on one of the three other masses (as we indicate in Eqs. 2.4 and 2.5 where the halo mass function requires the DMO equivalent mass from Eq. 2.11 as an input).

The DMO equivalent mass, Eq. 2.11, requires more explanation. We determine it from the following, simplifying but overall correct, assumption: the inclusion of baryon physics does not significantly affect the distribution of the dark matter. This assumption is corroborated by the findings of Duffy et al. (2010), Velliscig et al. (2014) and Schaller et al. (2015), who all find that in hydrodynamical simulations that are able to reproduce many observables related to the baryon distribution, the baryons do not significantly impact the dark matter distribution. This assumption breaks down on galaxy scales where the dark matter becomes more concentrated due to the condensation of baryons at the center of the halo. However, these scales are smaller than the scales of interest for upcoming weak lensing surveys. Moreover, at these scales the stellar component typically dominates over the dark matter. Assuming that the dark matter component will have the same scale radius as its DMO equivalent halo, we can convert the observed halo mass into its DMO equivalent. The first step is to compute the dark matter mass in the observed halo,

$$\frac{m_{500c,dm}}{m_{500c,obs}} = (1 - f_{\text{gas},500c,obs}(m_{500c,obs}) - f_{\star,500c,obs}(m_{200m,dmo}(m_{500c,obs}))). \quad (2.12)$$

The dark matter mass is obtained by subtracting the observed gas and stellar mass inside  $r_{500c,obs}$  from the observed total halo mass. The stellar fraction depends on the DMO equivalent halo mass since we take the stellar profiles from the `iHOD` model by Zu & Mandelbaum (2015, hereafter ZM15), which also uses a halo model that is based on the Tinker et al. (2008) halo mass function. This requires us to iteratively solve for the DMO equivalent mass  $m_{200m,dmo}$ . Next, we assume that the DMO equivalent halo mass at the radius  $r_{500c,obs}$  is given by  $m_{500c,dmo} = (1 - \Omega_b/\Omega_m)^{-1} m_{500c,dm}$ , which is consistent with our assumption that baryons do not change the distribution of dark matter. Subsequently, we can determine the halo mass  $m_{200m,dmo}$  by assuming a DMO concentration–mass relation, an NFW density profile, and solving  $m_{dmo}(\leq r_{500c,obs}; c_{dmo}(m_{200m,dmo})) = m_{500c,dmo}$  for  $m_{200m,dmo}$ . Thus, we determine  $m_{200m,dmo}$  (Eq. 2.11) by solving the following equation:

$$\begin{aligned} & 4\pi \int_0^{r_{500c,obs}} \rho_{\text{NFW}}(r; c_{dmo}(m_{200m,dmo}(m_{500c,obs}))) r^2 dr \\ &= \frac{m_{500c,obs}}{1 - \Omega_b/\Omega_m} (1 - f_{\text{gas},500c,obs}(m_{500c,obs}) - f_{\star,500c,obs}(m_{200m,dmo}(m_{500c,obs}))). \end{aligned} \quad (2.13)$$

We determine the stellar fraction at  $r_{500c,obs}$  by assuming the stellar profiles detailed in Section 2.2.3. Finally, we obtain the relation  $m_{200m,dmo}(m_{500c,obs})$  that assigns a DMO equivalent mass to each observed halo with mass  $m_{500c,obs}$ .

We initiate our model on an equidistant log-grid of halo masses  $10^{10} h^{-1} M_\odot \leq m_{500c,obs} \leq 10^{15} h^{-1} M_\odot$ , which we sample with 101 bins. We show that our results are

converged with respect to our chosen mass range and binning in App. 2.A. For each halo mass, we get the DMO equivalent mass  $m_{200m,dmo}$ , the stellar fraction  $f_{\star,i}(m_{200m,dmo})$ , with  $i \in \{\text{cen, sat}\}$ , and the concentration of the DMO equivalent halo  $c_{dmo}(m_{200m,dmo})$ . We will specify all of our different matter component profiles in Section 2.2.3.

### 2.2.3 Matter density profiles

In this section, we give the functional forms of the density profiles that we use in our halo model. We assume three different matter components: dark matter, gas and stars. The dark matter and stellar profiles are taken directly from the literature, whereas we obtain the gas profiles by fitting to observations from the literature. In our model, we only include the hot, X-ray emitting gas with  $T > 10^7$  K, thus neglecting the interstellar medium (ISM) component of the gas. The ISM component is confined to the scale of individual galaxies, where it can provide a similar contribution to the total baryonic mass as the stars. The only halo masses for which the total baryonic mass of the galaxy may be similar to that of the surrounding diffuse circum-galactic medium (CGM) are Milky Way-like galaxies, or even lower-mass haloes (Catinella et al., 2010; Saintonge et al., 2011). However, these do not contribute significantly to the total power at our scales of interest, as we will show in Section 2.5.3.

#### Hot gas

For the density profiles of hot gas, we assume traditionally used beta profiles (Cavaliere & Fusco-Femiano, 1978) inside  $r_{500c,\text{obs}}$  where we have observational constraints. We will extrapolate the beta profile as a power-law with slope  $-\gamma$  outside  $r_{500c,\text{obs}}$ . In our models with  $r_h > r_{200m,\text{obs}}$ , we will assume a constant density outside  $r_{200m,\text{obs}}$  until  $r_h$ , which will then be the radius where the halo reaches the cosmic baryon fraction. This results in the following density profile for the hot gas:

$$\rho_{\text{gas}}(r|m_h) = \begin{cases} \rho_0 (1 + (r/r_c)^2)^{-3\beta/2}, & r < r_{500c,\text{obs}} \\ \rho_{500c,\text{obs}} \left(\frac{r}{r_{500c,\text{obs}}}\right)^{-\gamma}, & r_{500c,\text{obs}} \leq r < r_{200m,\text{obs}} \\ \rho_{500c,\text{obs}} \left(\frac{r_{200m,\text{obs}}}{r_{500c,\text{obs}}}\right)^{-\gamma}, & r_{200m,\text{obs}} \leq r < r_h \\ 0, & r \geq r_h. \end{cases} \quad (2.14)$$

The normalisation  $\rho_0$  is determined by the gas fractions inferred from X-ray observations and normalises the profile to  $m_{\text{gas},500c,\text{obs}}$  at  $r_{500c,\text{obs}}$ :

$$\begin{aligned} \rho_0 &= \frac{m_{\text{gas},500c,\text{obs}}}{4/3\pi r_{500c,\text{obs}}^3 {}_2F_1(3/2, 3\beta/2; 5/2; -(r_{500c,\text{obs}}/r_c)^2)} \\ &= \frac{500\rho_c f_{\text{gas},500c,\text{obs}}(m_{500c,\text{obs}})}{{}_2F_1(3/2, 3\beta/2; 5/2; -(r_{500c,\text{obs}}/r_c)^2)}. \end{aligned} \quad (2.15)$$

Here  ${}_2F_1(a, b; c; d)$  is the Gauss hypergeometric function. The values for the core radius  $r_c$ , the slope  $\beta$ , and the hot gas fraction  $f_{\text{gas},500c,\text{obs}}(m_{500c,\text{obs}})$  are obtained by fitting

observations, as we explain in Section 2.3. The outer power-law slope  $\gamma$  is in principle a free parameter of our model, but as we explain below, it is constrained by the total baryon content of the halo. We choose a parameter range of  $0 \leq \gamma \leq 3$ .

For each halo, we determine  $r_{200m,\text{obs}}$  by determining the mean enclosed density for the total mass profile (i.e. dark matter, hot gas and stars). In the most massive haloes, a large part of the baryons is already accounted for by the observed hot gas profile. As a result, we need to assume a steep slope in these systems, since otherwise their baryon fraction would exceed the cosmic one before  $r_{200m,\text{obs}}$  is reached. Since the parameters of both the dark matter and the stellar components are fixed, the only way to prevent this is by setting a maximum value for the slope  $-\gamma$  once the observational best-fit parameters for the hot gas profile have been determined. For each  $\rho(r|m_h)$  we can calculate the value of  $\gamma$  such that the cosmic baryon fraction is reached at  $r_{200m,\text{obs}}$ . This will be the limiting value and only equal or steeper slopes will be allowed. We will show the resulting  $\gamma(m_{500c,\text{obs}})$ -relation in Section 2.4, since it depends on the best-fit density profile parameters from the observations that we will describe in Section 2.3. Being the only free parameter in our model,  $\gamma$  provides a clear connection to observations. Deeper observations that can probe further into the outskirts of haloes, can thus be straightforwardly implemented in our model.

We will look at two different cases for the size of the haloes, motivated by the observed hot gas fractions in Section 2.3 and by the lack of observational constraints outside  $r_{500c,\text{obs}}$ . We aim to include enough freedom in the halo outskirts such that the actual baryon distribution will be encompassed by the models. In both cases, we leave the power-law slope  $\gamma$  free outside  $r_{500c,\text{obs}}$ . The models differ outside  $r_{200m,\text{obs}}$  since there are no firm observational constraints on the extent of the baryonic distribution around haloes. In the first case, we will truncate the power-law as soon as  $r_{200m,\text{obs}}$  is reached, thus enforcing  $r_h = r_{200m,\text{obs}}$ . This corresponds to the halo definition that is used by Tinker et al. (2008) in constructing their halo mass function. For the least massive haloes in our model, this will result in haloes that are missing a significant fraction of their baryons at  $r_{200m,\text{obs}}$ , with lower baryon fractions  $f_{\text{bar},200m,\text{obs}}$  for steeper slopes, i.e. higher values of  $\gamma$ . Since we assume the linear power spectrum for the 2h term, we will still get the clustering predictions on the large scales right. We will denote this case with the quantifier *nocb*, since the cosmic baryon fraction  $f_b = \Omega_b/\Omega_m$  is not reached for most haloes in this case. In the second case, we will set  $r_h = r_{f_b} > r_{200m,\text{obs}}$  such that all haloes reach the cosmic baryon fraction at  $r_h$ , we will denote this case with the quantifier *cb*.

The *nocb* and the *cb* cases for each  $\gamma$  result in the same halo mass  $m_{200m,\text{obs}}$ , since they only differ for  $r > r_{200m,\text{obs}}$ . Thus, they have the same DMO equivalent halo mass and the same abundance  $n(m_{200m,\text{dmo}}(m))$  in Eq. 2.4. The difference between the two models is the normalization and the shape of the Fourier density profile  $\hat{\rho}(k|m)$  which depends on the total halo mass  $m_h$  and the distribution of the hot gas. The halo mass  $m_h$  will be higher in the *cb* case due to the added baryons between  $r_{200m,\text{obs}} < r < r_h$ , resulting in more power from the 1h term. Since the baryons in the *cb* case are added outside  $r_{200m,\text{obs}}$  there will also be an increase in power on larger scales.

For our parameter range  $0 \leq \gamma \leq 3$ , the *nocb* and *cb* cases encompass the possible power suppression in the Universe. For massive systems, we have observational constraints on the total baryon content inside  $r_{500c,\text{obs}}$  and our model variations capture

the possible variation in the outer density profiles. The distribution of the baryons in the hot phase outside  $r_{500c,obs}$  is not known observationally. However, it most likely depends on the halo mass. For the most massive haloes, Sunyaev-Zel'dovich (SZ) measurements of the hot baryons indicate that most baryons are accounted for inside 5  $r_{500c,obs} \approx 2 r_{200m,obs}$  (e.g. Planck Collaboration et al., 2013; Le Brun et al., 2015). This need not be the case for lower-mass systems where baryons can be more easily ejected out to even larger distances. Moreover, there are also baryons that never make it into haloes and that are distributed on large, linear scales. The main uncertainty in the power suppression at large scales stems from the baryonic content of the low-mass systems. The 1h term of low-mass haloes becomes constant for  $k \lesssim 1 h \text{ Mpc}^{-1}$ . Hence, on large scales we capture the extreme case where the low-mass systems retain no baryons (nocb and  $\gamma = 3$ ) and all the missing halo baryons are distributed on large, linear scales in the cosmic web. We can also capture the other extreme where the low-mass systems retain all of their baryons in the halo outskirts (cb and  $\gamma = 0$ ), since the details of the density profile do not matter on scales  $k < 1 h \text{ Mpc}^{-1}$ . Thus, the matter distribution in the Universe will lie somewhere in between these two extremes captured by our model.

## Dark matter

We assume that the dark matter follows a Navarro-Frenk-White (NFW) profile (Navarro et al., 1996) with the concentration determined by the  $c_{200c,dmo}(m_{200c,dmo}(m_{500c,obs}))$  relation from Correa et al. (2015), which is calculated using commah<sup>5</sup>, assuming Eq. 2.11 to get the DMO equivalent mass. We assume a unique  $c(m)$  relation with no scatter. We discuss the influence of shifting the concentration–mass relation within its scatter in App. 2.B.

The concentration in commah is calculated with respect to  $r_{200c,dmo}$  (the radius where the average enclosed density of the halo is 200  $\rho_c$ ), so we convert the concentration to our halo definition by multiplying by the factor  $r_{200m,dmo}/r_{200c,dmo}$  (for the DMO equivalent halo). This needs to be solved iteratively for haloes with different concentration  $c_{200m,dmo}(m_{200m,dmo})$ , since for each input mass  $m_{200c,dmo}$  and resulting concentration  $c_{200c,dmo}$ , we need to find the corresponding  $m_{200m,dmo}$  to convert  $c_{200c,dmo}$  to  $c_{200m,dmo}$ . We thus have for the dark matter component in Eq. 2.7

$$\rho_{dm}(r|m_h) = \begin{cases} \frac{m_x}{4\pi r_x^3} \frac{c_x^3}{Y(c_x)} \left( \frac{c_x r}{r_x} \right)^{-1} \left( 1 + \frac{c_x r}{r_x} \right)^{-2}, & r \leq r_h \\ 0, & r > r_h. \end{cases} \quad (2.16)$$

The halo radius  $r_h$  depends on the hot gas density profile and is either  $r_h = r_{200m,obs}$  in the case nocb, or  $r_h = r_{f_b}$ , the radius where the cosmic baryon fraction is reached, in the case cb. We define  $Y(c_x) = \log(1 + c_x) - c_x/(1 + c_x)$  and the concentration  $c_x = r_x/r_s$  with the scale radius  $r_s$  indicating the radius at which the NFW profile has logarithmic slope  $-2$ . The subscript ‘x’ indicates the radius at which the concentration is calculated, e.g. x = 200m. All of the subscripted variables are a function of the halo mass  $m_{500c,obs}$ . The normalization factor in our definition ensures that the NFW profile has mass  $m_x$  at

---

<sup>5</sup><https://github.com/astrodruff/commah>

radius  $r_x$ . For the dark matter component in our baryonic model, we require the mass at  $r_{500c,obs}$  to equal the dark matter fraction of the total observed mass  $m_{500c,obs}$

$$m_x = m_{500c,obs} (1 - f_{\text{gas},500c,obs}(m_{500c,obs}) - f_{\star,500c,obs}(m_{200m,dmo}(m_{500c,obs}))). \quad (2.17)$$

We require the scale radius for the dark matter to be the same as the scale radius of the equivalent DMO halo, thus

$$c_x = c_{200m,dmo}(m_{200m,dmo}(m_{500c,obs})) \cdot \frac{r_{500c,obs}}{r_{200m,dmo}}. \quad (2.18)$$

For the DMO power spectrum that we compare to in Eq. 2.6, we assume  $x = 200m, dmo$  in Eq. 2.16 and we use both the halo mass and the concentration derived for Eq. 2.11. The halo radius for the dark matter only case is the same as in the corresponding baryonic model. This is the logical choice since this means that in the case where our model accounts for all of the baryons inside  $r_h$ , the DMO halo and the halo including baryons will have the same total mass, only the matter distributions will be different. In the case where not all the baryons are accounted for, we can then see the influence on the power spectrum of baryons missing from the haloes.

## Stars

For the stellar contribution we do not try to fit density profiles to observations. We opt for this approach since it allows for a clear separation between centrals and satellites. Moreover, it provides the possibility of a self-consistent framework that is also able to fit the galaxy stellar mass function and the galaxy clustering. Our model can be straightforwardly modified to take stellar fractions and profiles from observations, as we did for the hot gas. We implement stars similarly to HOD methods, specifically the `iHOD` model by [ZM15](#). We will assume their stellar-to-halo mass relations for both centrals and satellites. The `iHOD` model can reproduce the clustering and lensing of a large sample of SDSS galaxies spanning 4 decades in stellar mass by self-consistently modelling the incompleteness of the observations. Moreover, the model independently predicts the observed stellar mass functions. In our case, since we have assumed a different cosmology, these results will not necessarily be reproduced. However, we have checked that shifting the halo masses at fixed abundance between the cosmology of [ZM15](#) and ours only results in relative shifts of the stellar mass fractions of  $\approx 10$  per cent at fixed halo mass.

We split up the stellar component into centrals and satellites

$$\rho_\star(r|m_h) = \rho_{\text{cen}}(r|m_h) + \rho_{\text{sat}}(r|m_h). \quad (2.19)$$

The size of typical central galaxies in groups and clusters is much smaller than our scales of interest, so we can safely assume them to follow delta profile density distributions, as is done in [ZM15](#)

$$\rho_{\text{cen}}(r|m_h) = f_{\text{cen},200m,dmo}(m_{200m,dmo}) m_{200m,dmo} \delta^D(\mathbf{r}), \quad (2.20)$$

here  $f_{\text{cen}}(m)$  is taken directly from the `iHOD` fit and  $\delta^D(\mathbf{r})$  is the Dirac delta function.

For the satellite galaxies, we assume the same profile as [ZM15](#) and put the stacked satellite distribution at fixed halo mass in an NFW profile

$$\rho_{\text{sat}}(r|m_h) = \begin{cases} \frac{m_x}{4\pi r_x^3} \frac{c_x^3}{Y(c_x)} \left(\frac{c_x r}{r_x}\right)^{-1} \left(1 + \frac{c_x r}{r_x}\right)^{-2}, & r \leq r_h \\ 0, & r > r_h, \end{cases} \quad (2.21)$$

which is the same NFW definition as Eq. [2.16](#). The profile also becomes zero for  $r > r_h$ . Clearly, there will still be galaxies outside of this radius in the Universe. However, in the halo-based picture, we need to truncate the halo somewhere. Since the stellar contribution is always subdominant to the gas and the dark matter at the largest scales, we can safely truncate the profiles without affecting our predictions at the percent level. We will take our reference values in Eq. [2.21](#) at  $x = 200m_{\text{dmo}}$ . As in [ZM15](#), the satellites are less concentrated than the parent dark matter halo by a factor 0.86

$$m_x = f_{\text{sat}}(m_{200m,\text{dmo}}) m_{200m,\text{dmo}} \quad (2.22)$$

$$\begin{aligned} c_x &= f_{c,\text{sat}} c_{200m,\text{dmo}}(m_{200m,\text{dmo}}) \\ &= 0.86 c_{200m,\text{dmo}}(m_{200m,\text{dmo}}). \end{aligned} \quad (2.23)$$

We take the stellar fraction from the best fit model of [ZM15](#).

This less concentrated distribution of satellites is also found in observations for massive systems in the local Universe ([Lin et al., 2004](#); [Budzynski et al., 2012](#); [van der Burg et al., 2015](#)). However, the observations generally find a concentration of  $c_{\text{sat}} \approx 2$  to 3 for group and cluster mass haloes, which is about a factor 2 lower than the dark matter concentration. Similar results are found in the BAHAMAS simulations ([McCarthy et al., 2017](#)). In low-mass systems, on the other hand, the satellites tend to track the underlying dark matter profile quite closely ([Wang et al., 2014](#)) with  $c_{\text{sat}}(m) \approx c(m)$ . The value of  $f_{c,\text{sat}} = 0.86$  is thus a good compromise between these two regimes. We have checked that assuming  $f_{c,\text{sat}} = 1$  results in differences  $< 0.03$  per cent at all  $k$ , with the maximum difference reached at  $k \approx 30 h \text{ Mpc}^{-1}$ .

## 2.3 X-ray observations

We choose to constrain the halo model using observations of the hot, X-ray emitting gas in groups and clusters of galaxies, since these objects provide the dominant contribution to the power spectrum at our scales of interest and their baryon content is dominated by hot plasma.

We combine two data sets of X-ray observations with *XMM-Newton* of clusters for which the individually measured electron density profiles were available, namely REXCESS ([Croston et al., 2008](#)) and the XXL survey (more specifically the XXL-100-GC subset, [Pacaud et al., 2016](#); [Eckert et al., 2016](#)). This gives a total of 131 (31 + 100) unique groups and clusters (there is no overlap between the two data sets) with masses ranging from  $m_{500c,\text{obs}} \approx 10^{13} m_{\text{sun}}$  to  $m_{500c,\text{obs}} \approx 2 \times 10^{15} M_{\odot}$ , with the XXL sample probing lower masses, as can be seen in Fig. [2.1](#). We extend our data with more sets of observations for the hydrostatic gas fraction of groups and clusters of galaxies, as shown

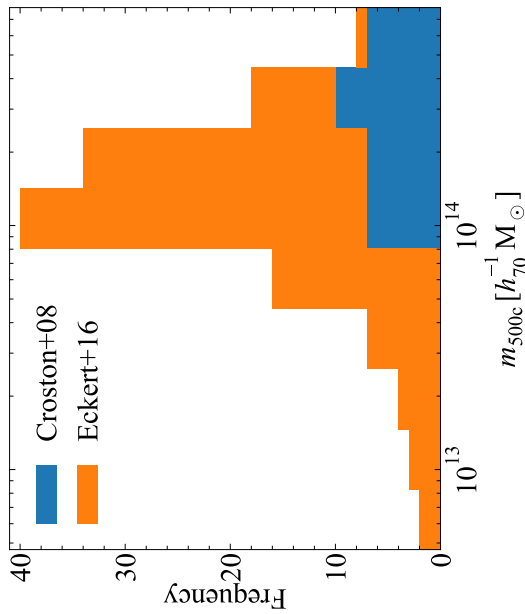


Figure 2.1: Stacked histogram for the masses of the haloes in our sample. The XXL-100-GC (Eckert et al., 2016) data probe lower masses than the REXCESS (Croston et al., 2008) data set, but it is clear that most of the haloes are clusters of galaxies with  $m_{500c,\text{obs}} > 10^{14} \text{ M}_\odot$ .

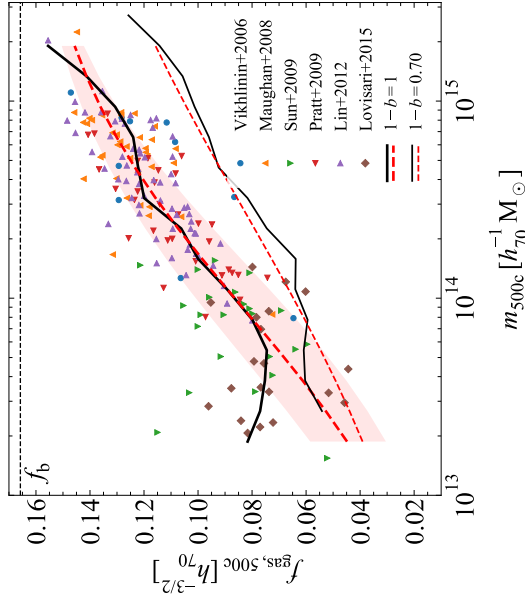


Figure 2.2: The X-ray hydrostatic gas fractions as a function of halo mass. The different data sets are explained in the text. The median  $f_{\text{gas},500c} - m_{500c,\text{obs}}$  relation (black, solid lines) and the best fit (red, dashed lines) using Eq. 2.25 are shown. We indicate the 15<sup>th</sup> and 85<sup>th</sup> percentile range by the red shaded region. We show the hydrostatic (thick lines) and bias corrected ( $1 - b = 0.7$ , thin lines) relations. Since, in the latter case, halo masses increase more than the gas masses, under the assumption of the best-fit beta profile to the hot gas density profiles, the gas fractions shift down. The fits deviate at low masses because we force  $f_{\text{gas},500c} \rightarrow 0$  for  $m_{500c,\text{obs}} \rightarrow 0$ .

in Fig. 2.2. We use a set of hydrostatic masses determined from *Chandra* archival data (Vikhlinin et al., 2006; Maughan et al., 2008; Sun et al., 2009; Lin et al., 2012) and from the NORAS and REFLEX (of which REXCESS is a subset) surveys (Pratt et al., 2009; Lovisari et al., 2015).

REXCESS consists of a representative sample of clusters from the REFLEX survey (Böhringer et al., 2007). It includes clusters of all dynamical states and aims to provide a homogeneous sampling in X-ray luminosity of clusters in the local Universe ( $z < 0.2$ ). Since all of the redshift bins are approximately volume limited (Böhringer et al., 2007), we do not expect significant selection effects for the massive systems ( $m_{500c} > 10^{14} h^{-1} M_\odot$ ) as it has been shown by Chon & Böhringer (2017) that the lack of disturbed clusters in X-ray samples (Eckert et al., 2011) is generally due to their flux-limited nature. The XXL-100-GC sample is flux-limited (Pacaud et al., 2016) and covers a wider redshift range ( $z \lesssim 1$ ). Since it is flux-limited, there is a bias to selecting more massive objects. At low redshifts, however, there is a lack of massive objects due to volume effects (Pacaud et al., 2016). From Chon & Böhringer (2017) we would also expect the sample to be biased to select relaxed systems.

Assuming an optically thin, collisionally-ionized plasma with a temperature  $T$  and metallicity  $Z$ , the deprojected surface brightness profile can be converted into a 3-D electron density profile  $n_e$ , which is the source of the thermal bremsstrahlung emission (Sarazin, 1986). For the REXCESS sample, the spectroscopic temperature within  $r_{500c,\text{obs}}$  was chosen with the metallicity also deduced from a spectroscopic fit, whereas for the XXL sample the average temperature within  $r < 300 \text{ kpc}$  was used with a metallicity of  $Z = 0.3 Z_\odot$ . We get the corresponding hydrogen and helium abundances by interpolating between the sets of primordial abundances,  $(X_0, Y_0, Z_0) = (0.75, 0.25, 0)$ , and of solar abundances,  $(X_\odot, Y_\odot, Z_\odot) = (0.7133, 0.2735, 0.0132)$ . We then find  $(X, Y, Z) = (0.73899, 0.25705, 0.00396)$  for  $Z = 0.3 Z_\odot$ . To convert this electron density into the total density, we will assume these interpolated abundances, since in general for clusters the metallicity  $Z \approx 0.3 Z_\odot = 0.00396$  (Voit, 2005; Grevesse et al., 2007). This is also approximately correct for the Croston et al. (2008) data, since for their systems the median metallicity (bracketed by 15<sup>th</sup> and 85<sup>th</sup> percentiles) is  $Z/Z_\odot = 0.27^{+0.09}_{-0.05}$ . Moreover, we assume the gas to be fully ionized. We know that the total gas density is given by

$$\begin{aligned} \rho_{\text{gas}} &= \mu m_H (n_e + n_H + n_{\text{He}}) \\ &= \frac{1 + Y/X}{2 + 3Y/(4X)} \frac{2 + 3Y/(4X)}{1 + Y/(2X)} m_H n_e \\ &\approx 0.6 \cdot 1.93 m_H n_e \end{aligned} \quad (2.24)$$

This results in the gas density profiles shown in Fig. 2.3. It is clear that at large radii the scatter is smaller for more massive systems. We bin the XXL data in 20 mass bins as the individual profiles have a large scatter at fixed radius. For each mass bin we only include the radial range where each profile in the bin is represented.

The two surveys derived the halo mass  $m_{500c,\text{obs}}$  differently. For REXCESS, the halo masses for the whole sample were determined from the  $m_{500c,\text{obs}} - Y_X$  relation of Arnaud et al. (2007), where  $Y_X = m_{\text{gas},500c} T_X$  is the thermal energy content of the intracluster

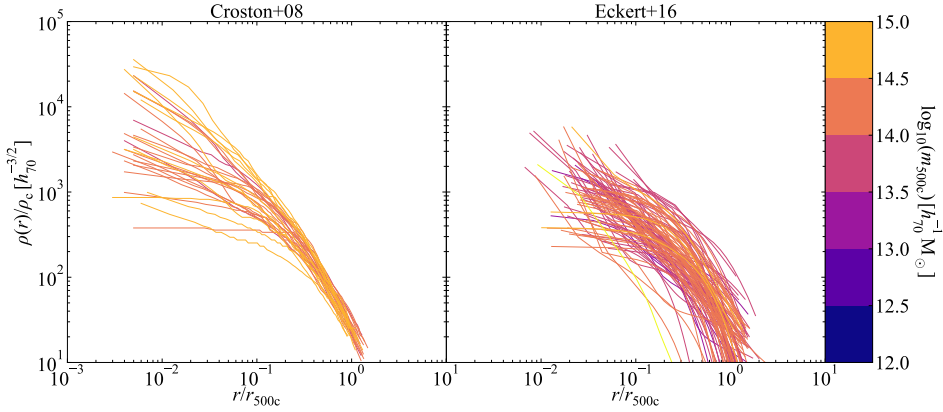


Figure 2.3: The hot gas density profiles inferred from the X-ray observations colour-coded by  $m_{500c,\text{obs}}$ . The left-hand panel shows the profiles from the REXCESS sample (31 nearby clusters with  $10^{14} \lesssim m_{500c,\text{obs}}/\text{M}_\odot \lesssim 10^{15}$ , [Croston et al., 2008](#)) and the right-hand panel from the XXL survey (100 bright clusters with  $10^{13} \lesssim m_{500c,\text{obs}}/\text{M}_\odot \lesssim 10^{15}$ , [Eckert et al., 2016](#)).

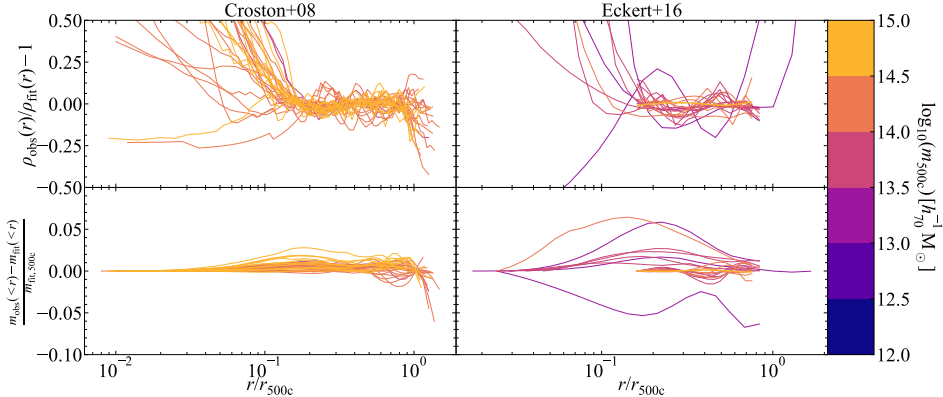


Figure 2.4: *Top row* Residual of beta profile fits to the hot gas density profiles in Fig. 2.3. The left-hand panel shows the residuals for the REXCESS sample ([Croston et al., 2008](#)) and the right-hand panel for the XXL-100-GC sample ([Eckert et al., 2016](#)). The fits are accurate within  $\sim 10$  per cent for the range  $0.1 < r/r_{500c,\text{obs}} < 1$ , with larger scatter in the inner region, where the beta profile generally underestimates the total mass. For the XXL-100-GC sample ([Eckert et al., 2016](#)) we binned the profiles into 20 mass bins since there is a large scatter in the individual ones. We only fit the profile at radial ranges where there is data for all the individual profiles in the bin. *Bottom row* Residual of beta profile fits to the cumulative mass fraction. The total amount of mass within the inner region is negligible compared to the total mass in the profile. In the inner regions the observed profiles always yield higher masses than the fits because of the core of the beta profile. We reproduce the total mass  $m_{\text{gas},500c}$  of the individual density profiles by construction.

medium (ICM). Arnaud et al. (2007) determined  $m_{500c,obs}$  under the assumption of spherical symmetry and hydrostatic equilibrium (see e.g. Voit, 2005). Eckert et al. (2016) take a different route. They determine halo masses using the  $m_{500c,obs} - T_X$  relation calibrated to weak lensing mass measurements of 38 clusters that overlap with the CFHTLenS shear catalog, as described in Lieu et al. (2016). As a result, the REXCESS halo mass estimates rely on the assumption of hydrostatic equilibrium, whereas Eckert et al. (2016) actually find a hydrostatic bias  $m_{X-ray}/m_{WL} = 1 - b = 0.72$ , consistent with the analyses of Von der Linden et al. (2014) and Hoekstra et al. (2015). Recently, Umetsu et al. (2019) used the Hyper Suprime-Cam (HSC) survey shear catalog, which overlaps the XXL-North field almost completely, to measure weak lensing halo masses with a higher limiting magnitude and, hence, number density of source galaxies than CFHTLenS. They do not rederive the gas fractions of Eckert et al. (2016), but they note that their masses are systematically lower by a factor  $\approx 0.75$  than those derived in Lieu et al. (2016), a finding which is consistent with Lieu et al. (2017), who find a factor  $\approx 0.72$ . These lower weak lensing halo masses result in a hydrostatic bias of  $b < 0.1$ .

To obtain a consistent analysis, we scale the halo masses from Eckert et al. (2016) back onto the hydrostatic  $f_{\text{gas},500c} - m_{500c,obs}$  relation, which we show in Fig. 2.2. We thus assume halo masses derived from the assumption of hydrostatic equilibrium. It might seem strange to take the biased result as the starting point of our analysis. However, we argue that this is an appropriate starting point. First, current estimates for the hydrostatic bias range from  $0.58 \pm 0.04 \lesssim 1 - b \lesssim 0.71 \pm 0.10$  corresponding to the results from Planck SZ cluster counts (Planck Collaboration et al., 2016b; Zubeldia & Challinor, 2019), or  $0.688 \pm 0.072 \lesssim 1 - b \lesssim 0.80 \pm 0.14$  from weak lensing mass measurements of Planck clusters (Von der Linden et al., 2014; Hoekstra et al., 2015; Medezinski et al., 2018). Second, we are not able to determine the mass dependence of the relation for groups of galaxies from current observations. We will check how our results change when assuming a constant hydrostatic bias of  $1 - b = 0.7$  in Section 2.5.5. The thin, black line in Fig. 2.2 shows the shift in the  $f_{\text{gas},500c}(m_{500c,obs})$  relation when assuming this constant hydrostatic bias.

We fit the cluster gas density profiles with beta profiles, following Eq. 2.14, within  $[0.15, 1] r_{500c,obs}$ , excising the core as usual in the literature, since it can deviate from the flat slope in the beta profile. In observations, it is common to assume a sum of different beta profiles to capture the slope in the inner  $0.15r_{500c,obs}$ . However, we correct for the mass that we miss in the core by fixing the normalization to reproduce the total gas mass of the profile, which is captured by the gas fraction  $f_{\text{gas},500c}$ . (This is equivalent to redistributing the small amount of mass that we would miss in the core to larger scales.) The slope at large radii,  $\beta$ , and the core radius,  $r_c$ , are the final two parameters determining the profile. We show the residuals of the profile fits in Fig. 2.4 where we also include the residuals of the cumulative mass profile. It is clear from the residuals in the top panels of Fig. 2.4 that the beta profile cannot accurately capture the inner density profile of the hot gas. Arnaud et al. (2010) show that the inner slope can vary from shallow to steep in going from disturbed to relaxed or cool-core clusters. This need not concern us because the deviations from the fit occur at such small radii that they will not be able to significantly affect the power at our scales of interest where the normalization of  $\hat{\rho}_{\text{gas}}(k)$  and, thus, the total mass of the hot gas component is the important parameter. In the

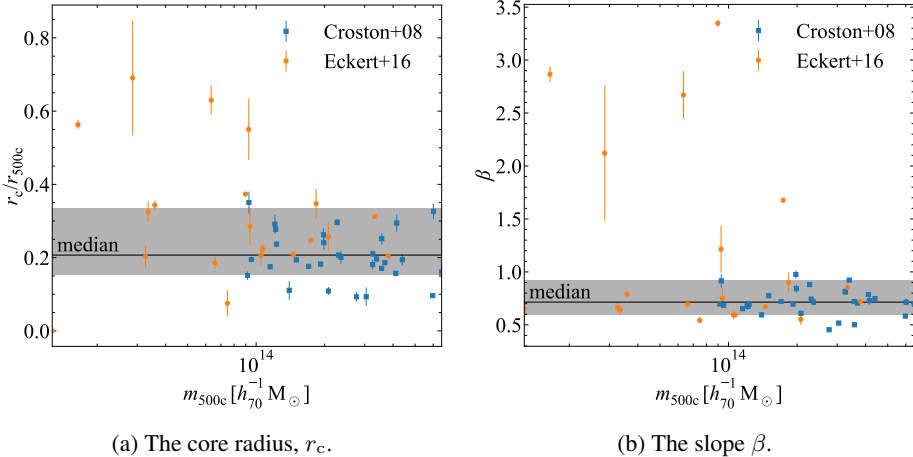


Figure 2.5: The mass dependence of (a) the core radius  $r_c$  and (b) the slope  $\beta$  of the beta hot gas density profile fits, Eq. 2.14. We indicate the 15<sup>th</sup> and 85<sup>th</sup> percentiles with the gray shaded region and the median by the solid line. The error bars indicate the standard deviation in the best-fit parameter. We have binned the Eckert et al. (2016) sample into 20 mass bins. There is no clear mass dependence.

bottom panel of Fig. 2.4 we show the residuals for the cumulative mass. The left-hand panel of the figure clearly shows that we force  $m_{\text{gas},500c}$  in the individual profiles to equal the observed mass.

We show the core radii,  $r_c$ , and slopes,  $\beta$ , that we fit to our data set in Figs. 2.5a and 2.5b, respectively. There is no clear mass dependence in the both of the fit parameters. Thus, we decided to use the median value for both parameters for all halo masses. This significantly simplifies the model, keeping the total number of parameters low.

We show the hydrostatic gas fractions from our observational data in Fig. 2.2. We fit the median  $f_{\text{gas},500c} - m_{500c,\text{obs}}$  relation with a sigmoid-like function given by

$$f_{\text{gas},500c}(m_{500c,\text{obs}}) = \frac{\Omega_b/\Omega_m}{2} \left( 1 + \tanh \left( \frac{\log_{10}(m_{500c,\text{obs}}/m_t)}{\alpha} \right) \right), \quad (2.25)$$

under the added constraint

$$f_{\text{gas},500c}(m_{500c,\text{obs}}) \leq f_b - f_{\star,500c}(m_{500c,\text{obs}}). \quad (2.26)$$

The function has as free parameters the turnover mass,  $m_t$ , and the sharpness of the turnover,  $\alpha$ . We fix the gas fraction for  $m_{500c,\text{obs}} \rightarrow \infty$  to the cosmic baryon fraction  $f_b = \Omega_b/\Omega_m \approx 0.166$ , which is what we expect for deep potential wells and what we also see for the highest-mass clusters. However, we shift down the final  $f_{\text{gas},500c}(m_{500c,\text{obs}})$  relation at halo masses where the cosmic baryon fraction would be exceeded after including the stellar contribution. We also fix the gas fraction for  $m \rightarrow 0$  to 0 since we know that low-mass dwarfs eject their baryons easily and are mainly dark matter dominated (e.g. Silk & Mamon, 2012; Sawala et al., 2015). Moreover, their virial temperatures are

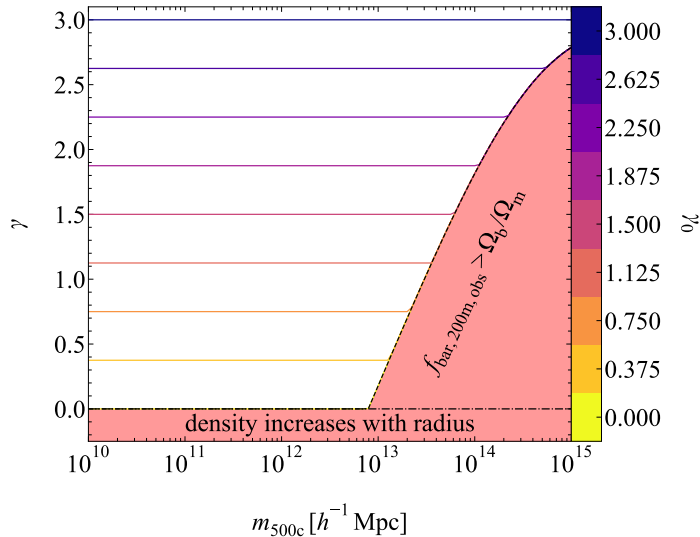


Figure 2.6: The allowed values for the extrapolated slope  $\gamma$  of the beta density profile, Eq. 2.14, as a function of halo mass  $m_{500c,\text{obs}}$ . We colour each line by the value  $\gamma_0 = \gamma(m_{500c,\text{obs}} \rightarrow 0)$ . Since we extrapolate haloes to  $r_{200m,\text{obs}}$ , the most massive haloes would contain too many baryons if  $\gamma$  would be too small. Hence, for each halo mass, we compute the limiting  $\gamma$  for which the halo is baryonically closed at  $r_{200m,\text{obs}}$ . This limit is indicated by the dashed line. For each halo mass only slopes steeper than this limit are allowed.

too low for them to contain X-ray emitting gas. Fixing  $f_{\text{gas},500c}(m \rightarrow 0) = 0$  is probably not optimal, especially since we know that the lower mass haloes will contain a significant warm gas ( $10^4 \lesssim T/\text{K} \lesssim 10^6$ ) component which should increase their baryonic mass. However, since we will use our freedom in correcting the gas fraction at  $r_h$  by assuming profiles outside  $r_{500c,\text{obs}}$ , this choice should not significantly impact our results as we already discussed at the end of Section 2.2.3. For our scales of interest, the shape of the profiles of low-mass systems will not matter as much as their total mass. Forcing the gas fraction to go to 0 for low halo masses causes a deviation from the observations at low halo masses. However, at low halo mass the X-ray observations will always be biased to systems with high gas masses, since these will have the highest X-ray luminosities.

In Fig. 2.2 we also show fits to the data  $f_{\text{gas},500c} - m_{500c,\text{obs}}$  relation assuming a constant hydrostatic mass bias of  $\frac{m_{\text{hydro}}}{m_{\text{true}}} = 1 - b = 0.7$ . In Section 2.5.5 we discuss how we compute this relation and the influence of this assumption on our results.

## 2.4 Model density components

We determined the best-fit parameters for the beta profile, Eq. 2.14, in Section 2.3. The only remaining free parameter in our model is now the slope  $\gamma$  of the extrapolated profile

outside  $r_{500c,\text{obs}}$ . As we explained in Section 2.3, not all values of  $\gamma$  are allowed for each halo mass  $m_{500c,\text{obs}}$ , since the most massive haloes contain a significant fraction of their total baryon budget inside  $r_{500c,\text{obs}}$ . Consequently, these haloes need steeper slopes  $\gamma$ , since otherwise they would exceed the cosmic baryon fraction before they reach the halo radius  $r_{200m,\text{obs}}$ . We thus determine the relation  $\gamma_{\min}(m_{500c,\text{obs}})$  that limits the extrapolated slope such that, given the best-fit beta profile parameters, the halo reaches exactly the cosmic baryon fraction at  $r_{200m,\text{obs}}$ . For each halo mass only slopes steeper than this limiting value are allowed. We show the resulting relation  $\gamma_{\min}(m_{500c,\text{obs}})$  in Fig. 2.6. We colour the curves by  $\gamma_0 = \gamma(m_{500c,\text{obs}} \rightarrow 0)$ . Since low-mass haloes have low baryon fractions at  $r_{500c,\text{obs}}$ , we find that all values of  $\gamma_0$  are allowed. For the most massive haloes, only the steepest slopes  $\gamma \gtrsim 2.8$  are allowed. The handful of observations that are able to probe clusters out to  $r_{200m,\text{obs}}$  indeed find that the slope steepens in the outskirts (Ghirardini et al., 2019).

Now we have all of the ingredients of our model at hand. We show the resulting profiles for our different matter components for 3 halo masses in Fig. 2.7. We show both the `nocb` and `cb` models, where the latter are just the former extended beyond  $r_{200m,\text{obs}}$  until the cosmic baryon fraction is reached. We colour the curves by  $\gamma_0$ . Given  $\gamma_0$ , the actual value of the slope  $\gamma$  for each halo mass can be determined by following the tracks in Fig. 2.6 from low to high halo masses, e.g. for the  $m_{500c,\text{obs}} = 10^{15} h^{-1} M_\odot$  halo all slopes  $\gamma_0 \leq 2.8$  correspond to the actual slope  $\gamma = 2.8$ . Besides the hot gas profiles, we also show the dark matter and stellar (satellite, since the central is modelled as a delta function) profiles. These profiles only depend on the value  $\gamma_0$  through their maximum radius, since the halo radius  $r_h$  is determined by how fast the cosmic baryon fraction is reached and thus depends on  $\gamma_0$ .

It is clear that models with flatter slopes reach their baryon budget at smaller radii. These models will thus capture the influence of a compact baryon distribution on the matter power spectrum. We show the halo baryon fraction at  $r_{200m,\text{obs}}$  for different values of  $\gamma_0$  in Fig. 2.8. The main shape of the gas fractions at  $r_{200m,\text{obs}}$  is set by the constraints on the gas fractions at  $r_{500c,\text{obs}}$ . The group-size haloes have the largest spread in baryon fraction with changing slope  $\gamma_0$ . Our model is thus able to capture a large range of different baryon contents for haloes that all reproduce the observations at  $r_{500c,\text{obs}}$ . The baryon fractions rise steeply between  $10^{11} < m_{200m,\text{obs}}/(h^{-1} M_\odot) < 10^{12}$  due to the peak in the stellar mass fraction in this halo mass range. For the low-mass haloes, the spread in baryon fraction is smaller at  $r_{200m,\text{obs}}$  because we hold the stellar component fixed in our model and their gas fractions are low. As a result, the low-mass systems do not differ much in the `nocb` model. (In the `cb` model they will differ due to the different halo radii  $r_h$  where the cosmic baryon fraction is reached.) For the slope  $\gamma$  between 0 to 3 we will have  $\approx 20$  to 50 per cent of the total baryons in the Universe outside haloes in the `nocb` model.

We have checked that the density profiles with varying  $\gamma_0$  for haloes with  $10^{14} < m_{500c,\text{obs}}/h^{-1} M_\odot < 10^{15}$  only cause a maximum deviation of  $\approx \pm 5$  per cent in the surface brightness profiles for projected radii  $R < r_{500c,\text{obs}}$  compared to the fiducial model with  $\gamma_0 = 3\beta$ . This variation is within the error on the surface brightness counts and the density profiles with varying  $\gamma_0$  are thus indistinguishable from the fiducial model in the investigated mass range. For haloes with  $m_{500c,\text{obs}} \leq 10^{14} h^{-1} M_\odot$ , the deviations

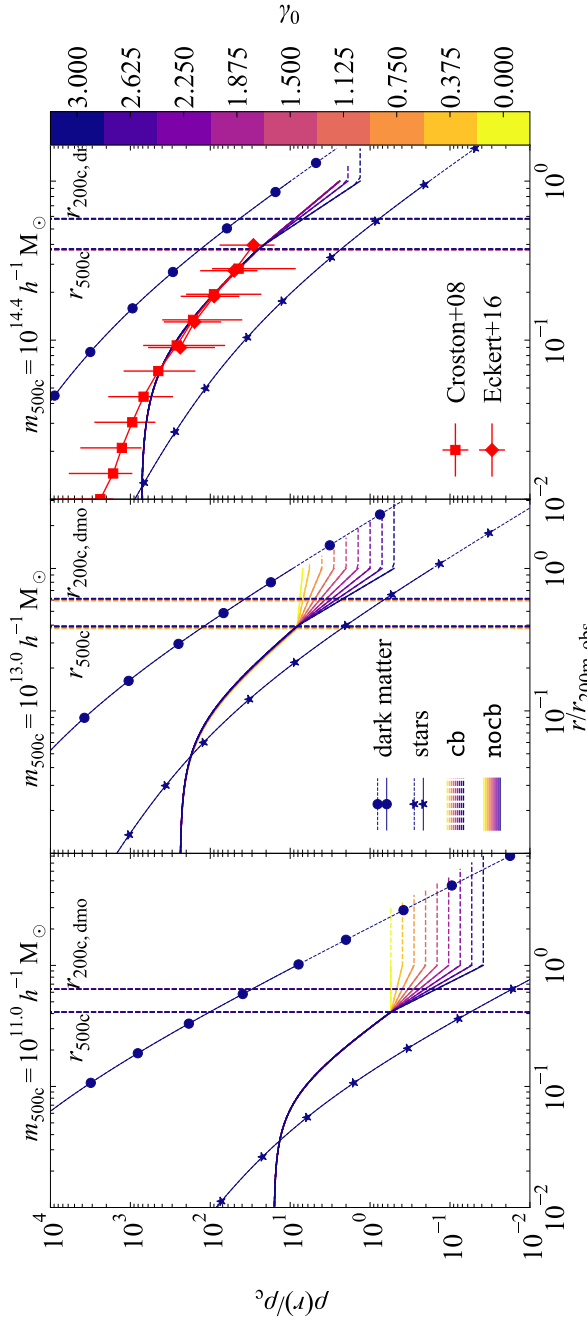


Figure 2.7: Model density profiles for  $m_{500c,\text{obs}} = 10^{11} h^{-1} M_\odot$  (left panel),  $m_{500c,\text{obs}} = 10^{13} h^{-1} M_\odot$  (middle panel), and  $m_{500c,\text{obs}} = 10^{14.4} h^{-1} M_\odot$  (right panel). In the right panel, we also show the median hot gas density profiles inferred from REX-CESS (red, connected squares, Croston et al., 2008) and XXL-100-GC (red, connected diamonds, Eckert et al., 2016) for a sample with the same median halo mass. The error bars indicate the 15<sup>th</sup> and 85<sup>th</sup> percentile range for each radial bin. The lines are colour-coded by  $\gamma_0 \equiv \gamma(m_{500c} \rightarrow 0)$ , the extrapolated power-law slope of the hot gas density profiles between  $r_{500c,\text{obs}}$  and  $r_{200m,\text{obs}}$ , with lower values of  $\gamma_0$  corresponding to flatter slopes. All profiles assume the best-fit beta profile up to  $r_{500c,\text{obs}}$ . Between  $r_{500c,\text{obs}}$  and  $r_{200m,\text{obs}}$  the profiles are extrapolated with a power-law slope of  $\gamma$ . In the case of nocb (solid, coloured lines), we cut off the profiles at the halo definition  $r_{200m,\text{obs}}$ , at which point the halo baryon fraction may be smaller than  $\Omega_b/\Omega_m$ . For the case cb (dashed, coloured lines), we extrapolate the hot gas density profile with a uniform profile until the cosmic baryon fraction is reached. For the case cb of the dark matter (dashed, connected circles) and stellar satellite (dashed, connected stars) profiles, we only show the models with  $\gamma_0 = 3$ , for the other values of  $\gamma_0$  the maximum radius equals that of the corresponding hot gas profile.

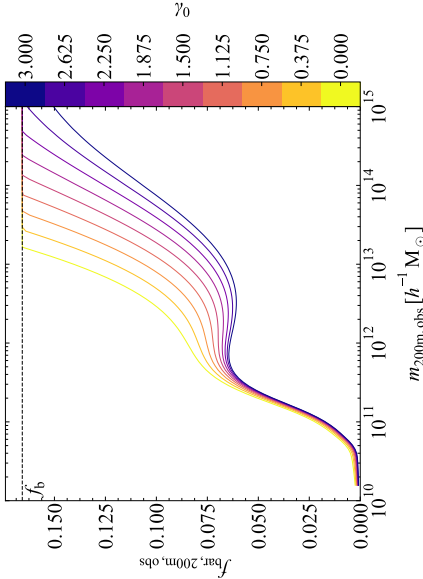


Figure 2.8: The halo baryon fraction at  $r_{200m,\text{obs}}$  as a function of halo mass  $m_{200m,\text{obs}}$ . The baryon fraction  $f_{\text{bar},200m,\text{obs}}$  is the same for both model nocb, which effectively assumes that the missing halo baryons are redistributed far beyond  $r_{200m,\text{obs}}$  on linear scales, and model cb, which adds the missing halo baryons in a uniform profile outside but near  $r_{200m,\text{obs}}$ . The lines are colour-coded by  $\gamma_0 \equiv \gamma(m_{500c} \rightarrow 0)$ , the extrapolated power-law slope of the hot gas density profiles between  $r_{500c,\text{obs}}$  and  $r_{200m,\text{obs}}$ , with lower values of  $\gamma_0$  corresponding to flatter slopes. The shape is set by the observed constraints on the baryon fractions at  $r_{500c,\text{obs}}$ . As  $\gamma_0$  decreases to 0, the halo baryon fractions increase. The knee at  $m_{200m,\text{obs}} \approx 10^{12} h^{-1} M_\odot$  is caused by the peak of the stellar mass fractions. The decreased range of possible baryon fractions for low-mass haloes is the consequence of their low gas fractions and the fixed prescription for the stellar component.

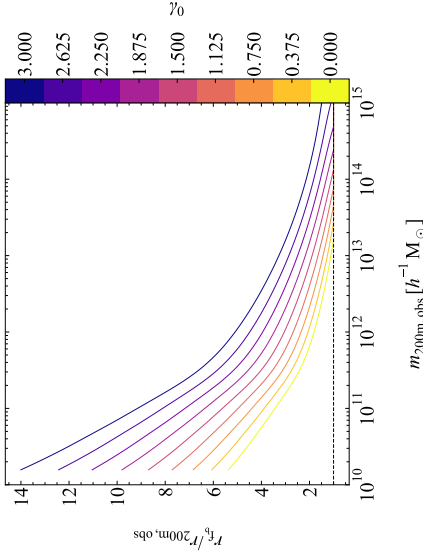


Figure 2.9: The radius where the cosmic baryon fraction is reached in units of  $r_{200m,\text{obs}}$  as a function of halo mass  $m_{200m,\text{obs}}$  for model cb, which adds the missing halo baryons in a uniform profile outside  $r_{200m,\text{obs}}$ . The lines are colour-coded by  $\gamma_0 \equiv \gamma(m_{500c} \rightarrow 0)$ , the extrapolated power-law slope of the hot gas density profiles between  $r_{500c,\text{obs}}$  and  $r_{200m,\text{obs}}$ , with lower values of  $\gamma_0$  corresponding to flatter slopes. As  $\gamma_0$  decreases to 0, the cosmic baryon fraction is reached closer to the halo radius  $r_{200m,\text{obs}}$ .

increase for lower values of  $\gamma_0$ , reaching 10 per cent for  $\gamma_0 = 1.5$  and  $m_{500c,\text{obs}} = 10^{13} h^{-1} M_\odot$ , but the observed hot gas density profiles at these halo masses also show a larger scatter.

We also have the cb model where we force all haloes to include all of the missing baryons in their outskirts. In Fig. 2.9 we show how extended the baryon distribution needs to be in the cb case as a function of the slope  $\gamma_0$ . The variations in the power-law slope paired with the cb and nocb models allow us to investigate the influence on the matter power spectrum of a wide range of possible baryon distributions that all reproduce the available X-ray observations for clusters with  $m_{500c,\text{obs}} \geq 10^{14} h^{-1} M_\odot$ .

## 2

## 2.5 Results

In this section we show the results and predictions of our model for the matter power spectrum and we discuss their implications for future observational constraints. First, we show the influence of assuming different distributions for the unobserved hot gas in Section 2.5.1. We show the influence of correcting observed halo masses to the dark matter only equivalent halo masses in order to obtain the correct halo abundances in Section 2.5.2. In Section 2.5.3, we show which halo masses dominate the power spectrum for which wavenumbers. Finally, we show the influence of varying the best-fit observed profile parameters in Section 2.5.4 and we investigate the effects of a hydrostatic bias in the halo mass determination in Section 2.5.5.

### 2.5.1 Influence of the unobserved baryon distribution

In this section, we will investigate the influence of the distribution of the unobserved baryons inside and outside haloes on the matter power spectrum. Since we currently have only a very tenuous grasp of the whereabouts of the missing baryons, it is important to explore how their possible distribution impacts the matter power spectrum.

As stated in Section 2.2.3, our model is characterized by the extrapolated power-law slope  $-\gamma$  for the hot gas density profile and by whether we assume the missing halo baryons to reside in the vicinity of the halo (model cb) or not (model nocb). As explained in Section 2.2.3, these two types of models only differ in  $\hat{\rho}(k|m)$  due to the inclusion of more mass outside the traditional halo definition of  $r_{200m,\text{obs}}$  in the cb case (see Figs. 2.7, 2.9). When discussing our model predictions for the power spectrum, we consider the range  $0.1 h \text{ Mpc}^{-1} \leq k \leq 5 h \text{ Mpc}^{-1}$  to be the vital regime since future surveys will gain their optimal signal-to-noise for  $k \approx 1 h \text{ Mpc}^{-1}$  (Amendola et al., 2018).

We show the response of the matter power spectrum to baryons for the nocb and cb models in, respectively, the top-left and top-right panels of Fig. 2.10. The lines are coloured by the assumed value of  $\gamma_0$ . We indicate our fiducial model, which extrapolates the best-fit  $\beta = 0.71_{-0.12}^{+0.20}$ , i.e.  $\gamma_0 = 3\beta = 2.14$ , from the X-ray observations, with the thick, black line. All models show a suppression of power on large scales with respect to the DMO prediction. All of our models have an upturn in the response for  $k \gtrsim 10 h \text{ Mpc}^{-1}$  and an enhancement of power for  $k \gtrsim 50 h \text{ Mpc}^{-1}$  due to the stellar component. This upturn is not present in other halo model approaches that only modify

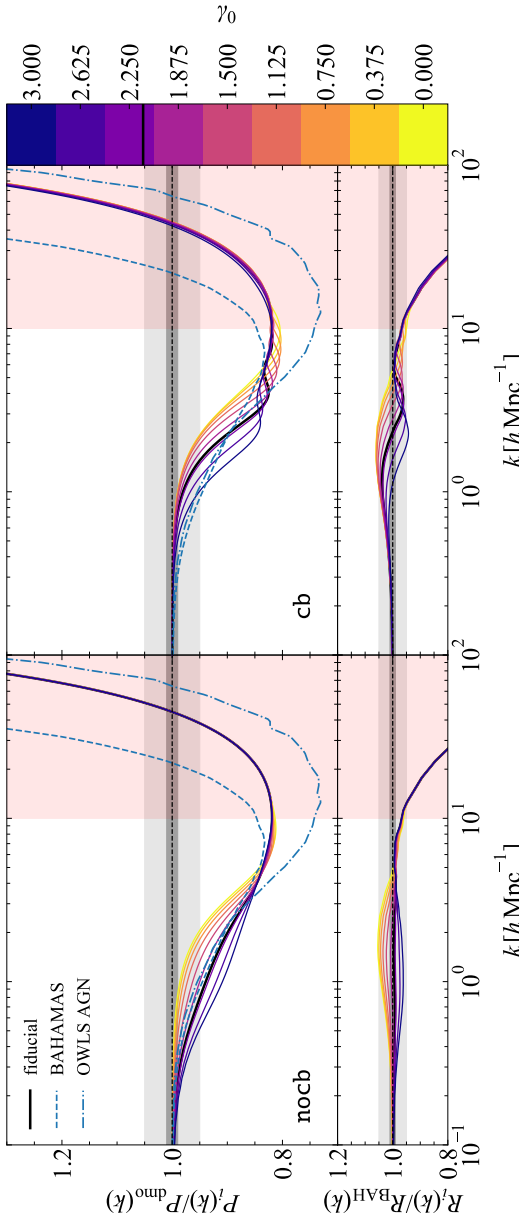


**Figure 2.10: Top row** The ratio of our halo model power spectra with baryons to the corresponding dark matter only prediction. The dark and light gray bands indicate the 1 per cent and 5 per cent intervals. The left-hand panel shows model nocb, which effectively assumes that the baryons missing from haloes are redistributed far beyond  $r_{200m,\text{obs}}$  on linear scales. The right-hand panel shows model cb, which adds the missing halo baryons in a uniform profile outside but near  $r_{200m,\text{obs}}$ . The red, lightly-shaded region for  $k > 10 h \text{ Mpc}^{-1}$  indicates the scales where our model is not a good indicator of the uncertainty because the stellar component is not varied. We indicate our fiducial model, which simply extrapolates the best-fit beta profile to the hot gas density profiles of clusters, with a thick black line. The lines are colour-coded by  $\gamma_0 \equiv \gamma(m_{500c} \rightarrow 0)$ , the extrapolated power-law slope of the hot gas density profiles between  $r_{500c,\text{obs}}$  and  $r_{200m,\text{obs}}$ , with lower values of  $\gamma_0$  corresponding to flatter slopes. The clear difference between the nocb and cb models on large scales indicates that it is very important to know where the missing halo baryons end up. Placing the missing halo baryons in the vicinity of the haloes increases the power on large scales significantly for fixed  $\gamma_0$ . Our model is flexible enough, especially in the nocb case, to encompass the behaviour of both the BAHAMAS (blue, dashed line) and OWLS (blue, dash-dotted line) simulations on large scales.

**Bottom row** The ratio between the matter power spectra responses to baryons predicted by our models and the BAHAMAS simulation. Both our fiducial models are within  $\approx 5$  per cent of BAHAMAS for  $k < 10 h \text{ Mpc}^{-1}$ .

the dark matter profiles (e.g. [Smith et al., 2003](#); [Mead et al., 2015](#)). We shade the region  $k > 10 h \text{ Mpc}^{-1}$  in red because the range in responses of our model does not span the range allowed by observations there. On the contrary, on these small scales all of our models behave the same, since the hot gas is completely determined by the best-fit beta profile to the X-ray observations, and the stellar component is held fixed.

The total amount of power suppression at large scales depends sensitively on the halo baryon fractions, since models with the highest values of  $\gamma_0$  also have the lowest baryon fractions  $f_{\text{bar},200\text{m,obs}}$  at all halo masses (see Fig. 2.8). Our results confirm the predictions from hydrodynamical simulations, which have shown similar trends ([van Daalen et al., 2011, 2019](#); [Hellwing et al., 2016](#); [McCarthy et al., 2017](#); [Springel et al., 2017](#); [Chisari et al., 2018](#)). However, our results do not rely on the uncertain assumptions associated with subgrid models for feedback processes. Our phenomenological model simply requires that we reproduce the density profiles of clusters without any assumptions about the underlying physics that resulted in the profiles.

The nocb model, shown in the left-hand panel of Fig. 2.10, results in a larger spread of possible responses because the final total halo mass is not fixed to account for all the baryons as in cb. The nocb models with the steepest extrapolated density profiles, i.e. the highest values for  $\gamma_0$ , function as upper limits on the response, since the missing halo baryons are in reality likely to reside in the vicinity of the haloes and because low-mass haloes likely contain more gas than predicted by our extrapolated relation. However, this gas may not be well described by our beta profile assumption derived from the hot gas properties of clusters. On the other hand, the cb models with flatter slopes (lower values for  $\gamma_0$ ), shown in the right-hand panel of Fig. 2.10, function as lower limits on the response of the power spectrum to baryons, since it is likely that a significant fraction of the baryons does not reside inside haloes but rather in the diffuse, warm-hot, intergalactic medium (WHIM, as has been predicted by simulations and recently inferred from observations, see e.g. [Cen & Ostriker, 1999](#); [Dave et al., 2001](#); [Nicastro et al., 2018](#)). Hence, we find that the (minimum, fiducial, maximum) value of the minimum wavenumber for which the baryonic effect reaches 1 per cent is  $(0.2, 0.3, 0.9) h \text{ Mpc}^{-1}$  in the nocb models and  $(0.5, 0.8, 1) h \text{ Mpc}^{-1}$  in the cb models. The 5 per cent threshold is reached for  $(0.5, 0.8, 2) h \text{ Mpc}^{-1}$  and  $(1, 1.4, 2) h \text{ Mpc}^{-1}$ , respectively, for the nocb and cb models.

We indicate the AGN\_TUNED\_nu0\_L400N1024\_WMAP9 results from the BAHAMAS simulation, which has been shown to reproduce a plethora of observations for massive systems ([McCarthy et al., 2017](#); [Jakobs et al., 2018](#)), and the result for the OWLS AGN simulation ([Schaye et al., 2010](#); [van Daalen et al., 2011](#)) which has been widely used as a reference model in weak lensing analyses and is also consistent with the observed cluster gas fractions ([McCarthy et al., 2010](#)). We show the ratio between our models and the BAHAMAS prediction of the power spectrum response to the presence of baryons in the bottom row of Fig. 2.10. Our models encompass both the BAHAMAS and OWLS predictions for  $k \lesssim 5 h \text{ Mpc}^{-1}$ , which is the range of interest here. In the cb case, our models all predict less power suppression than the simulations on large scales  $k \lesssim 1 h \text{ Mpc}^{-1}$ , which is most likely due to the fact that in the simulations there are actually baryons in the cosmic web that should not be accounted for by haloes, thus suggesting that models nocb may be more realistic. However, since there are no observational constraints on the location of the missing halo baryons, we cannot exclude the models cb. We stress that we

did not fit our model to reproduce these simulations. The overall similarity is caused by the simulations reproducing the measured X-ray hot gas fractions that we fit our model to.

In Fig. 2.11, we compare predictions for the power spectrum response to baryons from a large set of higher-resolution, but smaller-volume, cosmological simulations to the prediction of our fiducial model. We compare the EAGLE (Schaye et al., 2015; Hellwing et al., 2016), IllustrisTNG (Springel et al., 2017), Horizon-AGN (Chisari et al., 2018), and Illustris (Vogelsberger et al., 2014a) simulations. We can see that in all of these simulations, except for Illustris, which is known to have AGN feedback that is too violent on group and cluster scales (Weinberger et al., 2017), the baryonic suppression becomes significant only at much smaller scales than in OWLS, BAHAMAS and our own model. From the halo model it is clear that the total baryon content of haloes, and thus the cluster gas fractions, are the dominant cause of baryonic power suppression on large scales  $k \lesssim 1 h \text{ Mpc}^{-1}$ , since  $\hat{\rho}(k|m) \rightarrow m$  there. Indeed, van Daalen et al. (2019) explicitly demonstrated the link between cluster gas fractions and power suppression on large scales for a large set of hydrodynamical simulations including these. Since BAHAMAS and OWLS AGN reproduce the cluster hot gas fractions, they predict the same large-scale behaviour for the power spectrum response to baryons. However, the other small-volume, high-resolution simulations overpredict the baryon content of groups and clusters as was shown for EAGLE, IllustrisTNG, and Horizon-AGN by, respectively, Barnes et al. (2017), Barnes et al. (2018), and Chisari et al. (2018). We thus stress the importance of using simulations that are calibrated towards the relevant observations when training or comparing models aimed at predicting the matter power spectrum.

The small-scale behaviour of the power spectrum response to baryons is very sensitive to the stellar density profiles and as a result we see a large variation between the different simulation predictions in Fig. 2.11. As is shown by van Daalen et al. (2019), the small-scale power turnover in the simulations depends strongly on the resolution and subgrid physics of the simulation. We mentioned earlier that our model is fixed at these scales by the best-fit beta profiles to the X-ray observations and the fixed stellar component.

Recently, van Daalen et al. (2019) analyzed 92 hydrodynamical simulations, including all the ones shown in Fig. 2.11, and showed that there is a strong correlation between the total power suppression at a fixed scale  $k \lesssim 1 h \text{ Mpc}^{-1}$  and the baryon fraction at  $r_{500c}$  of haloes with  $m_{500c} = 10^{14} h^{-1} \text{ M}_\odot$ . We investigate the same relation with our model. We show the different relations that we assume for the gas fraction  $f_{\text{gas},500c}(m_{500c,\text{obs}})$  in Fig. 2.12. For these relations we assume the best-fit value  $\alpha = 1.35$  from our fit to the observed gas fractions in Eq. (2.25), but we vary the turnover mass from its best-fit value of  $\log_{10} m_t/(h^{-1} \text{ M}_\odot) = 13.94$ . Thus, we can capture a large range of possible gas fractions at  $r_{500c,\text{obs}}$ , allowing us to encompass both the observed and the simulated gas fractions of  $m_{500c,\text{obs}} = 10^{14} h^{-1} \text{ M}_\odot$  haloes. For all these relations we then compute the power spectrum response due to the inclusion of baryons at the fixed scale  $k = 0.5 h \text{ Mpc}^{-1}$ . We show the power suppression at this scale as a function of the halo baryon fraction in  $m_{500c,\text{obs}} = 10^{14} h^{-1} \text{ M}_\odot$  haloes in Fig. 2.13. Similarly to van Daalen et al. (2019), we find that higher baryon fractions at fixed halo mass result in smaller power suppression at fixed scale. In the nocb (cb) case, the model with  $\gamma_0 = 1.125$  ( $\gamma_0 = 3$ ) most closely tracks the prediction from the hydrodynamical simulations. However, since

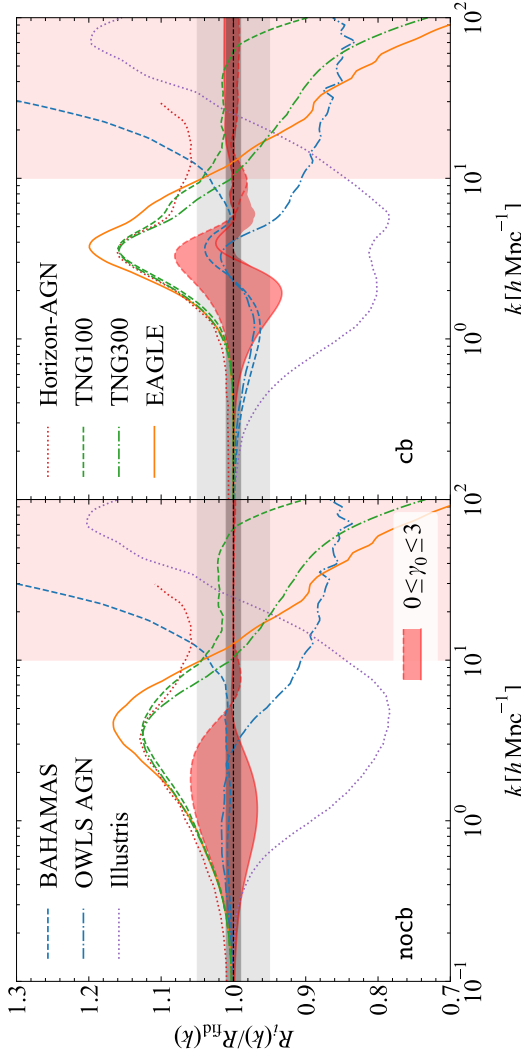


Figure 2.11: The ratio between the power spectrum response to baryons predicted by hydrodynamical simulations from the literature and our fiducial halo model, which simply extrapolates the best-fit beta profile to the hot gas density profiles of clusters. The dark and light gray bands indicate the 1 per cent and 5 per cent intervals. The left-hand panel shows model nocb, which effectively assumes that the baryons missing from haloes are redistributed far beyond  $r_{200m,obs}$  on linear scales. The right-hand panel shows model cb, which adds the missing halo baryons in a uniform profile outside but near  $r_{200m,obs}$ . The red, lightly-shaded region for  $k > 10 h \text{ Mpc}^{-1}$  indicates the scales where our model is not a good indicator of the uncertainty because the stellar component is not varied. The shaded red region shows the spread in our models for all values of  $\gamma_0$ , i.e. the extrapolated power-law slope of the hot gas density profiles between  $r_{500c,obs}$  and  $r_{200m,obs}$ , with red lines indicating  $\gamma_0 = 0$  (red, dashed line) and  $\gamma_0 = 3$  (red, solid line). The blue lines indicate simulations that reproduce the hot gas fractions of clusters, i.e. BAHAMAS (blue, dashed line, McCarthy et al., 2017) and OWLS AGN (blue, dash-dotted line, van Daalen et al., 2011). We show the higher-resolution but smaller-volume simulations which predict too large cluster gas fractions, i.e. EAGLE (orange, solid line, Hellwing et al., 2016), IllustrisTNG-100 and 300 (green, dashed and dash-dotted lines, respectively, Springel et al., 2017), Horizon-AGN (red, dotted line, Chisari et al., 2018). We also show the original Illustris result (purple, dotted line, Vogelsberger et al., 2014b), which underpredicts cluster gas fractions. Our empirical model encompasses the simulations that reproduce the cluster hot gas fractions on all scales  $k \lesssim 5 h \text{ Mpc}^{-1}$ , but the other simulations fall outside of the allowed range.

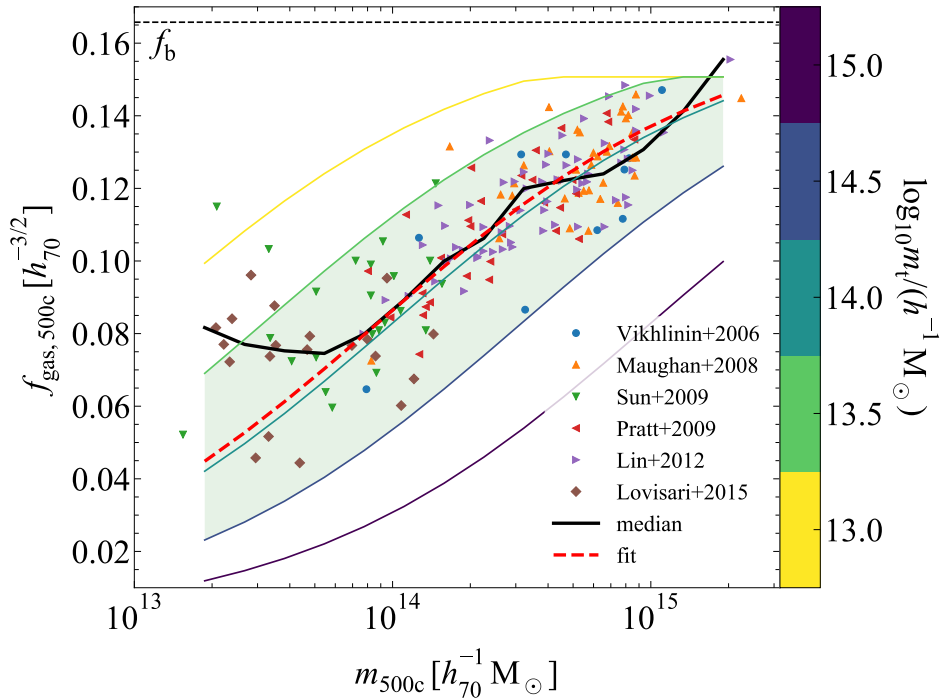


Figure 2.12: The X-ray hydrostatic gas fractions as a function of halo mass, as in Fig. 2.2. The curves show the sigmoid-like fit from Eq. (2.25) with the best-fit value for  $\alpha = 1.35$ , coloured by the value  $\log_{10} m_t / (h^{-1} M_\odot) \in \{13, 13.5, 14, 14.5, 15\}$  (the best-fit value is 13.94). The shaded green region indicates the area that is broadly in agreement with observations.

our model has complete freedom for the gas density profile in the halo outskirts, the range of possible power suppression is much larger than that found in the simulations analyzed by van Daalen et al. (2019). The matter distribution in simulations is constrained by the subgrid physics that is assumed. Hence, relying only on simulation predictions might result in an overly constrained and model-dependent parameter space, since other subgrid recipes might result in differences in the matter distribution at large scales.

We conclude that the total baryon fraction of massive haloes is of crucial importance to the baryonic suppression of the power spectrum. Our model and hydrodynamical simulations that reproduce the cluster gas fractions are in general agreement about the total amount of suppression at scales  $k \lesssim 5 h \text{ Mpc}^{-1}$ , with the exact amplitude depending on the details of the missing baryon distribution and varying by  $\approx \pm 5$  per cent around our fiducial model. Observations of the total baryonic mass for a large sample of groups and clusters would provide a powerful constraint on the effects of baryons on the matter power spectrum, provided we are able to reliably measure the cluster masses. Cluster gas masses can be determined with X-ray observations and their outskirts can be probed with SZ measurements. Groups are subject to a significant Malmquist bias in the X-ray regime and

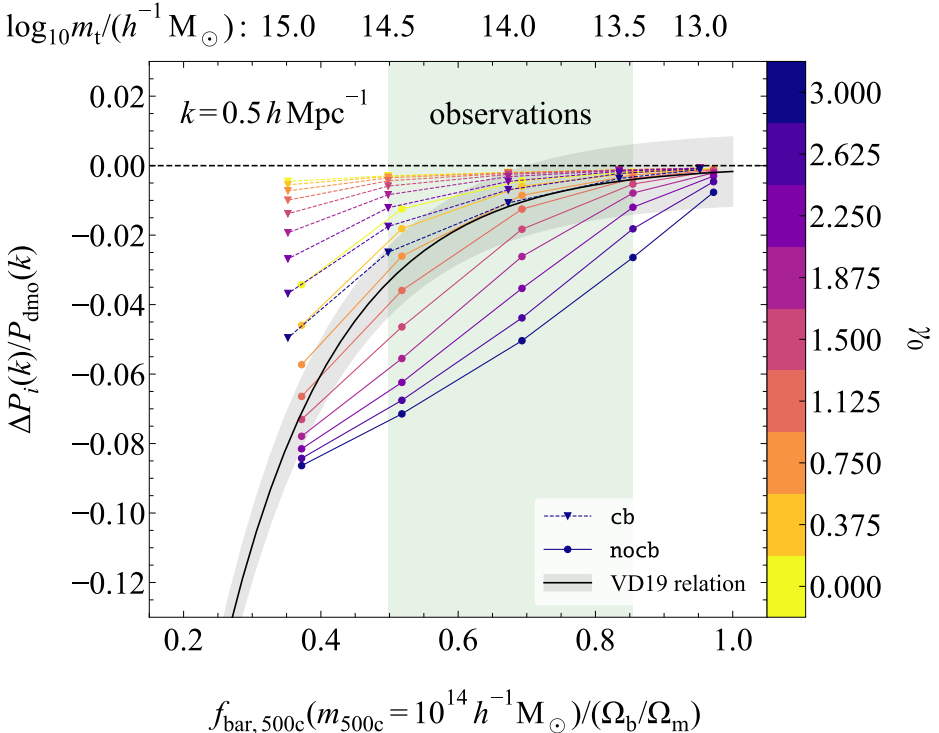


Figure 2.13: The power suppression due to the inclusion of baryons at the fixed scale  $k = 0.5 h \text{Mpc}^{-1}$  as a function of the baryon fraction of haloes with  $m_{500c,\text{obs}} = 10^{14} h^{-1} \text{M}_\odot$ . The shaded green region indicates the gas fractions that broadly agree with observations. The cb (dashed, connected triangles) and nocb (connected circles) models are coloured by  $\gamma_0$ , i.e. the value of the extrapolated power-law slope of the hot gas density profiles between  $r_{500c,\text{obs}}$  and  $r_{200m,\text{obs}}$ . We show the relation found by [van Daalen et al. \(2019\)](#) for hydrodynamical simulations and its  $\pm 1$  per cent variation (black line with grey, shaded region). We indicate the value of  $\log_{10} m_t/(h^{-1} \text{M}_\odot)$  in Eq. (2.25) along the top x-axis. Both our model and VD19 predict a positive correlation between the power suppression at fixed scale and the halo baryon fraction at fixed halo mass. However, it is clear that our model allows for a larger range in possible power suppression at fixed halo baryon fraction than is found in the simulations.

SZ measurements from large surveys like Planck ([Planck Collaboration et al., 2016a](#)), the Atacama Cosmology Telescope (ACTPol, [Hilton et al., 2018](#)), and the South Pole Telescope (SPT, [Bleem et al., 2015](#)) generally do not reach a high enough Signal-to-Noise ratio (SNR) to reliably measure the hot gas properties of group-mass haloes. Constraining the total baryon fraction of these haloes is thus challenging. However, progress could be made by adopting cross-correlation approaches between SZ maps and large redshift surveys as in [Lim et al. \(2018\)](#). Finally, accurately determining the baryon fraction re-

lies on accurate halo mass determinations for the observed systems. Halo masses can be determined from scaling relations between observed properties (e.g. the hot gas mass, the X-ray temperature, or the X-ray luminosity) and the total halo mass. However, these relations need to be calibrated to a direct measurement of the halo mass through e.g. a weak lensing total mass profile. We will investigate the influence of a hydrostatic bias in the halo mass determination in Section 2.5.5.

## 2.5.2 Influence of halo mass correction due to baryonic processes

Since halo abundances are generally obtained from N-body simulations, it is crucial that we are able to correctly link observed haloes to their dark matter only equivalents. However, astrophysical feedback processes result in the ejection of gas and, consequently, a modification of the halo profile and the halo mass  $m_{200m}$  (e.g. [Sawala et al., 2013](#); [Velliscig et al., 2014](#); [Schaller et al., 2015](#)). Thus, not accounting for the change in halo mass due to baryonic feedback would result in the wrong relation between halo density profiles and halo abundances in our model. Generally, feedback results in lower extrapolated halo masses  $m_{200m,obs}$  for the observed haloes than the DMO equivalent halo masses  $m_{200m,dmo}$ . Thus, using the observed mass instead of the DMO equivalent mass in the halo mass function would result in an overprediction of the abundance of the observed halo since  $n(m)$  decreases with increasing halo mass.

We described how we link  $m_{200m,obs}$  to  $m_{200m,dmo}$  in Section 2.2.2. We remind the reader that we assume that baryons do not significantly alter the distribution of dark matter. Thus, the dark matter component of the observed halo has the same scale radius as its DMO equivalent and a mass that is a factor  $1 - \Omega_b/\Omega_m$  lower. The baryonic component of the observed halo is determined by the observations and our different extrapolations for  $r > r_{500c,obs}$ . Then, from the total and rescaled DM density profiles of the observed halo, we can determine the masses  $m_{200m,obs}$  and  $m_{200m,dmo}$ , respectively. These two masses will differ because the baryons do not follow the dark matter. The haloes have the abundance  $n(m_{200m,dmo}(m_{200m,obs}))$  for which we use the halo mass function determined by [Tinker et al. \(2008\)](#). In this section, we test how this correction, i.e. using  $n(m_{200m,dmo}(m_{200m,obs}))$  instead of  $n(m_{200m,obs})$ , modifies our results.

We show the ratio of the observed halo mass to the DMO equivalent halo mass at fixed radius  $r_{200c,dmo}$  in Fig. 2.14. This ratio does not depend on the model type, i.e. cb or nocb, since their density profiles are the same for  $r < r_{200m,obs}$ . We indicate the range spanned by our models with  $0 \leq \gamma_0 \leq 3$  by the red shaded region. They converge at the high-mass end because not all slopes  $\gamma$  are allowed for high-mass haloes, as shown in Section 2.4. At the low-mass end, our models converge because the stellar component is fixed and hence does not depend on  $\gamma_0$ , and the gas fractions approach 0. The thin, black, dotted line indicates the ratio  $1 - f_b$  that our model converges to when the halo baryon fraction reaches 0.

We also show the same relation found in the OWLS AGN (low-mass haloes, [Schaye et al., 2010](#)) and cosmo-OWLS (high-mass haloes, [Le Brun et al., 2014](#)) simulations from [Velliscig et al. \(2014\)](#). There are systematic differences between the predictions from the simulations and our model. These differences occur for two reasons. First, our assumption that the baryons do not alter the distribution of the dark matter with respect to the DMO

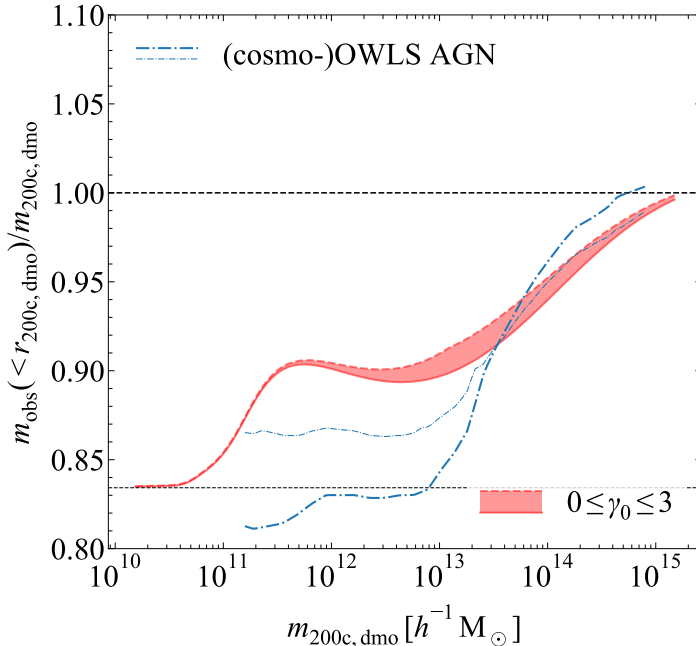


Figure 2.14: The ratio of the enclosed observed halo mass to the dark matter only equivalent mass at the fixed radius  $r_{200c,\text{dmo}}$  as a function of  $m_{200c,\text{dmo}}$ . The shaded red region shows the spread in our models for all values of  $\gamma_0$ , i.e. the extrapolated power-law slope of the hot gas density profiles between  $r_{500c,\text{obs}}$  and  $r_{200m,\text{obs}}$ , with red lines indicating  $\gamma_0 = 0$  (red, dashed line) and  $\gamma_0 = 3$  (red, solid line). The thin, black, dotted line indicates the ratio  $1 - f_b$  that our model converges to when the halo baryon fraction reaches 0. The mass ratios at fixed radius  $r_{200c,\text{dmo}}$  converge towards high halo masses since not all values of  $\gamma$  are allowed for massive haloes. For low masses, the ratios converge because the stellar component is held fixed and the gas fractions are low. The thick, blue, dash-dotted line shows the same relation at fixed radius  $r_{200c,\text{dmo}}$  in the (cosmo-)OWLS AGN simulation (Velliscig et al., 2014). The thin, blue, dash-dotted line shows the simulation relation corrected for changes in the dark matter mass profiles at  $r_{200c,\text{dmo}}$  with respect to the DMO equivalent haloes, since our model assumes that baryons do not affect the dark matter profile. The remaining difference in the mass ratio is due to differing baryon fractions between our model and the simulations.

equivalent halo, does not hold in detail. Velliscig et al. (2014) show that at the fixed radius  $r_{200c,\text{dmo}}$  there is a difference of up to 4 per cent between the dark matter mass of the observed halo and the dark matter mass of the DMO equivalent halo, rescaled to account for the cosmic baryon fraction. The dark matter in low-mass haloes expands due to feedback expelling baryons outside  $r_{200c,\text{dmo}}$ . In the highest-mass haloes, feedback is less efficient and the dark matter contracts in response to the cooling baryons. The thin, blue, dash-dotted line shows the relation in OWLS AGN when forcing the dark

matter mass of the halo to equal the rescaled DMO equivalent halo mass. Hence, the contraction due to the presence of baryons of the dark matter component for high-mass haloes explains the difference between our model and the simulations. For the low-mass end, the expansion of the dark matter component is not sufficient to explain all of the difference. The remaining discrepancy results from the higher baryons fractions in our model compared to the simulations.

We will neglect the response of the DM to the redistribution of baryons throughout the rest of the paper. We have checked that scaling the halo density profiles of the DMO equivalent haloes to match the mass ratios from the OWLS AGN simulation only affects our predictions of the power suppression at the  $\approx 1$  per cent level at our scales of interest (i.e.  $k < 10 h \text{ Mpc}^{-1}$ ). However, even this small correction is an upper limit because we have assumed a fixed ratio between the DM and rescaled DMO density profiles that exceeds the correction for the cosmic baryon fraction. Hence, even at large distances  $r \gg r_{200c,\text{dmo}}$  the mass ratio between the halo and its DMO equivalent does not converge, whereas the mass difference between hydrodynamical haloes and their DMO equivalents eventually decreases to 0 (see e.g. [Velliscig et al., 2014](#); [van Daalen et al., 2014](#)). We find such a small effect because the low-mass haloes, whose mass ratio differs the most between our model and the OWLS AGN simulation, only have a small effect on the total power at large scales, as we will show in Section 2.5.3.

We show how the correction of the halo abundance for the change in halo mass due to baryonic processes affects the predicted power spectrum response to baryons in Fig. 2.15. In the top row, we show the power spectrum response for both the nocb (left panel) and cb models (right panel) with (our fiducial models, solid lines) and without (dashed lines) the halo mass correction. When not correcting the halo abundance for the change in halo mass (i.e. when using  $n(m_{200m,\text{obs}})$ ), we actually find an increase in power with respect to the DMO model at scales  $k \lesssim 1 h \text{ Mpc}^{-1}$ , i.e.  $R_i(k) > 1$ , for both the nocb and cb models, since the inferred abundances for observed haloes with masses  $m_{200m,\text{obs}} \lesssim 10^{14} h^{-1} \text{ M}_\odot$  are too high. At these scales, the Fourier profiles become constant in the 1h term, i.e.  $\hat{\rho}(k|m_h) \rightarrow m_h$  in Eq. 2.4, and the power spectrum behaviour is thus dictated entirely by the halo abundance. Hence, the power suppression that we find in our fiducial models at these scales is the consequence of correcting the DMO equivalent halo masses to account for the ejection of matter due to feedback. We stress that our implementation of this effect is purely empirical and does not rely on any assumptions about the physics involved in baryonic feedback processes.

In the bottom row of Fig. 2.15, we show the ratio between the power spectrum response to the inclusion of baryons with and without the DMO equivalent halo mass correction. The correction is most significant for the steepest extrapolated density profile slopes, i.e. the highest values of  $\gamma_0$ , for which we see the smallest ratios. For  $\gamma_0 = 3$ , even the most massive haloes do not reach the cosmic baryon fraction inside  $r_{200m,\text{obs}}$  (see Fig. 2.8), and, hence, even their abundances would be calculated wrongly if the observed total mass was used, instead of the rescaled, observed DM mass, to compute the halo abundance. In the case of the cb models, there is an extra increase in power for scales  $k \lesssim 1 h \text{ Mpc}^{-1}$  due to the more extended baryon distribution.

It is striking how the halo mass correction modifies the suppression of power in the way required to encompass the simulation predictions at large scales. The correction to

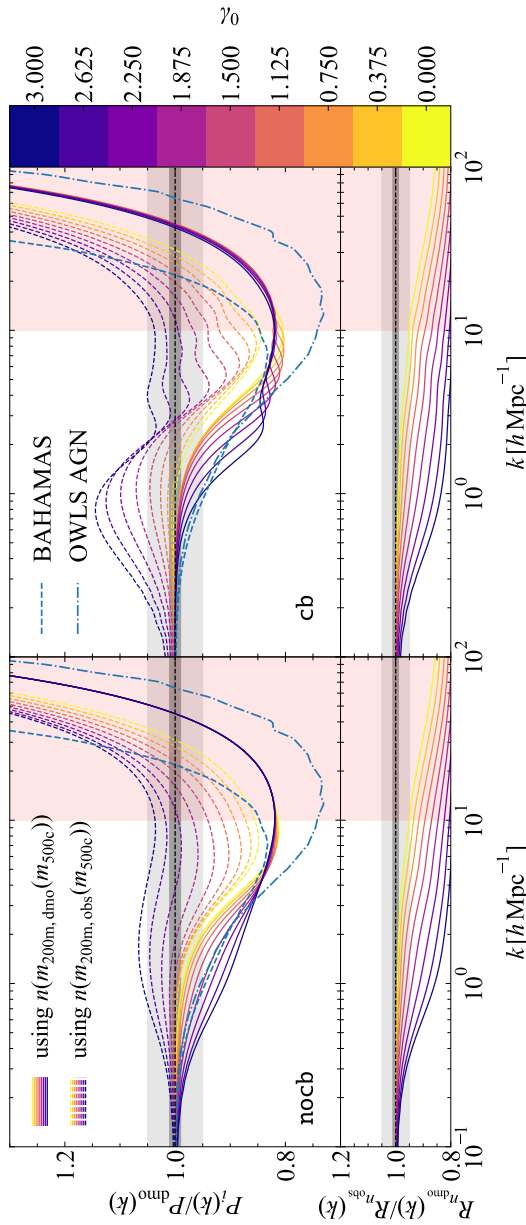


Figure 2.15: *Top row* The influence of correcting the halo abundance for the halo mass decrease due to baryonic processes. The dark and light gray bands indicate the 1 per cent and 5 per cent intervals. The left-hand panel shows model nocb, which effectively assumes that the baryons missing from haloes are redistributed far beyond  $r_{200m,\text{obs}}$  on linear scales. The right-hand panel shows model cb, which adds the missing halo baryons in a uniform profile outside but near  $r_{200m,\text{obs}}$ . The red, lightly-shaded region for  $k > 10h \text{Mpc}^{-1}$  indicates the scales where our model is not a good indicator of the uncertainty because the stellar component is not varied. The lines are colour-coded by  $\gamma_0 \equiv \gamma(m_{500c} \rightarrow 0)$ , the extrapolated power-law slope of the hot gas density profiles between  $r_{500c,\text{obs}}$  and  $r_{200m,\text{obs}}$ , with lower values of  $\gamma_0$  corresponding to flatter slopes. We show the power spectrum response with (our fiducial models, solid lines) and without (dashed lines) the correction for the halo masses applied. In the latter case, we find more power than in the DMO case at large scales because the abundance of low-mass haloes is overestimated due to not accounting for their mass loss compared to their DMO equivalents. *Bottom row* The ratio of the power spectrum with and without correction for the halo masses. Models with flatter slopes, i.e. lower values of  $\gamma_0$ , reach the cosmic baryon fraction at  $r_{200m,\text{obs}}$  for lower halo masses, resulting in the same total mass-abundance relation as the DMO equivalent halo for a larger range of halo masses and thus more similar power spectra.

the DMO equivalent halo masses is necessary for this match.

### 2.5.3 Contribution of different halo masses

To determine the observables that best constrain the matter power spectrum at different scales, it is important to know which haloes dominate the suppression of power at those scales. The dominant haloes will be determined by the interplay between the total mass of the halo and its abundance.

The halo model linearly adds the contributions from haloes of all masses to the power at each scale. We show the contributions for five decades in mass in Fig. 2.16 for our fiducial model in the nocb and cb cases. We integrate the 1-halo term, Eq. 2.4, over 5 different decades in mass, spanning  $10^{10} h^{-1} M_\odot < m_{500c,\text{obs}} < 10^{15} h^{-1} M_\odot$ , and then divide each by the DMO power spectrum, showing the contribution of different halo masses to the power spectrum. We also show the contribution of the 2-halo term, i.e. the linear power spectrum. The mass dependence of our model comes entirely from the 1h term, which dominates the total power for  $k \gtrsim 0.5 h \text{ Mpc}^{-1}$ .

We want to quantify the stellar contribution to the power spectrum to gauge whether we are allowed to neglect the ISM component of the gas. As explained in the beginning of Section 2.2.3, we can safely neglect the ISM if the stellar component contributes negligibly to the total power at our scales of interest ( $k \lesssim 5 h \text{ Mpc}^{-1}$ ). To this end, we also include the 1h term for the stellar component with all cross-correlations  $|\rho_*(k|m_h)\rho_i(k|m_h)|$  in Eq. (2.4) with  $i \in \{\text{dm, gas}\}$ . We only show this contribution for the nocb case, since the cb results are nearly identical. Fig. 2.16 clearly shows that the stellar component contributes negligibly to the power for all scales  $k \lesssim 5 h \text{ Mpc}^{-1}$  and, hence, we are justified in neglecting the contributions of the ISM to the gas component. However, for making predictions at the 1 per cent level on small scales ( $k \gtrsim 5 h \text{ Mpc}^{-1}$ ), the ISM and stellar components will become important and will need to be modelled more accurately.

At scales  $k \lesssim 10 h \text{ Mpc}^{-1}$ , the total power is dominated by groups ( $10^{13} h^{-1} M_\odot \leq m_{500c,\text{obs}} \leq 10^{14} h^{-1} M_\odot$ ) and clusters ( $10^{14} h^{-1} M_\odot \leq m_{500c,\text{obs}} \leq 10^{15} h^{-1} M_\odot$ ) of galaxies, with groups providing a similar or greater contribution than clusters. Similar results have been found in DMO simulations by van Daalen & Schaye (2015). Group-mass haloes have the largest range in possible baryon fractions in our model, depending on the slope  $\gamma_0$  of the gas density profile for  $r > r_{500c,\text{obs}}$ . We conclude that groups are crucial contributors to the power at large scales and thus measuring the baryon content of group-mass haloes will provide the main observational constraint on predictions of the baryonic suppression of the matter power spectrum.

### 2.5.4 Influence of density profile fitting parameters

So far, we have shown the impact of the baryon distribution and haloes of different masses on the matter power spectrum for different wavenumbers when assuming our model that best fits the observations. However, since we assume the median values for the parameters  $r_c$  and  $\beta$ , and the median relation  $f_{\text{gas},500c} - m_{500c,\text{obs}}$  for the observed hot gas density profiles and there is a significant scatter around these medians, it is important to see how

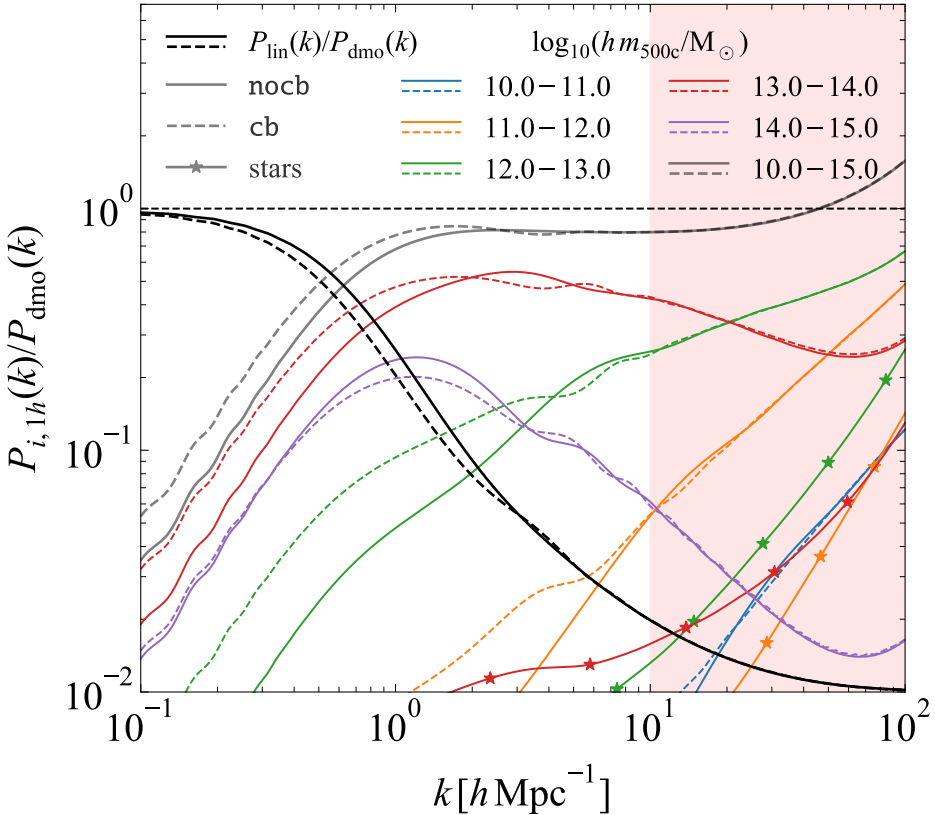


Figure 2.16: The contribution of the 1-halo term for different halo mass ranges to the total power spectrum at all scales for our fiducial models. The  $\text{nocb}$  (solid lines) and  $\text{cb}$  (dashed lines) models are shown and the mass ranges are indicated by the colours. We also show the contribution of the 2-halo term, i.e. the linear power spectrum (black lines). The stellar contribution (1h term and all cross-correlations between matter and stars, connected stars) is also included, but only for the  $\text{nocb}$  case, since the  $\text{cb}$  case traces the  $\text{nocb}$  lines. The red, lightly-shaded region for  $k > 10 h \text{ Mpc}^{-1}$  indicates the scales where our model is not a good indicator of the uncertainty because the stellar component is not varied. The 1h term dominates the total power for  $k \gtrsim 0.5 h \text{ Mpc}^{-1}$ . For the scales of interest here ( $k \lesssim 5 h \text{ Mpc}^{-1}$ ), most of the power is contributed by groups and clusters with  $10^{13} h^{-1} \text{ M}_{\odot} \leq m_{500c,\text{obs}} \leq 10^{15} h^{-1} \text{ M}_{\odot}$ . For the  $\text{cb}$  models, low-mass ( $\approx 10^{13} h^{-1} \text{ M}_{\odot}$ ) haloes contribute more and clusters ( $> 10^{14} h^{-1} \text{ M}_{\odot}$ ) less compared with the  $\text{nocb}$  models. The total stellar contribution to the power response is  $\lesssim 1$  per cent for all scales  $k \lesssim 5 h \text{ Mpc}^{-1}$  and only exceeds 2 per cent for  $k \gtrsim 10 h \text{ Mpc}^{-1}$ .

sensitive our predictions are to variations in the parameter values. In this section, we investigate the isolated effect of each observational parameter on the predicted matter power spectrum.

We remind the reader of the beta profile in Eq. 2.14 and the best fits for its parameters determined from the observations in Figs. 2.2, 2.5a, and 2.5b. In those figures, we indicated the median relations, which are used in our model, and the 15<sup>th</sup> and 85<sup>th</sup> percentiles of the observed values. We will test the model response to variations in the hot gas observations by varying each of the best-fit parameters between its 15<sup>th</sup> and 85<sup>th</sup> percentiles while keeping all other parameters fixed.

We show the result of these parameter variations for our fiducial model ( $\gamma_0 = 2.14$ ) in the nocb and cb cases in Fig. 2.17. We indicate the 15<sup>th</sup> (85<sup>th</sup>) percentile envelope with a dashed (solid), coloured line and shade the region enclosed by these percentiles. For both the cb and nocb cases, the parameters  $\beta$  and  $f_{\text{gas},500c}$  are the most important at large scales. Flatter outer slopes for the hot gas density profile, i.e. smaller values of  $\beta$ , will result in more baryons out to  $r_{200m,\text{obs}}$ , yielding a smaller suppression of power on large scales. Higher gas fractions within  $r_{500c,\text{obs}}$  will result in haloes that are more massive and contain more of the baryons, again yielding a smaller suppression of power on large scales. The core radius  $r_c$  is the least important parameter. Increasing the size of the core requires a lower density in the core to reach the same gas fraction at  $r_{500c,\text{obs}}$  and yields more baryons in the halo outskirts. Hence, we see more power at large scales and less power on small scales when increasing the value of  $r_c$  similarly to decreasing the value  $\beta$ . However, the core is relatively close to the cluster center and thus has no impact on the matter distribution at large scales.

There is an important difference between the nocb and cb cases, however. The fit parameters only start having an effect on the power suppression at scales  $k \gtrsim 1 h \text{ Mpc}^{-1}$  in the cb case, whereas in the nocb case they already start mattering around  $k \approx 0.3 h \text{ Mpc}^{-1}$ . If all baryons are accounted for in the halo outskirts, as in the cb case, the details of the baryon distribution do not matter for the power at the largest scales, since here the 1h term is fully determined by the mass inside  $r_h$ , which does not change for different values of  $\beta$  and  $f_{\text{gas},500c}$ . The nocb model is a lot more sensitive to the baryon distribution within the halo, since depending on the value of  $\beta$ , or how many baryons can already be accounted for inside  $r_{500c,\text{obs}}$ , the haloes can have large variations in mass  $m_{200m,\text{obs}}$ .

In conclusion, the most important parameter to pin down is the gas fraction of the halo, as we already concluded in Section 2.5.1 and Section 2.5.3. It has the largest effect on all scales in both the nocb and cb cases and varying its value within the observed scatter results in a  $\approx \pm 5$  per cent variation around the power spectrum response predicted by our fiducial model. At the scales of interest to future surveys, the effect of  $\beta$  is of similar amplitude. However, this parameter will be harder to constrain observationally than the gas content of the halo, especially for group-mass haloes, because X-ray observations cannot provide an unbiased sample and SZ observations cannot observe the density profile directly.

### 2.5.5 Influence of hydrostatic bias

All of our results so far assumed gas fractions based on halo masses derived from X-ray observations under the assumption of hydrostatic equilibrium (HE) and pure thermal pressure. Under the HE assumption non-thermal pressure and large-scale gas motions

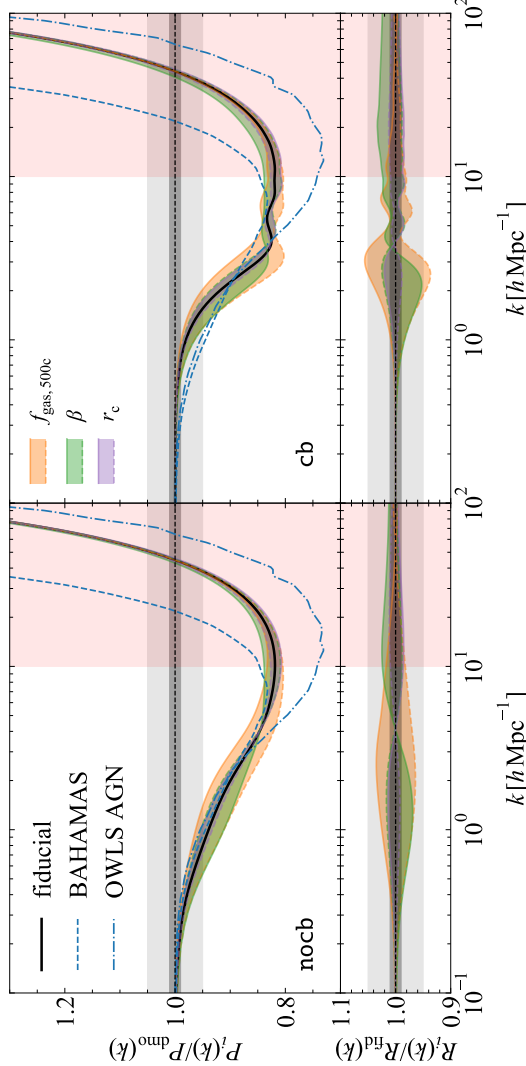


Figure 2.17: *Top row*: The variation in the power suppression due to baryonic effects when varying the best-fit hot gas density profile parameters independently within their 15<sup>th</sup> (dashed lines) and 85<sup>th</sup> (solid lines) percentile ranges (shaded regions) and keeping all other parameters fixed. The dark and light gray bands indicate the 1 per cent and 5 per cent intervals. The left-hand panel shows model nocb, which effectively assumes that the baryons missing from haloes are redistributed far beyond  $r_{200m, \text{obs}}$  on linear scales. The right-hand panel shows model cb, which adds the missing halo baryons in a uniform profile outside but near  $r_{200m, \text{obs}}$ . The red, lightly-shaded region for  $k > 10 h \text{Mpc}^{-1}$  indicates the scales where our model is not a good indicator of the uncertainty because the stellar component is not varied. The thick, solid, black line indicates our fiducial model with  $\gamma_0 = 3\beta = 2.14$ . *Bottom row*: The ratio between the region enclosed by the 15<sup>th</sup> – 85<sup>th</sup> percentiles for each fit parameter and the fiducial model. The parameters  $\beta$  and  $f_{\text{gas}, 500c}$  determine the behaviour in the outer regions and are most important. The same trends are present for both the nocb and cb cases, but the nocb case is sensitive to variations in the best-fit parameters out to larger scales. The uncertainty in any of the best-fit parameters allows at most a ±5 per cent variation in the power suppression for any scale.

are neglected in the Euler equation (see e.g. the discussion in Section 2.3 of [Pratt et al., 2019](#)). However, in massive systems in the process of assembly, there is no a priori reason to assume that simplifying assumption to hold. We expect the most massive clusters to depart from HE, since we know from the hierarchical structure formation paradigm, that they have only recently formed. Moreover, the pressure can have a non-negligible contribution from non-thermal sources such as turbulence ([Eckert et al., 2019](#)).

Investigating the relation between hydrostatically derived halo masses and the true halo mass requires hydrodynamical simulations (e.g. [Nagai et al., 2007](#); [Rasia et al., 2012](#); [Biffi et al., 2016](#); [Le Brun et al., 2017](#); [McCarthy et al., 2017](#); [Henson et al., 2017](#)) or weak gravitational lensing observations ([Mahdavi et al., 2013](#); [Von der Linden et al., 2014](#); [Hoekstra et al., 2015](#); [Medezinski et al., 2018](#)). In both cases, the pressure profile of the halo is derived from observations of the hot gas. Under the assumption of spherical symmetry and HE, this pressure profile is then straightforwardly related to the total mass profile of the halo. Subsequently, this hydrostatic halo mass can be compared to an unbiased estimate of the halo mass, i.e. the true mass in hydrodynamical simulations, or the mass derived from weak lensing observations.

The picture arising from both simulations and observations is that hydrostatic masses,  $m_{\text{HE}}$ , are generally biased low with respect to the weak lensing or true halo mass,  $m_{\text{WL}}$ , with  $m_{\text{HE}}/m_{\text{WL}} = 1 - b \simeq 0.6$  to 0.9 (e.g. [Mahdavi et al., 2013](#); [Von der Linden et al., 2014](#); [Hoekstra et al., 2015](#); [Le Brun et al., 2017](#); [Henson et al., 2017](#); [Medezinski et al., 2018](#)). The detailed behaviour of this bias depends on the deprojected temperature and density profiles, with more spherical systems being less biased.

Correcting for the observationally determined bias would result in higher halo masses and, consequently, a shift in the gas fractions away from the assumed best-fit  $f_{\text{gas},500c} - m_{500c,\text{obs}}$  relation. We argued previously that this is the most relevant observable to determine the suppression of power at scales  $k \lesssim 1 h \text{ Mpc}^{-1}$ . Thus, it is important to investigate how the HE assumption affects our predictions. Previously, [Schneider et al. \(2019\)](#) have shown for three different levels of hydrostatic bias ( $1 - b \in \{0.71, 0.83, 1\}$ ) that the predicted power suppression at large scales  $k < 1 h \text{ Mpc}^{-1}$  can vary by up to 5 per cent.

Staying in tune with Section 2.5.4, we adopt a single value for the bias to investigate its influence on our predictions. We will take  $1 - b = 0.7$  which is consistent with both [Von der Linden et al. \(2014\)](#) and [Hoekstra et al. \(2015\)](#). Moreover, although the bias tends to be higher for higher-mass systems because of the presence of cooler gas in their outskirts ([Henson et al., 2017](#)), we conservatively adopt this value for all halo masses. Correcting for the bias will influence our model in two ways. First, the inferred gas masses will increase slightly, since the true  $r_{500c,\text{obs}}$  will be larger than the value assumed from the hydrostatic estimate. We thus recompute the gas masses from our best-fit beta models to the observations. Second, the halo mass will increase by the bias factor which will result in new estimates for the gas fractions, which we show as the thin, solid, black line in Fig. 2.2. We then fit the median  $f_{\text{gas},500c} - m_{500c,\text{obs}}$  relation again, assuming Eq. 2.25, resulting in the thin, red, dashed line.

We show the resulting effect on the baryonic suppression of the power spectra in Fig. 2.18. The results are similar to varying  $f_{\text{gas},500c}$  in Fig. 2.17, since the bias-corrected relation is similar to the 15<sup>th</sup> percentile  $f_{\text{gas},500c} - m_{500c,\text{obs}}$  relation, but with a more

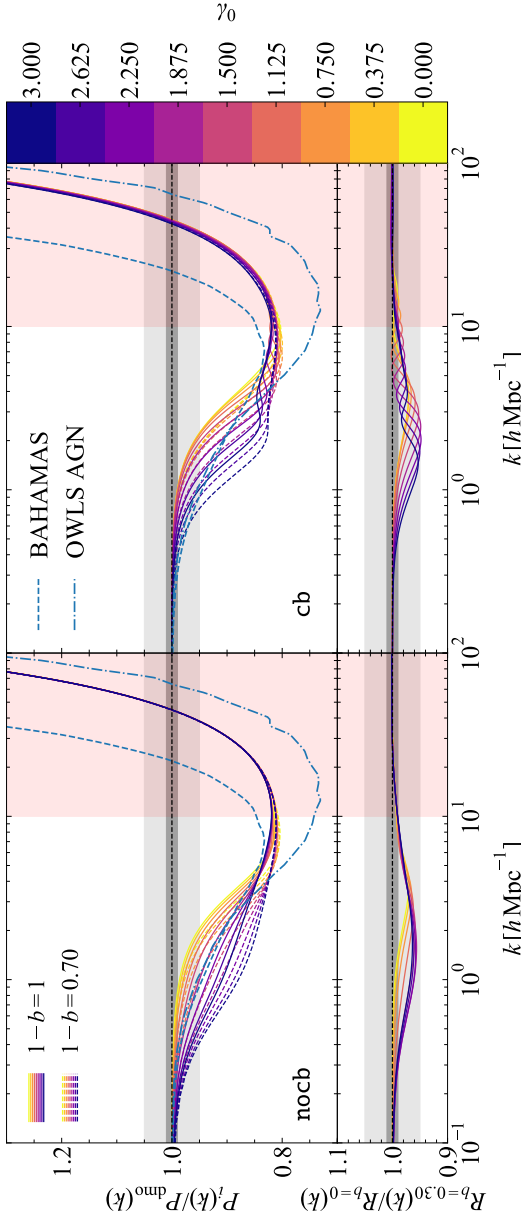


Figure 2.18: *Top row*: The response of the matter power spectrum to the presence of baryons with (dashed lines) and without (solid lines) accounting for a hydrostatic bias of  $1 - b = 0.7$  in the halo mass. The dark and light gray bands indicate the 1 per cent and 5 per cent intervals. The left-hand panel shows model nocb, which effectively assumes that the baryons missing from haloes are redistributed far beyond  $r_{200m,\text{obs}}$  on linear scales. The right-hand panel shows model cb, which adds the missing halo baryons in a uniform profile outside but near  $r_{200m,\text{obs}}$ . The red, lightly-shaded region for  $k > 10 h \text{ Mpc}^{-1}$  indicates the scales where our model is not a good indicator of the uncertainty because the stellar component is not varied. *Bottom row*: The ratio between the corrected and the uncorrected models. Haloes with lower values of  $\gamma_0$  are less strongly affected by the bias since they can add more baryons outside  $r_{500c,\text{obs}}$ . Without correcting for the bias, we underestimate the suppression of power by up to  $\approx 4$  per cent at  $k = 1 h \text{ Mpc}^{-1}$ .

dramatic suppression of the baryonic mass for clusters and hence more suppression of the power at large scales. In the bottom panels of Fig. 2.18, we find a maximum extra suppression of  $\approx 4$  per cent due to the hydrostatic bias at  $k = 1 h \text{ Mpc}^{-1}$  in both the no cb and cb cases, which is consistent with the findings of Schneider et al. (2019). The magnitude of the suppression is lower for lower values of  $\gamma_0$  since these models compensate for the lower baryon fraction within  $r_{500c,\text{obs}}$  by adding baryons between  $r_{500c,\text{obs}}$  and  $r_h$ .

Accounting for the bias breaks the overall agreement with the simulations on large scales for the models with high values of  $\gamma_0$ . However, in BAHAMAS and OWLS AGN, a hydrostatic bias of  $1 - b = 0.84$  and  $1 - b = 0.8$  is found, respectively, for groups and clusters (McCarthy et al., 2017; Le Brun et al., 2014). When we assume  $1 - b = 0.8$ , we find a maximum extra suppression of  $\approx 2$  per cent at  $k = 1 h \text{ Mpc}^{-1}$  instead of  $\approx 4$  per cent. At other scales the effect of the hydrostatic bias is similarly reduced.

In conclusion, it is crucial to obtain robust constraints on the hydrostatic bias of groups and clusters of galaxies. Current measurements of this bias suggest that hydrostatic halo masses underestimate the true masses and that this bias results in a downward shift of the cluster gas fractions that is more severe than the observational scatter in the relation. Because the shift affects cluster-mass haloes, it results in an additional power suppression of up to  $\approx 4$  per cent at  $k = 1 h \text{ Mpc}^{-1}$ , depending on how our model distributes the outer baryons. There are ways of measuring halo masses that do not rely on making the hydrostatic assumption, such as weak lensing observations, but these also carry their own intrinsic biases (Henson et al., 2017). Making mock observations in simulations allows us to characterize these separate biases (e.g. Henson et al., 2017; Le Brun et al., 2017), but the simulations still do not make a full like-for-like comparison with the observations. Finally, joint constraints on X-ray, SZ, and weak lensing halo mass scaling relations, including possible biases, as was done in Bocquet et al. (2019), could provide more robust halo mass estimates.

## 2.6 Discussion

We have presented an observationally constrained halo model to estimate the power suppression due to baryons without any reliance on subgrid recipes for the unresolved physics of baryons in hydrodynamical simulations. We reiterate that our main goal is not to provide the most accurate predictions of the matter power spectrum, but to investigate the possibility of using observations to constrain it. The fact that the clustering of matched haloes does not change between DMO and hydrodynamical simulations (van Daalen et al., 2014) implies that changes in the density profiles due to the baryons determine the change of the matter power spectrum. Hence, even though the halo model does not accurately predict the matter power spectrum, it can accurately predict the relative effect of baryonic processes on the power spectrum. The overall agreement between our model and hydrodynamical simulations that reproduce the observed distribution of baryons in groups and clusters, confirms that our model captures the first-order impact of baryons simply by reproducing the observed baryon content for groups and clusters.

In conclusion, the main strength of the model is that it allows us to quantify the impact of different halo masses, different halo baryon density distributions and observational

biases and uncertainties on the baryonic suppression of the matter power spectrum without any necessity for uncertain subgrid recipes for feedback processes. This in turn allows us to provide a less model-dependent estimate of the range of possible baryonic suppression and to predict which observations would provide the strongest constraints on the matter power spectrum.

There are other models in the literature that aim to model the effect of baryon physics on the matter power spectrum. `HMCODE` by Mead et al. (2015) is widely used to include baryon effects in weak lensing analyses. Although `HMCODE` is also based on the halo model, its aim is different from ours. Mead et al. (2015) modify the dark matter halo profiles and subsequently fit the parameters of their halo model to hydrodynamical simulations to provide predictions for the baryonic response of the power spectrum that are accurate at the  $\sim 5$  per cent level for  $k \lesssim 5 h \text{ Mpc}^{-1}$  with 2 free parameters related to the baryonic feedback (for a similar approach, see Sembolini et al., 2013). These feedback parameters can then be jointly constrained with the cosmology using cosmic shear data. However, even though the modifications to the dark matter profile are phenomenologically inspired, there is no guarantee that the final best-fit parameters correspond to the actual physical state of the haloes. We obtain similar accuracy in the predicted power response when viewing  $\gamma_0$  as a fitting parameter and comparing to hydrodynamical simulations. However, in our case, fitting  $\gamma_0$  preserves the agreement with observations. Indeed, the most important difference between our approach and that of Mead et al. (2015) is that we fit to observations instead of simulations.

The investigation of Schneider et al. (2019) most closely matches our goal. Schneider & Teyssier (2015) and Schneider et al. (2019) developed a *baryon correction model* to investigate the influence of baryon physics on the matter power spectrum. Their model shifts particles in DMO simulations according to the physical expectations from baryonic feedback processes. Since the model only relies on DMO simulations, it is not as computationally expensive as models that require hydrodynamical simulations to calibrate their predictions. Our simple analytic halo model is cheaper still to run, but it only results in a statistical description of the matter distribution, whereas the *baryon correction model* predicts the total matter density field for the particular realization that was simulated. Because our model combines the universal DMO halo mass function with observed density profiles, it can easily be applied to a wide variety of cosmologies without having to run an expensive grid of DMO simulations.

In the baryon correction model, the link to observations can also be made, making it similar to our approach. Schneider et al. (2019) fit a mass-dependent slope of the gas profile,  $\beta$  (note that their slope is not defined the same way as our slope  $\beta$ ), and the maximum gas ejection radius,  $\theta_{\text{ej}}$ , to the observed hot gas profiles of the XXL sample of Eckert et al. (2016) and a compendium of X-ray gas fraction measurements. They also include a stellar component that is fit to abundance matching results, similar to our `iHOD` implementation. They show that their model can reproduce the observed relations as well as hydrodynamical simulations when fit to their gas fractions. Schneider et al. (2019) use the observations to set a maximum range on their model parameters to then predict both the matter power spectrum and the shear correlation function. Our work, on the other hand, focusses on the impact of isolated properties of the baryon distribution on the power spectrum. Similarly to Schneider et al. (2019), we find that the power suppression on large

scales is very sensitive to the baryon distribution in the outskirts of the halo. However, our model allows us to clearly show that the halo baryon fractions are the crucial ingredient in setting the total power suppression at large scales,  $k \lesssim 1 h \text{ Mpc}^{-1}$ . Also similarly to Schneider et al. (2019), we find that the hydrostatic mass bias significantly affects the total power suppression at large scales.

So far, we have not included redshift evolution. Schneider et al. (2019) have found that the most important evolution of clusters and groups in cosmological simulations stems from the change in their abundance due to the evolution of the halo mass function in time, and not due to the change of the density profiles with time. This evolution can be readily implemented into our halo model.

## 2.7 Summary and conclusions

Future weak lensing surveys will be limited in their accuracy by how well we can predict the matter power spectrum on small scales (e.g. Sembolini et al., 2011; Copeland et al., 2018; Huang et al., 2019). These scales contain a wealth of information about the underlying cosmology of our Universe, but the interpretation of the signal is complicated by baryon effects. Our current theoretical understanding of the impact of baryons on the matter power spectrum stems from hydrodynamical simulations that employ uncertain subgrid recipes to model astrophysical feedback processes. This uncertainty can be bypassed by adopting an observational approach to link the observed distribution of matter to the matter power spectrum.

We have provided a detailed study of the constraints that current observations of groups and clusters of galaxies impose on the possible influence of the baryon distribution on the matter power spectrum. We introduced a modified halo model that includes dark matter, hot gas, and stellar components. We fit the hot gas to X-ray observations of clusters of galaxies and we assumed different distributions for the missing baryons outside  $r_{500c,\text{obs}}$ , the maximum radius probed by X-ray observations of the hot gas distribution. Subsequently, we quantified (i) how the outer, unobserved baryon distribution modifies the matter power spectrum (Fig. 2.10). We also investigated (ii) how the change in halo mass due to baryonic effects can be incorporated into the halo model (Fig. 2.15). We showed (iii) the contributions to the matter power spectrum of haloes of different masses at different spatial scales (Fig. 2.16), (iv) the influence of varying the individual best-fit parameters to the observed density profiles within their allowed range (Fig. 2.17), and (v) the influence of a hydrostatic mass bias on the matter power spectrum (Fig. 2.18).

Our model has one free parameter,  $\gamma_0$ , related to the slope of the hot gas density profile for  $r_{500c,\text{obs}} \leq r \leq r_{200m,\text{obs}}$ , where observational constraints are very poor. We considered two extreme cases for the baryons. First, the no cb models assume that haloes of size  $r_{200m,\text{obs}}$  do not necessarily reach the cosmic baryon fraction at this radius and that any missing baryons are located at such large distances that they only contribute to the 2-halo term. Second, in the cb models the missing baryons inside  $r_{200m,\text{obs}}$  are distributed with an assumed uniform density profile outside this radius until the cosmic baryon fraction is reached. These cases provide, respectively, the maximum and minimum power suppression of large-scale power due to baryonic effects.

All of our observationally constrained models predict a significant amount of suppression on the scales of interest to future surveys ( $0.2 \lesssim k/(h \text{ Mpc}^{-1}) \lesssim 5$ ). We find a total suppression of 1 per cent (5 per cent) on scales  $0.2$  to  $0.9 h \text{ Mpc}^{-1}$  ( $0.5$  to  $2 h \text{ Mpc}^{-1}$ ) in the `nocb` case and on scales  $0.5$  to  $1 h \text{ Mpc}^{-1}$  ( $1$  to  $2 h \text{ Mpc}^{-1}$ ) in the `cb` case for values  $\gamma_0 = 3$  to  $0$  (Fig. 2.10), where  $\gamma_0$  is the low-mass limit of the power-law slope  $\gamma$  between  $r_{500c,\text{obs}}$  and  $r_{200m,\text{obs}}$ , i.e.  $\gamma_0 = \gamma(m_{500c,\text{obs}} \rightarrow 0)$ . This large possible range of scales corresponding to a fixed suppression factor for each case illustrates the importance of the baryon distribution outside  $r_{500c,\text{obs}}$  (which is parameterised by  $\gamma_0$ ) in setting the total power suppression.

We found that massive groups of galaxies ( $10^{13} h^{-1} \text{ M}_\odot < m_{500c,\text{obs}} < 10^{14} h^{-1} \text{ M}_\odot$ ) provide a larger contribution than clusters to the total power at all scales (Fig. 2.16). This is unfortunate, since we have shown that the baryonic content of group- and cluster-sized haloes, which is set by the observed gas fractions  $f_{\text{gas},500c}$ , determines the large-scale ( $k \lesssim 1 h \text{ Mpc}^{-1}$ ) power suppression (Figs. 2.13 and 2.17). However, observations of the hot gas content of groups are scarcer than those of clusters and are also subject to a considerable Malmquist bias. Current X-ray telescopes cannot solve this problem, but a combined approach with Sunyaev-Zel'dovich or gravitational lensing observations could provide a larger sample of lower mass objects.

We found that our observationally constrained models only encompass the predictions of hydrodynamical simulations that reproduce the hot gas content of groups and clusters of galaxies (Fig. 2.11). Thus, we stress the importance of using simulations that reproduce the relevant observations when using such models to predict the baryonic effects on the matter distribution.

We found that accurately measuring the halo masses is of vital importance when trying to place observational constraints on the matter power spectrum. An unrecognized hydrostatic halo mass bias of  $1 - b = 0.7$  would result in an underestimate of the total power suppression by as much as 4 per cent at  $k = 1 h \text{ Mpc}^{-1}$  (Fig. 2.18). In addition, it is critical to correct the observed halo masses for the redistribution of baryons when estimating their abundance using halo mass functions based on DM only simulations (Fig. 2.15).

All in all, it is encouraging that we are able to quantify the baryonic suppression of the matter power spectrum with a simple, flexible but physical approach such as our modified halo model. Our investigation allows us to predict the observations that will be most constraining for the impact of baryonic effects on the matter power spectrum.

## 2.A Influence of the halo mass range

In this section, we investigate how our choice of mass grid influences our predictions. We have chosen an equidistant log-grid of halo masses  $10^{11} h^{-1} M_{\odot} \leq m_{500c,\text{obs}} \leq 10^{15} h^{-1} M_{\odot}$ , sampled with 101 bins. Doubling or halving the number of bins only affects our predictions at the < 0.1 per cent level for all  $k$ . Similarly, increasing the maximum halo mass to  $m_{500c,\text{max}} = 10^{16} h^{-1} M_{\odot}$  only results in changes at the < 0.1 per cent level for all  $k$ . The only significant change occurs when decreasing the minimum halo mass to  $m_{500c,\text{min}} = 10^6 h^{-1} M_{\odot}$ , but this only affects scales smaller than of interest here. In this case, our baryonic models predict less power compared to the higher minimum mass case, since the low-mass haloes have no stars and gas. Hence, they will always contain less matter than their DMO equivalents and the DMO power will be boosted relative to the baryonic one. However, our predictions only change at the 1 per cent level for  $k \gtrsim 60 h \text{ Mpc}^{-1}$ , thus our fiducial mass range is converged for our scales of interest,  $k < 10 h \text{ Mpc}^{-1}$ .

## 2.B Influence of concentration–mass relation

In this section, we investigate how changes in the concentration at fixed halo mass influences our predictions. While the concentration–mass relation does not show a strong mass dependence, the scatter about the median relation is significant (Jing, 2000; Bullock et al., 2001; Duffy et al., 2008; Dutton & Macciò, 2014). To investigate the potential influence of this scatter, we tested how our predictions for the power response due to baryons change when assuming the  $c(m)$  relation shifted up and down by its log-normal scatter  $\sigma_{\log_{10} c} = 0.15$  (Duffy et al., 2008; Dutton & Macciò, 2014). Increasing the concentration results in more (less) power at small (large) scales and thus a lower (higher) power suppression. Adopting this extreme shift in the concentration–mass relation results in a maximum variation of  $\pm 3$  per cent in suppression at scales  $k \lesssim 20 h \text{ Mpc}^{-1}$ . This variation is smaller than any of the hot gas density profile best-fit parameter variations in Section 2.5.4.

## Bibliography

- Amendola L., et al., 2018, *Living Rev. Relativ.*, 21, 2 → p. 36, 58
- Angulo R. E., Springel V., White S. D. M., Jenkins A., Baugh C. M., Frenk C. S., 2012, *Mon. Not. R. Astron. Soc.*, 426, 2046 → p. 36
- Arnaud M., Pointecouteau E., Pratt G. W., 2007, *Astron. Astrophys.*, 474, L37 → p. 50, 52
- Arnaud M., Pratt G. W., Piffaretti R., Böhringer H., Croston J. H., Pointecouteau E., 2010, *Astron. Astrophys.*, 517, A92 → p. 52
- Barnes D. J., et al., 2017, *Mon. Not. R. Astron. Soc.*, 471, 1088 → p. 37, 61
- Barnes D. J., Kannan R., Vogelsberger M., Marinacci F., 2018, preprint, 21, 1 ([arXiv:1812.01611](https://arxiv.org/abs/1812.01611)) → p. 61
- Biffi V., et al., 2016, *Astrophys. J.*, 827, 112 → p. 73
- Bleem L. E., et al., 2015, *Astrophys. Journal, Suppl. Ser.*, 216 → p. 64
- Bocquet S., et al., 2019, *Astrophys. J.*, 878, 55 → p. 75
- Böhringer H., et al., 2007, *Astron. Astrophys.*, 469, 363 → p. 50
- Bond J. R., Cole S., Efstathiou G., Kaiser N., 1991, *Astrophys. J.*, 379, 440 → p. 39
- Budzynski J. M., Koposov S. E., McCarthy I. G., McGee S. L., Belokurov V., 2012, *Mon. Not. R. Astron. Soc.*, 423, 104 → p. 48
- Bullock J. S., Kolatt T. S., Sigad Y., Somerville R. S., Kravtsov A. V., Klypin A. A., Primack J. R., Dekel A., 2001, *Mon. Not. R. Astron. Soc.*, 321, 559 → p. 79
- Cataneo M., Lombriser L., Heymans C., Mead A. J., Barreira A., Bose S., Li B., 2019, *Mon. Not. R. Astron. Soc.*, 488, 2121 → p. 41
- Catinella B., et al., 2010, *Mon. Not. R. Astron. Soc.*, 403, 683 → p. 44
- Cavaliere A., Fusco-Femiano R., 1978, *Astron. Astrophys.*, 70, 677 → p. 44
- Cen R., Ostriker J. P., 1999, *Astrophys. J.*, 514, 1 → p. 60
- Chisari N. E., et al., 2018, *Mon. Not. R. Astron. Soc.*, 480, 3962 → p. 37, 60, 61, 62
- Chon G., Böhringer H., 2017, *Astron. Astrophys.*, 606, L4 → p. 50
- Cooray A., Sheth R. K., 2002, *Phys. Rep.*, 372, 1 → p. 39, 40, 41
- Copeland D., Taylor A., Hall A., 2018, *Mon. Not. R. Astron. Soc.*, 480, 2247 → p. 77
- Correa C. A., Wyithe J. S. B., Schaye J., Duffy A. R., 2015, *Mon. Not. R. Astron. Soc.*, 452, 1217 → p. 46
- Croston J. H., et al., 2008, *Astron. Astrophys.*, 487, 431 → p. 48, 49, 50, 51, 56
- Croton D. J., 2013, *Publ. Astron. Soc. Aust.*, 30 → p. 39
- Cui W., Borgani S., Murante G., 2014, *Mon. Not. R. Astron. Soc.*, 441, 1769 → p. 42
- Dave R., et al., 2001, *Astrophys. J.*, 552, 473 → p. 60
- Dicke R. H., Peebles P. J. E., Roll P. G., Wilkinson D. T., 1965, *Astrophys. J.*, 142, 414 → p. 36
- Duffy A. R., Schaye J., Kay S. T., Dalla Vecchia C., 2008, *Mon. Not. R. Astron. Soc. Lett.*, 390, L64 → p. 79
- Duffy A. R., Schaye J., Kay S. T., Vecchia C. D., Battye R. A., Booth C. M., 2010, *Mon. Not. R. Astron. Soc.*, 405, 2161 → p. 43
- Dutton A. A., Macciò A. V., 2014, *Mon. Not. R. Astron. Soc.*, 441, 3359 → p. 79
- Eckert D., Molendi S., Paltani S., 2011, *Astron. Astrophys.*, 526, A79 → p. 50
- Eckert D., et al., 2016, *Astron. Astrophys.*, 592, A12 → p. 48, 49, 51, 52, 53, 56, 76
- Eckert D., et al., 2019, *Astron. Astrophys.*, 621, A40 → p. 73
- Fedeli C., 2014, *J. Cosmol. Astropart. Phys.*, 2014, 028 → p. 38
- Fedeli C., Sembolini E., Velliscig M., van Daalen M. P., Schaye J., Hoekstra H., 2014, *J. Cosmol. Astropart. Phys.*, 2014, 028 → p. 38
- Ghirardini V., et al., 2019, *Astron. Astrophys.*, 621, A41 → p. 55

- Grevesse N., Asplund M., Sauval A. J., 2007, *Space Sci. Rev.*, 130, 105 → p. 50
- Guillet T., Teyssier R., Colombi S., 2010, *Mon. Not. R. Astron. Soc.*, 405, 525 → p. 38
- Hearin A. P., Zentner A. R., Ma Z., 2012, *J. Cosmol. Astropart. Phys.*, 2012, 034 → p. 36
- Heitmann K., Higdon D., White M., Habib S., Williams B. J., Lawrence E., Wagner C., 2009, *Astrophys. J.*, 705, 156 → p. 36
- Heitmann K., White M., Wagner C., Habib S., Higdon D., 2010, *Astrophys. J.*, 715, 104 → p. 36
- Hellwing W. A., Schaller M., Frenk C. S., Theuns T., Schaye J., Bower R. G., Crain R. A., 2016, *Mon. Not. R. Astron. Soc. Lett.*, 461, L11 → p. 37, 60, 61, 62
- Henson M. A., Barnes D. J., Kay S. T., McCarthy I. G., Schaye J., 2017, *Mon. Not. R. Astron. Soc.*, 465, 3361 → p. 73, 75
- Hilton M., et al., 2018, *Astrophys. J. Suppl. Ser.*, 235, 20 → p. 64
- Hinshaw G., et al., 2013, *Astrophys. J. Suppl. Ser.*, 208, 19 → p. 39
- Hoekstra H., Jain B., 2008, *Annu. Rev. Nucl. Part. Sci.*, 58, 99 → p. 36
- Hoekstra H., Herbonnet R., Muzzin A., Babul A., Mahdavi A., Viola M., Cacciato M., 2015, *Mon. Not. R. Astron. Soc.*, 449, 685 → p. 52, 73
- Huang H.-j., Eifler T., Mandelbaum R., Dodelson S., 2019, *Mon. Not. R. Astron. Soc.*, 488, 1652 → p. 77
- Jakobs A., et al., 2018, *Mon. Not. R. Astron. Soc.*, 480, 3338 → p. 60
- Jenkins A., Frenk C. S., White S. D. M., Colberg J. M., Cole S., Evrard A. E., Couchman H. M. P., Yoshida N., 2001, *Mon. Not. R. Astron. Soc.*, 321, 372 → p. 39
- Jing Y. P., 2000, *Astrophys. J.*, 535, 30 → p. 79
- Kilbinger M., 2015, *Reports Prog. Phys.*, 78, 086901 → p. 36
- Lacey C. G., Cole S., 1993, *Mon. Not. R. Astron. Soc.*, 262, 627 → p. 39
- Lawrence E., Heitmann K., White M., Higdon D., Wagner C., Habib S., Williams B., 2010, *Astrophys. J.*, 713, 1322 → p. 36
- Le Brun A. M., McCarthy I. G., Schaye J., Ponman T. J., 2014, *Mon. Not. R. Astron. Soc.*, 441, 1270 → p. 65, 75
- Le Brun A. M. C., McCarthy I. G., Melin J. B., 2015, *Mon. Not. R. Astron. Soc.*, 451, 3868 → p. 46
- Le Brun A. M., McCarthy I. G., Schaye J., Ponman T. J., 2017, *Mon. Not. R. Astron. Soc.*, 466, 4442 → p. 73, 75
- Lieu M., et al., 2016, *Astron. Astrophys.*, 592, A4 → p. 52
- Lieu M., Farr W. M., Betancourt M., Smith G. P., Sereno M., McCarthy I. G., 2017, *Mon. Not. R. Astron. Soc.*, 468, 4872 → p. 52
- Lim S. H., Mo H. J., Li R., Liu Y., Ma Y.-Z., Wang H., Yang X., 2018, *Astrophys. J.*, 854, 181 → p. 64
- Lin Y.-t., Mohr J. J., Stanford S. A., 2004, *Astrophys. J.*, 610, 745 → p. 48
- Lin Y.-T., Stanford S. A., Eisenhardt P. R. M., Vikhlinin A., Maughan B. J., Kravtsov A., 2012, *Astrophys. J.*, 745, L3 → p. 50
- Lovisari L., Reiprich T. H., Schellenberger G., 2015, *Astron. Astrophys.*, 573, A118 → p. 50
- Mahdavi A., Hoekstra H., Babul A., Bildfell C., Jeltema T., Henry J. P., 2013, *Astrophys. J.*, 767 → p. 73
- Mandelbaum R., 2018, *Annu. Rev. Astron. Astrophys.*, 56, 393 → p. 36
- Maughan B. J., Jones C., Forman W., Van Speybroeck L., 2008, *Astrophys. J. Suppl. Ser.*, 174, 117 → p. 50
- McCarthy I. G., et al., 2010, *Mon. Not. R. Astron. Soc.*, 406, 822 → p. 60
- McCarthy I. G., Schaye J., Bird S., Le Brun A. M., 2017, *Mon. Not. R. Astron. Soc.*, 465, 2936 → p. 37, 48, 60, 62, 73, 75
- McCarthy I. G., Bird S., Schaye J., Harnois-Deraps J., Font A. S., van Waerbeke L., 2018, *Mon.*

- Not. R. Astron. Soc., 476, 2999 → p. 37, 41
- McClelland J., Silk J., 1977, *Astrophys. J.*, 217, 331 → p. 39
- Mead A. J., Peacock J. A., Heymans C., Joudaki S., Heavens A. F., 2015, *Mon. Not. R. Astron. Soc.*, 454, 1958 → p. 38, 60, 76
- Mead A. J., Heymans C., Lombriser L., Peacock J. A., Steele O. I., Winther H. A., 2016, *Mon. Not. R. Astron. Soc.*, 459, 1468 → p. 38, 41
- Medezinski E., et al., 2018, *Publ. Astron. Soc. Japan*, 70, 1 → p. 52, 73
- Mo H., van den Bosch F., White S. D. M., 2010, Galaxy Formation and Evolution., doi:10.1017/CBO9780511807244. → p. 40
- Mummery B. O., McCarthy I. G., Bird S., Schaye J., 2017, *Mon. Not. R. Astron. Soc.*, 471, 227 → p. 41
- Nagai D., Vikhlinin A., Kravtsov A. V., 2007, *Astrophys. J.*, 655, 98 → p. 73
- Navarro J. F., Frenk C. S., White S. D. M., 1996, *Astrophys. J.*, 462, 563 → p. 42, 46
- Nicastro F., et al., 2018, *Nature*, 558, 406 → p. 60
- Pacaud F., et al., 2016, *Astron. Astrophys.*, 592, A2 → p. 48, 50
- Peacock J. A., Smith R. E., 2000, *Mon. Not. R. Astron. Soc.*, 318, 1144 → p. 39
- Penzias A. A., Wilson R. W., 1965, *Astrophys. J.*, 142, 419 → p. 36
- Perlmutter S., et al., 1999, *Astrophys. J.*, 517, 565 → p. 36
- Peters A., Brown M. L., Kay S. T., Barnes D. J., 2018, *Mon. Not. R. Astron. Soc.*, 474, 3173 → p. 37
- Pillepich A., et al., 2017, *Mon. Not. R. Astron. Soc.* → p. 37
- Planck Collaboration et al., 2013, *Astron. Astrophys.*, 557, A52 → p. 46
- Planck Collaboration et al., 2016a, *Astron. Astrophys.*, 594, A13 → p. 64
- Planck Collaboration et al., 2016b, *Astron. Astrophys.*, 594, A24 → p. 52
- Pratt G. W., Croston J. H., Arnaud M., Böhringer H., 2009, *Astron. Astrophys.*, 498, 361 → p. 50
- Pratt G. W., Arnaud M., Biviano A., Eckert D., Ettori S., Nagai D., Okabe N., Reiprich T. H., 2019, *Space Sci. Rev.*, 215, 25 → p. 42, 73
- Press W. H., Schechter P., 1974, *Astrophys. J.*, 187, 425 → p. 39
- Rasia E., et al., 2012, *New J. Phys.*, 14 → p. 73
- Riess A. G., et al., 1998, *Astron. J.*, 116, 1009 → p. 36
- Rudd D. H., Zentner A. R., Kravtsov A. V., 2008, *Astrophys. J.*, 672, 19 → p. 36, 38
- Saintonge A., et al., 2011, *Mon. Not. R. Astron. Soc.*, 415, 32 → p. 44
- Sarazin C. L., 1986, *Rev. Mod. Phys.*, 58, 1 → p. 50
- Sawala T., Frenk C. S., Crain R. A., Jenkins A., Schaye J., Theuns T., Zavala J., 2013, *Mon. Not. R. Astron. Soc.*, 431, 1366 → p. 41, 65
- Sawala T., et al., 2015, *Mon. Not. R. Astron. Soc.*, 448, 2941 → p. 53
- Schaller M., et al., 2015, *Mon. Not. R. Astron. Soc.*, 451, 1247 → p. 43, 65
- Schaye J., et al., 2010, *Mon. Not. R. Astron. Soc.*, 402, 1536 → p. 36, 60, 65
- Schaye J., et al., 2015, *Mon. Not. R. Astron. Soc.*, 446, 521 → p. 37, 61
- Scherrer R. J., Bertschinger E., 1991, *Astrophys. J.*, 381, 349 → p. 39
- Schneider A., Teyssier R., 2015, *J. Cosmol. Astropart. Phys.*, 2015, 049 → p. 38, 76
- Schneider A., Teyssier R., Stadel J., Chisari N. E., Brun A. M. L., Amara A., Refregier A., 2019, *J. Cosmol. Astropart. Phys.*, 2019, 020 → p. 38, 41, 73, 75, 76, 77
- Seljak U., 2000, *Mon. Not. R. Astron. Soc.*, 318, 203 → p. 39
- Semboloni E., Hoekstra H., Schaye J., Van Daalen M. P., McCarthy I. G., 2011, *Mon. Not. R. Astron. Soc.*, 417, 2020 → p. 36, 37, 38, 77
- Semboloni E., Hoekstra H., Schaye J., 2013, *Mon. Not. R. Astron. Soc.*, 434, 148 → p. 37, 38, 76
- Sheth R. K., Tormen G., 1999, *Mon. Not. R. Astron. Soc.*, 308, 119 → p. 39
- Silk J., Mamon G. A., 2012, *Res. Astron. Astrophys.*, 12, 917 → p. 53

- Smith R. E., et al., 2003, *Mon. Not. R. Astron. Soc.*, 341, 1311 → p. 60  
Smith R. E., Desjacques V., Marian L., 2011, *Phys. Rev. D - Part. Fields, Gravit. Cosmol.*, 83, 1 → p. 41  
Springel V., et al., 2017, *Mon. Not. R. Astron. Soc.* → p. 37, 60, 61, 62  
Stafford S. G., McCarthy I. G., Crain R. A., Salcido J., Schaye J., Font A. S., Kwan J., Pfeifer S., 2019, preprint, 24, 1 ([arXiv:1907.09497](#)) → p. 41  
Sun M., Voit G. M., Donahue M., Jones C., Forman W., Vikhlinin A., 2009, *Astrophys. J.*, 693, 1142 → p. 50  
Tinker J., Kravtsov A. V., Klypin A., Abazajian K., Warren M.,Yepes G., Gottlöber S., Holz D. E., 2008, *Astrophys. J.*, 688, 709 → p. 39, 40, 43, 45, 65  
Umetsu K., et al., 2019, preprint ([arXiv:1909.10524](#)) → p. 52  
Velliscig M., van Daalen M. P., Schaye J., McCarthy I. G., Cacciato M., Le Brun A. M., Vecchia C. D., 2014, *Mon. Not. R. Astron. Soc.*, 442, 2641 → p. 36, 42, 43, 65, 66, 67  
Vikhlinin A., Kravtsov A., Forman W., Jones C., Markevitch M., Murray S. S., Van Speybroeck L., 2006, *Astrophys. J.*, 640, 691 → p. 50  
Vogelsberger M., et al., 2014a, *Mon. Not. R. Astron. Soc.*, 444, 1518 → p. 61  
Vogelsberger M., et al., 2014b, *Nature*, 509, 177 → p. 37, 62  
Voit G., 2005, *Rev. Mod. Phys.*, 77, 207 → p. 50, 52  
Von der Linden A., et al., 2014, *Mon. Not. R. Astron. Soc.*, 439, 2 → p. 52, 73  
Wang W., Sales L. V., Henriques B. M. B., White S. D. M., 2014, *Mon. Not. R. Astron. Soc.*, 442, 1363 → p. 48  
Weinberger R., et al., 2017, *Mon. Not. R. Astron. Soc.*, 465, 3291 → p. 61  
White M., 2004, *Astropart. Phys.*, 22, 211 → p. 38  
Zhan H., Knox L., 2004, *Astrophys. J.*, 616, L75 → p. 38  
Zu Y., Mandelbaum R., 2015, *Mon. Not. R. Astron. Soc.*, 454, 1161 → p. 43, 47, 48  
Zubeldia Í., Challinor A., 2019, *Mon. Not. R. Astron. Soc.* → p. 52  
van Daalen M. P., Schaye J., 2015, *Mon. Not. R. Astron. Soc.*, 452, 2247 → p. 38, 69  
van Daalen M. P., Schaye J., Booth C. M., Dalla Vecchia C., 2011, *Mon. Not. R. Astron. Soc.*, 415, 3649 → p. 36, 41, 60, 62  
van Daalen M. P., Schaye J., McCarthy I. G., Booth C. M., Vecchia C. D., 2014, *Mon. Not. R. Astron. Soc.*, 440, 2997 → p. 38, 42, 67, 75  
van Daalen M. P., McCarthy I. G., Schaye J., 2019, preprint, 25, 1 ([arXiv:1906.00968](#)) → p. 36, 37, 41, 60, 61, 63, 64  
van den Bosch F. C., More S., Cacciato M., Mo H., Yang X., 2013, *Mon. Not. R. Astron. Soc.*, 430, 725 → p. 39  
van der Burg R. F. J., Hoekstra H., Muzzin A., Sifón C., Balogh M. L., McGee S. L., 2015, *Astron. Astrophys.*, 577, A19 → p. 48



# 3 | How baryons can significantly bias cluster count cosmology

Based on

Stijn N. B. Debackere, Joop Schaye, Henk Hoekstra

*Monthly Notices of the Royal Astronomical Society, Volume 505, Issue 1,  
p. 593-609 (2021)*

We quantify two main pathways through which baryonic physics biases cluster count cosmology. We create mock cluster samples that reproduce the baryon content inferred from X-ray observations. We link clusters to their counterparts in a dark matter-only universe, whose abundances can be predicted robustly, by assuming the dark matter density profile is not significantly affected by baryons. We derive weak lensing halo masses and infer the best-fitting cosmological parameters  $\Omega_m$ ,  $S_8 = \sigma_8(\Omega_m/0.3)^{0.2}$ , and  $w_0$  from the mock cluster sample. We find that because of the need to accommodate the change in the density profile due to the ejection of baryons, weak lensing mass calibrations are only unbiased if the concentration is left free when fitting the reduced shear with NFW profiles. However, even unbiased total mass estimates give rise to biased cosmological parameters if the measured mass functions are compared with predictions from dark matter-only simulations. This bias dominates for haloes with  $m_{500c} < 10^{14.5} h^{-1} M_\odot$ . For a stage IV-like cluster survey without mass estimation uncertainties, an area  $\approx 15000 \text{ deg}^2$  and a constant mass cut of  $m_{200m,\min} = 10^{14} h^{-1} M_\odot$ , the biases are  $-11 \pm 1$  per cent in  $\Omega_m$ ,  $-3.29 \pm 0.04$  per cent in  $S_8$ , and  $9 \pm 1.5$  per cent in  $w_0$ . The statistical significance of the baryonic bias depends on how accurately the actual uncertainty on individual cluster mass estimates is known. We suggest that rather than the total halo mass, the (re-scaled) dark matter mass inferred from the combination of weak lensing and observations of the hot gas, should be used for cluster count cosmology.

### 3.1 Introduction

Clusters of galaxies are sensitive probes of structure formation in a universe where structure forms hierarchically, because they are still actively forming. Their abundance in a given volume as a function of mass and redshift contains a wealth of information about the formation history of the Universe, i.e. its total amount of matter, how clustered it is, and how its accelerated expansion changed in time (e.g. Allen et al., 2011). The fact that the cluster abundance drops exponentially with increasing mass enables precise constraints on the underlying cosmology, but it also necessitates accurate mass calibrations (e.g. Evrard, 1989; Bahcall et al., 1997).

Linking observed cluster number counts to the theoretical expectation for a given cosmology requires a well-defined cluster selection function and an accurately calibrated mass–observable relation. These requirements are not independent, as Mantz (2019) illustrated how the selection function also plays an important role in constraining the assumed scaling relations between the observable mass proxy and the true mass near the survey mass limit. All current abundance studies account for these effects in their analysis (Mantz et al., 2010; de Haan et al., 2016; Bocquet et al., 2019; DES Collaboration et al., 2020). While the cluster selection function is a crucial part of the cosmological analysis, it also depends on the cluster detection method and is thus survey-specific. Here, we will assume that the completeness of the sample can be modelled perfectly and focus solely on the calibration of the mass–observable relation.

To convert the observed cluster mass proxy, e.g. the Sunyaev-Zel'dovich (SZ) detection significance, into a mass, we need the mass–observable scaling relation. The mass–observable relation cannot be predicted robustly from first principles, since it relies on complex galaxy formation physics. Calibrating this scaling relation requires unbiased mass estimates for a subset of the cluster sample. Consequently, it is generally calibrated using weak lensing observations as they probe the total matter content of the cluster (e.g. Von der Linden et al., 2014a,b; Hoekstra et al., 2015; Schrabback et al., 2018; Dietrich et al., 2019; McClintock et al., 2019a).

Köhlinger et al. (2015) have shown the dramatic reduction in the statistical uncertainties and systematic errors in cluster mass estimates from an idealized weak lensing analysis due to the expected increase in area and background galaxy number density of stage IV-like surveys such as *Euclid*<sup>1</sup> and the Rubin Observatory Legacy Survey of Space and Time (*LSST*)<sup>2</sup>. However, the accuracy of weak lensing mass calibrations remains an open question, especially in the presence of baryons. Bahé et al. (2012) investigated the mass bias inferred from weak lensing observations in dark matter-only (DMO, i.e. gravity-only) simulations, finding cluster masses to be biased low by  $\approx 5$  per cent due to deviations of the cluster density profile from the assumed Navarro-Frenk-White (NFW, see Navarro et al. 1996) shape in the cluster outskirts. Similarly, Henson et al. (2017) found a bias of up to  $\approx 10$  per cent in hydrodynamical simulations. The main conclusion from these studies is that we need to correct weak lensing-derived masses for the lack of spherical symmetry of the observed halo using virtual observations of simulated haloes

<sup>1</sup><https://www.euclid-ec.org>

<sup>2</sup><https://www.lsst.org/>

(see e.g. Dietrich et al., 2019). Lee et al. (2018) used hydrodynamical simulations to show that while these effects are certainly important, the coherent suppression of the inner halo density profile due to baryonic physics also matters. The impact of this effect on cluster number count cosmology has not been isolated so far.

Simulations indicate that baryons significantly change the density profiles of haloes when comparing them to their matched DMO counterparts (e.g. Velliscig et al., 2014; van Daalen et al., 2014; Lee et al., 2018). In hydrodynamical simulations, baryonic effects lower the halo mass,  $m_{200c}$ , at the  $\lesssim 5$  (1) per cent level for cluster-sized haloes with  $m_{200c} > 10^{14}$  ( $10^{14.5}$ )  $h^{-1} M_\odot$  compared to the same halo mass in a gravity-only simulation<sup>3</sup>,  $m_{200c,\text{dmo}}$ . (e.g. Sawala et al., 2013; Cui et al., 2014; Velliscig et al., 2014; Martizzi et al., 2014; Bocquet et al., 2016; Castro et al., 2020). Hence, we should not expect cluster density profiles to follow the NFW shape, especially since baryons are preferentially ejected outside  $r \approx r_{500c}$ , where weak lensing observations reach their optimal signal-to-noise ratio. Balaguera-Antolínez & Porciani (2013) have investigated the impact of the halo mass change due to baryons on cluster count cosmology, but they did not include the effect of weak lensing mass calibrations. To isolate the effect of the change in the halo density profile due to baryons, we generated idealized, spherical clusters that consist of dark matter and hot gas that reproduces the observed cluster X-ray emission, thus bypassing the large inherent uncertainties associated with the assumed subgrid models in hydrodynamical simulations. These models allow us to study the bias in the inferred halo masses for a standard, mock weak lensing analysis that assumes NFW density profiles.

With the cluster masses determined, the number counts as a function of mass and redshift need to be linked to the underlying cosmology. Generally, the cosmology-dependence of the halo mass function is taken from N-body (i.e. gravity-only) simulations due to the need to simulate large volumes to obtain complete samples of clusters at high masses for a range of cosmologies and because of the large uncertainties associated with baryonic physics. Hence, the aforementioned change in halo density profile also complicates the link between observed haloes and their DMO equivalents whose abundance we can predict robustly (e.g. Cui et al., 2014; Cusworth et al., 2014; Velliscig et al., 2014). Since stage IV-like surveys will reliably detect clusters down to halo masses of  $m_{500c} \approx 10^{14} h^{-1} M_\odot$ , this disconnect between observed and DMO haloes will need to be taken into account in their cosmological analyses.

In this paper, we investigate the impact of baryonic effects on cluster number count cosmology. We build a self-consistent, phenomenological model that links idealized clusters whose baryon content matches that inferred from X-ray observations, to their DMO equivalents (Section 3.2). Our linking method relies on the assumption that the cluster dark matter profile does not change significantly due to the presence of baryons. Then, we determine the cluster masses from mock weak lensing observations assuming NFW profiles with either fixed or free concentration–mass relations (Section 3.3). We show how the resulting mass biases impact cosmological parameters for different surveys in Section 3.4. In Section 3.5 we explore the performance of aperture masses, which do not

<sup>3</sup>We define the spherical overdensity masses as the mass contained inside the physical radii  $r_{\Delta c}(z)$ ,  $r_{\Delta m}(z)$  that enclose an average density of  $\langle \rho \rangle = \Delta \rho_{\text{crit}}(z)$ ,  $\langle \rho \rangle = \Delta \rho_m(z) = \Omega_m \rho_{\text{crit}}(z=0)(1+z)^3$ , respectively, where  $\rho_{\text{crit}}(z=0) = 3H_0^2/(8\pi G)$ . That is,  $m_{\Delta c} = 4/3\pi \Delta \rho_{\text{crit}}(z) r_{\Delta c}^3(z)$  and  $m_{\Delta m}(z) = 4/3\pi \Delta \Omega_m \rho_{\text{crit}}(z=0)(1+z)^3 r_{\Delta m}^3(z)$ .

depend as sensitively on the halo density profile. The change in the inner density profile due to baryonic effects affects aperture masses less strongly than deprojected masses, resulting in a closer, but still not perfect, correspondence to the equivalent DMO halo masses. We compare our findings to the literature in Section 3.6 and conclude in Section 3.7.

## 3.2 Halo mass model

We construct an idealized model for the halo matter content as a function of halo mass that incorporates observations for the baryonic component. We modify the model used in our previous work, where we used a halo model to study the impact of baryonic physics on the matter power spectrum (Debackere et al., 2020). The goal here is to obtain halo density profiles that reproduce the observed hot gas density profiles from galaxy clusters while at the same time constraining their abundance through the mass of their equivalent DMO halo and the halo mass function calibrated with DMO simulations. This will allow us to self-consistently study the impact of baryonic physics on cluster number count cosmology.

3

### 3.2.1 Linking observed and DMO haloes

In short, a halo contains dark matter and baryons. In this paper, we assume that the latter consists entirely of hot gas, and we ignore the stars since they contribute only a small fraction ( $\approx 1$  per cent) of the total mass and since the satellite component, which dominates the stellar mass, approximately follows an NFW density profile, similarly to the dark matter (see e.g. van der Burg et al., 2015). The main assumption required to link observed haloes to their equivalent DMO haloes is that the presence of baryons does not significantly affect the bulk of the dark matter. If this is the case, the dark matter of the observed halo will follow the density profile of the equivalent DMO halo, but with a lower normalization, i.e.

$$m_{\text{dmo}}(< r) = \frac{m_{\text{dm}}(< r)}{1 - \Omega_b/\Omega_m}. \quad (3.1)$$

We can convert the observationally inferred total halo mass  $m(< r)$  to the DM mass at the same radius using the observed baryon fraction  $f_{\text{bar}}(r)$ ,

$$m_{\text{dm}}(< r) = (1 - f_{\text{bar}}(r))m(< r). \quad (3.2)$$

Imposing an NFW profile so that

$$m_{\text{dmo}}(< r; c(m_{200m,\text{dmo}}, z)) = 4\pi \int_0^r \rho_{\text{NFW}}(r; c(m_{200m,\text{dmo}}, z))r^2 dr, \quad (3.3)$$

and combining Eqs. (3.1) and (3.2), yields

$$m_{\text{dmo}}(< r; c(m_{200m,\text{dmo}}, z)) = \frac{1 - f_{\text{bar}}(r)}{1 - \Omega_b/\Omega_m} m(< r). \quad (3.4)$$

These relations fully determine the dark matter density profile and the equivalent DMO halo corresponding to the observed halo relying solely on the observed baryon fraction, the inferred total halo mass, and an assumed density profile for the DMO halo. We adopt an NFW density profile (Navarro et al., 1996) for the equivalent DMO halo and the median concentration–mass relation,  $c(m_{200m,\text{dmo}}, z)$ , for relaxed haloes without scatter of Correa et al. (2015). Brown et al. (2020) have shown that this relation accurately predicts the concentration of simulated DMO haloes in observationally allowed  $\Lambda$ CDM cosmologies. Explicitly, we assume that the dark matter of the observed halo has the same scale radius as the equivalent DMO halo, but a density that is a factor of  $1 - \Omega_b/\Omega_m$  lower.

Eq. (3.1) will not hold in detail since the dark matter does react to the presence of baryons (e.g. Gnedin et al., 2004; Duffy et al., 2010; Schaller et al., 2015). However, in the OWLS (Schaye et al., 2010) and cosmo-OWLS simulations (Le Brun et al., 2014) the dark matter mass enclosed within  $r_{200c}$  increases by < 1 per cent due to contraction for all halo masses that we include in our analysis (Velliscig et al., 2014). Hence, by not accounting for the contraction of the dark matter, we may overestimate the true equivalent DMO halo mass by up to  $\approx 1$  per cent, since  $m_{\text{dm}}(<r)/m_{\text{dmo}}(<r) > 1 - \Omega_b/\Omega_m$ . However, this effect will be smaller than the bias due to missing baryons for the abundant low-mass clusters ( $m_{500c} \lesssim 10^{14.5} h^{-1} M_\odot$ ) that are missing a significant fraction of the cosmic baryons.

## 3

### 3.2.2 Including observations of baryons

To determine the baryonic component of our model, we only require a fit to the hot gas density profiles inferred from the observed X-ray surface brightness of galaxy clusters. For a detailed description of how the X-ray surface brightness is converted into the density profile, we refer to Section 3 of Debackere et al. (2020). In short, the X-ray surface brightness is fit with a spherically symmetric, collisionally ionized electron plasma of temperature  $T$  and metallicity  $Z$ . Assuming mass abundances for hydrogen, helium and metals, we then convert the electron number density into a mass density profile. The halo masses for each cluster can then be determined from the hot gas density and temperature profiles under the assumption of hydrostatic equilibrium. We use observations from the Representative XMM-Newton Cluster Structure Survey (REXCESS, Böhringer et al. 2007) because the clusters constitute a local, high-quality, and volume-limited sample, representative of the local X-ray cluster population. Since the survey is not flux-limited, the sample suffers less from the well-known cool-core bias for X-ray cluster samples (Chon & Böhringer, 2017). However, the dynamical state of REXCESS clusters still differs from that of SZ selected samples (which suffer less from biases due to their approximate mass selection, see e.g. Rossetti et al., 2016). We evolve the inferred density profiles self-similarly to extrapolate to higher redshifts. In self-similar evolution, density profiles evolve with redshift as  $\rho(z) \propto E^2(z) = \Omega_m(1+z)^3 + \Omega_\Lambda$  (Kaiser, 1986). Consequently, masses defined with respect to the critical density of the Universe remain constant. In the top panel of Fig. 3.1, we show the median of the  $m_{500c}$ -binned observed hot gas density profiles,  $\rho_{\text{gas}}(r|m, z = 0.43)$ , evolved self-similarly to  $z = 0.43$  (the mean redshift of both the SPT and DES calibration samples, see Dietrich et al. 2019 and

[DES Collaboration et al. 2020](#), respectively), and the 16th and 84th percentile range from the REXCESS data of [Croston et al. \(2008\)](#).

Our procedure for obtaining the gas density profiles and corresponding cluster masses, relies on a couple of assumptions that we now justify. First, in linking the gas density profiles inferred from X-ray observations to the cluster masses, we have assumed hydrostatic equilibrium. This assumption implies that our resulting masses are lower limits on the true cluster masses since observations and simulations suggest that halo masses inferred from X-ray observations and hydrostatic equilibrium are underestimated by  $\approx 15 - 30$  per cent (e.g. [Mahdavi et al., 2013](#); [Von der Linden et al., 2014b](#); [Hoekstra et al., 2015](#); [Medezinski et al., 2018](#); [Barnes et al., 2020](#); [Herbonnet et al., 2020](#)). Looking at Eq. (3.4), the mass ratio  $m(< r)/m_{\text{dmo}}(< r)$ , whose bias we want to study, depends inversely on the inferred dark matter fraction at  $r$ ,  $1 - f_{\text{bar}}(r)$ . If the observed cluster were not in hydrostatic equilibrium, the fixed overdensity radius would increase along with the halo mass. If the halo baryon fraction increases with radius outside  $r_{500c}$  (which is a valid assumption, see e.g. [Vikhlinin et al. 2006](#)), the resulting enclosed baryon fraction would be higher than the one derived assuming hydrostatic equilibrium. In this case, the true mass ratio between the observed halo and its corresponding DMO halo,  $m(< r)/m_{\text{dmo}}(< r)$ , would be lower than our value inferred assuming hydrostatic equilibrium. Hence, our model provides an upper bound to the minimum possible mass ratio bias in Eq. (3.4) due to missing baryons.

Second, we have assumed that the hot gas density profiles evolve self-similarly with redshift. There is observational evidence that the redshift scaling of the cluster hot outer gas density profile is indeed close to self-similar (e.g. [McDonald et al., 2017](#)).

### 3.2.3 Fitting the gas density profiles

In [Debackere et al. \(2020\)](#), we constructed halo density profiles by fitting beta profiles to the galaxy cluster gas density profiles inferred from the observed X-ray emission. While this is certainly a valid approach, we take a different route here. In our previous work, we had to enforce steeper slopes for the observationally unconstrained outer hot gas density profile so that haloes did not exceed the cosmic baryon fraction. However, while this fine-tuning process ensures that the halo baryon fraction reaches the cosmic value at a fixed radius, it then gradually declines further out. Since we wish to ensure that the halo baryon fraction converges to the cosmic value in the halo outskirts, we decided not to fit the gas density profile, but the halo baryon fraction instead:

$$f_{\text{bar}}(r|m, z) = \frac{m_{\text{bar}}(< r|m, z)}{m_{\text{bar}}(< r|m, z) + m_{\text{dm}}(< r|m, z)}, \quad (3.5)$$

where  $m_{\text{bar}}(< r|m, z)$  and  $m_{\text{dm}}(< r|m, z)$  are the enclosed baryonic and dark matter mass within  $r$  for a halo of mass  $m$  at redshift  $z$ , respectively. We can enforce the convergence to the cosmic baryon fraction in the halo outskirts by choosing a functional form for  $f_{\text{bar}}(r)$  that asymptotes to  $\Omega_b/\Omega_m$ .

We construct the enclosed baryon fraction profiles from the observed gas density profiles  $\rho_{\text{gas}}(r|m, z)$  from the REXCESS data of [Croston et al. \(2008\)](#). For each cluster, we determine the dark matter mass at  $r_{500c}$  using Eq. (3.2) and the NFW scale radius by solving Eq. (3.4), assuming the hot gas accounts for all the halo baryons. Then, we

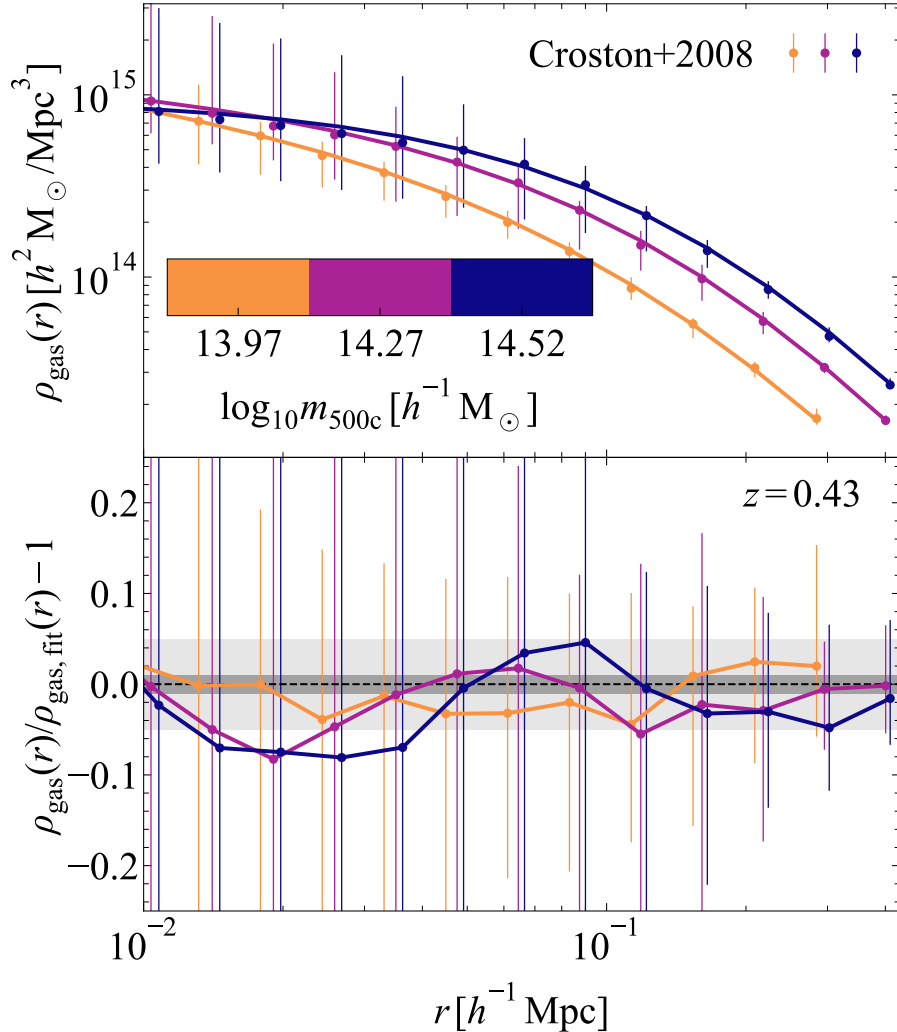


Figure 3.1: *Top panel:* The median hot gas density profiles, evolved self-similarly to  $z = 0.43$ , with their 16th and 84th percentile scatter for the halo mass-binned density profiles from Croston et al. (2008) (coloured circles). We also show the model gas density profiles inferred from fitting the halo baryon fractions (coloured lines). *Bottom panel:* The ratio between the observed hot gas density profiles and our best-fitting model. We recover the observed profile at the  $\approx 5$  per cent level for most of the radial range, which is well within the scatter of the object-to-object scatter for individual mass bins.

obtain  $f_{\text{bar}}(r|m, z)$  from Eq. (3.5). We show the halo baryon fraction inferred from the observations, also evolved self-similarly to  $z = 0.43$ , in the top panel of Fig. 3.2.

The baryonic density profiles can be recovered by taking the derivative of the enclosed baryonic mass profile (we drop the  $m$  and  $z$  dependence)

$$\begin{aligned}\rho_{\text{bar}}(r) &= \frac{1}{4\pi r^2} \frac{dm_{\text{bar}}(<r)}{dr} \\ &= \frac{1}{4\pi r^2} \frac{d}{dr} \left( \frac{f_{\text{bar}}(r)}{1 - f_{\text{bar}}(r)} m_{\text{dm}}(<r) \right) \\ &= \frac{f'_{\text{bar}}(r)m_{\text{dm}}(<r)}{4\pi r^2(1 - f_{\text{bar}}(r))^2} + \frac{f_{\text{bar}}(r)}{1 - f_{\text{bar}}(r)} \rho_{\text{dm}}(r),\end{aligned}\quad (3.6)$$

where  $' \equiv d/dr$ . For outer boundary conditions

$$\lim_{r \rightarrow \infty} f_{\text{bar}}(r) = \Omega_b/\Omega_m \quad (3.7)$$

$$\lim_{r \rightarrow \infty} f'_{\text{bar}}(r) = 0, \quad (3.8)$$

3

it is clear that the baryonic density profile will follow the dark matter in the halo outskirts. In fact, the total matter profile,  $\rho_{\text{bar}} + \rho_{\text{dm}}$ , will approach the equivalent DMO halo profile, since  $\rho_{\text{dm}}(r) = (1 - \Omega_b/\Omega_m)\rho_{\text{dm}}(r)$ . This is exactly what is found in simulations when comparing the halo-matter cross-correlation (which traces the average halo density profile for a given mass) between DMO and hydrodynamical simulations (van Daalen et al., 2014).

In this paper we will assume the baryon fraction goes to zero at small radii for simplicity. Different functional behaviours, for instance including a central increase in the baryon fraction that captures the stellar contribution, are also possible. However, we are interested in studying the change in the cluster weak lensing signal due to the inclusion of baryons. Since the lensing analysis usually excludes the central regions, and the central galaxy would only contribute  $\lesssim 1$  per cent of the total halo mass (see e.g. Zu & Mandelbaum, 2015), we can safely neglect its contribution. We assume the profile

$$f_{\text{bar}}(r|m, z) = \frac{\Omega_b/\Omega_m}{2} \left( 1 + \tanh \left( \frac{\log_{10} r - \log_{10} r_t(m, z)}{\alpha(m, z)} \right) \right), \quad (3.9)$$

which gives

$$f'_{\text{bar}}(r|m, z) = \frac{\Omega_b/\Omega_m}{2 \ln(10) \alpha(m, z) r} \cosh^{-2} \left( \frac{\log_{10}(r/r_t(m, z))}{\alpha(m, z)} \right), \quad (3.10)$$

where  $r_t(m, z)$  determines where the increase in the baryon fraction turns over and  $\alpha(m, z)$  sets the sharpness of the turnover ( $\alpha \gg 1$  is smooth,  $\alpha \ll 1$  is sharp). We show the best-fitting  $f_{\text{bar}}(r|m, z)$  profiles to the REXCESS data, assuming Eqs. (3.6), (3.9), and (3.10), in the top panel of Fig. 3.2. In the bottom panel of Fig. 3.2, we show the ratio of our model to the observations. We are able to capture the observed behaviour at the  $\approx 5$  per cent level for all halo masses and over most of the radial range. This accuracy is well within the observed scatter of the individual gas density profiles. The benefit of

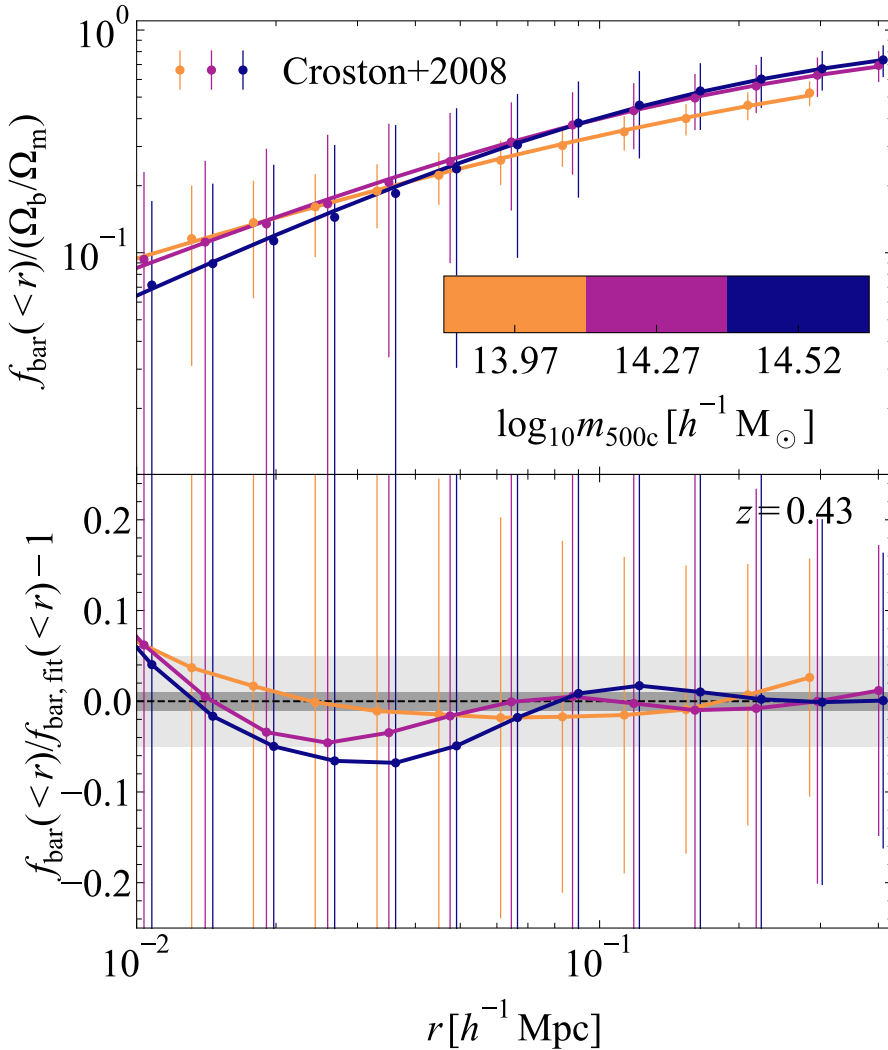


Figure 3.2: *Top panel:* The enclosed baryon fraction as a function of radius for the median, mass-binned hot gas density profiles, evolved self-similarly to  $z = 0.43$ , including their 16th and 84th percentile scatter from Croston et al. (2008) (coloured circles). The dark matter mass is obtained by subtracting the gas mass from the inferred total halo mass. We assume the dark matter follows an NFW profile with a scale radius determined by the equivalent DMO halo that accounts for all cosmic baryons within  $r_{500c}$ , i.e.  $m_{\text{dmo}}(<r_{500c}) = 1/(1 - \Omega_b/\Omega_m)m_{\text{dm}}(<r_{500c})$ . Our best-fitting model assuming Eq. (3.9) is shown as the coloured lines. *Bottom panel:* The ratio between the inferred enclosed baryon fraction from X-ray observations and our best-fitting model. We recover the correct baryon fractions at the  $\approx 5$  per cent level for all radii and halo masses, which is well within the scatter of the object-to-object scatter for individual mass bins.

fitting the halo baryon fraction instead of the gas density, is that the outer baryonic density automatically traces the dark matter, while accounting for all of the cosmic baryons.

To extrapolate our model beyond the observed cluster masses and redshifts, we scale the density profiles self-similarly and fit  $r_t(m, z)$  and  $\alpha(m, z)$ , opting for the following  $(m, z)$  dependencies

$$\log_{10}(r_t/r_x)(m_x, z) = \tilde{r}(z)(\log_{10} m_x - \tilde{m}(z)) \quad (3.11)$$

$$\alpha(m_x, z) = \tilde{\alpha}(z)(\log_{10} m_x - \tilde{\mu}(z)), \quad (3.12)$$

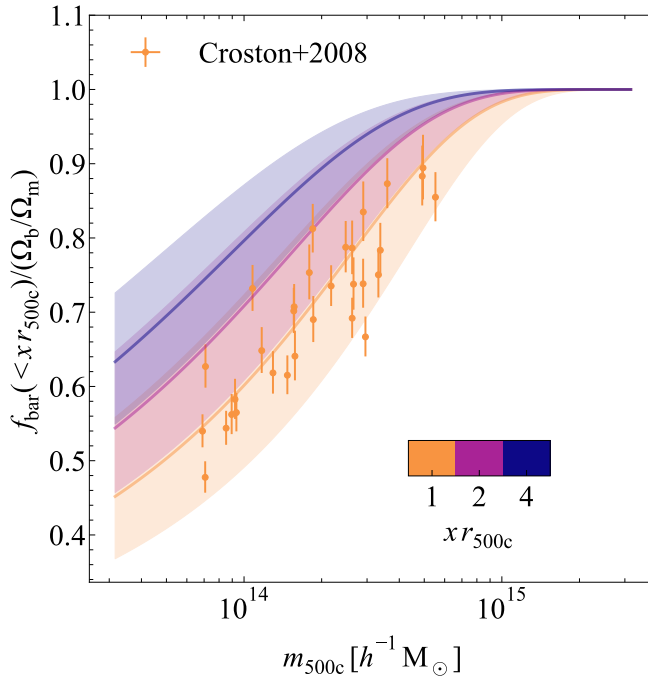
where  $[\tilde{r}(z), \tilde{m}(z), \tilde{\alpha}(z), \tilde{\mu}(z)]$  are free fitting parameters at 10 redshift bins  $z \in [0.1, 2]$  (we interpolate for intermediate values of  $z$ ) and  $m_x$  is the chosen halo mass definition,  $m_{500c}$  in our case. The chosen linear behaviour captures the average mass dependence of the fit parameters quite well, as we show in Appendix 3.A.

We stress that the assumed functional form for  $f_{\text{bar}}(r|m, z)$  implicitly fixes the gas density profile in the halo outskirts. To account for different outer gas density profiles, we also fit the halo baryon fractions inferred from the 16th and 84th percentiles of the hot gas density profiles in Fig. 3.1. To ensure that these fits bracket the median profile results for all masses and redshifts, we fix  $\alpha(m, z)$  to the best-fitting behaviour of the median profiles, and leave  $r_t(m, z)$  free to vary. These different profile behaviours can quantify the effect of higher and lower outer gas densities, which are difficult to constrain observationally, on the inferred halo masses from weak lensing observations.

We show the halo baryon fractions as a function of mass and for different outer radii, in Fig. 3.3. We also show the gas fractions at  $r_{500c}$  inferred from the REXCESS data. Our model closely reproduces the median behaviour. The fits to the 16th and 84th percentiles of the hot gas density profiles capture the full range of the observational uncertainty. Hence, our model is fully representative of the REXCESS galaxy cluster population.

As a consequence of our chosen functional form for the radial profile of the halo baryon fraction, Eq. (3.9), haloes with masses  $m_{500c} \gtrsim 10^{15} h^{-1} M_\odot$  contain the cosmic baryon fraction within  $r_{500c}$ . In simulations, however, halo baryon fractions might exceed the cosmic value at  $r_{500c}$  for these massive haloes since their strong potential wells prevent the ejected baryons from leaving the halo (see e.g. fig. A1 of Velliscig et al. 2014 or fig. 2 of Lee et al. 2018). The REXCESS clusters are not massive enough to observe this behaviour. Moreover, even if this were the case, the lower-mass haloes most tightly constrain the shape and normalization of the halo mass function since they are more abundant.

Another possibly important effect is that at radii larger than  $r_{500c}$  the hot gas pressure might prevent further infall of cosmic baryons, lowering the asymptotic baryon fraction below the cosmic value. Our mock weak lensing observations are performed at scales  $\approx r_{500c}$  for the most massive haloes, and should not be significantly affected by the gas distribution in the halo outskirts. Our profiles assume that the baryon fraction asymptotes to the universal fraction. If the baryon fraction at large radii were smaller than assumed, then the true halo mass,  $m_{200m,\text{true}}$ , would be lower than our model prediction. In that case, the ratio  $m_{200m,\text{true}}/m_{200m,\text{dmo}}$  would be smaller than what we find, since the linked DMO halo mass would remain the same. Hence, our model provides an upper limit to the true mass ratio and, consequently, a lower limit on the bias in the measured



3

Figure 3.3: The REXCESS X-ray hydrostatic gas fractions as a function of halo mass from Croston et al. (2008). The median  $f_{\text{bar}}(< xr_{500c}) - m_{500c}$  relations (thick, coloured lines) and the 16th to 84th percentile ranges (shaded regions) from our model fits to the inferred radial gas fractions of the observed density profiles are shown. We also show the extrapolated enclosed gas fractions at larger radii than observed.

cosmological parameters from cluster counts. We stress that Eq. (3.5) would be able to capture these behaviours if an appropriate functional form is chosen.

In conclusion, our model accurately captures the baryonic content of the average cluster population, since we fit it to the median halo mass-binned gas density profiles inferred from cluster X-ray surface brightness profiles. This also justifies our assumption of spherical symmetry, since deviations due to the presence of substructure or triaxiality of individual haloes average out in a stacked analysis if the cluster selection is unbiased. In Section 3.3, we will use our model to compare the halo masses inferred from a mock weak lensing analysis to the true halo masses.

### 3.3 Mock observational analysis

Mass calibrations of observed samples of clusters are carried out for a subset of the sample for which weak lensing observations are available or follow-up observations are made (e.g. Applegate et al., 2014; Hoekstra et al., 2015; Schrabback et al., 2018; Dietrich

et al., 2019). Different groups use different assumptions to derive weak lensing masses. To minimize the statistical noise in the mass determination of individual clusters due to the degeneracy between mass and concentration (see e.g. Hoekstra et al., 2011), one generally assumes a fixed concentration (as in Applegate et al. 2014 and Von der Linden et al. 2014a) or a concentration–mass relation from simulations (as in Hoekstra et al. 2015; Schrabbach et al. 2018; Dietrich et al. 2019). The weak lensing derived halo masses are then used to calibrate a scaling relation between a survey observable mass proxy and the weak lensing-derived halo mass.

Using our idealized halo model described in Section 3.2, we can generate mock weak lensing observables for clusters with realistic baryonic density profiles. We investigate how accurately the aforementioned weak lensing derived halo mass recovers the true halo mass in the presence of baryons and how the best-fitting mass from the mock weak lensing observations compares to the mass of the same halo in a gravity-only universe, for which we can reliably predict the abundance. The mismatch between these masses determines the bias in the cosmological parameters inferred from a cluster count cosmological analysis as we will perform in Section 3.4.

### 3

The observable of interest for weak lensing is the reduced shear

$$g_T(\theta) = \frac{\gamma_T(\theta)}{1 - \kappa(\theta)}, \quad (3.13)$$

where  $\kappa(\theta) = \Sigma(\theta)/\Sigma_{\text{crit}}$  is the convergence,  $\gamma_T(\theta)$  is the tangential shear, and  $\Sigma_{\text{crit}}$  is the critical surface mass density, defined as

$$\Sigma_{\text{crit}} = \frac{c^2}{4\pi G} \frac{1}{\beta D_1}, \quad (3.14)$$

where  $D_1$  and  $\beta = \max(0, D_{\text{ls}}/D_s)$  are the angular diameter distance between the observer and the lens, and the lensing efficiency for a source at a distance  $D_s$  from the observer and a distance  $D_{\text{ls}}$  behind the lens (which is negative for sources in front of the lens), respectively.

For clusters, generally  $\kappa \approx \gamma_T \approx 0.01 - 0.1$  at the scales probed with weak lensing observations ( $0.5 \lesssim R \lesssim 5 h^{-1}$  Mpc). Assuming a cosmological model, the angular position,  $\theta$ , can be converted into a projected physical distance,  $R$ , using the observed angular diameter distance,  $D$ , as  $\theta = R/D$ . The tangential shear is given by

$$\gamma_T(R|m, z) = \frac{\bar{\Sigma}(<R|m, z) - \Sigma(R|m, z)}{\Sigma_{\text{crit}}}, \quad (3.15)$$

where  $\Sigma(R|m, z)$  is the projected surface mass density profile for a halo with mass  $m$  at redshift  $z$ ,

$$\begin{aligned} \Sigma(R|m, z) &= \int_{-\infty}^{\infty} \rho(R, l|m, z) dl \\ &= 2 \int_R^{\infty} dr \rho(r|m, z) \frac{r}{\sqrt{r^2 - R^2}}, \end{aligned} \quad (3.16)$$

which we compute with a Gauss-Jacobi quadrature to ensure convergence in the presence of the singularity at  $r = R$ , and  $\bar{\Sigma}(<R|m, z)$  is the mean enclosed surface mass density inside  $R$

$$\bar{\Sigma}(<R|m, z) = \frac{2}{R^2} \int_0^R dR' R' \Sigma(R'|m, z). \quad (3.17)$$

The halo model described in Section 3.2 enters in Eqs. (3.16) and (3.17) through the total density profile

$$\rho(r|m, z) = \rho_{\text{dm}}(r|m, z) + \rho_{\text{bar}}(r|m, z). \quad (3.18)$$

Here, we obtain the normalization of the dark matter NFW density profile,  $\rho_{\text{dm}}$ , by taking the halo mass at  $r_{500c}$  and correcting it for the gas fraction inferred from observations of the X-ray surface brightness profiles of the REXCESS clusters (Eq. 3.2). We assume that the dark matter has the same NFW scale radius as the equivalent DMO halo, which can be derived by combining Eqs. (3.1) and (3.3). The baryonic density profile,  $\rho_{\text{bar}}$ , is obtained by fitting Eq. (3.9) to the radial baryon fraction profiles inferred from observations.

We show the reduced shear profiles for different halo mass bins in the top panel of Fig. 3.4. We have assumed a mean lensing efficiency  $\langle\beta\rangle = 0.5$  in Eq. (3.14) (in agreement with the SPT calibration sample; Dietrich et al. 2019) to generate observations in 10 radial bins between  $0.75 h^{-1}$  Mpc and  $2.5 h^{-1}$  Mpc at  $z = 0.43$ , (similar to the mean redshift of the calibration samples for SPT and DES,  $\langle z \rangle = 0.42$  and  $\langle z \rangle = 0.45$ , respectively; Dietrich et al. 2019; DES Collaboration et al. 2020). The observational uncertainty in the reduced shear due to the intrinsic galaxy shape noise for each bin  $R_i$  with bin size  $\Delta R_i$  decreases with the total number of galaxies in the bin, and is taken to be

$$\sigma_{\text{obs}}^2 = \frac{\sigma_{\text{gal}}^2}{2\pi\bar{n}R_i\Delta R_i}, \quad (3.19)$$

with the intrinsic galaxy shape noise  $\sigma_{\text{gal}} = 0.25$  (e.g. Hoekstra et al., 2000), and the mean background galaxy number density  $\bar{n} = 10 \text{ arcmin}^{-2}$  (similar to Dietrich et al., 2019). In a stacked analysis the shape noise would decrease by a factor of  $\sqrt{N}$ , where  $N$  is the number of clusters in the stack. However, this would not affect our best-fitting models since we do not include scatter in the mock observational data. Our mock observations are overly optimistic in this sense. However, given enough clusters, the derived mass–observable relation should converge to the one we find. We choose radial bins within the range  $0.75 < R_i/(h^{-1} \text{ Mpc}) < 2.5$  corresponding to angular sizes  $3.2 < \theta/\text{arcmin} < 10.7$  at  $z = 0.43$  for a Planck Collaboration et al. (2020) cosmology (similar to Dietrich et al., 2019). The inner radius corresponds to  $\approx 1.6$  (0.5)  $r_{500c}(z = 0.43)$  for haloes of masses  $m_{500c} = 10^{14}$  ( $10^{15.5}$ )  $h^{-1} \text{ M}_\odot$ . At smaller scales, cluster miscentring and contamination become important. At larger scales, the large-scale structure contributions to the surface mass density become important. For different redshifts, we scale the radial range of the observations by  $(1+z)^{-1}$ , i.e.  $R_i(z) = 1.43/(1+z)R_i(z = 0.43)$ , to ensure that we are not greatly exceeding  $r_{500c}(z)$  in the fitting range.

The dashed lines in Fig. 3.4 indicate the best-fitting NFW profile to the observed data points, assuming the median Correa et al. (2015) concentration–mass relation. We also show the resulting NFW profile when leaving the scale radius,  $r_s$ , free as the dotted

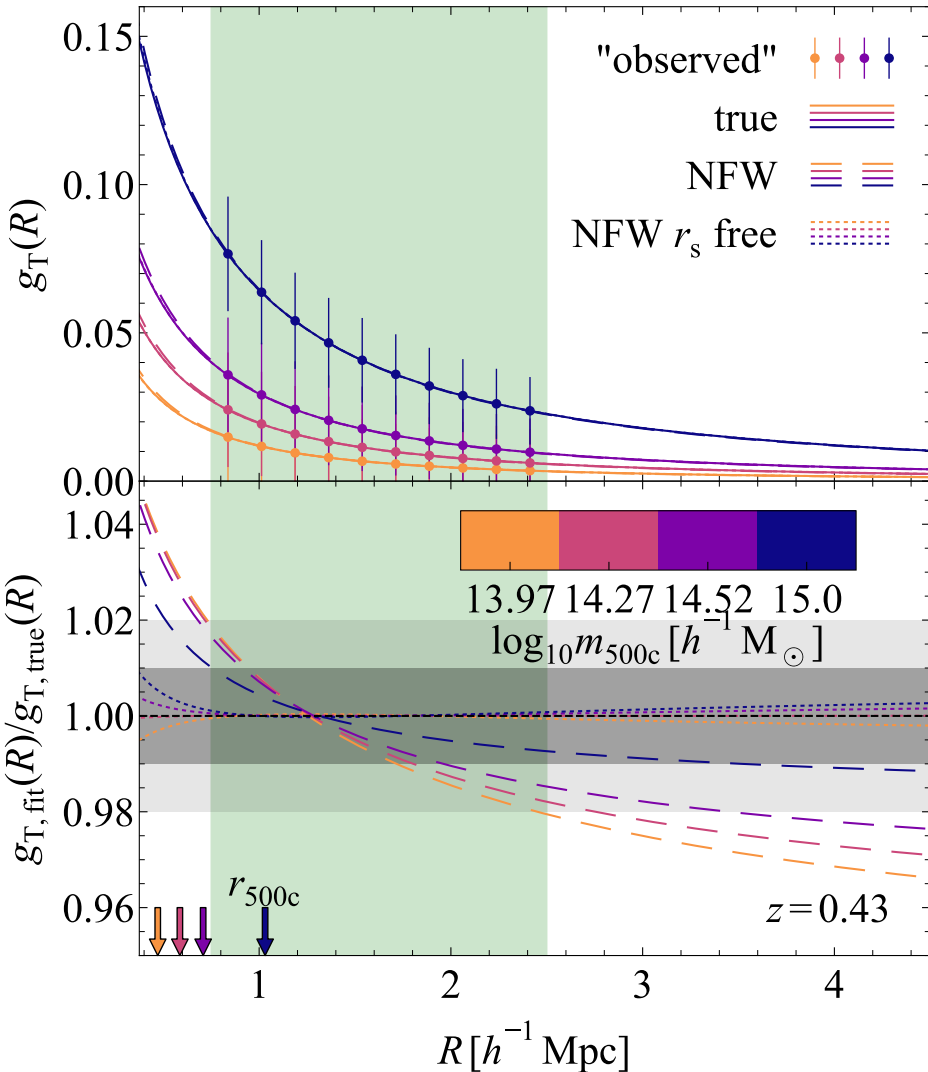


Figure 3.4: *Top panel:* The reduced shear profiles for different halo mass bins (different colours) at  $z = 0.43$ . The mock observations with uncertainties for a single halo set by an intrinsic galaxy shape noise of  $\sigma_{\text{gal}} = 0.25$  and mean background galaxy density of  $\bar{n} = 10 \text{ arcmin}^{-2}$  are shown on top of the underlying true density profile (coloured dots and solid lines). The green shaded region indicates the fitting range for the mock weak lensing observations. The coloured arrows in the bottom panel indicate  $r_{500c}$  for the different halo mass bins. The best-fitting NFW profiles with fixed (free) scale radius,  $r_s$ , are also shown as dashed lines (dotted lines). *Bottom panel:* The ratio of the best-fitting NFW profiles to the true profiles. Leaving the NFW scale radius free results in accurate fits to the true profiles. Fixing the scale radius to a concentration–mass relation for DMO haloes overestimates the signal in the core, where baryons are missing, and underestimates the signal in the outskirts. The mismatch decreases with increasing halo mass as more massive haloes have higher baryon fractions within the fitting range.

lines. Observationally, they would be difficult to distinguish from the true profile because the difference due to baryons is negligible compared to the shape noise of an individual cluster. The lower panel of Fig. 3.4 shows the ratio between the best-fitting NFW reduced shear profiles and the true profiles. Clearly, with currently attainable source background densities, we cannot discern the true reduced shear profile from the best-fitting NFW profiles, which would require per cent level precision for the shear measurements. We have checked that even a stage IV-like survey with  $\bar{n} = 30 \text{ arcmin}^{-2}$  could only observe the difference between the true density profile and the NFW fit with fixed concentration–mass relation at the  $\approx 2\sigma$  level in a stack of  $\mathcal{O}(10^4)$  clusters with  $m_{500c} > 10^{14} h^{-1} M_\odot$ .

We obtain deprojected enclosed total halo mass profiles  $m_{\text{NFW}}(< r)$  from the best-fitting NFW density profiles to the reduced shear. We show the ratio between the NFW reconstructed enclosed halo mass with fixed and free scale radius,  $r_s$ , and the true halo mass in Fig. 3.5 for haloes with masses  $m_{500c} = 10^{14}, 10^{14.5}, 10^{15}, 10^{15.5} h^{-1} M_\odot$ . The results of both fitting methods are generally within  $\approx 5$  per cent of the true enclosed mass profiles for all halo masses we show. However, fixing the concentration–mass relation of the NFW density results in substantially more biased halo mass estimates. The best-fitting NFW profile is determined by the fitting range of the observations and minimizes the  $\chi^2$  error by balancing the over- and underestimation of the true profile, as can be seen in the bottom panel of Fig. 3.4. Since feedback processes redistribute the baryons to larger scales, the best-fitting NFW profiles consistently overestimate the halo mass internal to the minimum radius of the fit. Moreover, since the NFW profile cannot capture the more rapidly increasing baryonic mass towards the halo outskirts, the outer halo mass is consistently underestimated. This behaviour is general: the inner radius of the observational fitting range approximately determines the physical scale at which the inferred total deprojected halo masses are unbiased. For radii progressively smaller (larger) than the inner fitting radius, total deprojected masses are overestimated (underestimated) with increasing amplitude.

This bias can be reduced, however, by leaving the NFW scale radius as a free parameter. The inner halo mass will still be biased, but the extra freedom allows for practically unbiased outer halo mass estimates (see Fig. 3.5). This behaviour is clearly visible in the top panel of Fig. 3.6, where we show the ratio  $m_{200m,\text{NFW}}/m_{200m,\text{true}}$  for both fitting methods. The bottom panel of Fig. 3.6 shows how  $r_s$  needs to increase with respect to the true value to capture the less centrally concentrated halo baryons. However, this is not possible when fixing the concentration–mass relation, resulting in overestimated (underestimated) masses when  $r_{200m,\text{true}} \lesssim (\gtrsim) 1 h^{-1} \text{ Mpc}$  (at  $\approx 1 h^{-1} \text{ Mpc}$  and  $z = 0.43$ , the enclosed mass estimates are unbiased for our chosen fitting range, this corresponds to  $m_{500c} \approx 10^{14.1} h^{-1} M_\odot$ ).

The halo mass  $m_{200m,\text{NFW}}$  from the best-fitting NFW density profile can be used to obtain unbiased estimates of the true halo mass  $m_{200m,\text{true}}$  if the concentration–mass relation is left free. However, for cluster abundance studies, the mass of interest is not  $m_{200m,\text{true}}$  of the observed halo, but the halo mass of the equivalent DMO halo,  $m_{200m,\text{dmo}}$ . All calibrated fitting functions and emulators of the halo mass function are obtained from DMO simulations (e.g. Tinker et al., 2008; McClintock et al., 2019b; Nishimichi et al., 2019; Bocquet et al., 2020), since the matter distribution in hydrody-

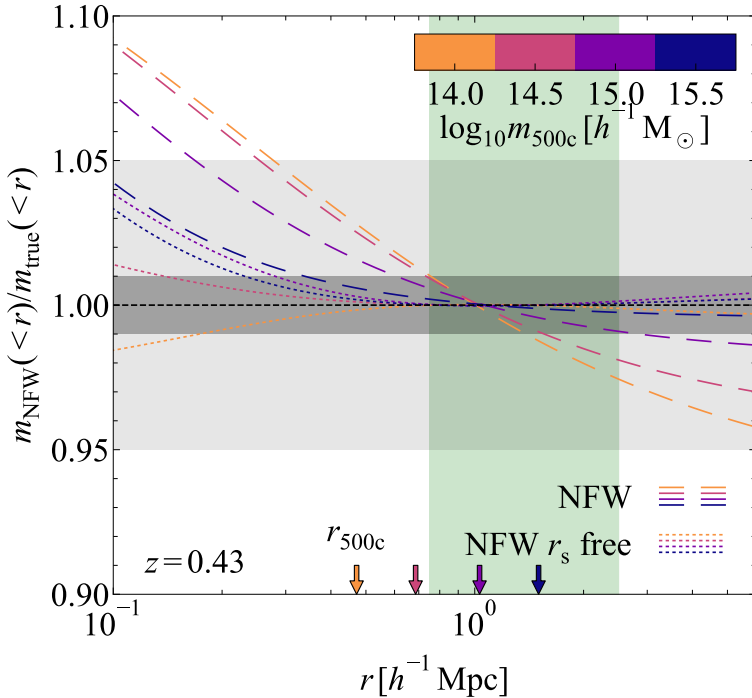
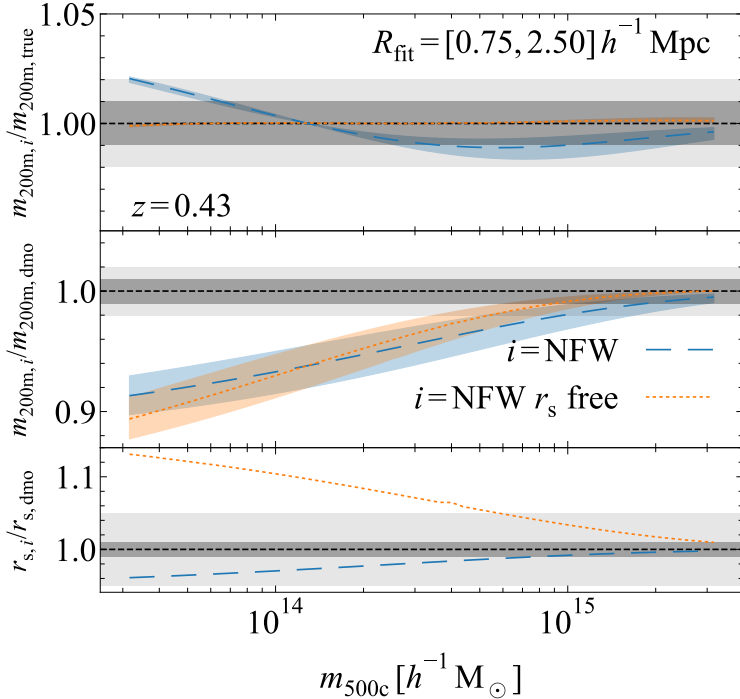


Figure 3.5: The ratio of the 3D enclosed total mass recovered from the best-fitting NFW profiles to the reduced shear with fixed and free scale radius,  $r_s$ , to the true mass profile (dashed and dotted lines, respectively) for haloes of different masses at  $z = 0.43$ . The green, shaded region indicates the radial range for the fit. The overdensity radii  $r_{500c}$  corresponding to the true density profiles are indicated with arrows. Fixing the concentration–mass relation of the NFW profile consistently overestimates (underestimates) the inner (outer) halo mass, where the baryonic mass is lower (higher) than the NFW prediction. Leaving the concentration of the NFW profile free removes the underestimation of the outer halo mass.

namical simulations depends sensitively on the assumed “subgrid” physics recipes required to model the complex galaxy formation processes (e.g. [Velliscig et al., 2014](#)).

We show the ratio  $m_{200m,\text{NFW}}/m_{200m,\text{dmo}}$  as a function of halo mass  $m_{500c}$  in the middle panel of Fig. 3.6. We do not show the ratio  $m_{200m,\text{true}}/m_{200m,\text{dmo}}$  for the actual halo mass since it matches the relation for the best-fitting NFW density profile with a free scale radius (shown as the dotted line) almost exactly (the halo mass  $m_{200m,\text{NFW}}$  is nearly unbiased when the NFW scale radius is left free). The suppression of the true halo mass with respect to the equivalent DMO halo stems from the missing halo baryons within  $r_{200m,\text{true}}$ . Fixing the concentration–mass relation of the NFW density profile (shown as the dashed line) results in biases similar to leaving the NFW scale radius free, except for the small modulation due to the mass bias in  $m_{200m,\text{NFW}}$  with respect to  $m_{200m,\text{true}}$ .



3

Figure 3.6: *Top panel:* The ratio of the 3D enclosed total overdensity mass,  $m_{200m,\text{NFW}}$ , inferred from the best-fitting NFW profiles to the reduced shear, to the true halo mass  $m_{200m,\text{true}}$  as a function of  $m_{500c}$ . The dashed and dotted lines show the mass ratio  $m_{200m,\text{NFW}}/m_{200m,\text{true}}$  for the best-fitting NFW density profiles with fixed and free scale radius for a fitting range of  $R_{\text{fit}} = [0.75 - 2.5] h^{-1} \text{Mpc}$ , respectively. Fixing the scale radius results in biased estimates for  $m_{200m,\text{true}}$ , leaving the scale radius free removes this bias. *Middle panel:* The ratio of the inferred halo mass  $m_{200m,\text{NFW}}$  to the equivalent dark matter-only halo mass  $m_{200m,\text{dmo}}$  as a function of  $m_{500c}$ . The resulting mass ratios are biased for both mass determination methods, since the missing halo baryons bias  $m_{200m,\text{true}}$  with respect to  $m_{200m,\text{dmo}}$ . *Bottom panel:* The ratio of the scale radius of the best-fitting NFW profile to the true dark matter-only NFW scale radius  $r_{s,\text{dmo}}$ . Leaving the scale radius free results in larger values, since the baryons are less centrally concentrated than the dark matter.

(see the top panel of Fig. 3.6). As mentioned earlier, this bias stems from the chosen radial fitting range for the weak lensing observations. Decreasing (increasing) the inner fitting radius shifts the crossover between over- and underestimated  $m_{200m,\text{true}}$  to lower (higher) halo masses and changes the overall amplitude of the bias. Remarkably, for low-mass haloes ( $m_{500c} \lesssim 10^{14.1} h^{-1} \text{M}_\odot$ ), the overestimation of  $m_{200m,\text{true}}$  when fixing the concentration–mass relation results in a less biased estimate of  $m_{200m,\text{dmo}}$ . However, we would preferably not rely on more biased estimates of the true halo mass to obtain less

biased cosmological parameters.

We find a slightly stronger suppression in the ratio  $m_{200m,\text{true}}/m_{200m,\text{dmo}}$  in our model compared to cosmo-OWLS (for  $r_s$  free we find > 1 per cent suppression for  $m_{500c} \lesssim 10^{15} h^{-1} M_\odot$  compared to  $m_{500c} \lesssim 10^{14.5} h^{-1} M_\odot$  in [Velliscig et al. 2014](#)). The reason for this is twofold. First, we do not include a stellar component in our model. Since stars are more centrally concentrated than the hot gas, the NFW fits in cosmo-OWLS perform slightly better in the inner regions, capturing an extra  $\approx 1$  per cent of the total halo mass there and reducing the mass ratio bias. Second, in cosmo-OWLS contraction of the dark matter component due to the baryons at these halo masses slightly reduces the bias since more dark matter mass is included in the central regions than we are accounting for in Eq. (3.1). However, for  $m_{500c} \gtrsim 10^{14} h^{-1} M_\odot$ , the dark matter contraction increases the enclosed halo mass ratio  $m_{\text{dm}}(< r)/m_{\text{dmo}}(< r)$  in Eq. (3.1) by only  $\lesssim 1$  per cent (see fig. 3 of [Velliscig et al., 2014](#)). For  $m_{500c} \lesssim 10^{14} h^{-1} M_\odot$ , the dark matter actually slightly expands, lowering the dark matter mass and increasing the bias.

## 3

We decided not to include a stellar component or dark matter contraction to keep our model simple. Moreover, when investigating the impact of the halo mass determination on the inferred cosmological parameters, lower-mass haloes with  $m_{500c} \lesssim 10^{14.5} h^{-1} M_\odot$  dominate the signal since they are significantly more abundant and hence the fit is more sensitive to any bias in this mass range. At low masses, all the aforementioned effects are clearly much less important than the change in halo mass due to the missing halo gas. Hence, we conclude that our model provides a reasonable estimate of the halo mass bias induced by the change in halo density profiles due to the presence of baryons.

## 3.4 Influence on cosmological parameter estimation

In this section we will investigate how the bias in the halo masses inferred from mock weak lensing observations that we derived in Section 3.3, biases the measurement of cosmological parameters from a number count analysis of a mock cluster sample.

### 3.4.1 Mock cluster sample generation

We create a cluster sample by drawing  $(\log_{10} m_{200m}, z)$  pairs from the Poisson distribution with mean number density

$$\frac{dN(m, z; \mathcal{C})}{d \log_{10} m dz} = \Omega_{\text{survey}} \frac{dV_c(z; \mathcal{C})}{dz d\Omega} \frac{dn(m, z; \mathcal{C})}{d \log_{10} m dz}, \quad (3.20)$$

with the halo mass function  $dn/d \log_{10} m dz$  of [Tinker et al. \(2008\)](#) and the comoving volume  $V_c(z)$  for a [Planck Collaboration et al. \(2020\)](#) cosmology with

$$\begin{aligned} \mathcal{C} &\equiv \{\Omega_m, \Omega_b, \Omega_\Lambda, \sigma_8, n_s, h\} \\ &= \{0.315, 0.049, 0.685, 0.811, 0.965, 0.674\}. \end{aligned} \quad (3.21)$$

The sky area,  $\Omega_{\text{survey}}$ , depends on the specific survey. We use the `CCL`<sup>4</sup> library to calculate the halo mass function (Chisari et al., 2019). We draw samples from the non-homogeneous Poisson distribution by thinning the homogeneous expectation on a grid of  $(\log_{10} m_{200m}, z)$  bins following the method of Lewis & Shedler (1979).

Since the Tinker et al. (2008) mass function was calibrated on DMO simulations, the resulting mock cluster sample corresponds to a universe that contains only dark matter. As we have shown in Section 3.3, however, there is a mismatch between the true halo mass,  $m_{200m,\text{true}}$ , and the mass of the equivalent DMO halo,  $m_{200m,\text{dmo}}$ , due to the ejection of baryons (see the middle panel of Fig. 3.6). Moreover, the halo masses inferred from mock weak lensing observations,  $m_{200m,\text{NFW}}$ , can be biased with respect to the true halo mass (see the top panel of Fig. 3.6). If these baryonic biases are not taken into account in the cluster count analysis, the measured cosmological parameters will be biased.

For each DMO halo in the cluster sample, we determine the biased halo mass estimate of the corresponding halo with baryons,  $m_{200m,\text{NFW}}(m_{200m,\text{dmo}}, z)$ , inferred from the NFW fits to the mock weak lensing observations with either a fixed or free scale radius in Section 3.3. We interpolate the relation between the mass of the halo including baryons and the mass of its equivalent DMO halo,  $m_{500c}(m_{200m,\text{dmo}}, z)$ , from our halo model and determine the corresponding mass ratio  $m_{200m,\text{NFW}}/m_{200m,\text{dmo}}$  (see the middle panel of Fig. 3.6 for the ratio at  $z = 0.43$ ). We will investigate how severely this baryonic mass bias affects the measured cosmological parameters for stage III and stage IV-like surveys in Sections 3.4.2 and 3.4.3, respectively.

We start with a best-case scenario, where we have assumed a one-to-one mapping between the observable mass proxy (e.g. the SZ detection significance) and the halo masses inferred from weak lensing, i.e. we neglect the measurement uncertainties in the mass estimation of individual clusters (we consider a more realistic scenario in Sec. 3.4.3). This allows us to take the weak lensing inferred halo masses as the starting point of our analysis. When connecting haloes to their DMO equivalents, we also do not account for the intrinsic scatter due to the differing mass distributions of individual haloes that arise from their unique mass accretion histories. We assign the weak lensing inferred halo masses to the DMO haloes without scatter. This is consistent with our choice in Section 3.2.3, where we fit to the median halo mass-binned cluster population of REXCESS, neglecting differences between individual clusters in each mass bin.

Ignoring the mass estimation uncertainty and the intrinsic scatter in the halo population would bias the observable–mass relation in an observed cluster sample due to the preferential scatter of more abundant low-mass haloes into higher mass bins. Hence, in a full cosmological analysis, converting the observable to the true halo mass requires the inclusion of the mass estimation uncertainty, and the intrinsic scatter in the halo population, while accounting for the change in abundance of clusters as a function of mass and redshift. This involves a joint fit to the abundance and the observable–mass relation of the cluster sample as a function of cosmology (see e.g. Bocquet et al., 2019). In the more realistic scenario in Sec. 3.4.3, we will implicitly assume that the scatter is constrained by the cluster abundances, so that the precision of cosmological parameter estimation is not significantly affected by not performing such a joint analysis.

<sup>4</sup><https://github.com/LSSTDESC/CCL>

### 3.4.2 Stage III-like survey

For a stage III-like cluster survey (e.g. SPT or DES; [Bocquet et al. 2019](#) and [DES Collaboration et al. 2020](#), respectively), we set the survey area to  $\Omega_{\text{survey}} = 2500 \text{ deg}^2$  to generate the cluster sample using Eq. (3.20).

We want to quantify the statistical bias and uncertainty of the cosmological parameters due to the baryonic halo mass bias. Hence, we generate 1000 independent cluster samples and fit the Maximum A-posteriori Probabilities (MAPs) of the posterior distribution for each of the halo samples. We follow [Cash \(1979\)](#) and [de Haan et al. \(2016\)](#) and obtain the posterior distribution for the cosmological parameters  $\mathcal{C} = \{\Omega_m, \sigma_8, w_0\}$  by sampling the Poisson likelihood, which is given up to a constant by

$$\ln \mathcal{L} \propto 2 \left( \sum_i \ln \frac{dN(m_i, z_i; \mathcal{C})}{dm dz} - \int dm dz \frac{dN(m, z; \mathcal{C})}{dm dz} \right), \quad (3.22)$$

where  $i$  runs over the individual clusters in the sample and the integral is performed between  $(z_{\min} = 0.25, m_{200m,\min} = 10^{14.5} h^{-1} M_\odot)$  and  $(z_{\max} = 2, m_{200m,\max} = 10^{16} h^{-1} M_\odot)$ . The lower bounds are set by the sample selection and the upper bounds are chosen high enough that the integral approaches the limit for  $z, m \rightarrow \infty$ . We assume flat prior distributions  $\Omega_m \sim U(0.1, 0.6)$ ,  $\sigma_8 \sim U(0.5, 1.1)$ , and  $w_0 \sim U(-1.5, -0.5)$ , where  $U(a, b)$  indicates the uniform distribution between  $a$  and  $b$ . We fix the remaining cosmological parameters to the assumed [Planck Collaboration et al. \(2020\)](#) values.

We show the resulting distribution of MAPs in  $(\Omega_m, S_8 = \sigma_8(\Omega_m/0.3)^{0.2}, w_0)$  for each of the different observational mass inferences in Fig. 3.7. The dashed contours show the unbiased halo sample. For this unbiased sample, all cosmological parameters are unbiased and we find relative uncertainties of  $\approx \pm 10$  per cent in  $\Omega_m$ ,  $\approx \pm 0.7$  per cent in  $S_8$ , and  $\approx \pm 16$  per cent in  $w_0$  for a current stage III-like cluster survey. The quoted precision of all parameters underestimates the true uncertainty, since we have performed an idealized analysis that does not include observational uncertainties or intrinsic scatter in the derived halo masses, as mentioned before. However, as we have already shown in Fig. 3.6, the inferred halo masses are biased with respect to the equivalent DMO halo mass due to the missing halo baryons. Hence, NFW inferred halo masses with fixed and free scale radii (blue and orange contours, respectively) are both predominantly biased in  $S_8$ , with a median bias and 16th-84th percentile uncertainties of  $\Delta S_8/S_8 = -0.023^{+0.007}_{-0.008}$ , where the negative value indicates that  $S_8$  is underestimated. Neither  $\Omega_m$  nor  $w_0$  show a significant bias for the different mass determination methods. We list the cosmological parameter constraints for both methods in Table 3.1.

The shifts in the cosmological parameters can be understood in the following way. At a given redshift and for a fixed number count, the mass bias results in an underestimation of the true halo mass. Hence, the number of clusters assigned to the inferred halo mass is lower than it should be, since the number density of clusters increases with decreasing mass. This underestimation is then explained by decreasing the amount of structure in the Universe, assuming that we are unaware of any mass bias.

In summary, current stage III-like cluster abundance surveys with ideal mass estimations would find a biased cosmology (mainly in  $S_8$ ) due to the mismatch between

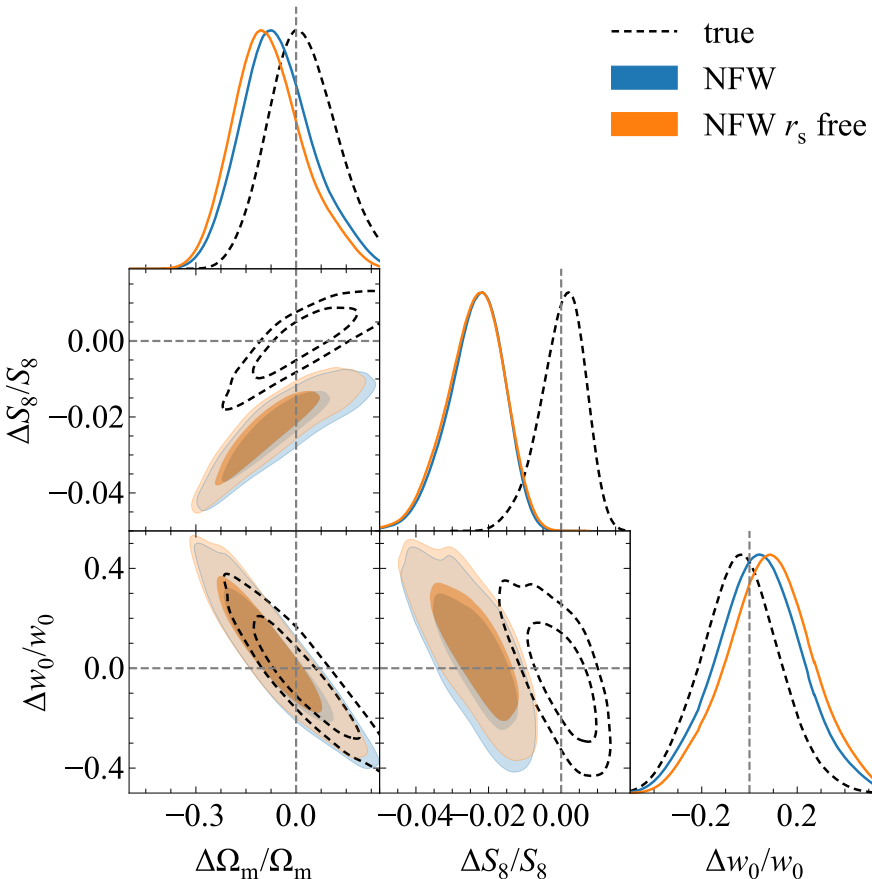


Figure 3.7: The distribution of the maximum a-posteriori probabilities in  $(\Omega_m, S_8 = \sigma_8(\Omega_m/0.3)^{0.2}, w_0)$  for 1000 independent stage III-like cluster abundance surveys. Dashed contours show the results for a halo sample with no mass bias. Blue (orange) contours include a mass bias due to an NFW fit to mock weak lensing observations of the reduced shear, with a fixed (free) scale radius,  $r_s$ . Neither  $\Omega_m$  nor  $w_0$  are significantly biased due to baryonic effects. Relative constraints on  $S_8$ , however, are biased by  $-0.023^{+0.007}_{-0.008}$  ( $\approx 3\sigma$ ) for both fixed and free scale radii in the NFW fit.

Table 3.1: Inferred median bias and 16th-84th percentile statistical uncertainties of the individual best-fitting cosmological parameters for the different mass determination for a stage III-like survey with survey area  $\Omega_{\text{survey}} = 2500 \text{ deg}^2$  and limiting redshift and halo mass ( $z_{\min} = 0.25$ ,  $z_{\max} = 2$ ,  $m_{200m,\min} = 10^{14.5} h^{-1} M_{\odot}$ ). The columns correspond to cosmological parameters inferred from cluster samples with halo masses inferred from weak lensing fits with (a) fixed and (b) free NFW scale radii, and (c) the true cluster masses.

	(a) NFW $r_s$ fixed	(b) NFW $r_s$ free	(c) true
$\Delta\Omega_m/\Omega_m$	$-0.06^{+0.12}_{-0.10}$	$-0.09^{+0.11}_{-0.09}$	$0.02^{+0.11}_{-0.10}$
$\Delta S_8/S_8$	$-0.023^{+0.007}_{-0.008}$	$-0.023^{+0.007}_{-0.008}$	$0.001^{+0.005}_{-0.007}$
$\Delta w_0/w_0$	$0.02^{+0.19}_{-0.16}$	$0.09^{+0.18}_{-0.18}$	$-0.03^{+0.16}_{-0.16}$

$m_{200m,\text{true}}$  and  $m_{200m,\text{dmo}}$ . However, due to the uncertainties induced by the mass estimation, which are larger than the statistical uncertainty of our idealized survey, the baryonic mass bias is currently not highly significant. As a reference, the current quoted uncertainties for SPT (DES; [Bocquet et al. 2019](#) and [DES Collaboration et al. 2020](#), respectively) are  $\pm 17$  (17) per cent in  $\Omega_m$ ,  $\pm 3$  (6) per cent in  $S_8$  (with  $S_8$  definitions differing from ours for both SPT and DES), and  $\pm 26$  (–) per cent in  $w_0$  (DES does not constrain  $w_0$ ), respectively. These values exceed our statistical uncertainties of  $\pm 10$  per cent,  $\pm 0.7$  per cent and  $\pm 16$  per cent, respectively. The baryonic bias in the cosmological parameters that our model predicts corresponds to a statistical significance of  $0.5\sigma$  ( $0.5\sigma$ ) in  $\Omega_m$ ,  $0.8\sigma$  ( $0.4\sigma$ ) in  $S_8$ ,  $0.3\sigma$  (–) in  $w_0$  for the precision of SPT (DES). In Sec. 3.4.3, we show that the precision of the inferred cosmological parameters is set by the accuracy with which the uncertainty in the mass estimation is known. The mass estimation uncertainty is strongly degenerate with  $S_8$  and imposing an uninformative prior on the uncertainty of individual cluster masses results in a significant decrease in the precision of the constraint on  $S_8$ , in line with the comparison to SPT and DES.

### 3.4.3 Stage IV-like survey

For a stage IV-like survey such as *Euclid*, the survey area increases dramatically to  $\Omega_{\text{survey}} = 15000 \text{ deg}^2$ . These surveys will generally rely on observed galaxy overdensities to detect clusters and will, consequently, have more complex selection functions that depend on the magnitude limit of the survey (see e.g. [Sartoris et al. 2016](#)). We take a simple mass cut of  $m_{200m,\min} = 10^{14} h^{-1} M_{\odot}$  and redshift cuts of  $z_{\min} = 0.1$  and  $z_{\max} = 2$ . Due to the increase in survey area and the decrease in  $m_{200m,\min}$ , the total number of clusters increases by about two orders of magnitude compared with a stage III-like survey. The Poisson likelihood in Eq. (3.22) becomes intractable, especially if different mass calibrations are to be included, such as in [de Haan et al. \(2016\)](#). We therefore switch to the Gaussian likelihood for bins where the number of observed clusters,

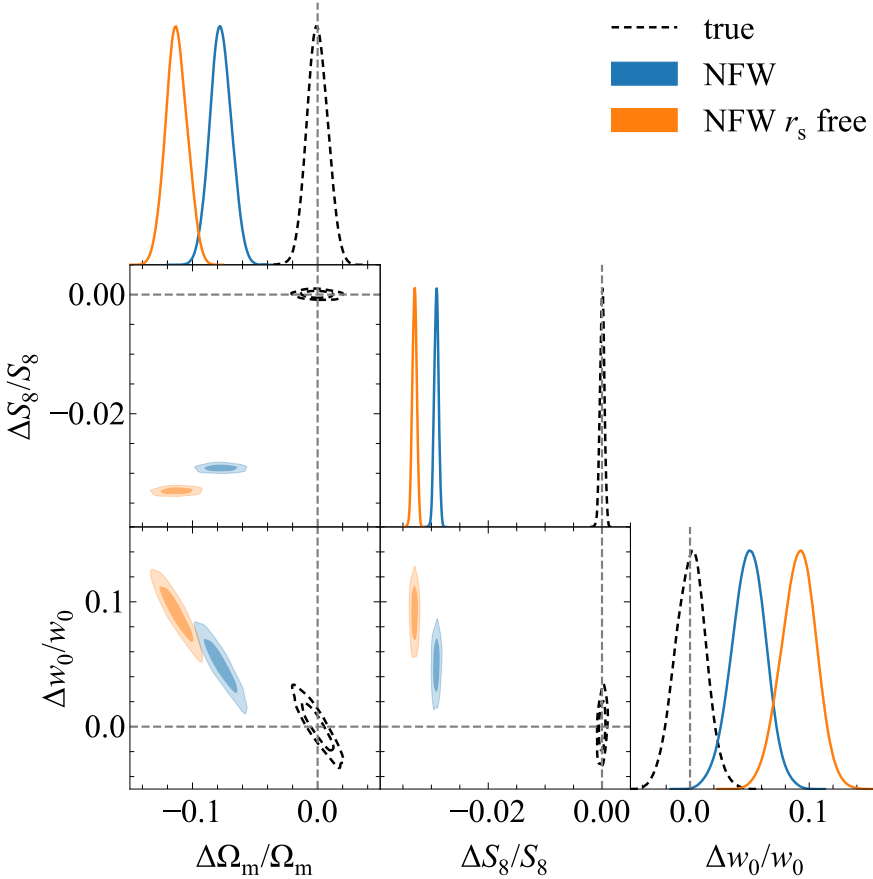


Figure 3.8: The distribution of the maximum a-posteriori probabilities in  $(\Omega_m, S_8 = \sigma_8(\Omega_m/0.3)^{0.2}, w_0)$  for 1000 independent stage IV-like cluster abundance surveys. Dashed contours show the results for a halo sample with no mass bias. Blue (orange) contours include a mass bias due to an NFW fit to mock weak lensing observations of the reduced shear, with a fixed (free) scale radius,  $r_s$ . Relative constraints on  $S_8$  are very highly biased for both NFW fitting methods to the cluster density profiles including baryons. Similarly,  $\Omega_m$  and  $w_0$  are biased by up to  $13\sigma$  and  $6\sigma$ , respectively.

$$N_{\text{obs}}(m_i, z_j) > 10$$

$$\begin{aligned} \ln \mathcal{L} \propto \sum_{m_i, z_j} -\frac{(N_{\text{obs}}(m_i, z_j) - N(m_i, z_j; \mathcal{C}))^2}{2N(m_i, z_j; \mathcal{C})} \\ - \frac{\ln N(m_i, z_j; \mathcal{C})}{2}, \end{aligned} \quad (3.23)$$

and we use the Poisson likelihood for the other bins

$$\begin{aligned} \ln \mathcal{L} \propto \sum_{m_i, z_j} N_{\text{obs}}(m_i, z_j) \ln N(m_i, z_j; \mathcal{C}) - N(m_i, z_j; \mathcal{C}) \\ - \ln N_{\text{obs}}(m_i, z_j)! , \end{aligned} \quad (3.24)$$

where  $(m_i, z_j)$  run over the logarithmic bins in  $m_{200m}$  and the linear bins in  $z$ , respectively. We transition at the value  $N_{\text{obs}}(m_i, z_j) = 10$  since Eq. (3.23) is biased with respect to Eq. (3.24) by a factor of  $1 + O(N_{\text{obs}}^{-1/2})$ , as worked out by Cash (1979). The Gaussian likelihood makes it easier to include contributions from the sample variance, which will also need to be included for the lower-mass haloes probed by stage IV-like surveys (Hu & Kravtsov, 2003). We have neglected the sample covariance in generating our halo sample and, hence, we do not include it in our likelihood analysis. We include the Poisson likelihood for the bins with low number counts since the Gaussian likelihood cannot properly account for the discreteness of the number count data, biasing the cosmological parameter estimates, as we show in Appendix 3.B. In a more realistic setting, the sample variance should be included in the cluster catalogue generation and the cluster number count analysis. For stage IV-like surveys with low limiting masses, the sample variance can dominate the shot noise, increasing the uncertainty on the cluster number density, which reduces the bias for the bins with low number counts. We choose 40 equally spaced bins between  $\log_{10} m_{200m,\min}/(h^{-1} M_\odot) = 14.0$  and the highest halo mass present in each cluster sample. For the redshift, we take 8 equally spaced bins for  $z \in [0.1, 2]$ . We assume the same priors as we did in Section 3.4.2.

We show the resulting distribution of MAPs for the stage IV-like survey in Fig. 3.8. The relative uncertainties for the unbiased sample shrink to  $\approx \pm 1.0$  per cent in  $\Omega_m$ ,  $\approx \pm 0.04$  per cent in  $S_8$ , and  $\approx \pm 1.5$  per cent in  $w_0$  for a stage IV-like cluster survey. Again, we stress that we underestimate the true uncertainty, since we do not include any mass calibration uncertainties. However, in our idealized analysis, the bias from ignoring baryonic effects in the NFW inferred halo masses becomes catastrophic for  $S_8$ , both for fixed and free scale radii. Moreover, we also find very significant biases of up to  $13\sigma$  in  $\Omega_m$  and up to  $6\sigma$  in  $w_0$  (for the exact values, see Table 3.2).

However, the statistical precision of the cosmological parameters is overly optimistic since we neglect any uncertainty on the individual cluster masses inferred, resulting in extremely significant biases due to baryonic effects. For stage IV-like surveys, the amplitude of the mean observable–mass relation can reach per cent level accuracy due to the large number of clusters detected (see e.g. Köhlinger et al., 2015). However, the mass of an individual cluster derived from the survey observable mass proxy will still have an uncertainty. For an observable with a scatter of  $\pm 20$  per cent in the distribution  $P(m|\mathcal{O})$

of the true total halo mass,  $m$ , given the observable,  $\mathcal{O}$  (similarly to the richness, see e.g. Rykoff & Rozo, 2014; Mantz et al., 2016; Sereno et al., 2020), we expect an uncertainty of  $\pm 20$  per cent on the inferred masses of an unbiased cluster sample.

In our idealized setting, we know the true underlying halo masses. We mimic the uncertainty by adding a log-normal scatter of  $\pm 20$  per cent to the true halo masses of the unbiased cluster samples and to the weak lensing inferred halo masses of the biased cluster samples. We modify Eq. (3.20) to include an unknown mass uncertainty  $\sigma_{\log_{10} m}$  for each mass bin  $i$ , following Lima & Hu (2005)

$$\frac{dN_i(m, z; \mathcal{C})}{d \log_{10} m dz} = \frac{1}{2} \frac{dN(m, z; \mathcal{C})}{d \log_{10} m dz} (\text{erfc}(x_i) - \text{erfc}(x_{i+1})), \quad (3.25)$$

where

$$x_i = \frac{\log_{10} m_i^{\text{obs}} - \log_{10} m}{\sqrt{2\sigma_{\log_{10} m}^2}}, \quad (3.26)$$

with  $i$  and  $i + 1$  the edges of mass bin  $i$ . Adding the observational uncertainty will result in haloes scattering to different mass bins, with each bin gaining relatively more low-

3

Table 3.2: Inferred median bias and 16th-84th percentile statistical uncertainties of the individual best-fitting cosmological parameters for the different mass determination methods for a stage IV-like survey with  $\Omega_{\text{survey}} = 15000 \text{ deg}^2$  and ( $z_{\min} = 0.1, z_{\max} = 2, m_{200m, \min} = 10^{14} h^{-1} M_{\odot}$ ). The rows show cosmological parameters inferred from cluster samples with halo masses inferred from weak lensing fits with fixed or free NFW scale radii, and the true cluster masses. The columns show the results for samples with (a) ideal mass determinations, a mass uncertainty of  $\pm 20$  per cent either (b) marginalized over  $\sigma_{\ln m} \sim N(\ln 1.2, \ln 1.02)$ , or (c) included with a uniform prior  $\sigma_{\ln m} \sim U(\ln 1.001, \ln 2)$  in the cosmological parameter estimation.

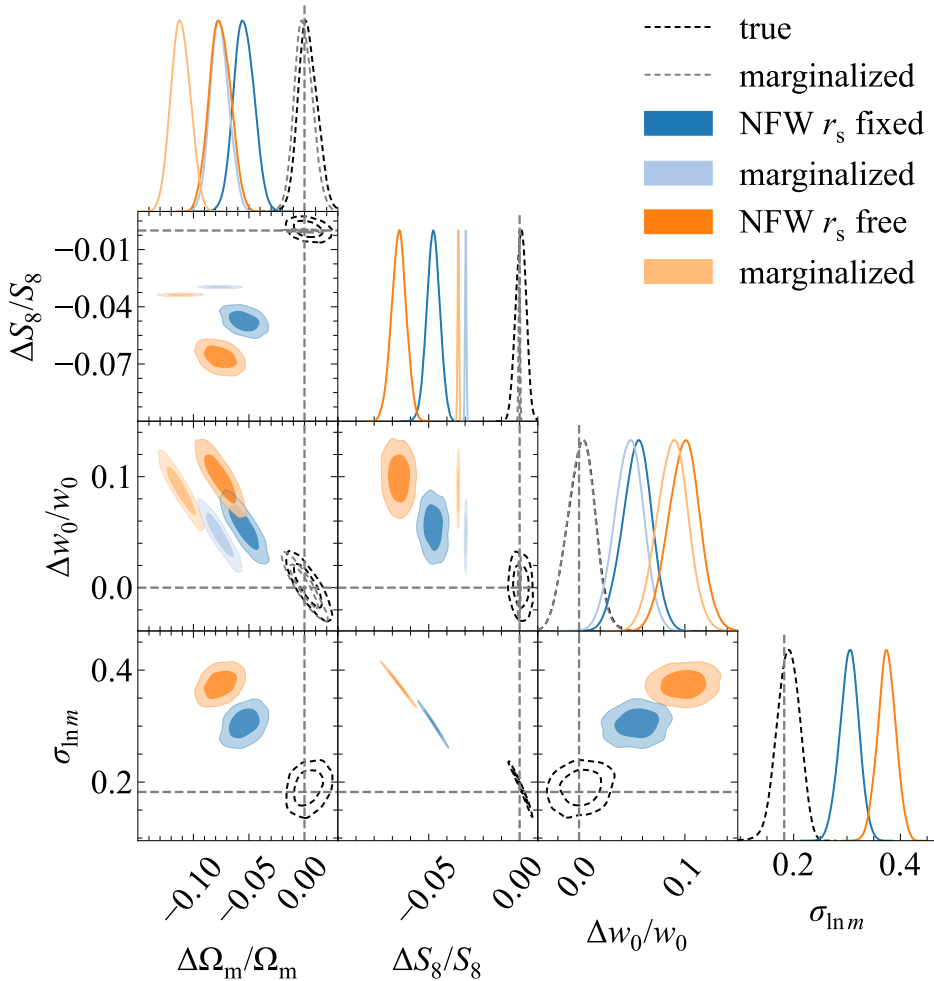
Mass	[per cent]	<sup>(a)</sup> ideal [0]	<sup>(b)</sup> marg. [ $\pm 20$ ]	<sup>(c)</sup> uniform [ $\pm 20$ ]
uncertainty				
NFW	$\Delta\Omega_m/\Omega_m$	$-0.078^{+0.009}_{-0.008}$	$-0.077^{+0.009}_{-0.008}$	$-0.055^{+0.010}_{-0.009}$
$r_s$ fixed	$\Delta S_8/S_8$	$-0.0291^{+0.0004}_{-0.0004}$	$-0.0297^{+0.0004}_{-0.0004}$	$-0.047^{+0.004}_{-0.004}$
	$\Delta w_0/w_0$	$0.055^{+0.014}_{-0.015}$	$0.047^{+0.013}_{-0.014}$	$0.055^{+0.013}_{-0.014}$
NFW	$\Delta\Omega_m/\Omega_m$	$-0.113^{+0.009}_{-0.008}$	$-0.112^{+0.009}_{-0.009}$	$-0.076^{+0.010}_{-0.009}$
$r_s$ free	$\Delta S_8/S_8$	$-0.0329^{+0.0004}_{-0.0004}$	$-0.0337^{+0.0004}_{-0.0004}$	$-0.066^{+0.004}_{-0.004}$
	$\Delta w_0/w_0$	$0.091^{+0.014}_{-0.015}$	$0.089^{+0.014}_{-0.015}$	$0.100^{+0.014}_{-0.016}$
true	$\Delta\Omega_m/\Omega_m$	$-0.0^{+0.009}_{-0.008}$	$-0.001^{+0.009}_{-0.008}$	$0.003^{+0.010}_{-0.008}$
	$\Delta S_8/S_8$	$0.0^{+0.0003}_{-0.0004}$	$-0.0002^{+0.0004}_{-0.0004}$	$0.001^{+0.003}_{-0.003}$
	$\Delta w_0/w_0$	$0.001^{+0.011}_{-0.014}$	$0.002^{+0.012}_{-0.013}$	$0.002^{+0.012}_{-0.013}$

mass haloes due to their higher abundance. We assume a uniform distribution for the mass uncertainty with  $\sigma_{\log_{10} m} \sim U(\log_{10} 1.001, \log_{10} 2)$ . In practice, we will have some prior knowledge of the mass uncertainty of individual clusters. We quantify this effect by including a cosmological analysis with a marginalization over the mass uncertainty distribution  $\sigma_{\log_{10} m} \sim N(\log_{10} 1.2, \log_{10} 1.02)$ , corresponding to the case where the mass uncertainty is known to within 2 per cent.

We show the resulting MAPs for the 1000 cluster samples with both an uninformative prior (dark contours) and a marginalization (light contours) over the individual cluster mass uncertainty in Fig. 3.9. For the former case, we show the posterior constraints on  $\sigma_{\ln m}$  (which equals  $\sigma_{\log_{10} m} / \log_{10} e$ , and approximately corresponds to the per cent error on the halo mass). In the uninformative case, the mass uncertainty is strongly degenerate with  $S_8$ , since an overestimate (underestimate) of the true uncertainty would result in more (less) haloes predicted to scatter into higher mass bins. At fixed observed number count  $N(m_i, z_j)$ , this effect is compensated by decreasing (increasing)  $S_8$ .

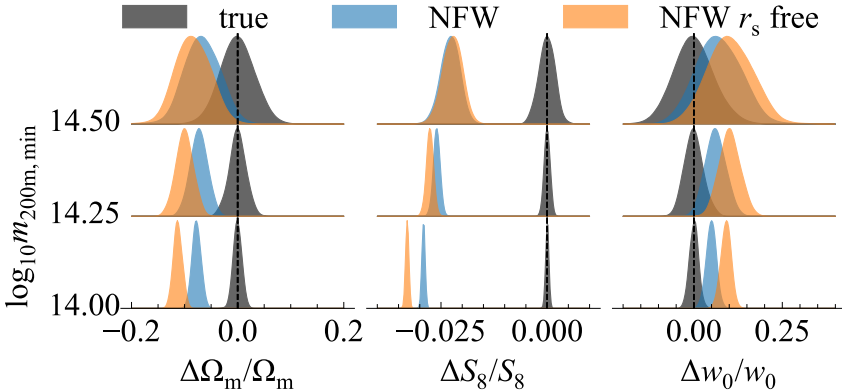
Compared to cluster samples with unbiased masses and no mass estimation uncertainty, we find that the figure of merit (which we take as the inverse of the area enclosed by 95 per cent of the surveys) for cluster samples with unbiased masses and no prior knowledge of the cluster mass uncertainty of  $\pm 20$  per cent (dark, dashed contours), decreases by factors of 7.1, 1.4, and 7.6 in the  $(\Omega_m, S_8)$ ,  $(\Omega_m, w_0)$  and  $(S_8, w_0)$  planes, respectively. Similarly, the 1D marginalized regions containing 68 per cent of the surveys increase by factors of 1.05, 7.7, and 1.02 for  $\Omega_m$ ,  $S_8$ , and  $w_0$ , respectively. However, with accurate prior knowledge of the individual cluster mass estimation uncertainty (light, dashed contours), the inferred cosmological parameters and their precision are fully consistent with the ideal mass estimation case. This can be seen by comparing the dashed and light dashed contours from Figs. 3.8 and 3.9, respectively, or by comparing the cosmological parameter constraints in columns (a) and (b) for the true halo masses in Table 3.2.

We find similar results when comparing the cluster samples that include a baryonic bias and an uncertainty in the halo mass determination to samples that include the baryonic bias but no mass estimation uncertainty. In the case of the uniform prior on  $\sigma_{\ln m}$  (dark, coloured contours), the figure of merit in the  $(\Omega_m, S_8)$ ,  $(\Omega_m, w_0)$  and  $(S_8, w_0)$  planes for a weak lensing fit with free (fixed) NFW scale radius, decreases by factors of 11.2 (9.8), 1.7 (1.5), and 9.6 (8.9), respectively. Similarly, the 1D marginalized regions for  $\Omega_m$ ,  $S_8$ , and  $w_0$  containing 68 per cent of the surveys, increase by factors of 1.1 (1.1), 10.1 (9.4), and 1 (0.9), respectively. However, if the mass uncertainty is known to within 2 per cent (light, coloured contours), then the ideal case is recovered nearly identically. This can be seen by comparing the coloured and light coloured contours from Figs. 3.8 and 3.9, respectively, or by comparing the cosmological parameter constraints in columns (a) and (b) for the NFW fits with fixed and free scale radii in Table 3.2. We note that the distribution of the MAPs for the cluster samples with a baryonic mass bias do not match between the informative and uninformative cases. This is because the halo number counts calculated with Eq. (3.25) do not account for the mass-dependent baryonic bias. Hence, when leaving the mass uncertainty as a free parameter, a more likely solution is found by significantly increasing its value from the actual uncertainty, resulting in a decrease in  $S_8$ . This does not happen for the cluster samples without a mass bias.



3

Figure 3.9: The marginalized maximum a-posteriori probability density functions for  $\Omega_m$ ,  $S_8 = \sigma_8(\Omega_m/0.3)^{0.2}$ ,  $w_0$ , and  $\sigma_{\ln m}$  for 1000 independent stage IV-like cluster abundance surveys with an uncertainty of  $\pm 20$  per cent on the individual cluster masses, assuming a mixed Gaussian-Poisson likelihood. Dashed contours show the results for a halo sample with no mass bias. Blue (orange) contours include a mass bias due to an NFW fit to mock weak lensing observations of the reduced shear, with a fixed (free) scale radius,  $r_s$ . Dark contours also sample the individual cluster mass uncertainty  $\sigma_{\ln m}$ , whereas light contours have marginalized over a Gaussian distribution  $\sigma_{\ln m} \sim N(\ln 1.2, \ln 1.02)$ . Due to the preferential scatter of low-mass haloes into higher mass bins, an underestimate (overestimate) of  $\sigma_{\ln m}$  for a fixed true value of  $\sigma_{\ln m} = \ln 1.02$ , results in an overestimate (underestimate) of  $S_8$ . Marginalizing over the mass uncertainty recovers the constraints obtained without mass uncertainty nearly identically.



**3** Figure 3.10: The marginalized maximum a-posteriori probability density functions for  $\Omega_m$ ,  $S_8 = \sigma_8(\Omega_m/0.3)^{0.2}$  and  $w_0$  for 1000 independent stage IV-like cluster abundance surveys with different mass cuts  $m_{200m,\min}$  and perfect mass determinations. Gray PDFs show the results for a halo sample with no mass bias. Blue (orange) PDFs include a mass bias due to baryonic effects resulting from an NFW fit to mock weak lensing observations of the reduced shear, with a fixed (free) scale radius,  $r_s$ . The bias in  $S_8$  is reduced by a factor of  $\approx 8$  if the mass cut is increased from  $m_{200m,\min} = 10^{14} h^{-1} M_\odot$  to  $m_{200m,\min} = 10^{14.5} h^{-1} M_\odot$ , but is still highly significant, while the bias in  $\Omega_m$  and  $w_0$  is reduced to within  $2.5\sigma$ .

Any bias in the cosmological parameters can be reduced at the expense of a larger uncertainty by increasing the mass cut of the cluster sample. We show the marginalized 1D probability density functions for the cosmological parameters for cluster samples without mass uncertainties using different limiting masses in Fig. 3.10. Increasing the mass cut from  $m_{200m,\min} = 10^{14} h^{-1} M_\odot$  to  $m_{200m,\min} = 10^{14.5} h^{-1} M_\odot$  reduces the bias in  $S_8$  by a factor  $\approx 8$  to  $10\sigma$ , while the bias in  $\Omega_m$  and  $w_0$  is reduced to within  $2.5\sigma$ . However, this increase in the mass cut comes at the expense of a large increase of the statistical errors.

In reality, there will be extra uncertainties due to the photometric redshift estimation of the clusters and the lensed source galaxies, which will scatter clusters between redshift and mass bins. Moreover, the mass uncertainty is a combination of observational systematic uncertainties that evolve differently with mass and redshift (Köhlinger et al., 2015). We have shown that the precision of the inferred cosmological parameters will ultimately be set by the accuracy with which the mass uncertainty of individual cluster masses can be determined. The accuracy of the inferred cosmological parameters will depend on how accurately the bias between the inferred halo masses and the equivalent DMO halo masses can be determined.

Our results clearly indicate the need for more advanced mass inference methods from weak lensing observations and a better calibration between the observed and theoretical

halo masses. Under our assumption that the dark matter distribution is not significantly affected by the presence of baryons, it is possible to obtain unbiased halo mass estimates. This suggests that combining measurements of the total and baryonic halo mass, through, e.g., combined weak lensing and X-ray or SZ observations, respectively, would provide significantly less biased mass estimates of the dark matter mass and hence, after scaling by the universal baryon fraction, of the equivalent DMO halo. In Section 3.5, we explore the possibility of using aperture masses, which are less sensitive to the assumed halo density profile.

### 3.5 Aperture masses

In Section 3.3, we found that we cannot infer unbiased equivalent DMO halo masses from mock weak lensing observations, even when the inferred total halo mass is unbiased. This follows from the deviation of the baryonic component from the assumed NFW density profile and the fact that the baryon fraction is smaller than the universal value in the radial range of the weak lensing observations.

It might be necessary to rethink how we link observed haloes to the theoretical halo mass function, since this is the main baryonic uncertainty. Preferably, the inferred halo masses should differ as little as possible from their equivalent DMO haloes. It has been shown by Herbonnet et al. (2020) that projected halo masses derived from a weak lensing analysis capture the true projected halo mass more accurately than deprojected methods can. The aperture mass is a powerful tool, because it can be computed directly from the data under minimal assumptions about the halo density profile (see e.g. Clowe et al., 1998; Hoekstra et al., 2015). Moreover, we would expect the mass enclosed in a sufficiently large aperture to converge to the equivalent DMO halo mass as long as a larger fraction of the cosmic baryons is included for a larger aperture.

We have performed aperture mass measurements of our mock weak lensing data in the following way. First, we convert the reduced shear to the tangential shear, assuming the best-fitting NFW density profile with a fixed or free scale radius, to compute  $\kappa_{\text{NFW}}(R)$

$$\gamma_T(R) = (1 - \kappa_{\text{NFW}}(R))g_T(R). \quad (3.27)$$

Here, the difference between  $\kappa_{\text{NFW}}(R)$  and the true convergence is  $\lesssim 2$  per cent over the radial range of the observations, resulting in negligible error due to the wrong density profile assumption. Then, we compute the aperture mass using the statistic introduced by Clowe et al. (1998)

$$\begin{aligned} \zeta_c(R_1) &= \bar{\kappa}(R < R_1) - \bar{\kappa}(R_2 < R \leq R_{\max}) \\ &= 2 \int_{R_1}^{R_2} \langle \gamma_T \rangle d \ln R + \frac{2}{1 - R_2^2/R_{\max}^2} \int_{R_2}^{R_{\max}} \langle \gamma_T \rangle d \ln R, \end{aligned} \quad (3.28)$$

where  $\langle \gamma_T \rangle$  is the azimuthally averaged tangential shear, for which we use the tangential shear from Eq. (3.27), derived from mock weak lensing observations of the reduced shear.

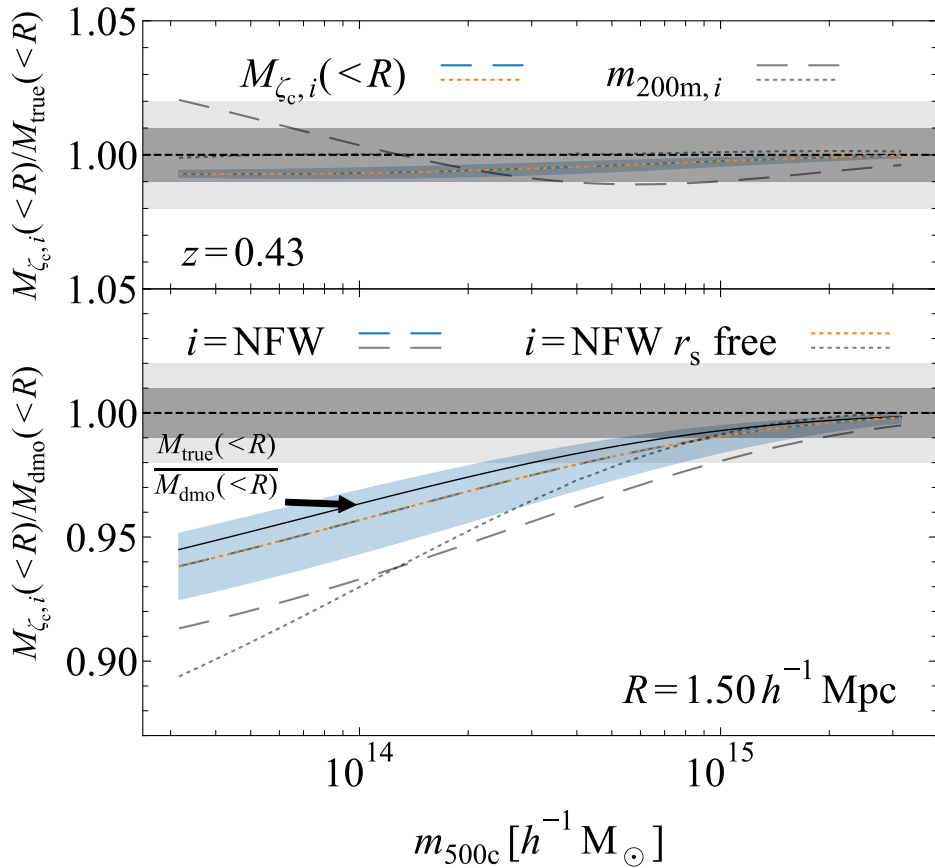


Figure 3.11: *Top panel:* The ratio of the total aperture mass within  $R < 1.5 h^{-1} \text{ Mpc}$  derived from mock weak lensing observations, to the true aperture mass. The coloured, dashed and dotted lines show the ratio of the aperture masses inferred for the best-fitting NFW density profiles, with fixed and free scale radius, respectively, to the true aperture mass using the statistic from Eq. (3.29). The gray dashed and dotted lines show the ratio of the measured and true deprojected masses,  $m_{200m,\text{NFW}}/m_{200m,\text{true}}$ , for the same NFW fits. For the aperture masses, there is practically no difference between using a fixed or free NFW scale radius, indicating insensitivity to the assumed density profile. The derived aperture mass is within 1 per cent of the true aperture mass for all halo masses. *Bottom panel:* The ratio of the total aperture mass within  $R < 1.5 h^{-1} \text{ Mpc}$  derived from mock weak lensing observations, to the same aperture mass of the equivalent DMO halo. Line styles are the same as in the top panel. The ratio of the true to the equivalent DMO halo aperture mass is shown as the solid, black line. The aperture masses are less biased with respect to the equivalent DMO mass than the deprojected masses,  $m_{200m}$ , which are shown as the gray lines.

The aperture mass is then given by

$$M(R < R_1) = \pi R^2 \Sigma_{\text{crit}} (\zeta_c(R_1) + \bar{\kappa}(R_2 < R \leq R_{\max})), \quad (3.29)$$

where we can use the best-fitting NFW profile to determine  $\bar{\kappa}(R_2 < R \leq R_{\max})$ , which is a small correction that again differs negligibly from the true convergence profile due to the NFW assumption. The aperture masses inferred from the above equations recover the true projected halo mass at sub-per cent accuracy over the entire mass range, as we show in the top panel of Fig. 3.11. Aperture masses are thus a very accurate measure of the true enclosed halo mass, more so due to the fact that they depend so little on assumptions about the underlying true density profile.

However, the problem of linking the observed haloes to their equivalent DMO counterparts still remains, although it is slightly alleviated. In the bottom panel of Fig. 3.11, we show the ratio of the aperture masses from mock weak lensing observations within a fixed aperture of  $R < 1.5 h^{-1}$  Mpc to the mass of the equivalent DMO halo within the same aperture. We choose this aperture size since it is within the range of our mock weak lensing observations in Section 3.3 and it is larger than the fixed overdensity radius  $r_{200m}$  for haloes with  $m_{500c} < 10^{14.5} h^{-1} M_\odot$ , for which  $r_{200m}(z = 0.43) \approx 1.3 h^{-1}$  Mpc, resulting in a larger fraction of the universal baryons within it for these abundant haloes. We choose the outer annulus for the correction factor in Eq. (3.28) between  $R_2 = 2.4 h^{-1}$  Mpc and  $R_{\max} = 2.5 h^{-1}$  Mpc such that the NFW correction term is small compared to  $\zeta_c$ . Aperture masses perform better at recovering the mass of the linked DMO halo than the deprojected NFW masses in Sec. 3.3 as long as  $R_1 \gtrsim r_{200m}$ , i.e. for all haloes with  $m_{500c} \lesssim 4 \times 10^{14} h^{-1} M_\odot$  at  $z = 0.43$ , as can be seen from the comparison of the coloured dashed and dotted lines with the gray lines in the bottom panel of Fig. 3.11. This follows from the fact that the halo baryon fractions converge to the cosmic value in the cluster outskirts. This is one of our main conclusions: to link observed haloes to their DMO equivalents, we need to make sure that we are accounting for the ejected baryons. Otherwise, any mass estimate, while not necessarily biased with respect to the *true halo* mass, will be biased with respect to the *equivalent DMO halo* mass. It is this latter bias that is fatal for accurate cluster cosmology.

The fact that the statistic in Eq. (3.29) is practically unbiased with respect to the true aperture mass, regardless of the assumed density profile, makes it an appealing alternative to the deprojected mass determination methods. The problem of calibrating the observed halo masses to their equivalent DMO counterparts, while alleviated, still remains. Since there are so far no theoretical calibrations for the halo aperture mass function, we do not check the performance of the aperture mass determinations for cluster cosmology.

## 3.6 Discussion

We have introduced a phenomenological model that reproduces the baryon content inferred from the X-ray surface brightness profiles of the average observed cluster population in the REXCESS survey. We have shown how we can include observed baryonic density profiles in a halo model, while ensuring that the halo baryon fraction converges to the cosmic value in the halo outskirts, by fitting the inferred radial halo baryon fraction

with the correct asymptotic value. By assuming that baryons do not significantly alter the distribution of the dark matter, we were able to link observed haloes to their equivalent haloes in a DMO universe, which allowed us to predict their number density. Then, we performed mock weak lensing observations to quantify the effect of the changing halo density profile due to the ejection of baryons on the inferred halo masses. Finally, we investigated the bias due to baryons in the measured cosmological parameters from a number count analysis of a mock cluster sample with masses inferred from weak lensing observations. We have justified that our simplifications result in robust lower bounds on the amplitude of the shift due to baryons of both cluster masses and cosmological parameters from an idealized cluster count cosmology analysis. The survey-specific systematic uncertainties set the statistical significance of these shifts. We have shown that the baryonic bias in the cosmological parameters is highly significant even when not including prior knowledge of the uncertainty in the cluster mass inferred from an observable mass proxy. Now we situate our results in the wider context of the literature.

**3**

[Balaguera-Antolínez & Porciani \(2013\)](#) studied the effect of baryons on the cosmological parameters inferred from cluster counts. They used the observed baryon fractions of clusters to infer their equivalent DMO halo masses, similarly to our method. They also find significant biases in the inferred cosmological parameters, mainly a strong suppression in  $\Omega_m$  and a slight increase in  $\sigma_8$  (the exact bias in  $\sigma_8$  depends on their chosen cluster baryon fraction relation). The amplitude and direction of the bias differ from ours as [Balaguera-Antolínez & Porciani \(2013\)](#) use a single, smaller mock cluster sample ( $\approx 2.8 \times 10^4$  clusters compared to  $\approx 1.7 \times 10^5$ ) that spans a lower redshift range and they did not include the effect of baryons on the cluster weak lensing mass determinations.

Previously, weak lensing mass determinations have been studied in both DMO (e.g. [Bahé et al., 2012](#)) and hydrodynamical simulations (e.g. [Henson et al., 2017](#); [Lee et al., 2018](#)). While [Bahé et al. \(2012\)](#) and [Henson et al. \(2017\)](#) find different values for the mass bias, i.e.  $\approx 5$  per cent and  $\approx 10$  per cent, respectively, they both conclude that these biases result from fitting complex, asymmetric clusters with idealized NFW profiles. (Importantly, these analyses leave the concentration free, which is not the case in most observational analyses.) If this is the case, then we could reduce the weak lensing mass bias by performing a stacked analysis, if we have an unbiased cluster sample. Or, since [Henson et al. \(2017\)](#) find a similar bias at fixed halo mass for haloes in both hydrodynamical and DMO simulations (see the top panel of their fig. 11), it seems feasible to model the mass bias due to triaxiality, substructures and departures from the NFW shape, by performing mock observations of DMO haloes (as in e.g. [Dietrich et al., 2019](#)). However, we have shown, as has also been pointed out by [Lee et al. \(2018\)](#), that the distribution of observed cluster baryons implies an intrinsic difference in the density profiles between observed clusters and their DMO equivalents that cannot be captured when assuming a fixed concentration–mass relation. Hence, the inferred halo masses would still be biased, even when accounting for the bias due to halo asymmetry. We found that leaving the concentration of the haloes free mitigates this baryonic mass bias, as was also shown in [Lee et al. \(2018\)](#). However, we showed that the bias in the measured cosmological parameters from a cluster count analysis actually *increases* when leaving the concentration–mass relation free in the weak lensing analysis. This is because low-mass cluster masses are overestimated when fixing the concentration–mass relation, which compensates for some

of the missing baryons and thus reduces the bias with respect to the equivalent DMO halo mass for these abundant clusters.

For cluster cosmology, the vital part is then linking these inferred cluster masses to the equivalent DMO haloes whose number counts we can predict, as argued by Cui et al. (2014), Cusworth et al. (2014) and Velliscig et al. (2014). In the cosmo-OWLS simulations, Velliscig et al. (2014) found differences of  $\lesssim 1$  per cent between cluster masses in the hydrodynamical and DMO simulations for clusters with  $m_{500c} \gtrsim 10^{14.5} h^{-1} M_\odot$ . In our model, we only find such small biases for haloes with masses  $m_{500c} \gtrsim 10^{15} h^{-1} M_\odot$ . As discussed previously, if we optimistically assume that the predictions from cosmo-OWLS are correct, then this difference could be due to our neglect of the back-reaction of the baryons on the dark matter, and the stellar component. However, for low-mass haloes ( $m_{500c} \lesssim 10^{14.5} h^{-1} M_\odot$ ), which will dominate the signal for stage IV-like surveys, these effects are negligible compared to the mass suppression due to the missing baryons.

Using the Magneticum simulation set, Bocquet et al. (2016) and Castro et al. (2020) studied the change in the halo mass function due to baryons and its impact on cluster cosmology. Bocquet et al. (2016) performed a cluster count analysis using halo mass functions calibrated on DMO simulations, to measure the cosmological parameters from a cluster sample generated from the halo mass function of their hydrodynamical simulation. They did not find significant biases for stage III-like surveys, but their shifts in  $\Omega_m$  and  $S_8$  for an eROSITA-like survey are qualitatively similar to our stage IV-like survey predictions. The difference for the stage III-like surveys could be caused by a smaller mismatch between the halo masses in their hydrodynamical and DMO simulations than we infer from observations.

Castro et al. (2020) made Fisher forecasts for a joint cluster number count and clustering analysis of a *Euclid*-like survey using the baryonic and DMO halo mass functions in the Magneticum simulations. They confirmed that correcting for the baryonic mass bias brings the different halo mass functions into closer agreement. However, they find less significant baryonic mass suppression than we do. The resulting biases in the cosmological parameters are significantly smaller than what we find. This difference is most likely caused by both the lower baryonic mass suppression in Magneticum and a different sample selection. We have chosen a minimum redshift  $z_{\min} = 0.1$  and a constant limiting mass cut of  $m_{200m,\min} = 10^{14} h^{-1} M_\odot$ , whereas Castro et al. (2020) use  $z_{\min} = 0.2$  and a redshift-dependent mass threshold varying around  $m_{200c,\min} \approx 10^{14} h^{-1} M_\odot$  within 0.1 dex (see their fig. 13). Consequently, our sample includes more low-mass clusters which increases the statistical significance of the bias (as we show in Fig. 3.10).

An important difference between our work and previous work is that we have used a phenomenological model that reproduces the *observed* baryon content of clusters. Hence, we do not suffer from the uncertainty related to the assumed subgrid models in hydrodynamical simulations. We only rely on the fact that hydrodynamical simulations imply that the baryonic mass suppression of matched haloes explains the difference between their halo mass function and that derived from DMO simulations. All in all, even though the exact value of the baryonic mass bias between observed and equivalent DMO halo masses, and, consequently, the halo mass function, can differ by up to a few per cent de-

pending on which simulations or observations are used, the general behaviour is the same and implies the need to account for baryonic effects in cluster count cosmology.

### 3.7 Conclusions

We set out to investigate the implications for cluster count cosmology of the disconnect between the robust theoretical understanding of cluster-sized ( $m_{500c} > 10^{14} h^{-1} \text{ M}_\odot$ ) dark matter-only haloes and the observed cluster population, an issue which was pointed out by Cui et al. (2014), Cusworth et al. (2014), and Velliscig et al. (2014). They found that in hydrodynamical simulations, there is a significant mismatch between the enclosed halo masses at fixed radius that is determined by the halo baryon fraction. We study how the change in the halo density profiles due to the observed distribution of baryons affects the estimated masses from mock weak lensing observations and the resulting cosmological parameters from a cluster number count analysis.

Our model relies on X-ray observations from the REXCESS data (Croston et al., 2008) to constrain the baryonic density profile of cluster-mass haloes. Under the assumption that the dark matter density profile does not change significantly in the presence of baryons, we can link observed haloes to their DMO equivalents. The distribution of a fraction of the DMO halo mass, i.e. the cosmic baryon fraction, will change in the observed halo. Once this link has been established, we can study the change resulting from this baryonic mass bias in cosmological parameters inferred from a number count analysis. We showed that the currently standard weak lensing mass calibrations that assume NFW density profiles and a fixed concentration–mass relation from DMO simulations, are inherently biased for cluster-mass haloes. Fixing the concentration of the halo results in underestimated halo masses since baryons are ejected beyond the typical radial range that the weak lensing observations are sensitive to. The density profile is fit out to radii where baryons are missing and is not flexible enough to capture the increase in baryonic mass towards larger radii. However, we showed that there is enough freedom in the NFW density profile to provide unbiased halo mass estimates if the concentration is left free (see Fig. 3.5), in agreement with Lee et al. (2018).

However, even unbiased total halo masses result in biased cosmological parameter estimates because of the mismatch between the observed haloes and their DMO equivalents due to ejected baryons (see the middle panel of Fig. 3.6). This is the dominant baryonic bias. A fiducial weak lensing analysis with fixed concentration–mass relation for a stage IV-like survey would result in highly significantly biased estimates of the cosmological parameters, underestimating  $\Omega_m$  and  $S_8$  by up to  $9\sigma$  and  $76\sigma$ , respectively, and overestimating  $w_0$  by  $3.5\sigma$  (see Fig. 3.8 and Table 3.2 for the exact values of the bias). Although leaving the concentration–mass relation free in the weak lensing analysis decreases the bias in the total mass, it actually *increases* the bias in the cosmological parameters to  $13\sigma$ ,  $82\sigma$  and  $6\sigma$ , respectively. This is because the masses of low-mass clusters are overestimated when fixing the concentration–mass relation, which results in a smaller bias compared to the equivalent DMO mass.

We showed that including a constant uncertainty of  $\pm 20$  per cent in the individual, unbiased cluster masses only reduces the precision of the inferred cosmological param-

eters if the mass uncertainty itself is not accurately determined. An uninformative prior on the mass uncertainty decreases the precision of  $\Omega_m$ ,  $S_8$ , and  $w_0$  by factors of 1.05, 7.8, and 1.02, respectively. However, assuming the mass uncertainty of individual clusters is known to within  $\pm 2$  per cent results in constraints that are nearly identical to those derived from ideal cluster masses (see Fig. 3.9 and Table 3.2).

The picture changes slightly for cluster samples that include the baryonic mass bias. To quantify how neglecting the baryonic mass bias affects the inferred cosmological parameters, we do not account for the mass-dependent baryonic bias when fitting the cluster number counts. Since the model without prior knowledge of the mass uncertainty can vary the mass uncertainty as well as the cosmological parameters, the best-fitting parameters differ between the cases with and without prior knowledge of the mass uncertainty. The uninformative prior on the mass uncertainty decreases the precision of  $\Omega_m$ ,  $S_8$ , and  $w_0$  by factors of up to 1.1, 10.7, and 1.02, respectively. Knowing the mass uncertainty to within  $\pm 2$  per cent again results in constraints that cannot be distinguished from those derived from ideal cluster masses (see Fig. 3.9 and Table 3.2). The baryonic bias is thus highly statistically significant, even in the presence of mass estimation uncertainties. The accuracy of the cosmological parameters inferred from cluster number counts depends on how accurately inferred halo masses can be linked to their equivalent DMO halo masses. The precision of the cosmological parameter estimates is determined by how accurately the individual cluster mass estimation uncertainty is known.

For stage III-like surveys and assuming a fixed (free) concentration–mass relation, we found biases of  $\approx 0.6\sigma$  ( $0.9\sigma$ ),  $3\sigma$  ( $3\sigma$ ) and  $0.1\sigma$  ( $0.5\sigma$ ) in  $\Omega_m$ ,  $S_8$ , and  $w_0$ , respectively, again, assuming ideal cluster mass estimations (see Fig. 3.7 and Table 3.1). However, we stressed that the uncertainties induced by the mass estimation for current stage III-like surveys exceed the statistical uncertainty of our idealized survey.

We also measured aperture masses, since they are expected to provide less biased estimates of the total projected mass than deprojected mass estimates, independently of the assumed density profile of the cluster (see the top panel of Fig. 3.11) and they are more closely related to the actual weak lensing observable (e.g. Clowe et al., 1998; Herbonnet et al., 2020). However, even though it is slightly alleviated, the problem of linking observed haloes to their DMO equivalents remains (see the middle panel of Fig. 3.11). We expect the total projected mass to approach the projected DMO mass at large radii (van Daalen et al., 2014). One problem is that correlated large-scale structure becomes important near the cluster virial radius (e.g. Oguri & Hamana, 2011), which requires accurate modelling of the cluster-mass halo bias. We did not include this effect in our model. Using aperture mass estimates would also require a recalibration of halo mass function predictions to this observable.

Any attempt to use clusters for cosmology will need to include a robust method for linking observed haloes to their DMO equivalents. A joint approach, combining weak lensing observations with, for example, hot gas density profiles from X-ray telescopes like eROSITA—and, in the future, Athena—and/or SZ observations would allow the reconstruction of the cluster dark matter mass, which has already been shown to be much less biased with respect to the equivalent DMO halo mass (Velliscig et al., 2014). This is an essential avenue to be explored. If we cannot robustly establish the link to DMO haloes, we cannot obtain unbiased cosmological parameters.

## Data availability

The 1000 mock cluster samples for the stage III-like cluster survey and the MAPs for both the stage III and stage IV-like surveys are publically available through Zenodo at [10.5281/zenodo.4469436](https://zenodo.org/record/105281). The stage IV-like mock cluster samples can be obtained upon request since they exceed the file size limit of Zenodo. The code for the analysis is available at [https://github.com/StijnDebackere/lensing\\_haloes/](https://github.com/StijnDebackere/lensing_haloes/).

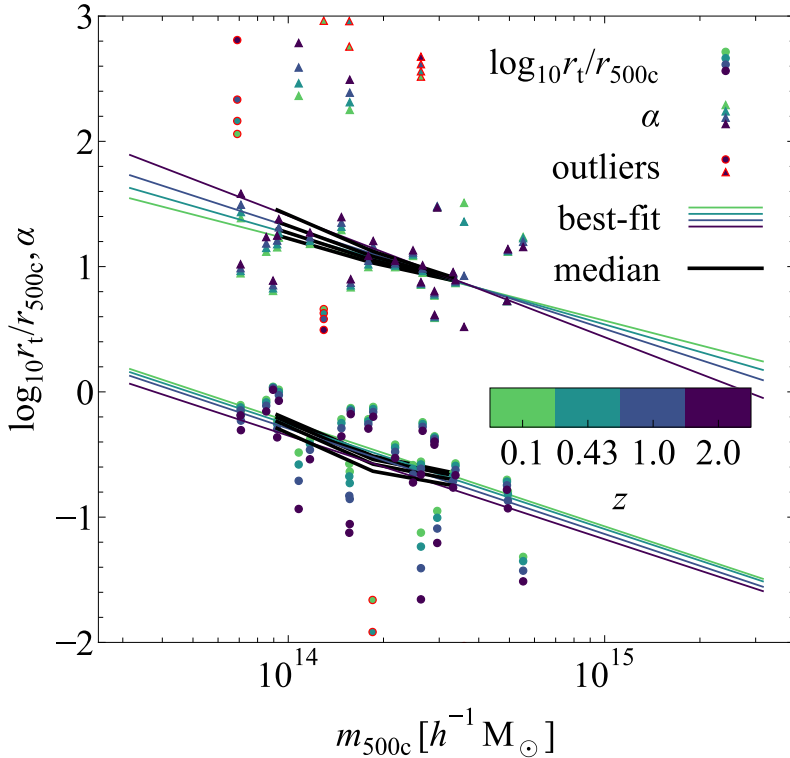


Figure 3.12: The best-fitting  $\log_{10}(r_t/r_{500c})$  and  $\alpha$  values for the REXCESS clusters, self-similarly rescaled to different redshifts (coloured points), their median, mass-binned values (black lines) and the best-fitting linear relations from Eqs. (3.11) & (3.12) (coloured lines). The median relation is captured well with the linear model for each redshift. There are some outliers (red outlined markers), whose density profiles are shown in Fig. 3.13.

### 3.A Model fits

Fig. 3.12 shows the best-fitting  $r_t(m_{500c}, z)$  and  $\alpha(m_{500c}, z)$  for the radial baryon fraction fits (Eq. 3.9) to each cluster in the REXCESS data, self-similarly scaled to the indicated redshifts. We also show the results for the binned clusters as the black lines, and the best-fitting linear relations, following Eqs. (3.11) & (3.12), as the coloured lines. Most of the clusters are described quite well by the best-fitting relations. In Fig. 3.13, we show the outliers (marked in red in Fig. 3.12) with  $|\Delta \log_{10}(r_t/r_{500c})/\log_{10}(r_t/r_{500c})| > 1.5$  and  $|\Delta \alpha/\alpha| > 1.5$ . All these clusters have a high central density core that cannot be captured by our monotonic relation for the baryon fraction (Eq. 3.9). These clusters would be better described by, for example, a double beta profile fit. However, these are only 6 out of the total of 31 clusters, spanning the entire mass range. Hence, they do not bias the median

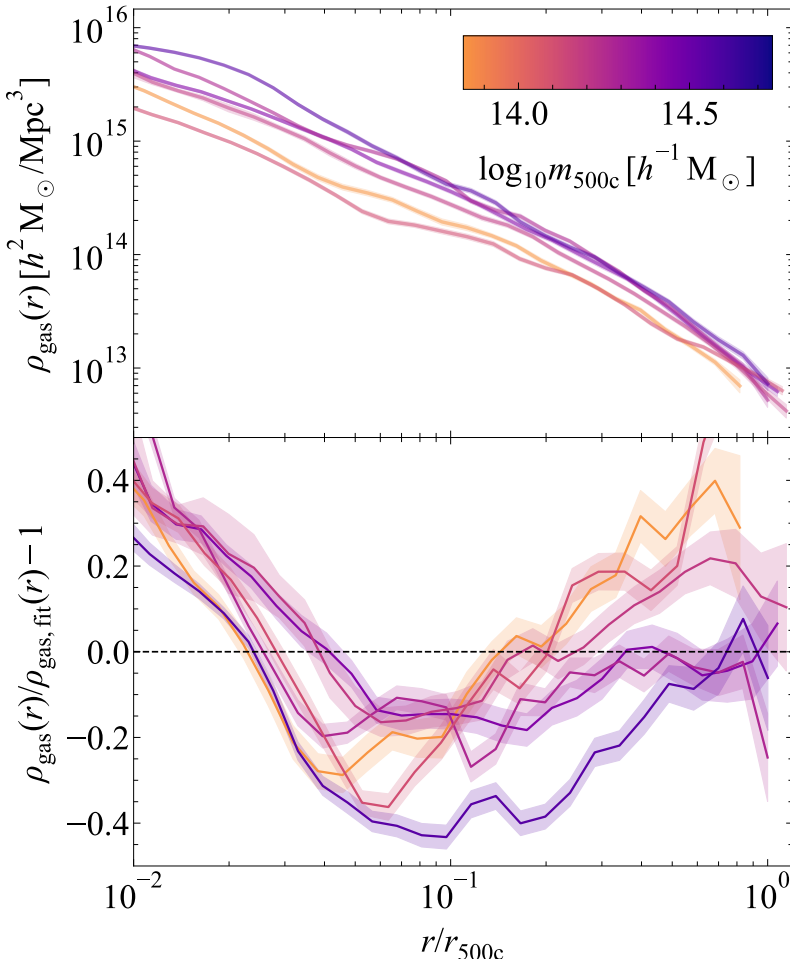


Figure 3.13: *Top panel:* The density profiles of the clusters that are outliers to our best-fitting relations for  $\log_{10}(r_t/r_{500c})$  and  $\alpha$ . *Bottom panel:* The ratio between the observed hot gas density profiles and our best-fitting model. The outliers cannot be accurately described by our simple monotonic increase in the baryon fraction because they have a high density core.

mass-binned cluster profiles.

### 3.B Mixed likelihood

In Fig. 3.14 we show the difference in cosmological parameter constraints for a stage IV-like cluster abundance survey when using a pure Gaussian likelihood, i.e. Eq. (3.23), versus the mixed Gaussian-Poisson likelihood that uses Eq. (3.24) for bins with  $N_{\text{obs}}(m_i, z_j) <$

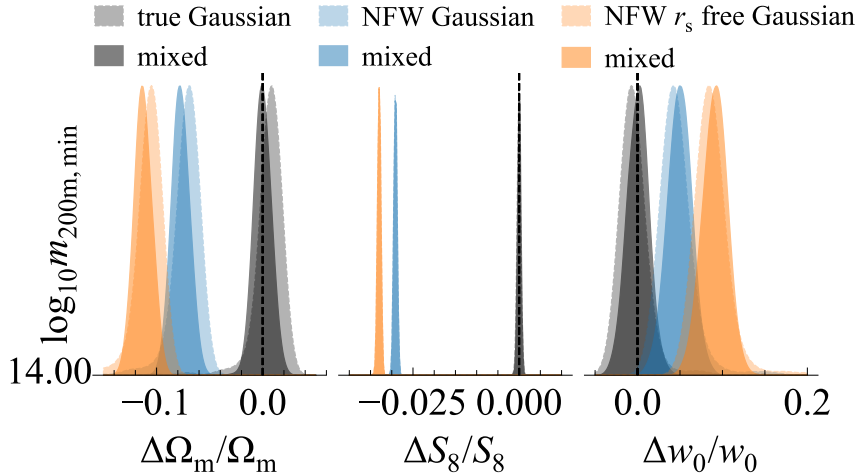


Figure 3.14: The marginalized maximum a-posteriori probability density functions for  $\Omega_m$ ,  $S_8 = \sigma_8(\Omega_m/0.3)^{0.2}$  and  $w_0$  for 1000 independent stage IV-like cluster abundance surveys assuming a Gaussian likelihood (lightly shaded contours), or a mixed Gaussian-Poisson likelihood (darkly shaded contours). Gray PDFs show the results for a halo sample with no mass bias. Blue (orange) PDFs include a mass bias due to an NFW fit with a fixed (free) scale radius,  $r_s$ . The Gaussian likelihood biases  $\Omega_m$  ( $w_0$ ) towards higher (lower) values.

3

10. The Gaussian likelihood cannot deal with the discreteness of the number counts at high redshift and high halo masses. The absence of clusters in these bins pushes the theoretical prediction of the halo mass function towards lower values in the Gaussian likelihood. Meanwhile, the number counts for low-mass haloes, which are more abundant and thus better described by the Gaussian likelihood, need to remain the same. For the mass cut  $m_{200m, \text{min}} = 10^{14} h^{-1} M_\odot$ , the lower number counts for high-mass haloes are achieved by decreasing  $w_0$  and increasing  $\Omega_m$  in such a way that the decrease in number counts for low-mass haloes due to  $w_0$  is offset by the increase due to  $\Omega_m$ .  $S_8$  seems unaffected by the choice in likelihood. The mixed Gaussian-Poisson likelihood results in unbiased cosmological parameter estimates.

## Bibliography

- Allen S. W., Evrard A. E., Mantz A. B., 2011, *Annu. Rev. Astron. Astrophys.*, 49, 409 → p. 86
- Applegate D. E., et al., 2014, *Mon. Not. R. Astron. Soc.*, 439, 48 → p. 95, 96
- Bahcall N. A., Fan X., Cen R., 1997, *Astrophys. J.*, 485, L53 → p. 86
- Bahé Y. M., McCarthy I. G., King L. J., 2012, *Mon. Not. R. Astron. Soc.*, 421, 1073 → p. 86, 116
- Balaguera-Antolínez A., Porciani C., 2013, *J. Cosmol. Astropart. Phys.*, 2013 → p. 87, 116
- Barnes D. J., Vogelsberger M., Pearce F. A., Pop A.-R., Kannan R., Cao K., Kay S. T., Hernquist L., 2020, preprint, 20, 1 ([arXiv:2001.11508](https://arxiv.org/abs/2001.11508)) → p. 90
- Bocquet S., Saro A., Dolag K., Mohr J. J., 2016, *Mon. Not. R. Astron. Soc.*, 456, 2361 → p. 87, 117
- Bocquet S., et al., 2019, *Astrophys. J.*, 878, 55 → p. 86, 103, 104, 106
- Bocquet S., Heitmann K., Habib S., Lawrence E., Uram T., Frontiere N., Pope A., Finkel H., 2020, *Astrophys. J.*, 901, 5 → p. 99
- Böhringer H., et al., 2007, *Astron. Astrophys.*, 469, 363 → p. 89
- Brown S. T., McCarthy I. G., Diemer B., Font A. S., Stafford S. G., Pfeifer S., 2020, *Mon. Not. R. Astron. Soc.*, 495, 4994 → p. 89
- Cash W., 1979, *Astrophys. J.*, 228, 939 → p. 104, 108
- Castro T., Borgani S., Dolag K., Marra V., Quartin M., Saro A., Sefusatti E., 2020, *Mon. Not. R. Astron. Soc.*, 500, 2316 → p. 87, 117
- Chisari N. E., et al., 2019, *Astrophys. J. Suppl. Ser.*, 242, 2 → p. 103
- Chon G., Böhringer H., 2017, *Astron. Astrophys.*, 606, L4 → p. 89
- Clowe D., Luppino G. A., Kaiser N., Henry J. P., Gioia I. M., 1998, *Astrophys. J.*, 497, L61 → p. 113, 119
- Correa C. A., Wyithe J. S. B., Schaye J., Duffy A. R., 2015, *Mon. Not. R. Astron. Soc.*, 452, 1217 → p. 89, 97
- Croston J. H., et al., 2008, *Astron. Astrophys.*, 487, 431 → p. 90, 91, 93, 95, 118
- Cui W., Borgani S., Murante G., 2014, *Mon. Not. R. Astron. Soc.*, 441, 1769 → p. 87, 117, 118
- Cusworth S. J., Kay S. T., Battye R. A., Thomas P. A., 2014, *Mon. Not. R. Astron. Soc.*, 439, 2485 → p. 87, 117, 118
- DES Collaboration et al., 2020, *Phys. Rev. D*, 102, 023509 → p. 86, 90, 97, 104, 106
- Debackere S. N. B., Schaye J., Hoekstra H., 2020, *Mon. Not. R. Astron. Soc.*, 492, 2285 → p. 88, 89, 90
- Dietrich J. P., et al., 2019, *Mon. Not. R. Astron. Soc.*, 483, 2871 → p. 86, 87, 89, 95, 96, 97, 116
- Duffy A. R., Schaye J., Kay S. T., Vecchia C. D., Battye R. A., Booth C. M., 2010, *Mon. Not. R. Astron. Soc.*, 405, 2161 → p. 89
- Evrard A. E., 1989, *Astrophys. J.*, 341, L71 → p. 86
- Gnedin O. Y., Kravtsov A. V., Klypin A. A., Nagai D., 2004, *Astrophys. J.*, 616, 16 → p. 89
- Henson M. A., Barnes D. J., Kay S. T., McCarthy I. G., Schaye J., 2017, *Mon. Not. R. Astron. Soc.*, 465, 3361 → p. 86, 116
- Herbonnet R., et al., 2020, *Mon. Not. R. Astron. Soc.*, 497, 4684 → p. 90, 113, 119
- Hoekstra H., Franx M., Kuijken K., 2000, *Astrophys. J.*, 532, 88 → p. 97
- Hoekstra H., Hartlap J., Hilbert S., van Uitert E., 2011, *Mon. Not. R. Astron. Soc.*, 412, 2095 → p. 96
- Hoekstra H., Herbonnet R., Muzzin A., Babul A., Mahdavi A., Viola M., Cacciato M., 2015, *Mon. Not. R. Astron. Soc.*, 449, 685 → p. 86, 90, 95, 96, 113
- Hu W., Kravtsov A. V., 2003, *Astrophys. J.*, 584, 702 → p. 108
- Kaiser N., 1986, *Mon. Not. R. Astron. Soc.*, 222, 323 → p. 89

- Köhlinger F., Hoekstra H., Eriksen M., 2015, *Mon. Not. R. Astron. Soc.*, 453, 3107 → p. 86, 108, 112
- Le Brun A. M., McCarthy I. G., Schaye J., Ponman T. J., 2014, *Mon. Not. R. Astron. Soc.*, 441, 1270 → p. 89
- Lee B. E., Le Brun A. M. C., Haq M. E., Deering N. J., King L. J., Applegate D., McCarthy I. G., 2018, *Mon. Not. R. Astron. Soc.*, 479, 890 → p. 87, 94, 116, 118
- Lewis P. A. W., Shedler G. S., 1979, *Nav. Res. Logist. Q.*, 26, 403 → p. 103
- Lima M., Hu W., 2005, *Phys. Rev. D - Part. Fields, Gravit. Cosmol.*, 72, 1 → p. 109
- Mahdavi A., Hoekstra H., Babul A., Bildfell C., Jeltema T., Henry J. P., 2013, *Astrophys. J.*, 767, 116 → p. 90
- Mantz A. B., 2019, *Mon. Not. R. Astron. Soc.*, 485, 4863 → p. 86
- Mantz A., Allen S. W., Rapetti D., Ebeling H., 2010, *Mon. Not. R. Astron. Soc.*, 406, 1759 → p. 86
- Mantz A. B., et al., 2016, *Mon. Not. R. Astron. Soc.*, 463, 3582 → p. 109
- Martizzi D., Mohammed I., Teyssier R., Moore B., 2014, *Mon. Not. R. Astron. Soc.*, 440, 2290 → p. 87
- McClintock T., et al., 2019a, *Mon. Not. R. Astron. Soc.*, 482, 1352 → p. 86
- McClintock T., et al., 2019b, *Astrophys. J.*, 872, 53 → p. 99
- McDonald M., et al., 2017, *Astrophys. J.*, 843, 28 → p. 90
- Medezinski E., et al., 2018, *Publ. Astron. Soc. Japan*, 70, 1 → p. 90
- Navarro J. F., Frenk C. S., White S. D. M., 1996, *Astrophys. J.*, 462, 563 → p. 86, 89
- Nishimichi T., et al., 2019, *Astrophys. J.*, 884, 29 → p. 99
- Oguri M., Hamana T., 2011, *Mon. Not. R. Astron. Soc.*, 414, 1851 → p. 119
- Planck Collaboration et al., 2020, *Astron. Astrophys.*, 641, A6 → p. 97, 102, 104
- Rossetti M., et al., 2016, *Mon. Not. R. Astron. Soc.*, 457, 4515 → p. 89
- Rykoff E., Rozo E. S., 2014, *Astrophys. J.*, 783, 80 → p. 109
- Sartoris B., et al., 2016, *Mon. Not. R. Astron. Soc.*, 459, 1764 → p. 106
- Sawala T., Frenk C. S., Crain R. A., Jenkins A., Schaye J., Theuns T., Zavala J., 2013, *Mon. Not. R. Astron. Soc.*, 431, 1366 → p. 87
- Schaller M., et al., 2015, *Mon. Not. R. Astron. Soc.*, 451, 1247 → p. 89
- Schaye J., et al., 2010, *Mon. Not. R. Astron. Soc.*, 402, 1536 → p. 89
- Schrabback T., et al., 2018, *Mon. Not. R. Astron. Soc.*, 474, 2635 → p. 86, 95, 96
- Sereno M., et al., 2020, *Mon. Not. R. Astron. Soc.*, 497, 894 → p. 109
- Tinker J., Kravtsov A. V., Klypin A., Abazajian K., Warren M., Yepes G., Gottlöber S., Holz D. E., 2008, *Astrophys. J.*, 688, 709 → p. 99, 102, 103
- Velliscig M., van Daalen M. P., Schaye J., McCarthy I. G., Cacciato M., Le Brun A. M., Vecchia C. D., 2014, *Mon. Not. R. Astron. Soc.*, 442, 2641 → p. 87, 89, 94, 100, 102, 117, 118, 119
- Vikhlinin A., Kravtsov A., Forman W., Jones C., Markevitch M., Murray S. S., Van Speybroeck L., 2006, *Astrophys. J.*, 640, 691 → p. 90
- Von der Linden A., et al., 2014a, *Mon. Not. R. Astron. Soc.*, 439, 2 → p. 86, 96
- Von der Linden A., et al., 2014b, *Mon. Not. R. Astron. Soc.*, 443, 1973 → p. 86, 90
- Zu Y., Mandelbaum R., 2015, *Mon. Not. R. Astron. Soc.*, 454, 1161 → p. 92
- de Haan T., et al., 2016, *Astrophys. J.*, 832, 1 → p. 86, 104, 106
- van Daalen M. P., Schaye J., McCarthy I. G., Booth C. M., Vecchia C. D., 2014, *Mon. Not. R. Astron. Soc.*, 440, 2997 → p. 87, 92, 119
- van der Burg R. F. J., Hoekstra H., Muzzin A., Sifón C., Balogh M. L., McGee S. L., 2015, *Astron. Astrophys.*, 577, A19 → p. 88



# 4 | Why are we still using 3D masses for cluster cosmology?

Based on

Stijn N. B. Debackere, Joop Schaye, Henk Hoekstra, Katrin Heitmann,  
Salman Habib

*Monthly Notices of the Royal Astronomical Society, Volume 515, Issue 3,  
p. 3383-3405 (2022)*

The abundance of clusters of galaxies is highly sensitive to the late-time evolution of the matter distribution, since clusters form at the highest density peaks. However, the 3D cluster mass cannot be inferred without deprojecting the observations, introducing model-dependent biases and uncertainties due to the mismatch between the assumed and the true cluster density profile and the neglected matter along the sightline. Since projected aperture masses *can* be measured directly in simulations and observationally through weak lensing, we argue that they are better suited for cluster cosmology. Using the Mira–Titan suite of gravity-only simulations, we show that aperture masses correlate strongly with 3D halo masses, albeit with large intrinsic scatter due to the varying matter distribution along the sightline. Nonetheless, aperture masses can be measured  $\approx 2 - 3$  times more precisely from observations, since they do not require assumptions about the density profile and are only affected by the shape noise in the weak lensing measurements. We emulate the cosmology dependence of the aperture mass function directly with a Gaussian process. Comparing the cosmology sensitivity of the aperture mass function and the 3D halo mass function for a fixed survey solid angle and redshift interval, we find the aperture mass sensitivity is higher for  $\Omega_m$  and  $w_a$ , similar for  $\sigma_8$ ,  $n_s$ , and  $w_0$ , and slightly lower for  $h$ . With a carefully calibrated aperture mass function emulator, cluster cosmology analyses can use cluster aperture masses directly, reducing the sensitivity to model-dependent mass calibration biases and uncertainties.

## 4.1 Introduction

The next decade of cosmological galaxy surveys such as *Euclid*<sup>1</sup> and the Rubin Observatory Legacy Survey of Space and Time (LSST)<sup>2</sup> will elucidate the late-time evolution of the Universe by measuring the large-scale distribution of galaxies out to a redshift of  $z \approx 2$ . The sheer volume of these surveys will result in the detection of over a billion galaxies that can be used to trace the underlying dark matter distribution. The main focus of these surveys is on measuring the matter distribution through the clustering of galaxies and through the lensing-induced distortion of galaxy shapes due to the intervening large-scale structure, the cosmic shear.

Galaxy clusters, located at the most significant peaks of the density field, will be another particularly powerful probe. Due to the hierarchical growth of structure, the abundance of clusters as a function of mass and time depends sensitively on the amount of matter,  $\Omega_m$ , how clustered it is,  $\sigma_8$ , and also on the late-time expansion due to dark energy, quantified by its equation-of-state parameter  $w_0$  and its time derivative  $w_a$  (e.g. Haiman et al., 2001; Allen et al., 2011; Pratt et al., 2019). More than  $10^5$  galaxy clusters will be detected in the coming decade (e.g. Sartoris et al., 2016), transforming galaxy cluster cosmology into a cosmological probe limited only by our understanding of its systematic uncertainties (e.g. Köhlinger et al., 2015).

Observationally, clusters are identified as highly significant peaks in maps of some observed signal,  $\mathcal{O}$ , that traces the total mass distribution, such as the galaxy overdensity, the weak lensing shear, the X-ray emission, or the Sunyaev-Zel'dovich (SZ) effect signal. Next, after some quality cuts on the cluster candidates, we are left with a cluster catalogue for the surveyed volume. To derive cosmological constraints from this catalogue, we need a theoretical prediction for the cosmology-dependent cluster abundance, and a way to link the theoretical predictions to the observed clusters. In principle, any halo property that depends on cosmology can be used, but the halo mass,  $\mathcal{M}$ , is the most obvious candidate. This then requires knowledge of the dependence of the halo mass function,  $n(\mathcal{M}|\Omega)$ , on the cosmological parameters,  $\Omega$ , the mass–observable relation,  $P(\mathcal{O}|\mathcal{M})$ , and the cluster selection function,  $\mathcal{S}$ . Any systematic error in these quantities will degrade the cosmological constraints from cluster cosmology.

To calibrate the mass–observable relation, we need observational measurements of the halo mass,  $\mathcal{M}$ , for a subsample of the detected clusters. We will denote the halo mass inferred from observations as  $\mathcal{M}_{\text{obs}}$ . There are multiple ways in which halo masses can be defined, since haloes do not have clear boundaries. Weak lensing observations have become the de facto standard to calibrate cluster masses as they provide the only way to directly probe both baryonic and dark matter (for a review, see Hoekstra et al., 2013). Masses can be obtained from weak lensing observations either by fitting a density profile to the observed shear and inferring the mass within some radius, or by directly adding up the surface mass density—which can be obtained from the shear—within some aperture. Since we are only able to securely identify clusters above some threshold in the observed

<sup>1</sup><https://www.euclid-ec.org>

<sup>2</sup><https://www.lsst.org/>

signal,  $\mathcal{O}_{\text{lim}}$ , a correct calibration of the mass–observable relation also requires the abundance of clusters to be taken into account. After all, the number of haloes around the detection limit will depend not only on the uncertainty in the mass–observable relation, but also on the expected number of haloes at that given mass (see [Mantz, 2019](#) for a clear discussion of this effect).

A full cluster cosmology analysis then calibrates the cosmology- and redshift-dependent relations  $P(\mathcal{O}, z | \mathcal{M}_{\text{obs}}, \Omega, \mathcal{S})$  and  $P(\mathcal{M}_{\text{obs}}, z | \mathcal{M}, \Omega, \mathcal{S})$ , by fitting them jointly with the theoretical halo abundance,  $n(\mathcal{M}, z | \Omega, \mathcal{S})$ , to the observed cluster number counts within bins  $\mathcal{O}_i$  and  $z_j$ ,  $N(\mathcal{O}_i, z_j)$ . The halo abundance possibly depends on the selection function for quality cuts based on the halo environment, for example to exclude chance alignments or mergers. We write out the forward model as

$$N(\mathcal{O}_i, z_j | \Omega, \mathcal{S}) = \Omega_{\text{sky}} \int_{\mathcal{O}_i}^{\mathcal{O}_{i+1}} d\mathcal{O} \int_{z_j}^{z_{j+1}} dz \frac{dV(z, \Omega)}{d\Omega dz} \int d\mathcal{M} d\mathcal{M}_{\text{obs}} \\ \times P(\mathcal{O}, z | \mathcal{M}_{\text{obs}}, \Omega, \mathcal{S}) P(\mathcal{M}_{\text{obs}}, z | \mathcal{M}, \Omega, \mathcal{S}) \\ \times n(\mathcal{M}, z | \Omega, \mathcal{S}), \quad (4.1)$$

where  $\mathcal{O}$  and  $z$  are integrated over their respective bins, and  $\mathcal{M}_{\text{obs}}$  and  $\mathcal{M}$  over all possible values. We convert the halo number density to the number counts taking into account the cosmology-dependent comoving volume at redshift  $z$ ,  $V(z, \Omega)$ , probed by a survey covering a solid angle  $\Omega_{\text{sky}}$ . Correctly modelling the cluster selection is of vital importance in any attempt to derive cosmological constraints from galaxy clusters. Ideally, we would detect clusters through an observable that has a straightforward selection function. Since the selection function depends on the survey under consideration, we will assume here that the selection has been modelled correctly. This simplifies the derivation of the main points we want to make.

Currently, cluster analyses infer 3D halo masses from weak lensing observations to determine the mass–observable relation (see e.g. [Bocquet et al., 2020](#); [DES Collaboration et al., 2020](#)). The appeal of 3D halo masses stems from analytic arguments such as the (extended) Press-Schechter theory ([Press & Schechter, 1974](#); [Bond et al., 1991](#)), that predict that the 3D halo mass function has a universal shape set only by the significance of the seed perturbation of a halo in the initial Gaussian density field. In recent years, however, ever larger suites of cosmological dark matter-only (DMO) simulations have shown that the assumed *universality* of the 3D halo mass function does not hold in detail. Simulated abundances can deviate from the universal prediction by > 10 per cent depending on the redshift and the exact cosmology (see e.g. [Tinker et al., 2008](#); [Bhattacharya et al., 2011](#); [Despali et al., 2016](#); [Diemer, 2020](#)). Hence, suites of large-volume cosmological simulations run on a grid of different cosmological parameter values are vital to capture the cosmology dependence of the halo mass function through either analytic fitting functions ([Tinker et al., 2008](#); [Bhattacharya et al., 2011](#)) or emulators ([McClintock et al., 2019](#); [Nishimichi et al., 2019](#); [Bocquet et al., 2020](#)).

Problemsatically, 3D halo masses cannot be measured directly from observations, which first need to be deprojected. Generically, deprojection requires the assumption of a spherically symmetric density profile, which will be affected by baryons and scatter

introduced by halo triaxiality, substructures, and correlated structures (see e.g. Becker & Kravtsov, 2011; Oguri & Hamana, 2011; Bahé et al., 2012; Henson et al., 2017; Debackere et al., 2021). This introduces model-dependent biases and increases the uncertainty in the inferred 3D halo masses, degrading the cosmological constraints from cluster cosmology. Note that this step is only required to transform the observations to theory predictions. As we argue in this paper, such a procedure is not necessary.

Since modern theoretical predictions for the halo abundance already rely on large simulation suites, it is possible to perform the cluster mass calibrations with halo properties that *can* be measured directly in both observations and simulations. This has the additional advantage that dark matter-only simulations can optionally be replaced by hydro-dynamical simulations in order to account for baryonic effects on the halo mass function (e.g. Velliscig et al., 2014) or to directly predict a baryonic observable. We focus on weak lensing observations because they probe the total matter content and are thus less sensitive to uncertainties in how baryonic matter traces the dark matter. From the weak lensing shear signal we can directly measure projected aperture masses within apertures of a fixed angular or physical size, without the need to assume any density profile (see e.g. Schneider, 1996; Bartelmann & Schneider, 2001). Importantly, these aperture masses can also be measured directly in simulations.

Aperture masses have been studied before in the context of cluster cosmology with purely shear-selected samples in order to bypass uncertainties due to the selection based on some baryonic observable such as the X-ray luminosity, the SZ signal or the galaxy overdensity citep[e.g.][]reblinsky1999a. Marian et al. (2010) argued that future surveys would no longer need to convert shear peaks to 3D halo masses, if predictions for the halo abundance as a function of their aperture mass were available. However, Hennawi & Spergel (2005) showed that while almost all massive clusters produce significant aperture mass peaks, there is a large population of significant peaks that cannot be ascribed to a single cluster but rather is the result of chance superpositions along the line-of-sight due to the broad lensing kernel. Hence, to decrease the number of false-positive cluster detections, baryonic observables are still required for confirmation. More recently, Hamana et al. (2015), Shan et al. (2018) and Martinet et al. (2018) have used peaks identified from weak lensing observations to constrain the matter density and clustering of the Universe.

With the availability of large-volume simulation suites run for many different cosmological models, it is now possible to calibrate the cosmology dependence of the halo aperture mass function. Importantly, with aperture mass measurements the theoretical model assumptions separate cleanly from the purely observational data in Eq. (4.1). That is, Eq. (4.1) splits into an observational scaling relation,  $P(\mathcal{O}, z | \mathcal{M}_{\text{obs}}, \Omega, \mathcal{S})$ , independent of the cluster density profile, and a calibration between the observed and the simulated aperture mass measurement,  $P(\mathcal{M}_{\text{obs}}, z | \mathcal{M}, \Omega, \mathcal{S})$ . The uncertainty in the observational scaling relation will depend on how accurately  $\mathcal{O}$  can be measured in the survey, and how strongly it correlates with the aperture mass. The theoretical calibration, on the other hand, will have a fixed uncertainty set by the shape noise of the observations, since the aperture mass measured from the weak lensing shear is an unbiased measure of the true aperture mass (Schneider, 1996). Moreover, as shown by Debackere et al. (2021), halo aperture masses are expected to be less sensitive to baryonic effects, especially when measured within larger apertures that are able to capture more of the ejected halo baryons. We

study how baryons modify aperture mass measurements in [Debackere et al. \(2022\)](#).

Here, we investigate the behaviour of the different components that enter the model for the cluster number counts in Eq. (4.1), that is, the uncertainty in the mass–observable relation and the halo mass function for halo aperture masses. We will show that the mass–observable relation can be calibrated more precisely with aperture masses than with the standard deprojected 3D halo masses. Additionally, we will use an emulator calibrated on the Mira–Titan suite of large-volume cosmological N-body simulations to show that the halo aperture mass function is also highly sensitive to variations in the cosmological parameters, in agreement with [Marian et al. \(2010\)](#). This study serves as a proof-of-concept that can be applied in future cosmological analyses when carefully calibrated emulators for the halo aperture mass function are available.

The paper is structured as follows: first, we introduce the large-volume simulation suite that we use for our analysis in Section 4.2. Then, in Section 4.3, we study the dependence of the aperture mass on both the 3D halo mass and the aperture size, and use the clean separation between the theoretical and observational uncertainties in aperture mass measurements to study the behaviour of the mass–observable relation. In Section 4.4, we build an emulator to investigate the sensitivity of the aperture mass function to changes in the cosmological parameters, comparing it to the 3D halo mass function. We compare our analysis with the wider literature, discuss advantages and possible difficulties, and provide future applications in Section 4.5. Finally, we conclude in Section 4.6.

## 4.2 Simulations

We use the Mira–Titan suite of cosmological, gravity-only simulations, run with the HACC N-body code (Hardware/Hybrid Accelerated Cosmology Code, [Habib et al. 2016](#)). This simulation suite is well-suited to our purpose: it contains large-volume simulations with cosmological parameters sampled using a nested space-filling design that is ideal for interpolating the simulation predictions. The simulations include dynamical dark energy and massive neutrinos. The publically available data products of the simulation suite are described in more detail in [Heitmann et al. \(2019\)](#). So far, Mira–Titan has been used to construct emulators for the matter power spectrum ([Heitmann et al., 2016](#); [Lawrence et al., 2017](#)) and the 3D halo mass function ([Bocquet et al., 2020](#)).

The simulation suite consists of a grid of 111 simulations that vary 8 different cosmological parameters. The cosmological parameters are chosen according to a nested lattice design that enforces space-filling properties at multiple design steps (see Section 3 of [Heitmann et al., 2016](#)). This design works well with Gaussian process emulators and has an important global convergence property that allows systematic improvement of emulation accuracy as more design points are added. All cosmologies are spatially flat with  $\Omega_k = 0$ . The models vary the cosmological parameters within the ranges shown in Table 4.1. The full grid of cosmological parameters is shown in figure 1 of [Bocquet et al. \(2020\)](#).

The Mira–Titan suite consists of 3 nested tessellations that refine the higher level grids (M011–M036, M037–M065, and M066–M111, respectively). These models all include massive neutrinos. To enable accurate predictions for the Standard Model of cosmology

Table 4.1: Cosmological parameter values for the Mira–Titan suite of large-volume, cosmological N-body simulations.

Parameter	Min	Max
$\Omega_m h^2$	0.12	0.155
$\Omega_b h^2$	0.0215	0.235
$\Omega_\nu h^2$	0.0	0.01
$\sigma_8$	0.7	0.9
$h$	0.55	0.85
$n_s$	0.85	1.05
$w_0$	-1.3	-0.7
$w_b \equiv (-w_0 - w_a)^{1/4}$ †	0.3	1.3
$w_a$	-1.56	1.29

† [Heitmann et al. \(2016\)](#) show that this rescaling improves the prediction accuracy of cosmological models with  $w_0 + w_a \approx 0$  by putting slightly more points near the  $w_0 + w_a = 0$  boundary.

with massless neutrinos, the simulation suite includes an additional 10 simulations with  $m_\nu = 0$  with the remaining 7 cosmological parameters sampled on a symmetric Latin hypercube (M001–M010). All simulations have box sizes of 2.1 Gpc (except for M006, M023, and M046 with 2.091, 2.085, and 1.865 Gpc, respectively) and include  $3200^3$  particles with masses  $m_{\text{dm}} = 7.23 \times 10^9 - 1.22 \times 10^{10} M_\odot$  depending on the cosmology. Hence, groups and clusters with  $m > 10^{13} M_\odot$  are generally resolved with  $> 1000$  particles. All simulations use a force softening length of  $\epsilon = 6.6$  kpc. For our analysis, we focus on the 100 simulations with massive neutrinos (M011–M110, for the distribution of the cosmological parameters, see fig. 1 of [Bocquet et al. 2020](#)).

We now briefly describe how dynamical dark energy and massive neutrinos are included in the simulations, referring to [Upadhye et al. \(2014\)](#) and [Heitmann et al. \(2016\)](#) for the full details. Both massive neutrinos and dynamical dark energy are included at the level of the background evolution,  $H(z)$ , and the initial conditions. Particularly, the linear  $z = 0$  transfer function includes dark matter, baryons, and massive neutrinos and is normalized to the correct  $\sigma_8$ . Then, the matter component including dark matter and baryons is evolved back to the initial redshift assuming a scale-independent growth factor including all species in the homogeneous background and used to determine the initial particle positions and velocities. This ensures that the  $z = 0$  linear power spectrum of the simulation is correct on large scales. For power spectrum calculations, the neutrino contribution needs to be included by hand. Hence, the simulations do not account for neutrino clustering, which is no cause for concern, since this effect is much smaller than the suppression of the halo mass function due to neutrino free-streaming for the neutrino mass range considered.

The saved simulation data products had to be chosen carefully due to the large volume of the simulations and the size of the cosmological parameter hypercube. For each simulation output, the full particle data is downsampled by a factor 100 before saving. Simulation haloes are identified on the fly, i.e. from the full particle data, using a friends-of-friends (FoF) algorithm with linking length  $b = 0.168$ . Subsequently, spherical overdensity masses, defined as  $m_{\Delta c}(z) = 4/3\pi\Delta\rho_{\text{crit}}(z)r_{\Delta c}^3(z)$ , with overdensity  $\Delta = 200$

are determined around the potential minimum of the FoF halo. For all haloes with  $> 1000$  particles (corresponding to  $m_{\text{FoF}} \gtrsim 10^{13} M_\odot$ ), all the particles belonging to the FoF halo are also saved separately. We will use the downsampled particle catalogues to compute the projected aperture masses around the identified FoF haloes with spherical overdensity masses  $m_{200c} > m_{200c,\text{lim}} = 10^{13.5} M_\odot$ . In Fig. 4.2 and Section 4.3.1, we show that the Poisson noise due to the downsampling introduces an uncertainty of  $> 15$  per cent in the measured aperture masses of haloes with  $m_{200c} < 10^{14} M_\odot$ . Hence, we will mainly focus on haloes with  $m_{200c} > 10^{14} M_\odot$  in the rest of this paper.

## 4.3 Aperture mass–observable relation

To quantify the uncertainties in the aperture mass–observable relation, we first need to measure the halo aperture masses. In Section 4.3.1, we describe how we extract the halo aperture masses from the Mira–Titan suite. We show how halo aperture masses depend on the 3D halo mass and the aperture size in Section 4.3.2. Finally, we investigate the possible theoretical and observational uncertainties in the aperture mass–observable relation and compare our results to 3D halo masses in Section 4.3.3.

### 4.3.1 Extraction from the simulations

We will use the term aperture mass, in accordance with the literature, to refer to the projected mass difference

$$\begin{aligned}\Delta M(< R_1 | R_2, R_m) &= \pi R_1^2 (\bar{\Sigma}(\leq R_1) - \bar{\Sigma}(R_2 < R \leq R_m)) \\ &= M(\leq R_1) - M_{\text{bg}}(\leq R_1),\end{aligned}\quad (4.2)$$

where we have introduced the mean enclosed surface mass density,  $\bar{\Sigma}$ , which is defined as

$$\bar{\Sigma}(R_2 < R \leq R_m) = \frac{2}{R_m^2 - R_2^2} \int_{R_2 < R < R_m} dR R \Sigma(R). \quad (4.3)$$

The second term in Eq. (4.2) corrects the mass within the aperture  $R_1$  for the average surface mass density within the control annulus bounded by  $R_2$  and  $R_m$ , which acts as a local background subtraction,  $M_{\text{bg}}$ . Both terms get the same contribution from the mean cosmological background density along the line-of-sight, which cancels out in the difference. The background subtraction makes the aperture mass independent of the line-of-sight integration length, provided it is large compared with the clustering length (as also noted by Marian et al., 2010). We verify this below.

The power of the aperture mass defined in Eq. (4.2) is that it can be obtained directly from weak lensing observations, as shown in Eq. (4.26) in Appendix 4.A. Moreover, choosing fixed physical or angular aperture sizes removes the need to assume a cluster density profile, in contrast to spherical overdensity radii. We will measure aperture masses within three different but fixed apertures of  $R_1 = [0.5, 1.0, 1.5] \text{ cMpc}$ , with  $R_2 = 2.0 \text{ cMpc}$  and  $R_m = 3.0 \text{ cMpc}$ . These apertures are similar to the typical aperture sizes used in weak lensing cluster mass calibrations (e.g. Hoekstra et al., 2015; Applegate et al., 2014). Moreover, they also roughly correspond to the halo radii for haloes

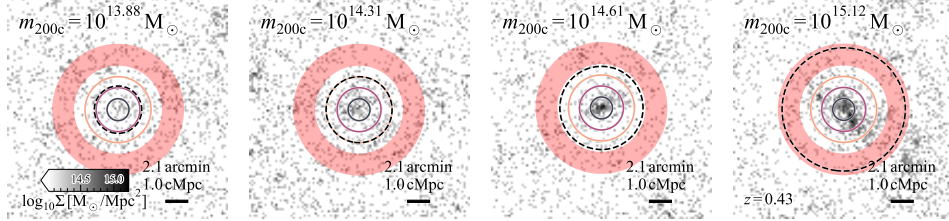


Figure 4.1: Surface mass density maps for randomly selected haloes in mass bins  $\log_{10} m_{200c}/M_\odot \in [13.5, 14.0, 14.5, 15, 15.5]$  for simulation M000 at  $z = 0.43$ . Each cutout has size  $10 \text{ cMpc} \times 10 \text{ cMpc}$  and is plotted on the same colour scale. The dashed circles indicate the spherical overdensity radius  $r_{200c}$  for each halo. With the coloured lines, we show the inner apertures  $R_1 = [0.5, 1.0, 1.5] \text{ cMpc}$  which we use throughout this work. The red shaded region shows the outer control annulus between  $R_2 = 2.0 \text{ cMpc}$  and  $R_m = 3.0 \text{ cMpc}$  for the background subtraction.

with  $m_{200c} > 10^{13} M_\odot$ . Smaller apertures will give better signal-to-noise ratios (SNRs) for lower-mass haloes since they are better matched to their sizes (Schneider, 1996). To compare these results with aperture masses inferred from observations, the distances in the simulations need to be converted into angular positions,  $\theta$ , using the angular diameter distance to the lens for the simulated cosmology.

## 4

Since the aperture mass from weak lensing observations is inferred from the shear signal within the annulus between  $R_1$  and  $R_m$ , the optimal choice of the aperture sizes balances the increased signal from decreasing  $R_1$  and increasing  $R_m$ , respectively, against the increased modelling uncertainty due to contamination from cluster member galaxies and miscentring errors, and the contribution of cosmic noise in the cluster outskirts (e.g. Mandelbaum et al., 2010). We stress that the aperture mass in Eq. (4.2) will be computed directly from the simulation data without any assumptions about the weak lensing observations. Any observational uncertainty in converting the weak lensing signal to the surface mass density will thus be included in the  $P(\Delta M_{\text{obs}}|\Delta M, z)$  term in Eq. (4.1), leaving the aperture mass function unaffected. We discuss such observational uncertainties in Section 4.3.3. In practice, the observed weak lensing aperture mass includes the contribution of mass along the line-of-sight, weighted by the lensing kernel. However, as we will show in Fig. 4.3, the total aperture mass is dominated by the correlated structure within  $\approx 30 \text{ cMpc}$  of the cluster, which justifies neglecting the lensing kernel weighting in our analysis.

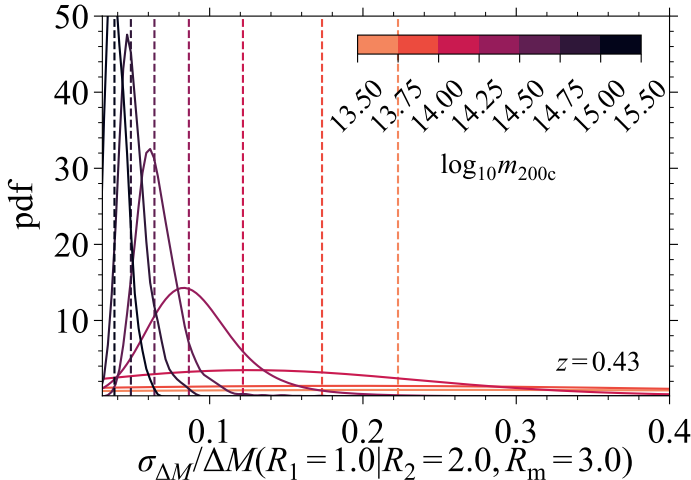
Given the downsampled particle catalogue, calculating halo aperture masses is relatively straightforward. First, we correct the particle catalogues for the downsampling (see Section 4.2) by increasing the particle masses by a factor 100. We investigate the effect of this downsampling on the accuracy of the derived halo masses below. We generate projected maps of the surface mass density,  $\Sigma$ , along the three principal axes of the simulation volume on a grid of  $21000 \times 21000$  pixels, corresponding to a pixel size of  $(L/21000)^2 = (0.1 \text{ cMpc})^2$  (except for the simulations with smaller box sizes). Subsequently, we can directly obtain halo aperture masses from the surface mass density maps

by calculating Eq. (4.2) centred on the identified halo centres.

In Fig. 4.1, we show the surface mass density maps centred on 4 random haloes within mass bins with bin edges specified by  $\log_{10} m_{200c}/M_\odot \in [13.5, 14.0, 14.5, 15.0, 15.5]$  for reference simulation M000 at  $z = 0.43$ . Clearly, the downsampling of the particle catalogue results in emptier and noisier mass maps. Every particle in the simulation has a  $p = 0.01$  chance of being included in the downsampled particle catalogue. As a result, particle catalogues of downsampled haloes will include a shot-noise contribution of  $pN$ , resulting in a fractional uncertainty on the final 3D halo mass of  $\delta m/m = \sqrt{pN^{-1}}$ , which is  $\approx [20, 10, 6, 3, 2]$  per cent for haloes located at the mass bin edges. Since the spherical overdensity halo masses were saved on the fly, the downsampling does not affect the halo mass catalogues. The aperture masses, however, are affected by the particle downsampling. We show the distribution of the fractional aperture mass uncertainty due to the finite number of particles for different 3D halo mass bins in Fig. 4.2. We show the fractional uncertainty,  $\sigma_{\log \Delta M} = \sigma_{\Delta M}/\Delta M$ , for  $R_1 = 1.0$  cMpc, since this aperture size is similar to the virial radius for haloes with  $10^{13.5} < m_{200c}/M_\odot < 10^{14}$ . We calculate the uncertainty by adding the shot noise contributions to  $M(< R_1)$  and  $M_{\text{bg}}(< R_1)$  in quadrature. Even though the individual contributions to the aperture mass in Eq. (4.2) can be determined at high accuracy due to the extra particles included along the line-of-sight, their difference has a large fractional uncertainty. Hence, we will limit our halo sample to haloes with  $m_{200c} > 10^{14} M_\odot$  whose aperture masses can be determined with a median fractional uncertainty of  $\lesssim 15$  per cent from the available particle data. We note that even though the median uncertainty of the mass bin  $10^{14.0} < m_{200c}/M_\odot < 10^{14.25}$  is  $\lesssim 15$  per cent, there are also significant outliers.

It is important to verify that the background subtraction in the aperture mass definition, Eq. (4.2), actually makes the aperture mass independent of the line-of-sight integration depth. In Fig. 4.3, we show the calculated aperture masses as a function of the line-of-sight integration length,  $L$ , centred on 10000 random positions (first column) or on all haloes within different halo mass bins that have  $x$ -coordinates that are within  $\pm 5$  cMpc of the midpoint of the  $x$ -axis of the simulation box (second to fourth columns) for simulation M000 at  $z = 0.43$ . When centring on random positions, the aperture masses are consistent with zero since the average surface mass densities within  $R_1$  and the control annulus are equal. The scatter in the aperture masses for randomly-positioned apertures, which is equivalent to measuring the cosmic shear on the scale of the aperture, increases with the line-of-sight integration depth, since larger modes contribute to the dispersion  $\langle \Delta M^2(< R_1, < L | R_2, R_m) \rangle$  (see e.g. Schneider et al., 1998). This effect is also present when centring on haloes, but since the cosmic shear introduces a fixed scatter, the effect is relatively smaller for more massive haloes (Hoekstra, 2001). For haloes, the average aperture mass generally converges to its final value within  $\approx 30$  cMpc. However, the individual halo trajectories along the line-of-sight can increase or decrease significantly when encountering massive structures within  $R_1$  or  $R_2 < R < R_m$ , respectively. Hence, we confirm that the aperture mass measurements are converged with respect to the line-of-sight integration length of  $L = 2100$  cMpc.

The aperture mass measurements in the simulations automatically include the intrinsic scatter due to halo triaxiality and substructure, and due to both correlated and uncorrelated large-scale structures. We do not include observational uncertainties since these



**4** Figure 4.2: Distribution of the uncertainty in the aperture mass, given in Eq. (4.2), for different 3D halo mass bins due to the factor of 100 downsampling of the saved simulation particle catalogues. We add the Poisson uncertainties of the downsampled number of simulation particles within  $R < R_1 = 1.0 \text{ cMpc}$  and  $R_2 \leq R < R_m$  in quadrature for all haloes with  $m_{200c} > 10^{13.5} \text{ M}_\odot$  in M000 at  $z = 0.43$ . Different coloured lines correspond to different 3D halo mass bins and the dashed lines indicate the median uncertainty. The downsampling results in a significant uncertainty in the derived aperture masses for haloes with  $m_{200c} < 10^{14.25} \text{ M}_\odot$ .

will depend on the survey of interest. One source of observational systematic uncertainty is the shear map generation, which relies on the accuracy of the shape measurements of the background source galaxies and the determination of their redshift distribution (e.g. [Von der Linden et al., 2014](#); [Hoekstra et al., 2015](#)). Another source of uncertainty is the centring of the aperture on the halo. In the simulations, we centre the surface mass density maps exactly on the potential minimum of the spherical overdensity, but observationally this centre cannot be identified so unambiguously. However, [Hoekstra et al. \(2012\)](#) showed that deprojected mass estimates derived from aperture mass measurements within large apertures corresponding to overdensity radii with  $\Delta < 1000$ , are only affected by  $\lesssim 5$  per cent for miscentring radii up to  $0.5 h_{70}^{-1} \text{ cMpc}$ . For reference, the distribution of the offset,  $\Delta R$ , between the SZ signal peak and the location of the brightest cluster galaxy position shows that the bulk of clusters ( $\approx 95$  per cent) are well centred with  $\sigma_{\Delta R} \lesssim 0.2 R_{500c}$ , which is smaller than  $0.5 h_{70}^{-1} \text{ cMpc}$  for all clusters with  $m_{500c} \lesssim 5 \times 10^{15} \text{ M}_\odot$ , while the remaining clusters show a larger dispersion  $\sigma_{\Delta R} \approx 0.7 R_{500c}$  (see e.g. [Saro et al., 2015](#); [Bleem et al., 2020](#)). In the same vein as the results of [Hoekstra et al. \(2012\)](#), aperture masses measured within apertures considerably larger than the miscentring radius of the cluster should not be significantly affected by miscentring. Hence, ignoring miscentring does not change the conclusions of our work. Next, we will show the dependence of halo aperture masses on the 3D halo mass and the

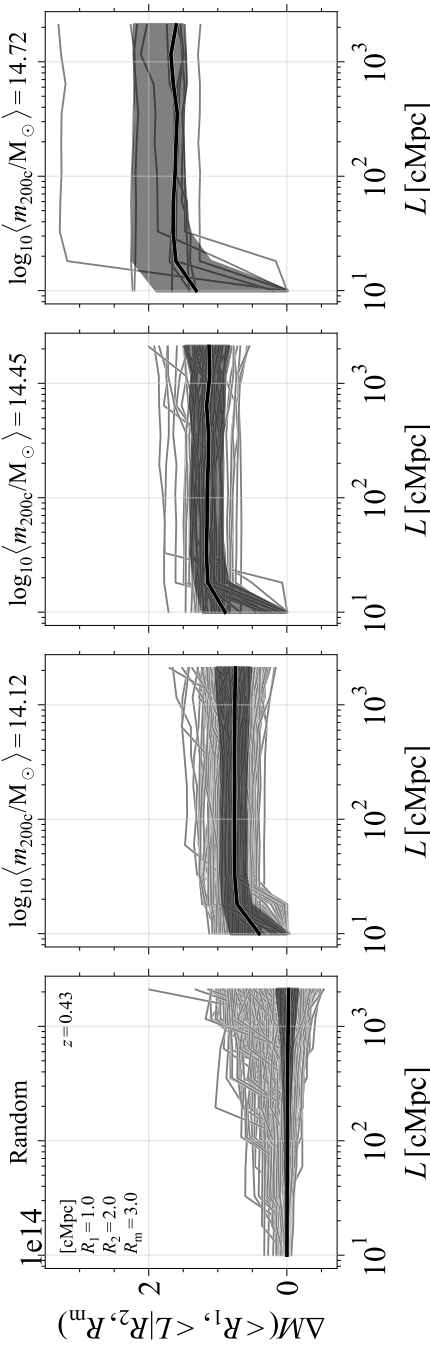


Figure 4.3: Convergence of the aperture mass,  $\Delta M$ , with the line-of-sight depth,  $L$ , centred on random positions (*first column*), and haloes within increasing  $m_{200c}$  bins (*second to fourth columns*). Light grey lines indicate the individual positions/haloes, which were chosen to have  $x$ -coordinates within  $\pm 5$  cMpc of the centre of the  $x$ -axis along which we project. The median and 16th to 84th percentile scatter are indicated with thick black lines and the shaded region, respectively. The median aperture mass along random lines-of-sight is zero, as expected, with a slight increase in the scatter for larger line-of-sight integration lengths. Lines-of-sight centred on haloes generally converge within  $\approx 30$  cMpc along the line-of-sight, with a large scatter that increases slightly with increasing  $L$ . The aperture mass for individual haloes can increase or decrease significantly when encountering a massive structure along the line-of-sight within  $R_1$  or  $R_2 < R < R_m$ , respectively.

aperture.

### 4.3.2 Aperture mass behaviour

Since halo properties are mostly studied as a function of their 3D mass, we show the distribution of aperture masses for  $R_1 = 1.0 \text{ cMpc}$ ,  $R_2 = 2 \text{ cMpc}$ , and  $R_m = 3 \text{ cMpc}$  as a function of the 3D halo mass,  $m_{200c}$ , at  $z = 0.43$  in the M011 simulation in the top panel of Fig. 4.4. The median  $\Delta M - m_{200c}$  relation, indicated with the solid line, is slightly shallower than one-to-one: the aperture mass for haloes with  $r_{200c} \gtrsim (\lesssim) R_1$  is smaller (larger) than  $m_{200c}$  since the halo mass represents a larger (smaller) fraction of the total aperture mass. For simulation M011, the halo radius  $r_{200c} = R_1 = 1.0 \text{ cMpc}$  for  $m_{200c} \approx 10^{13.65} \text{ M}_\odot$ . Haloes at fixed  $m_{200c}$  can have greatly differing aperture masses due to differences in the matter distribution along the line-of-sight of haloes at fixed 3D mass (see also Fig. 4.3). For low-mass haloes the scatter around the median relation increases significantly since mass outside the halo contributes relatively more to the mass within the aperture.

In the bottom panel of Fig. 4.4, we show the logarithmic scatter around the median  $\Delta M - m_{200c}$  relation. We calculate the scatter as half the difference between the 84th and the 16th percentile of  $\log \Delta M$ . The scatter increases strongly for low-mass haloes, partially due to the particle downsampling of the halo catalogues shown in Fig. 4.2, but also since matter outside the halo contributes more to the aperture mass. The intrinsic scatter in the aperture mass at fixed halo mass decreases from  $\sigma_{\log \Delta M} \approx 0.45$  for  $m_{200c} = 10^{14} \text{ M}_\odot$  to  $\lesssim 0.2$  for  $m_{200c} > 10^{14.5} \text{ M}_\odot$ , which is similar to the scatter in the weak lensing-inferred 3D halo mass at fixed halo mass due to triaxiality and substructure (see Fig. 4.7 and Section 4.3.3 for a comparison with the mock weak lensing analysis from Bahé et al. 2012). The scatter at high halo masses is dominated by differences in the projected structure along the line-of-sight to the halo, both correlated and uncorrelated, since the downsampling has a negligible effect on high-mass haloes.

Since different apertures are naturally tuned to detect haloes of different mass and size, we show the median relation between the aperture mass,  $\Delta M$ , measured in different apertures and the 3D halo mass,  $m_{200c}$ , for all cosmologies in the hypercube in the left panel of Fig. 4.5. Smaller apertures more closely capture the 3D mass of lower-mass haloes, however, as is clear from Fig. 4.4, there is a large scatter around the median relation due to the differing matter distributions along the line-of-sight to different haloes. For higher-mass haloes, measuring the mass in different apertures allows the characterization of the halo density profile, since the matter belonging to the halo dominates the total aperture mass out to larger apertures.

In the right-hand panel of Fig. 4.5, we show the redshift evolution of the aperture mass within a fixed aperture of  $R_1 = 1 \text{ cMpc}$ . Since we measure within fixed comoving apertures, the uncorrelated large-scale structure contribution to both  $M(< R_1)$  and  $M_{\text{bg}}(< R_1)$  should be the same on average. Hence, the redshift evolution is dominated by the local overdensity changes around the halo. At fixed  $m_{200c}$ , the virial radius  $r_{200c}$  will increase less rapidly with increasing time than the aperture radius does as the critical density—and also  $r_{200c}(z)$ —approaches a constant in the dark energy-dominated era. As a result, the aperture mass increases with time, since more matter outside of the halo is

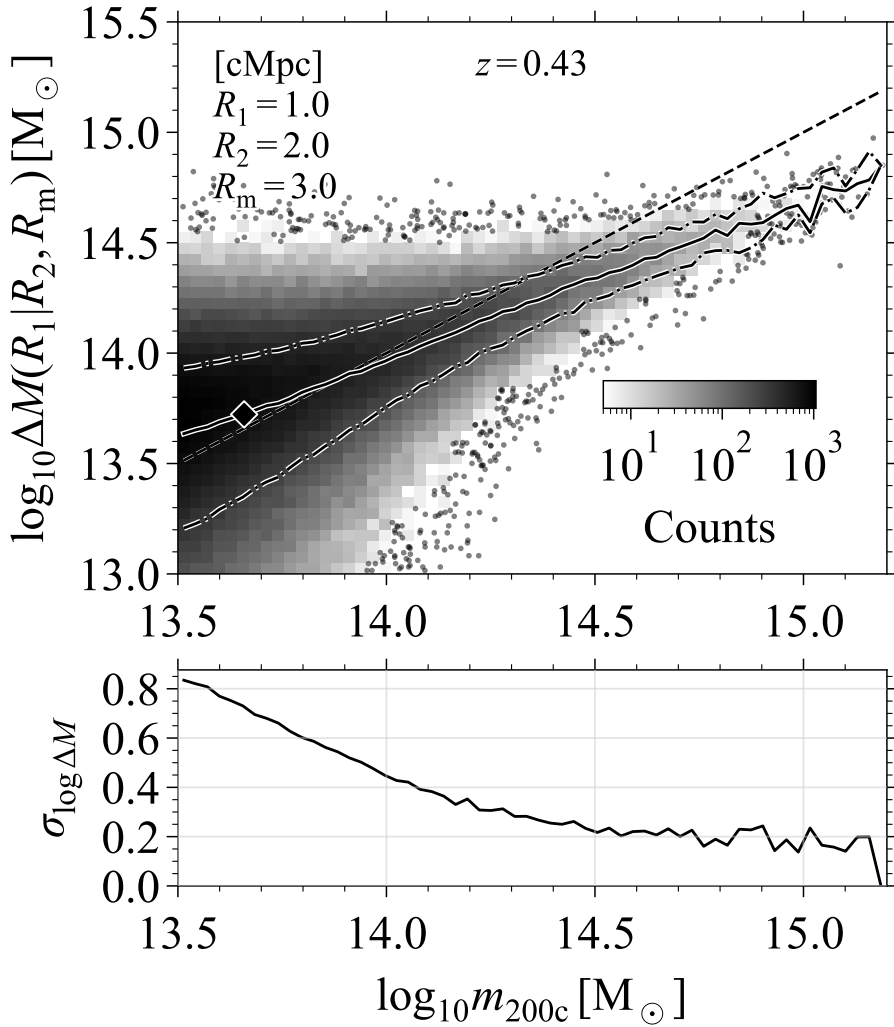
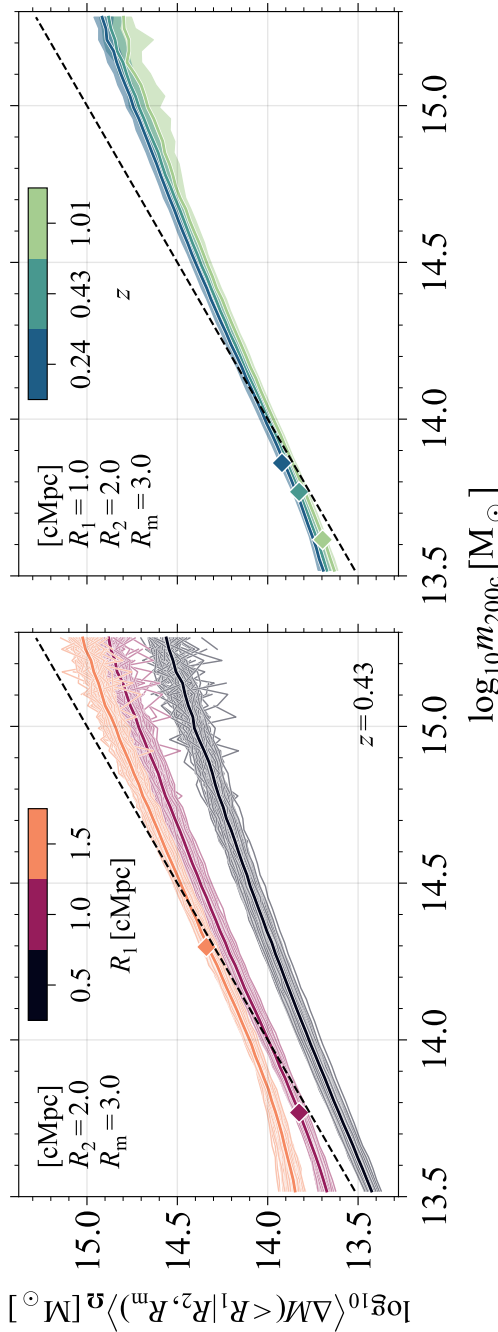


Figure 4.4: *Top panel:* The distribution of aperture masses,  $\Delta M(< R_1 = 1.0 \text{ cMpc} | R_2 = 2.0 \text{ cMpc}, R_m = 3.0 \text{ cMpc})$ , as a function of the 3D spherical overdensity mass  $m_{200c}$  for simulation M011 at  $z = 0.43$ . The dashed line indicates the one-to-one relation, the solid line indicates the median relation, and the dash-dotted lines the 16th and 84th percentile scatter. The diamond indicates the 3D halo mass for which  $r_{200c} = R_1$ . The large scatter in  $\Delta M$  at fixed  $m_{200c}$  is caused by the large variation in the matter distribution along the line-of-sight. *Bottom panel:* The logarithmic scatter in the aperture mass distribution at fixed  $m_{200c}$ , calculated as half the difference between the 84th and the 16th percentiles. The scatter decreases from  $\sigma_{\log \Delta M} \approx 0.45$  at  $m_{200c} = 10^{14} \text{ M}_\odot$  to  $\lesssim 0.2$  for  $m_{200c} > 10^{14.5} \text{ M}_\odot$ .



**Figure 4.5:** *Left panel:* The relation between the median projected aperture masses of all cosmologies in the hypercube,  $\langle \Delta M(< R_1 | R_2, R_m) \rangle_\Omega$ , within different apertures  $R_1$  (thick coloured lines) and the 3D spherical overdensity mass  $m_{200c}$ . The thin, transparent lines show the results for individual simulations. The black, dashed line indicates the one-to-one relation. The coloured diamonds show the halo mass for which  $r_{200c} = R_1$ . The reference annulus for all aperture mass measurements spans the region between  $R_2 = 2$  cMpc and  $R_m = 3$  cMpc. Masses measured within larger apertures more closely match the 3D masses of more massive haloes. *Right panel:* The redshift evolution of the relation between the median aperture mass of all cosmologies and  $m_{200c}$ . At fixed  $m_{200c}$ , the ratio of the virial radius,  $r_{200c}$  and the comoving aperture radius decreases with time due to increasing contribution of dark energy to the critical density. The extra contribution of the halo outskirts within the fixed comoving aperture increases the measured aperture masses with time.

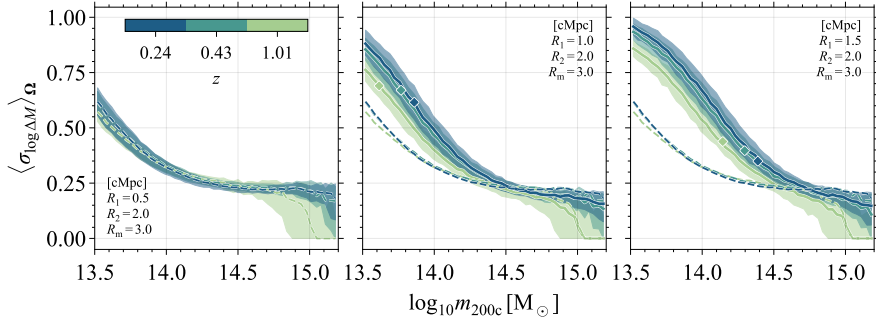


Figure 4.6: The median redshift evolution of the scatter in the  $\Delta M - m_{200c}$  distribution measured in apertures  $R_1 \in [0.5, 1.0, 1.5]$  cMpc for all simulations (*left to right columns*). Coloured lines and shaded regions indicate the median and the 16th to 84th percentile scatter for all cosmologies at different redshifts. The  $R_1 = 0.5$  cMpc distribution is indicated with dashed lines and repeated in the other panels. The coloured diamonds show the median halo mass for which  $r_{200c} = R_1$  (these masses are smaller than  $10^{14} M_\odot$  for  $R_1 < 1.5$  cMpc). At fixed  $m_{200c}$  and  $R_1$ , the scatter increases significantly with time for haloes whose virial radius,  $r_{200c}$ , is not significantly larger than the aperture (low-mass haloes) or whose number density increases (high-mass haloes). Increasing  $R_1$  at fixed  $m_{200c}$  increases the scatter when the virial radius becomes comparable to the aperture due to the increased sensitivity to matter outside the halo.

included within the same comoving aperture at fixed halo mass. For angular apertures, there would be an additional change due to the changing angular diameter distance. For a halo mass defined with respect to the mean matter density, such as  $m_{200m}$ , the virial radius and the comoving aperture radius do not evolve with redshift at fixed halo mass and, hence, the redshift evolution would be set by the change in the halo density profile.

To study how the scatter in  $\Delta M$  at fixed  $m_{200c}$  changes with cosmology and redshift, we show the redshift evolution of the median scatter,  $\sigma_{\log \Delta M}$ , of all cosmologies in the Mira–Titan suite for the different apertures in the panels of Fig. 4.6. The shaded regions show the 16th to 84th percentile scatter. We indicate the median halo mass for which  $r_{200c} = R_1$  with a coloured diamond. The overall trends are the same as in the bottom panel of Fig. 4.4, i.e. less scatter for higher-mass haloes. Within the smallest aperture,  $R_1 = 0.5$  cMpc, there is very little redshift evolution: the aperture is significantly smaller than  $r_{200c}$  for all halo masses shown, and the halo matter dominates the aperture mass. For all apertures, the increase in the scatter with time for the most massive haloes results mainly from their increasing number density with time. For the most massive haloes, the scatter only changes by  $\approx \pm 5$  per cent for different aperture sizes, as can be seen by comparing the dashed lines (which are for  $R_1 = 0.5$  cMpc in every panel) with the results for larger apertures in the middle and rightmost panels of Fig. 4.6. For lower-mass haloes, however, the scatter is more sensitive to the aperture and increases when the halo radius becomes comparable to the aperture.

So far, we have shown that aperture masses can be measured easily in simulations and that they correlate strongly with the true, 3D halo mass, albeit with a large intrinsic scatter

due to their sensitivity to the matter along the line-of-sight to the halo. Paradoxically, this could give the aperture mass an advantage in the context of cluster cosmology since it means that the line-of-sight structure contributes to the aperture mass signal, not its noise. We will investigate the possible strengths and difficulties of aperture mass calibrations for cluster cosmology next.

### 4.3.3 Uncertainties

For cluster cosmology, it is crucial that cluster masses inferred from observations can be calibrated accurately, that is without bias and, ideally, also with small uncertainties. Due to the exponential sensitivity of the halo abundance to the halo mass, biases and uncertainties that are not accounted for in the cluster mass measurement can introduce catastrophic biases in the inferred cosmological parameters. Consequently, minimizing the uncertainty in the mass–observable relation can dramatically increase the constraining power of cluster surveys. Previously, we have shown that the intrinsic scatter between the aperture mass and the 3D halo mass can be large, particularly for low-mass haloes. We will now consider the strengths and the difficulties of aperture masses for cluster cosmology.

Taking Eq. (4.1) as our guide, we see that the uncertainty in the mass–observable relation is due to the uncertainty in the relation between the measured observable and the measured aperture mass,  $P(\mathcal{O}|\mathcal{M}_{\text{obs}})$ , and the observational uncertainty between the measured aperture mass and the true halo aperture mass,  $P(\mathcal{M}_{\text{obs}}|\mathcal{M})$ , sometimes referred to in the literature as the intrinsic uncertainty (e.g. Becker & Kravtsov, 2011). First, we will look into the intrinsic measurement uncertainty of the halo aperture mass, comparing it to that of 3D halo masses.

The stringent requirements on the accuracy of the shear measurements for future surveys mean that the finite number of background galaxies used to sample the shear field and the source redshift distribution set the baseline, minimum uncertainty for any weak lensing mass measurement (e.g. Köhlinger et al., 2015). The source redshift distribution determines the critical surface mass density that enables the conversion from measured weak lensing shear to surface mass density. This uncertainty will affect any weak lensing mass measurement similarly, so we do not include it here. The uncertainty of aperture mass measurements is then fully determined by the galaxy shape noise, as shown by Schneider (1996). In comparison, 3D halo masses inferred from deprojected weak lensing observations are intrinsically highly sensitive to the large variation in the line-of-sight matter distribution at fixed, true 3D halo mass.

To quantify the intrinsic measurement uncertainties for 3D halo masses of individual clusters, we look at the literature. Bahé et al. (2012) have estimated the uncertainty of the  $P(\mathcal{M}_{\text{obs}}|\mathcal{M})$  scaling relation by generating mock weak lensing observations of clusters with  $m_{200c} > 10^{14} \text{ M}_\odot$  at  $z \approx 0.2$ , a shape noise of  $\sigma_{\text{gal}} = 0.2$ , and with a mean lensed background galaxy number density  $\bar{n}_{\text{gal}} = 30 \text{ arcmin}^{-2}$  for sources at  $z = 1$ . This set-up assumes perfect knowledge of the source redshift distribution and the critical surface mass density. They find a large uncertainty of  $\sigma_{\log m_{\text{obs}}} = 0.45$  (0.25) for haloes with  $m_{200c} = 10^{14}$  ( $10^{15}$ )  $\text{M}_\odot$  when inferring  $m_{\text{obs}}$  from fitting NFW density profiles to the observed lensing shear. Importantly, Bahé et al. (2012) only include the local,

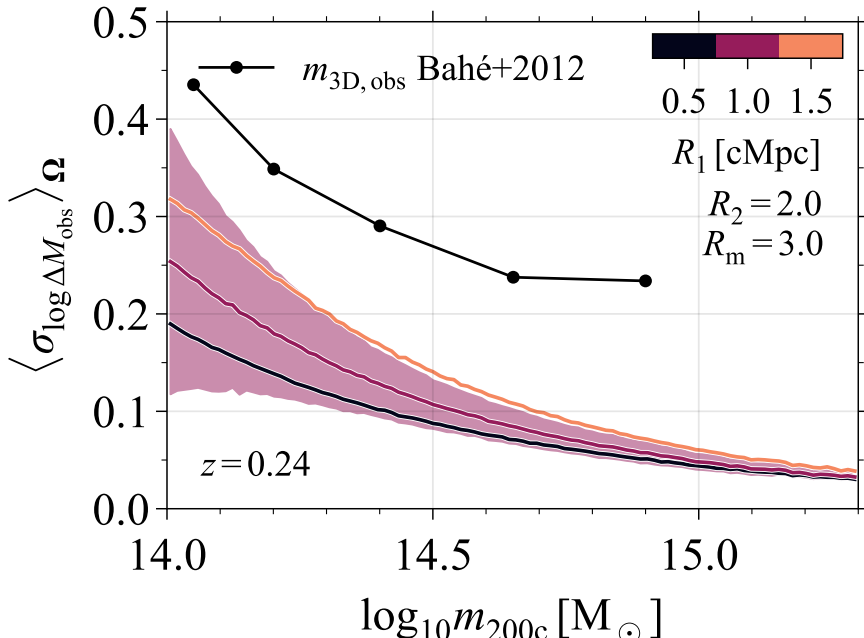
correlated large-scale structure within 10 cMpc of the halo when generating the lensing signal. However, uncorrelated large-scale structures add to the scatter of the true lensing signal (e.g. Hoekstra, 2001, 2003). Hence, their results should be considered a lower limit on the true scatter in the inferred 3D halo masses. Becker & Kravtsov (2011) similarly find an uncertainty of  $\sigma_{\log m_{\text{obs}}} \approx 0.3$  for a mock sample with  $m_{200c} > 10^{14.5} h^{-1} M_{\odot}$  that does include the cosmic noise due to uncorrelated large-scale structure.

On the other hand, for the same set-up as Bahé et al. (2012), weak lensing aperture masses are only affected by the shape noise due to the finite number of galaxies used to sample the shear field. More specifically, the uncertainty is given by Eq. (4.22) in Appendix 4.A. We derive a fixed uncertainty  $\sigma_{\Delta M_{\text{obs}}} = 1.16 \times 10^{13} M_{\odot}$  for  $R_1 = 0.5 \text{ cMpc}$ ,  $R_2 = 2 \text{ cMpc}$ , and  $R_m = 3 \text{ cMpc}$ . For reference, from Fig. 4.5 we see that  $\Delta M(m_{200c} = 10^{14} M_{\odot}, R_1 = 0.5 \text{ cMpc}) \approx 10^{13.75} M_{\odot}$ , implying a fractional uncertainty  $\sigma_{\log \Delta M_{\text{obs}}} \approx 0.2$ , i.e. more than 2 times smaller than the fractional uncertainty in the 3D mass and without any dependence on an assumed density profile. Importantly, the fractional uncertainty scales inversely with the halo aperture mass, giving fractional uncertainties of  $\approx 0.1$  and  $0.05$  for  $\Delta M/M_{\odot} = 10^{14}$  and  $10^{14.5}$ , respectively.

In Fig. 4.7, we show the aperture radius dependence of the median fractional observational uncertainty,  $\sigma_{\log \Delta M_{\text{obs}}}$ , at fixed halo mass,  $m_{200c}$ , calculated from Eq. (4.22), for a lensing cluster at  $z = 0.24$  and source galaxies at  $z = 1$  with background density  $n_{\text{gal}} = 30 \text{ arcmin}^{-2}$  and shape noise  $\sigma_{\text{gal}} = 0.2$ , similar to Bahé et al. (2012). The aperture mass uncertainty in Eq. (4.22) additionally depends on the chosen filter, that is the aperture radii  $R_1$ ,  $R_2$ , and  $R_m$ . To obtain the fractional uncertainty, we divide  $\sigma_{\Delta M_{\text{obs}}}$  from Eq. (4.22) by the aperture mass,  $\Delta M$ . For  $R_1 = 1 \text{ cMpc}$ , we indicate the median uncertainty in the aperture mass at fixed  $m_{200c}$  over all cosmologies (the solid line in the middle panel of Fig. 4.6) as the shaded region. For comparison, we show the observational uncertainty in 3D halo masses inferred from the mock weak lensing observations of Bahé et al. (2012). Over the entire halo mass range, the aperture mass can be determined at least 2 times more precisely than the 3D halo mass for apertures similar to the halo radius. Increasing the inner aperture radius,  $R_1$ , increases the observational uncertainty since the weak lensing signal is inferred from the smaller number of galaxies within  $R_1$  and  $R_m$ . Hence, aperture masses can be measured more cleanly from observations than 3D halo masses since the line-of-sight structure contributes to the signal as opposed to the noise.

The uncertainty in aperture mass calibrations for cluster surveys with baryonic observables, such as the galaxy overdensity, the SZ signal or the X-ray luminosity, will also depend on the relation between the observable,  $\mathcal{O}$ , and the measured aperture mass,  $\Delta M_{\text{obs}}$ . As mentioned before, this relation depends solely on observational properties of the clusters and the uncertainty will be highly sensitive to the observable  $\mathcal{O}$  under consideration.

A particularly ill-suited scenario for aperture masses would be an observable that is not sensitive to projection effects, such as the X-ray luminosity or the thermal energy of the hot gas,  $Y_X$ . These observables depend strongly on the gas density and predominantly trace the cluster core. Due to the tight correlation with small scatter between the X-ray luminosity and the 3D halo mass,  $m$ , the uncertainty in  $P(\mathcal{O}|\Delta M_{\text{obs}})$  can be approximated by  $P(m|\Delta M_{\text{obs}})$ . As can be seen from the spread in  $m_{200c}$  at fixed  $\Delta M$  in the top panel



**4** Figure 4.7: The median observational fractional uncertainty in the aperture mass at fixed halo mass within different apertures for a lensing cluster at  $z = 0.24$  and source galaxies at  $z = 1$  with a mean background density of  $\bar{n}_{\text{gal}} = 30 \text{ arcmin}^{-2}$  and shape noise  $\sigma_{\text{gal}} = 0.2$ . The thick, coloured lines indicate the median uncertainty over all cosmologies for  $m_{200c}$  and within different apertures. The shaded region shows the variation of the observational uncertainty for  $R_1 = 1 \text{ cMpc}$  due to the median scatter in  $\Delta M$  at fixed  $m_{200c}$  for all cosmologies, shown in Fig. 4.6. The black points show the scatter in the 3D masses inferred from mock weak lensing observations by Bahé et al. (2012). Smaller apertures have a lower observational uncertainty due to the larger number of background galaxies as the masses are measured within  $R_1 < R \leq R_m$ . Aperture masses can be determined more precisely than 3D masses over the full halo mass range.

of Fig. 4.4, this uncertainty is considerable. Such an observable is ideal for 3D halo mass calibrations. However, the uncertainty between the observable,  $\mathcal{O}$ , and the true halo mass,  $m$ , will still be limited by the uncertainty floor in  $P(m_{\text{obs}}|m)$ , set by the deprojection of the lensing profile.

In the best-case scenario for aperture masses, the observable closely traces the total projected mass with small uncertainty. Andreon & Congdon (2014) show that the richness is such an observable when measured within the same aperture as the weak lensing aperture mass. Other studies also find that the stellar mass fraction, when measured sufficiently far away from the brightest cluster galaxy, is approximately constant in groups and clusters (e.g. Bahcall & Kulier, 2014; Budzynski et al., 2014; Zu & Mandelbaum, 2015; Wang et al., 2018). For observables related to the stellar mass of clusters, aperture masses

provide mass calibrations with low uncertainty and without any model dependence which is ideal for cluster cosmology.

We would also expect the SZ signal to be sensitive to projection effects since it is independent of redshift, and since its pressure dependence allows it to probe larger scales. However, the steep scaling of the SZ signal with the 3D halo mass due to its scaling with the gas temperature and density, means that low-mass haloes will constitute an approximately constant background that can be corrected for (e.g. Angulo et al., 2012; Le Brun et al., 2015). Hence, the SZ signal is likely less sensitive to projection effects than the cluster stellar mass, but more sensitive than cluster X-ray properties.

A full comparison between the performance of aperture and 3D mass calibrations for different survey observables would require generating mock surveys and mimicking the aperture mass measurement and the 3D mass inference from mock weak lensing observations, which is beyond the scope of this work.

All in all, halo aperture masses provide clear advantages for cluster cosmology. The direct connection between aperture masses measured from simulations and observations make them practically independent from assumptions about the density profile of clusters. Moreover, the relation between the cluster observable of interest and the true cluster aperture mass cleanly separates in a purely observational scaling relation and an intrinsic measurement uncertainty between the observed and the true aperture mass, which can be calibrated using simulations. Next, we turn our attention to the final ingredient for cluster cosmology in Eq. (4.1): the aperture mass function.

## 4.4 Halo aperture mass function

Having introduced the aperture mass and compared it to the 3D halo mass, we now study the aperture mass function. We show how the aperture mass function depends on the aperture mass in Section 4.4.1. Then, we briefly explain how we fit a Gaussian process emulator to capture the cosmology dependence of the aperture mass function in Section 4.4.2, leaving the details of the implementation to Appendix 4.B and the verification to Appendix 4.C. Finally, we discuss the cosmology sensitivity of the aperture mass function in Section 4.4.3.

### 4.4.1 Aperture mass function behaviour

We compute the aperture mass function by dividing the number of haloes in mass bins of  $\log_{10} \Delta M$  by the simulated volume and the bin width. The number density,  $n$ , dependent on the cosmological parameters,  $\Omega_i$ , can be defined either as a function of the comoving volume,  $V$ ,

$$n_V(\Delta M, z, \Omega_i) = \frac{dN(\Delta M, z, \Omega_i)}{dV(z, \Omega_i) d\log_{10} \Delta M} \quad (4.4)$$

or as a function of the probed survey volume

$$n_\Omega(\Delta M, z, \Omega_i) = \frac{dN(\Delta M, z, \Omega_i)}{d\Omega(z, \Omega_i) dz d\log_{10} \Delta M}. \quad (4.5)$$

We have introduced the cosmology-dependent differential solid angle,  $d\Omega$ , and the redshift range,  $dz$ . For cosmological simulations,  $n_V$  naturally matches the data since we can divide the mass-binned number counts directly by the comoving simulation volume. The growth of structure from the initial density field fixes the cosmology dependence of the volumetric number density,  $n_V$ . The cosmology dependence of the *observed* halo number density, however, receives an additional geometric contribution since we observe our past lightcone. We obtain the observed number density from the volumetric number density as

$$n_\Omega(\Delta M, z, \Omega_i) = n_V(\Delta M, z, \Omega_i) \frac{dV(z, \Omega_i)}{d\Omega dz}, \quad (4.6)$$

where the geometric conversion depends on the comoving distance and the transverse comoving distance at redshift  $z$  for the assumed cosmology. The conversion scales the amplitude of the volumetric aperture mass in a cosmology and redshift-dependent way. The same geometric factor also applies to the simulated 3D halo mass function.

Since the weak lensing aperture mass receives contributions from structure along the past lightcone weighted by the lensing kernel, technically, the scatter in the aperture mass at fixed halo mass adds a geometry sensitivity to the volumetric aperture mass function. However, as we have shown in Fig. 4.3, for higher-mass haloes this scatter becomes less important compared to the intrinsic scatter due to the differing matter distribution close ( $L \lesssim 30$  cMpc) to the cluster. Hence, neglecting the past lightcone should not significantly change our conclusions.

In what follows, we will initially show results for  $n_V$  as is generally done for the 3D halo mass function in the literature to aid in the interpretation of our results. However, only  $n_\Omega$  includes the full cosmology dependence of both the aperture mass function and the 3D halo mass function. We will use  $n_\Omega$  to investigate the cosmology sensitivity of the aperture mass function in Section 4.4.3.

In the left-hand panel of Fig. 4.8, we show the median aperture mass function,  $n_V$ , and its 16th to 84th percentile scatter for all cosmologies in the parameter hypercube and aperture masses measured within different apertures. All aperture masses have been computed with the same control annulus between  $R_2 = 2$  cMpc and  $R_m = 3$  cMpc, and only haloes with  $m_{200c} > m_{200c,\text{lim}} = 10^{13.5} M_\odot$  are included within the sample. Since larger apertures will result in higher aperture masses for the same halo, increasing the aperture size shifts the aperture mass function to higher aperture masses. The aperture mass function decreases towards both high and low aperture masses. The former is caused by the rarity of high-mass haloes and the latter by the halo mass selection of the sample and the large scatter in aperture mass at fixed halo mass. When a significant fraction of the haloes at fixed aperture mass has 3D masses near the selection limit, the number density starts decreasing. We show this by highlighting the 84th percentile aperture mass for haloes with 3D masses at the selection limit with a cross. These crosses coincide almost perfectly with the peak in the aperture mass function. The right-hand panel of Fig. 4.8 shows that the aperture mass function increases with redshift as more massive haloes form, just like the traditional halo mass function does. The peak of the aperture mass function shifts towards higher aperture masses with time due to the increased scatter at the fixed 3D halo mass limit (see Fig. 4.6).

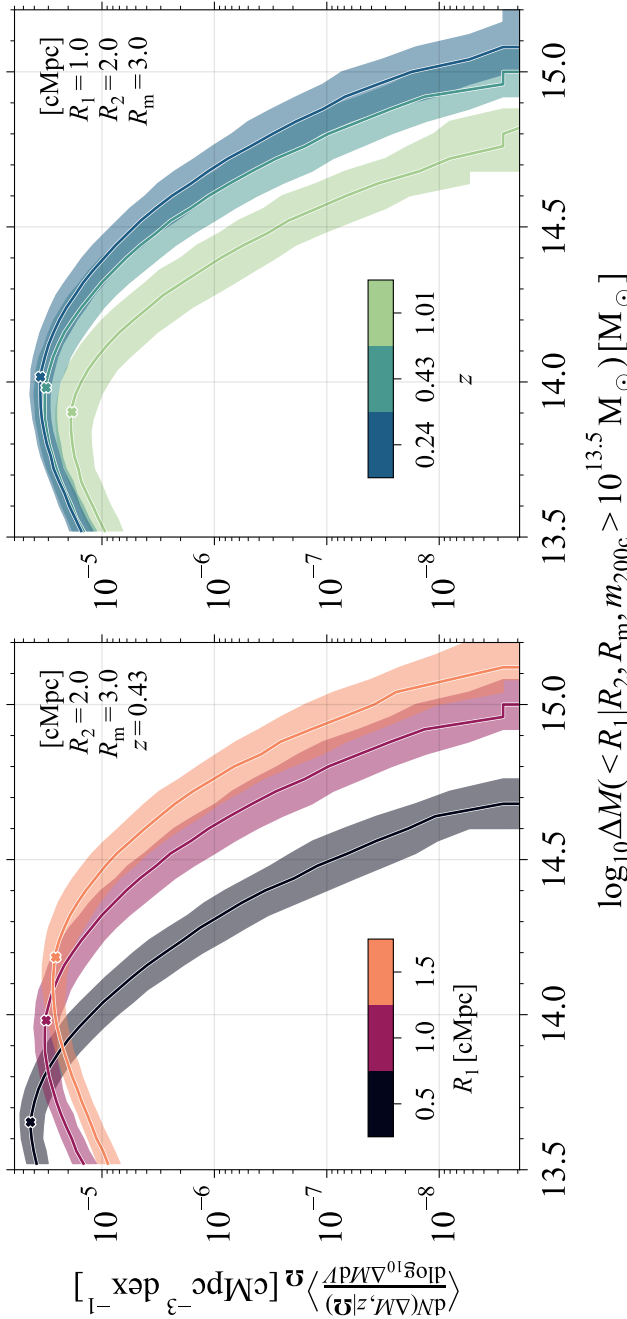


Figure 4.8: *Left panel:* The median aperture mass function, for a fixed comoving volume,  $n_V$ , of all cosmologies in the hypercube for aperture masses measured within different apertures  $R_1$  (thick coloured lines) at  $z = 0.43$  for all haloes with  $m_{200c} > 10^{13.5} M_\odot$ . The shaded regions show the 16th to 84th percentile scatter. The reference annulus for all aperture mass measurements spans the region between  $R_2 = 2$  cMpc and  $R_m = 3$  cMpc. Larger apertures result in higher aperture masses and shift the aperture mass function to the right. The number density decreases for low aperture masses if a significant fraction of the haloes has 3D masses near the selection limit, indicated by the crosses that show the 84th percentile aperture mass for haloes with  $m_{200c,\text{lim}} = 10^{13.5} M_\odot$ . *Right panel:* The redshift evolution of the median aperture mass function with  $R_1 = 1$  cMpc. The number density increases with time as haloes grow more massive. The peak of the aperture mass function shifts to larger values with time due to the increased scatter at the fixed 3D halo mass limit.

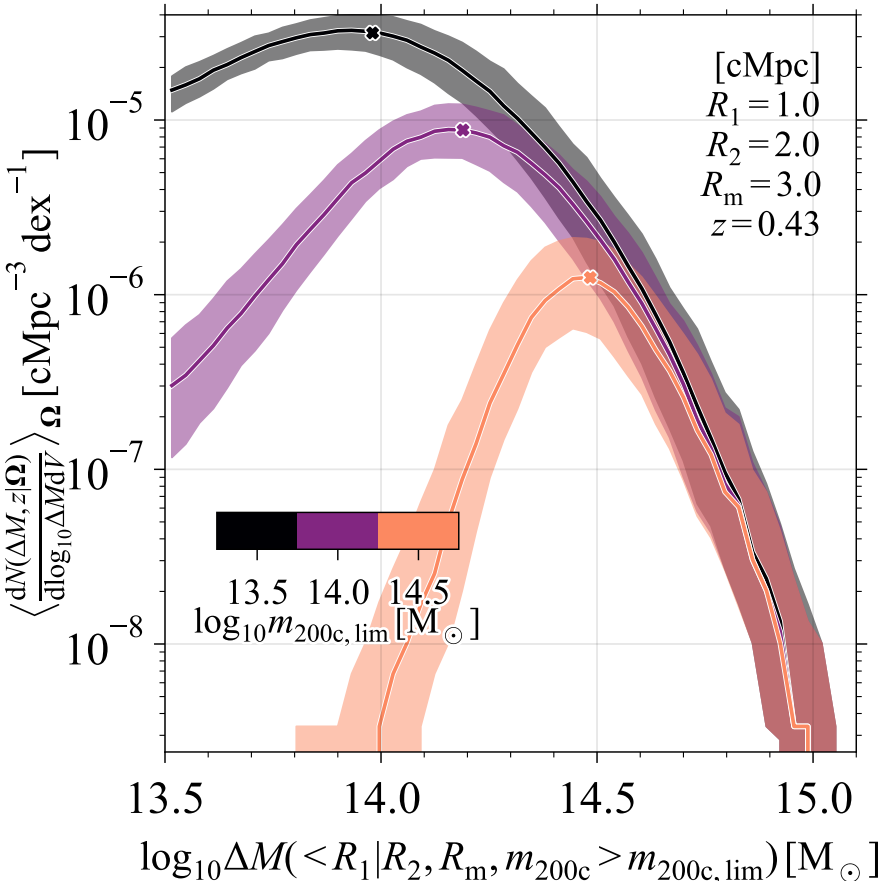


Figure 4.9: The change in the median aperture mass function for a fixed comoving volume,  $n_V$ , for all cosmologies at fixed aperture size when increasing the mass selection limit,  $m_{200c,\text{lim}}$ . The thick, coloured lines show the different mass limits,  $m_{200c,\text{lim}}$ . The crosses indicate the 84th percentile aperture mass for haloes with  $m_{200c} = m_{200c,\text{lim}}$ . The scatter in the aperture mass for haloes at the mass limit sets the peak of the aperture mass function.

In Fig. 4.9, we show how the aperture mass function changes when increasing the 3D mass limit,  $m_{200c,\text{lim}}/\text{M}_\odot$ , from  $10^{13.5}$  to  $10^{14.5}$ . The number density for the largest aperture mass haloes is not strongly affected since the scatter in the aperture mass at the mass limit decreases with increasing mass limit. For all mass limits, the cross indicates the 84th percentile aperture mass for haloes with 3D masses at the selection limit. Since the  $\Delta M - m_{200c}$  relation is sublinear, the median aperture mass at  $m_{200c,\text{lim}}$ , and, therefore, also the peak mass increase less strongly than the 3D halo mass when increasing  $m_{200c,\text{lim}}$ . The number density for aperture masses beyond the peak is still affected by

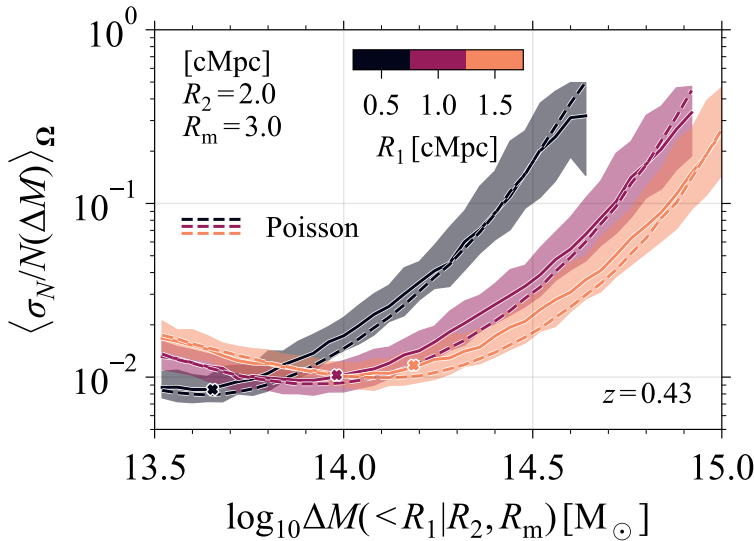


Figure 4.10: The median fractional variance in the aperture mass function for different apertures for all cosmologies at  $z = 0.43$  (solid, coloured lines). All haloes are selected to have  $m_{200c} > 10^{13.5} M_\odot$ . The reference annulus for all aperture mass measurements spans the region between  $R_2 = 2$  cMpc and  $R_m = 3$  cMpc. The shaded regions show the 16th to 84th percentile scatter and the dashed lines show the median shot-noise expectation. The crosses indicate the peak of the aperture mass function. The aperture mass function variance generally exceeds the shot-noise.

the mass limit, albeit less so. Hence, for aperture mass cosmological analyses, it will be important to select clusters using observables that either have small scatter with respect to the aperture mass, or whose scatter is well-understood.

We stress that the haloes in Fig. 4.9 are selected solely based on their 3D halo mass. However, low-mass haloes that scatter to much higher aperture masses than the median relation for their halo mass, are either part of the correlated structure or chance alignments with a massive cluster. In realistic observational scenarios, such haloes would not be part of the cluster sample, as they would blend in with the larger cluster. However, this also requires such haloes to be excluded from the theoretical aperture mass function calculation. The same problem applies to the 3D mass function; end-to-end pipelines are needed to model such effects.

Finally, we investigate the sample variance of the aperture mass function, which we will need to accurately calibrate the emulator. Since large-scale modes can locally and coherently boost or suppress the number counts, the variance of the aperture mass function needs to be estimated by resampling the data over sufficiently large volumes that include the inherent correlation structure. Crocce et al. (2010) and Smith & Marian (2011) have shown that the 3D halo mass function variance is dominated by Poisson noise at high halo masses, and that a jackknife-type resampling can recover the true variance accurately. For this reason, we use bootstrap resampling to divide the projected mass maps

into  $(n, n)$  subregions. We then compute the aperture mass function variance for 10,000 halo samples generated by including  $n^2 = 25$  randomly chosen, possibly repeating, sub-areas. This way, we can estimate the sample variance of the aperture mass function for cluster samples obtained from an equal simulation volume.

We show the bootstrapped fractional aperture mass variance in Fig. 4.10. We also include the Poisson expectation based on the number of haloes at fixed aperture mass. We find that the sample variance of the aperture mass function exceeds the Poisson expectation by up to a factor of  $\approx 1.5$ , except for the lowest- and highest-aperture mass haloes. We will use the bootstrapped variance estimates for the individual simulations when fitting the aperture mass function emulator in the following Section.

#### 4.4.2 Emulating the aperture mass function

We construct an emulator to infer the general cosmology dependence of the aperture mass function from the available grid of cosmological parameters. Usually, emulators fit some compressed form of the true underlying data, such as the cosmology dependence of either the parameters of a theoretical fitting function (e.g. McClintock et al., 2019) or the weights of the principal components of either the data or some functional approximation (e.g. Bocquet et al., 2020). However, all these methods assume that those compressed models accurately capture the underlying halo mass function behaviour for all masses. While this assumption can be checked as long as haloes are abundant, it might not hold in the exponentially declining tail which contains important cosmological information, potentially resulting in confident but inaccurate predictions.

We therefore fit a Gaussian process *directly* to the simulated data at each redshift independently, only assuming Gaussian correlations in the latent function and a discrete likelihood for the *observed* number counts. Previously, fitting a Gaussian process directly to large datasets with non-Gaussian likelihoods was not feasible: there was no well-understood and unified way to both account for general, non-Gaussian likelihoods, and deal with the computationally intensive inversion of the covariance matrix in the model optimization. However, since the work of Titsias (2009) and Hensman et al. (2014), this is no longer an issue. We gain a subtle but important advantage by modelling the number counts directly with a Gaussian process: the high-mass tail of cosmological models with no observed clusters can be fit consistently with the correct likelihood and without assuming any functional form for the aperture mass function.

We provide a detailed description of our emulator implementation and the performance in Appendices 4.B and 4.C, respectively, but detail the main insights here. Briefly, we will fit the normalized aperture mass function

$$f(\mathbf{x}_i = (\Delta M, \boldsymbol{\Omega}_i)^T) = \log n(\Delta M, \boldsymbol{\Omega}_i) - \log \langle n(\Delta M, \boldsymbol{\Omega}_i) \rangle_{\Omega}, \quad (4.7)$$

to reduce the dynamic range and the impact of the peak in the aperture mass function on the emulator calibration. We have checked that training the emulator on  $n_V$  and  $n_{\Omega}$ , defined in Eqs. (4.4) and (4.5), respectively, gives consistent performance. Then, we

assume a Gaussian process prior for the mean and the variance of  $f$

$$\mathbb{E}[f(\mathbf{x}_i)] = \mu \quad (4.8)$$

$$\text{Var}[f(\mathbf{x}_i), f(\mathbf{x}_j)] = k(\mathbf{x}_i, \mathbf{x}_j), \quad (4.9)$$

where  $k(\mathbf{x}_i, \mathbf{x}_j)$  is the covariance function between inputs  $\mathbf{x}_i$  and  $\mathbf{x}_j$ . We will be using the radial basis function (or squared exponential) kernel for  $k$ :

$$k(\mathbf{x}, \mathbf{x}') = \sigma^2 \prod_{i=0}^d \exp\left(-\frac{((\mathbf{x})_i - (\mathbf{x}')_i)^2}{2\ell_i^2}\right), \quad (4.10)$$

where  $i$  runs over the  $d = 9$  dimensions of  $\mathbf{x}$  and each dimension has its own covariance lengthscale  $\ell_i$ , resulting in hyperparameters  $\theta = (\mu, \sigma^2, \ell)$ . The hyperparameters,  $\theta$ , can be optimized to accurately capture the cosmology dependence of the aperture mass function, assuming the likelihood of the simulated number counts,  $(\mathbf{x}_i, N_i)$ , given the model,  $f(\mathbf{x}_i)$ .

We leave the details of optimizing this Gaussian process to Appendix 4.B, but the scalable, variational inference method developed by [Titsias \(2009\)](#) and [Hensman et al. \(2014\)](#) allows us to fit directly to the large, simulated dataset, assuming a discrete likelihood that naturally matches the simulated number counts, meaning that we do not need to assume any functional form for the aperture mass function.

We find that the Gaussian process emulator is able to predict most of the simulated aperture mass functions to within  $\pm 2$  per cent in the high-abundance regime and to within the shot-noise for high-aperture masses (see Fig. 4.15 in Appendix 4.C). The emulator also generalizes well in a leave-one-out-test as it is generally able to predict most simulations within  $\pm 5$  per cent when not including them in the emulator calibration (see Fig. 4.16 in Appendix 4.C).

At this point, we are satisfied with the emulator performance in capturing the underlying cosmology dependence of the aperture mass function. However, we want to reiterate that our goal has not been to calibrate the emulator to the level of accuracy required for future surveys. Such an emulator needs to be calibrated specifically to the survey specifications such as the chosen angular aperture size, the probed redshift range, the selection function of the observable, and needs to compute the aperture masses from the full past lightcone. We require the emulator only to be able to investigate how varying individual cosmological parameters affects the aperture mass function.

#### 4.4.3 Cosmology dependence of the aperture mass function

We can use the calibrated emulator to investigate the cosmological sensitivity of the aperture mass function. Previously, [Marian et al. \(2009, 2010\)](#) showed that the aperture mass function for a filter that optimizes the cluster SNR, closely follows the cosmology dependence of the 3D mass function, suggesting a similar cosmology sensitivity. However, their chosen filter required assuming a typical density profile for clusters, which we have been careful to avoid.

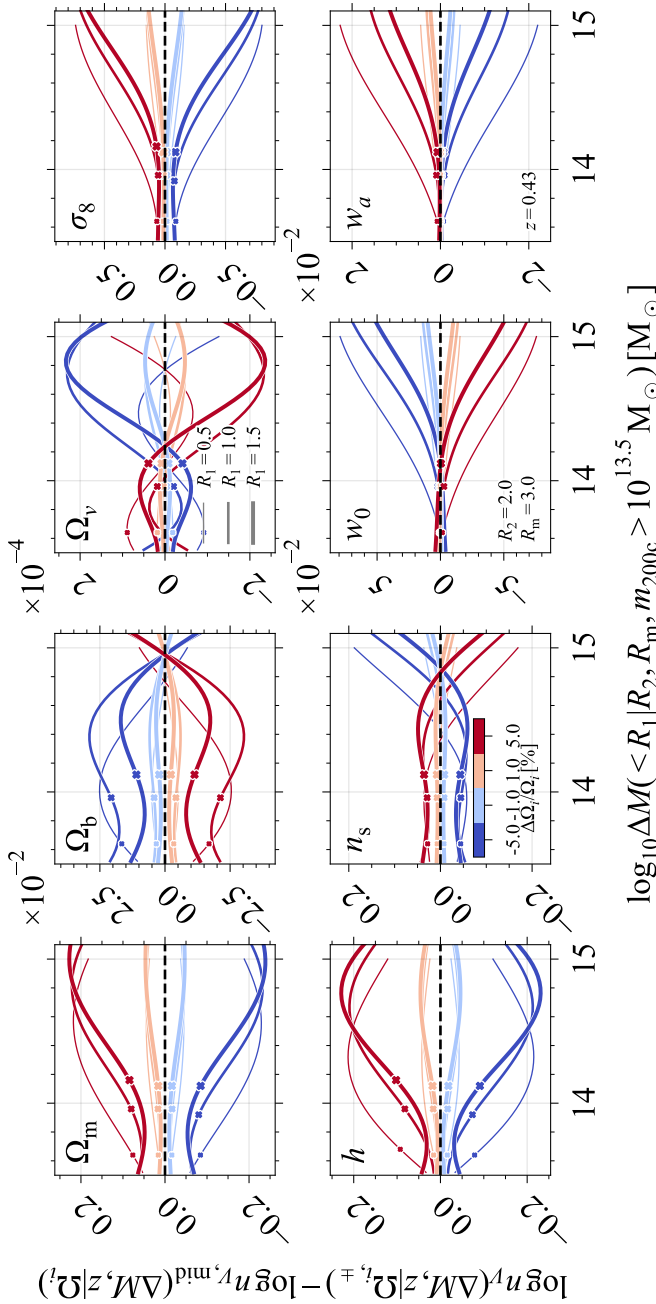


Figure 4.11: The sensitivity of the aperture mass function for a fixed comoving volume,  $n_V$ , to changing individual cosmological parameter values by  $\pm 1, 5$  per cent at  $z = 0.43$ . The cosmological parameter being varied is indicated in the top-left corner of each panel (note the different  $y$ -axis scaling for the different parameters). We assume  $w_a = \pm 0.01, \pm 0.05$  since the fiducial value is 0. Coloured lines indicate the fractional change in the individual cosmological parameters with respect to the fiducial **Planck20** cosmology, with the line thickness varying from thin to thick for  $R_1 = 0.5, 1.0, 1.5$  Mpc. All aperture masses were measured with  $(R_2, R_m) = (2, 3)$  cMpc and all haloes have  $m_{200c} > 10^{13.5} M_\odot$ . The peak of the aperture mass function is indicated with a cross. Increasing the aperture size mainly shifts the aperture mass function to higher masses. The amplitude also changes noticeably for different aperture sizes when varying  $\Omega_b$  and  $\Omega_\nu$ . The aperture mass function is most sensitive to changes in  $\sigma_8$ ,  $\Omega_m$ , and  $h$ , with additional sensitivities to the scalar spectral index of the initial power spectrum,  $n_s$ , and the dark energy equation-of-state parameters  $w_0$  and  $w_a$ .

Fig. 4.11 shows the sensitivity of the volumetric aperture mass function to changes in individual cosmological parameters (different panels) and the aperture (different line thickness) at fixed redshift. We reiterate that the full cosmology dependence of the *observed* aperture mass function also depends on the geometry through the volume of the past lightcone, as Eq. (4.6) shows. We adopt a fiducial Planck Collaboration et al. (2020, hereafter Planck20) cosmology with

$$\begin{aligned}\boldsymbol{\Omega} &\equiv \{\Omega_m, \Omega_b, \Omega_\nu, \sigma_8, h, n_s, w_0, w_a\} \\ &= \{0.315, 0.049, 0.0014, 0.811, 0.674, 0.965, -1, 0\},\end{aligned}\quad (4.11)$$

with  $\Omega_\nu$  corresponding to  $M_\nu = 0.06$  eV, and separately vary each of the cosmological parameters by  $\pm 1$  and 5 per cent (different colours). For  $w_a$ , we assume fixed values  $\pm 0.01$  and  $\pm 0.05$ , since the fiducial value is 0. In agreement with the 3D halo mass function, to which we explicitly compare in Fig. 4.13, the shape of the aperture mass function at fixed redshift is most sensitive to changes in  $\sigma_8$  and  $\Omega_m$ , with a  $\pm 1$  per cent change in  $\sigma_8$  ( $\Omega_m$ ) resulting in  $> 10$  per cent (up to 5 per cent) changes in the aperture mass function. Besides  $\Omega_m$  and  $\sigma_8$ , the aperture mass function is also sensitive to both the dimensionless Hubble parameter,  $h$ , and the scalar spectral index of the linear power spectrum,  $n_s$ . The equation-of-state parameters,  $w_0$  and  $w_a$ , mainly affect the abundance of high-aperture mass haloes. Increasing the aperture size shifts the aperture mass function to larger aperture masses. However, apart from this approximate shift for different aperture sizes, the amplitude of the aperture mass function also changes noticeably for  $\Omega_b$  and  $\Omega_\nu$ .

In Fig. 4.12, we show the cosmology sensitivity of the aperture mass function for masses measured within  $R_1 = 1$  cMpc at different redshifts. At all redshifts, the aperture mass function is most sensitive to changes in  $\sigma_8$ ,  $\Omega_m$ , and  $h$ . For most cosmological parameter changes, the abundance changes more strongly at higher redshifts. Noticeably, the dark energy equation-of-state parameters affect the halo abundance more significantly at higher redshifts. The peak of the aperture mass function, which is indicated with a cross, shifts to higher aperture masses with decreasing redshift.

The dominant cosmology dependence of the aperture mass function can be understood from the 3D halo mass function, since

$$n(\Delta M, z | \boldsymbol{\Omega}) = \int_0^\infty dm_{200c} n(m_{200c}, z | \boldsymbol{\Omega}) P(\Delta M, z | m_{200c}, \boldsymbol{\Omega}). \quad (4.12)$$

The large scatter in aperture mass at fixed 3D halo mass does cause differences in the detailed mass dependence. In Fig. 4.13, we compare the cosmology sensitivity of the 3D halo mass function (dash-dotted lines) and aperture mass function (solid lines) for the median aperture mass at  $m_{200c}$  for all cosmologies in the hypercube,  $\langle \Delta M | m_{200c} \rangle_\Omega$ . The individual cosmological parameters vary by  $\pm 5$  per cent around the Planck20 best-fit parameters (coloured lines in the different panels). For the 3D halo mass function, the peak height of haloes determines their abundance, with more significant peaks being less abundant. Increasing  $\sigma_8$  while fixing the remaining cosmological parameters boosts the average variance on all scales equally, which decreases the peak height at all halo masses and results in an increased abundance, as can be seen in the top-right panel of Fig. 4.13.

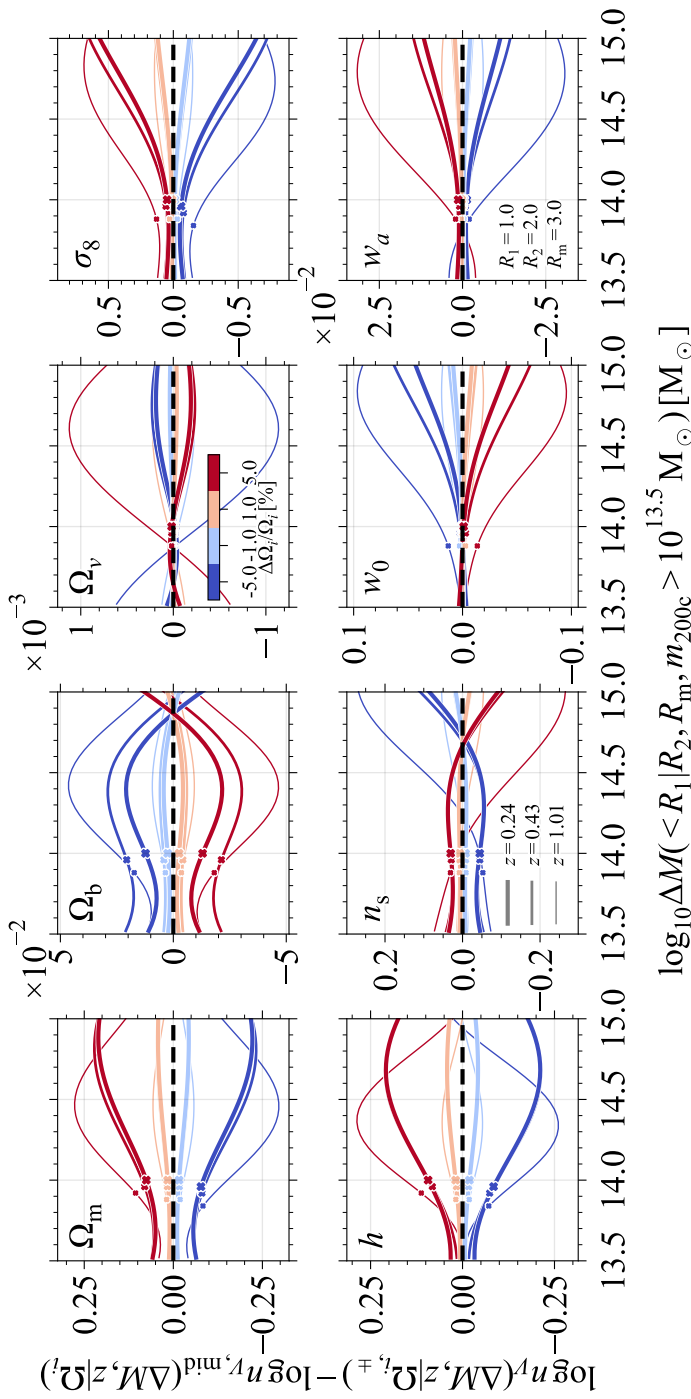


Figure 4.12: The sensitivity of the aperture mass function for a fixed comoving volume,  $n_V$ , to changing individual cosmological parameter values by  $\pm 1.5$  per cent for  $R_1 = 1 \text{ cMpc}$  and different redshifts. We assume  $w_a = \pm 0.01, \pm 0.05$  since the fiducial value is 0. The cosmological parameter being varied is indicated in the top-left corner of each panel. Coloured lines indicate the fractional change in the individual cosmological parameters with respect to the fiducial **Planck20** cosmology, with the line thickness varying from thick to thin for the redshifts  $z = 0.24, 0.43, 1.01$ . All aperture masses were measured with  $(R_1, R_2, R_m) = (1, 2, 3) \text{ cMpc}$ , and all haloes have  $m_{200c} > 10^{13.5} M_\odot$ . The peak of the aperture mass functions is indicated with a cross. The peak of the mass function shifts to higher masses for lower redshifts. The aperture mass function is most sensitive to changes in  $\sigma_8$ ,  $\Omega_m$ , and  $h$ . The relative impact of changing the cosmological parameters on the abundance increases with redshift.

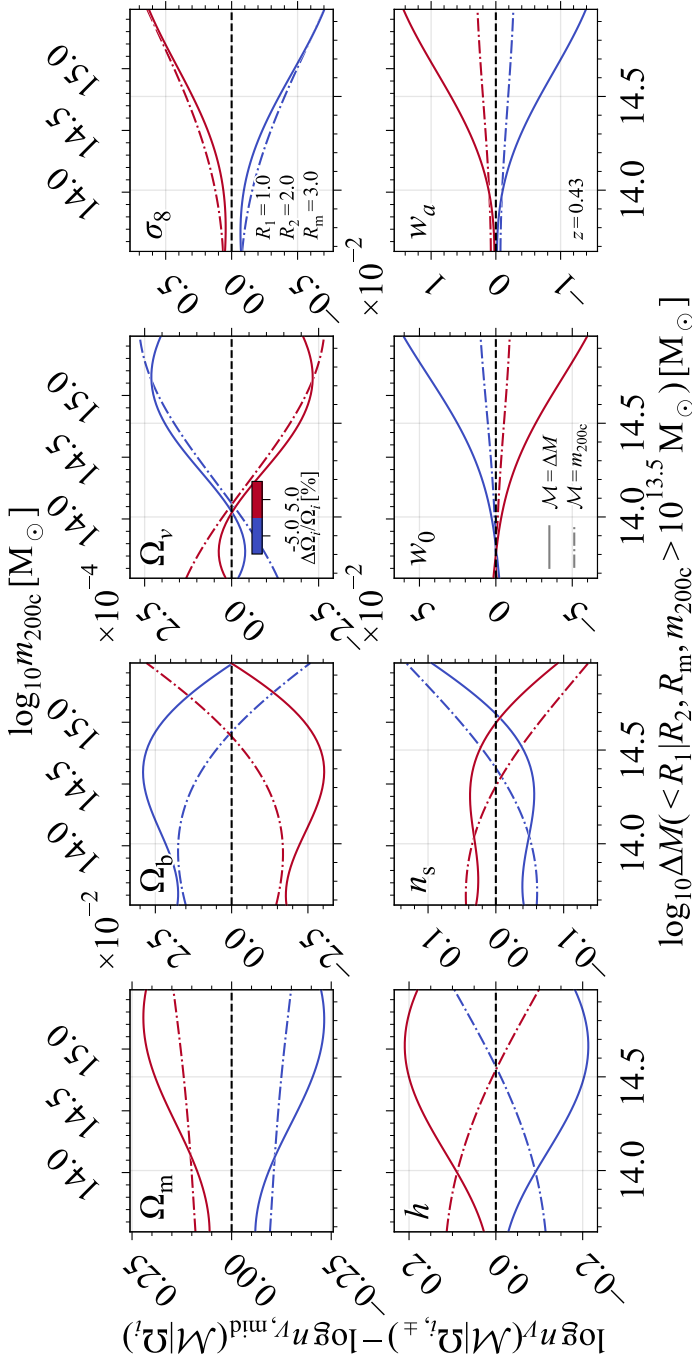


Figure 4.13: Comparison between the cosmology sensitivity of the 3D halo mass function (dash-dotted lines) and the aperture mass function (solid lines), for a fixed comoving volume, to changing individual cosmological parameter values by  $\pm 5$  per cent at  $z = 0.43$ . We assume  $w_a = \pm 0.05$  since the fiducial value is 0. The aperture mass function is plotted for the median aperture mass at  $m_{200c}$  for all the simulations in the hypercube, and for apertures  $(R_1, R_2, R_m) = (1, 2, 3)$  cMpc. All haloes have  $m_{200c} > 10^{13.5} M_\odot$ . The cosmological parameters are indicated in the top-left corner of each panel. Coloured lines indicate the fractional change in the individual cosmological parameters with respect to the fiducial **Planck20** cosmology. Both the 3D mass and the aperture mass function show similar sensitivity to changes in the  $\sigma_8$ ,  $n_s$  and  $\Omega_\nu$ . The aperture mass function is more sensitive to changes in  $\Omega_m$ ,  $h$ , the dark energy equation-of-state parameters,  $w_0$  and  $w_a$ , and  $\Omega_b$ .

In the exponentially declining tail, the constant decrease in the peak height increases the abundance more dramatically. The aperture mass function follows these trends.

When changing the other cosmological parameters, it is important to remember that we fix  $\sigma_8$ , implying that the initial normalization of the matter power spectrum,  $A_s$ , does change. Fixing  $\sigma_8$  instead of  $A_s$  reduces the impact of changing the other cosmological parameters on the mass function. Increasing  $\Omega_m$  in a flat universe will result in deeper dark matter potential wells, a faster growth of structure, and a delayed onset of dark energy domination. The peak height decreases for all haloes, resulting in higher abundances. The top-left panel of Fig. 4.13 shows that the abundance of low-aperture mass haloes changes less than the 3D halo mass function for low halo masses due to the increasing incompleteness at fixed, low aperture mass (see Fig. 4.9). At high aperture masses the large scatter in aperture mass at fixed  $m_{200c}$  results in a larger sensitivity of the aperture mass function compared to the 3D halo mass function due to the contribution of abundant low-mass haloes.

Increasing  $h$  at fixed  $\Omega_m$  increases the density which results in faster structure formation and makes haloes at fixed  $m_{200c}$  more compact, decreasing their peak height and increasing their abundance. The aperture mass function is significantly more sensitive to changes in  $h$  than the 3D halo mass function. Increasing the scalar spectral index,  $n_s$ , at fixed  $\sigma_8$  shifts the power from large to small scales, resulting in more low-mass and fewer high-mass haloes for both the 3D and the aperture mass function. Finally, increasing the magnitude of the equation-of-state parameter of dark energy,  $w_0$ , damps the growth of the most massive haloes, reducing their abundance. Again, the aperture mass function is more sensitive to these changes than the 3D halo mass function.

Finally, in Fig. 4.14, we compare the volumetric mass functions, defined in Eq. (4.4) (thin lines), to the observed mass functions including the cosmology-dependent volume of the past lightcone, defined in Eq. (4.5) (thick lines), for both the 3D halo mass function (dash-dotted lines) and the aperture mass function (solid lines). Changing the background evolution of the Universe modifies the number of observed haloes per fixed solid angle,  $d\Omega$ , and redshift interval,  $dz$ , due to the change in the probed comoving volume. The background evolution does not depend on  $\sigma_8$ ,  $n_s$ , and  $\Omega_b$  (since  $\Omega_m$  is fixed).

The background evolution is most sensitive to changes in the Hubble parameter. Increasing (decreasing)  $h$  reduces (increases) the distance to redshift  $z$ . As a result, a fixed survey area at redshift  $z$  will probe a smaller (larger) comoving volume. Hence, we would observe fewer (more) haloes for a fixed volumetric number density. The bottom-left panel of Fig. 4.14 shows that the decrease in the probed volume is larger than the increase in the volumetric number density due to the increased matter density. Changing  $h$  results in the largest difference between the observed and the volumetric mass functions, making the 3D halo mass function more sensitive to changes in  $h$ , and the aperture mass function less sensitive.

Increasing the matter density,  $\Omega_m$ , similarly reduces the probed volume for a fixed survey area at fixed redshift. This suppresses the observed number density,  $n_\Omega$ , compared to the volumetric number density,  $n_V$ , for both the 3D halo mass function and the aperture mass function. The aperture mass function is still more sensitive to changes in  $\Omega_m$  than the 3D halo mass function. The comoving volume for a fixed area on the sky increases (decreases) significantly when increasing (decreasing) the magnitude of  $w_0$ , resulting in

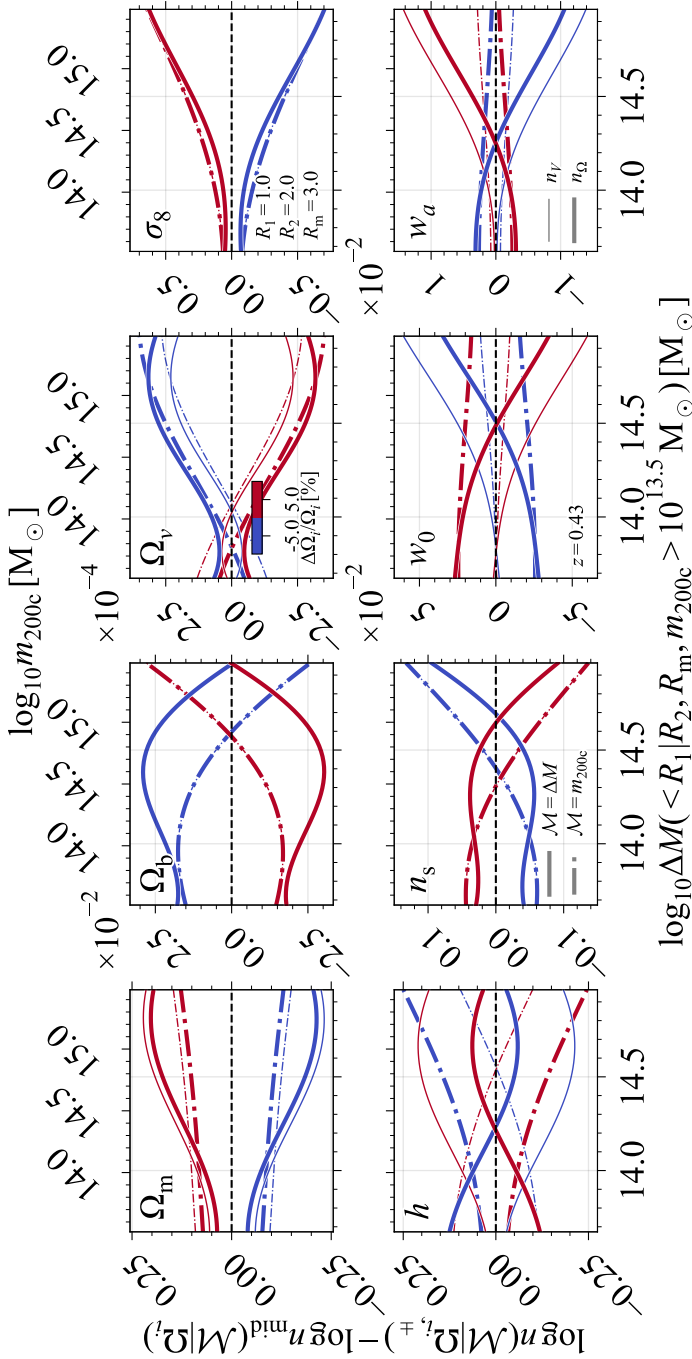


Figure 4.14: Comparison between the cosmology sensitivity of the 3D halo mass function (dash-dotted lines) and the aperture mass function (solid lines with  $n_\Omega$ , thick lines) including the cosmology dependence of the survey solid angle and redshift interval at  $z = 0.43$ . The cosmological parameter being varied by  $\pm 5$  per cent (coloured lines) with respect to the fiducial **Planck20** cosmology is indicated in the top-left corner of each panel. We assume  $w_a = \pm 0.05$  since the fiducial value is 0. The aperture mass function is plotted for the median aperture mass at  $m_{200c}$  for all the simulations in the hypercube, and for apertures  $(R_1, R_2, R_m) = (1, 2, 3)$  cMpc. All haloes have  $m_{200c} > 10^{13.5} M_\odot$ . The probed comoving volume for a fixed observed area is mainly sensitive to  $h$ ,  $\Omega_m$ ,  $w_0$  and  $w_a$ . Compared to the 3D halo mass function, the aperture mass function is more sensitive to changes in  $\Omega_m$  and  $w_a$ , similarly sensitive to  $\sigma_8$  and  $w_0$ , and less sensitive to  $h$ .

more (fewer) observed haloes. This geometric effect is stronger than the decrease (increase) in the volumetric number density due to the less (more) efficient structure formation. Increasing (decreasing)  $w_a$  decreases (increases) the magnitude of  $w(z)$  for  $z > 0$ , which in turn lowers (raises) the observed number density compared to the volumetric number density. The aperture mass function becomes less sensitive to changes in  $w_0$  and  $w_a$ . However, compared to the 3D halo mass function, the total sensitivity to changes in  $w_a$  remains higher and the sensitivity to  $w_0$  becomes similar.

Providing a detailed comparison between the performance of aperture masses and 3D halo masses in a cluster cosmology analysis is more complicated than investigating the percentage differences in the mass functions given a difference in the cosmological parameters. Eq. (4.1) shows that the number counts depend on the integral over the mass function taking into account the uncertainty in the mass–observable relation. Even though we have shown that the intrinsic measurement uncertainty in aperture mass measurements is much lower than that in 3D halo mass inference, the total uncertainty in the mass–observable relation still depends on the scatter between the survey selection observable and the measured aperture or 3D mass. For surveys that do not select clusters based on their weak lensing shear signal, the scatter in the observable at fixed aperture mass can still result in a significant total uncertainty in the aperture mass–observable relation. Hence, a comparison between 3D and aperture mass calibrations in a full cosmological analysis also needs to take into account the survey observable.

In conclusion, the sensitivity of the aperture mass function to small changes in the cosmological parameters opens the possibility of calibrating cluster masses with weak lensing aperture masses, bypassing the modelling uncertainty introduced when deprojecting the observations.

## 4

## 4.5 Discussion

We have provided arguments for calibrating cluster masses with weak lensing aperture masses. As long as we do not have predictions for the halo abundance directly as a function of the survey observable, such as the galaxy overdensity, the X-ray luminosity, or the SZ signal, cluster cosmology needs to follow a two step process. Assuming that the selection function has been accounted for, the mass–observable relation needs to be calibrated, and the cosmology dependence of the mass function needs to be understood. Eq. (4.1) shows that the mass calibration requires both the calibration between the observable and the mass inferred from observations, and the calibration between the inferred mass and the theoretical mass used in the mass function.

To more closely match weak lensing observations, it makes sense to calibrate cluster masses with the projected aperture mass, which can also be measured in simulations. The mass calibration then separates cleanly into a purely observational relation between the measured aperture mass and the observable, and a calibration between the theoretical and the measured aperture mass. This clean separation does not hold for 3D cluster masses, which can only be inferred by deprojecting the observations under the assumption of a density profile. Any mismatch between the assumed and the true cluster density profile

biases the inferred 3D masses. The large variation in the matter distribution along the lines-of-sight to different clusters adds further uncertainty.

We showed that aperture masses correlate strongly with the 3D mass, albeit with large scatter due to the matter along the line-of-sight. We found that the aperture masses can be measured much more precisely than 3D masses, since the precision is only limited by the shape noise of the background galaxies. Next, we calibrated an emulator to reproduce the cosmology dependence of the aperture mass function, finding that it is also highly sensitive to variations in the cosmological parameters. Now we will discuss some of the difficulties that arise in cluster cosmology, and how they affect the aperture mass specifically. We will also position our contribution within the wider literature.

#### 4.5.1 Impact of the selection function

One vital ingredient of a cluster cosmology analysis that we did not discuss in this paper is the selection function of the cluster sample. The completeness, i.e. the fraction of all clusters that is detected, and the purity, i.e. the fraction of detections that are real clusters, of the cluster sample should be as high as possible (e.g. [Allen et al., 2011](#); [Aguena & Lima, 2018](#)). We have studied the aperture mass function in the idealized setting of perfect purity since we have centred directly on the known clusters in the simulations. Our halo sample becomes increasingly incomplete for aperture mass bins that contain a significant fraction of haloes with 3D masses near our selection limit, as can be seen from Fig. 4.9. Future aperture mass function emulators should thus ensure that they can reliably measure aperture masses for haloes with masses significantly below the expected detection limit of the survey, which we were unable to do due to the downsampling inherent to the Mira–Titan particle catalogues (although this is not a problem in principle for simulations).

Since haloes with masses below the mean expected mass at the observable selection limit can scatter above the signal threshold, the completeness of the cluster sample near the selection limit depends on the scatter of the mass–observable relation (e.g. [Mantz, 2019](#)). The main benefit of aperture masses is the ease with which they can be measured both in simulations and in observations, which significantly decreases the intrinsic measurement uncertainty in the mass calibration,  $P(\mathcal{M}_{\text{obs}}|\mathcal{M})$ , compared to 3D masses, as we showed in Section 4.3.3. However, this gain can be lost if the observable used to select clusters has a significantly larger scatter at fixed aperture mass compared to its scatter at fixed 3D mass. Hence, aperture masses could greatly increase the performance of cluster surveys based on observables that correlate with the aperture mass with small uncertainty. This will be the case for observables that are more sensitive to projection effects, such as the SZ signal (e.g. [Hallman et al., 2007](#)), galaxy overdensities (e.g. [van Haarlem et al., 1997](#); [Erickson et al., 2011](#)), and, naturally, the shear signal.

The purity of the halo sample will depend sensitively on the cluster detection method, with shear-selected samples only reaching a maximum purity of  $\approx 85$  per cent since chance line-of-sight alignments can generate a significant signal due to the broadness of the lensing kernel (e.g. [Hennawi & Spergel, 2005](#)). The purity of other detection methods that are also susceptible to such projection effects, such as the SZ signal or the galaxy overdensity, will need to be modelled in simulations. Baryonic observables that predominantly trace the inner cluster density profile, such as the X-ray luminosity, on the other

hand, should reach higher purity (e.g. Voit et al., 2001). However, samples selected from these observables are necessarily more sensitive to the halo density profile, introducing possible detection biases near the selection limit (e.g. Chon & Böhringer, 2017).

We highlight one final important point about the synergy between observed and simulated aperture mass measurements. Since the detection bias for observables such as the SZ signal and the galaxy overdensity is in large part due to projection effects (e.g. Shirasaki et al., 2016; Zhang & Annis, 2022), this bias is naturally included in aperture masses measured in simulations. Hence, emulators calibrated on a cluster sample generated by mimicking the survey selection in the simulations will naturally include the survey detection bias while providing aperture mass measurements that are directly comparable to those measured observationally.

#### 4.5.2 Impact of systematic uncertainties

In a realistic cosmological analysis, different observational systematic effects need to be taken into account. Any weak lensing mass measurement will be sensitive to the systematic errors in the shape measurements, the redshift distribution of the sources, contamination of the lensing signal due to uncertainty in the photometric redshift determination of cluster galaxies, and miscentring of the cluster (e.g. Von der Linden et al., 2014; Hoekstra et al., 2015).

The main advantage of aperture masses over 3D masses is that no density profile needs to be assumed in the analysis, eliminating the impact of this modelling uncertainty. The aperture mass within  $R_1$  is actually measured from the lensing signal of galaxies *outside*  $R_1$ , significantly reducing the impact of sources of systematic error near the cluster centre, such as miscentring and contamination (e.g. Mandelbaum et al., 2010). The optimal choice of  $R_1$  balances the reduced contamination of the lensing signal by cluster galaxies when increasing  $R_1$  against the increase in the statistical uncertainty due to the reduced number of background galaxies. Since the bulk of the haloes have miscentring radii  $< 0.2R_{500c}$  (e.g. Saro et al., 2015; Bleem et al., 2020), apertures can be chosen large enough such that the mass within the aperture should only be slightly affected, while limiting the increased statistical uncertainty.

Another advantage stems from the fact that aperture masses can always be computed unambiguously, even for triaxial and merging systems. As long as the choice of aperture in the mass function and the observations is consistent, the mass measurement should yield similar results. Moreover, since emulators can be calibrated for different aperture sizes, the consistency of the inferred cosmology for an analysis using different apertures can pinpoint possible biases in the cosmological analysis.

A limitation of our preliminary study is the fact that we did not construct convergence maps from the full past lightcone. The lensing efficiency of matter structures at redshift  $z_l$  for source galaxies at a fixed redshift  $z_s$ ,  $\epsilon(z_l, z_s) = D_l D_{ls} / D_s$ , is very broad. This means that matter over a significant range of redshifts can contribute to the lensing signal of a given background galaxy. A full line-of-sight in simulation M000 with  $L = 2100$  cMpc at  $z = 0.5$  corresponds to a redshift range  $z \approx [0.2, 0.85]$ . Hence, projecting the mass along the simulation volume at fixed  $z$  does not take into account the time evolution of the included structures or the change in the angular diameter distance across the length

of the box. As such, aperture mass functions should really be calibrated on simulation lightcone outputs, not on single snapshots. This makes the analysis more complex since the resulting lensing maps need to be reconstructed for different source redshifts,  $z_s$ .

Finally, since we have used gravity-only simulations, we have not included the impact of baryonic physics on the aperture mass function. For 3D halo mass functions, it is well established that the mass of haloes with  $m_{200m,\text{dmo}} \lesssim 10^{14.5} M_\odot$  decreases significantly due to galaxy formation physics processes (e.g. [Velliscig et al., 2014](#)). We expect baryonic physics to also impact the cluster aperture mass measurements, albeit less significantly due to the projected nature of the measurement (e.g. [Debackere et al., 2021](#)). We study the impact of baryonic physics on the aperture mass measurements in a companion paper [Debackere et al. \(2022\)](#).

### 4.5.3 Comparison to previous work

The abundance of clusters is a powerful probe of the cosmological evolution of the Universe, so an active effort is underway to minimize the impact of mass calibration uncertainties. For example, [Grandis et al. \(2021\)](#) directly calibrate the mass–observable relation,  $P(\mathcal{O}|\mathcal{M})$ , using simulations. They generate lensing profiles from hydrodynamical simulations which they fit with NFW density profiles with a fixed concentration and assuming a miscentring distribution. They then calibrate the resulting relation between the best-fit NFW mass and the true mass of the matched cluster in DMO simulations. This method then converts a weak lensing-inferred 3D halo mass into the 3D halo mass of the matching DMO halo, allowing the use of 3D halo mass function emulators calibrated on DMO simulations. This method is still explicitly limited by the scatter between the inferred and the true 3D halo mass due to the assumed density profile.

[Cromer et al. \(2021\)](#) improve the accuracy of weak lensing-inferred 3D halo masses by fitting the lensing shear with an emulated cluster density profile that includes a phenomenological contribution due to baryons. Their model results in more accurate cluster mass estimates, but, again, relies on the ultimately inaccurate assumption that the complex cluster density profile can be modelled accurately with simplified, spherically symmetric profiles.

[Marian et al. \(2009, 2010\)](#) carry out analyses that are the most similar to ours. They generate lensing maps for different slabs in DMO simulations to which they apply a hierarchical peak finder that extracts the aperture mass within a filter designed to optimally detect the cluster signal. They show that the resulting peak abundance function has a similar cosmological sensitivity as the 3D mass function. Similarly to us, they find that the peak aperture masses show a large scatter at fixed halo mass. However, at the time of their work, large suites of cosmological simulations and emulators were not yet available. Hence, they resorted to constructing an analytic framework to extract cosmological information from weak lensing peak counts.

Another option is to neglect the cluster selection entirely and use the distribution of shear peaks as a function of their signal-to-noise ratio to constrain the cosmology (see e.g. [Wang et al., 2009; Dietrich & Hartlap, 2010; Kratochvil et al., 2010](#)). However, since the evolution of clusters with time contains a wealth of cosmological information, stronger cosmological constraints can be obtained by including redshift information for

the observed peaks, as suggested by [Hennawi & Spergel \(2005\)](#). The main difficulty with these shear-selected analyses is that a significant fraction of the high significance peaks arises from chance line-of-sight alignments due the broadness of the lensing kernel (e.g. [Hennawi & Spergel, 2005](#); [Yang et al., 2011](#)). In recent studies, [Hamana et al. \(2015\)](#), [Shan et al. \(2018\)](#) and [Martinet et al. \(2018\)](#) have used peaks identified from weak lensing observations to constrain the matter density and clustering of the Universe.

We locate our work in between peak abundance studies and cluster analyses based on 3D cluster masses: our method corresponds to an idealized survey that selects clusters based on a secondary observable that perfectly correlates with the 3D halo mass, while the cluster masses are determined through aperture masses which would in practice be derived from weak lensing observations. Hence, our work is very similar to a standard cluster cosmology analysis, as worked out in detail by [Mantz et al. \(2010a,b\)](#), but now using the aperture mass to calibrate the cluster masses. In such an analysis, one assumes a functional form for the mass–observable relation, which gets calibrated simultaneously with the cosmology-dependent aperture mass function by forward modelling the observed cluster abundance as a function of the observable signal, taking into account the selection function of the observable for a given survey. Importantly, any cosmology dependence in the mass–observable relation needs to be taken into account implying that the cosmology dependence of both  $P(\Delta M_{\text{obs}}|\Delta M, \Omega, z)$  and  $P(\mathcal{O}|\Delta M_{\text{obs}}, \Omega, z)$  need to be calibrated from mock observations in realistic cosmological and, preferably, hydrodynamical simulations (e.g. [Dietrich et al., 2019](#)).

## 4

## 4.6 Conclusions

We have argued that cluster cosmology analyses can decrease their sensitivity to modelling assumptions by using weak lensing-like excess aperture mass measurements to calibrate cluster masses. As long as predictions for the cosmology-dependent abundance of clusters as a function of their observed signal are not available, cluster cosmology necessarily relies on an accurately determined and well-understood mass–observable relation and a theoretical prediction for the cosmology dependence of the mass function. Only suites of large-volume simulations with varying cosmological parameters can predict the mass function at the accuracy required for future surveys. If we are using simulations, however, we might as well predict the aperture mass function instead of (or along with) the 3D halo mass function.

Aperture masses are a natural choice for cluster mass calibrations since they can be measured accurately both in observations and in simulations, with an uncertainty determined solely by the background galaxy shape noise in the weak lensing observations. In contrast, 3D halo masses can only be inferred by deprojecting observations assuming a density profile. The mismatch between the assumed density profile and the true, triaxial halo density profile, including substructure and correlated matter, and the neglected matter along the line-of-sight, introduce a model-dependent bias and scatter in the inferred mass.

We used the Mira–Titan suite of large-volume, DMO simulations to measure the excess projected mass of clusters within fixed aperture sizes of  $R_1 = 0.5, 1.0, 1.5 \text{ cMpc}$  with

a background subtraction calculated in an outer annulus between  $2 < R/\text{cMpc} < 3$ . We studied the behaviour of these aperture masses and the corresponding aperture mass function. We showed that the aperture mass correlates strongly with the 3D halo mass, with aperture masses being larger (smaller) than the halo virial mass when measured within apertures larger (smaller) than the virial radius (Fig. 4.5). The aperture mass exhibits large scatter at fixed halo mass when the halo virial radius is not significantly larger than the aperture due to the contribution of matter outside the halo (Fig. 4.6). Advantageously, the uncertainty in the *measurement* of the aperture mass is between 2 to 3 times smaller than that of the inferred 3D mass (Fig. 4.7). This is because the measurement uncertainty depends only on the background galaxy shape noise in the weak lensing observations, and since line-of-sight structures contribute to the aperture mass signal whereas they introduce noise in the deprojection for 3D masses.

We did not investigate the scatter between the survey observable and the aperture mass since the Mira–Titan suite does not include hydrodynamics to model the complex baryonic processes related to galaxy formation. However, we argued that observables such as the SZ signal, the galaxy overdensity, and the shear should correlate strongly with aperture masses with small uncertainty, since they are also sensitive to line-of-sight matter structures beyond the halo. X-ray luminosities, on the other hand, due to their steep scaling with the 3D halo mass, may show large scatter at fixed aperture mass, similarly to the 3D halo mass. The uncertainty between the observable and the measured aperture mass will ultimately determine the scatter in the mass–observable relation, given the small intrinsic scatter of the measured aperture mass with respect to the true aperture mass. Investigating the uncertainty between the observable and the measured aperture mass in hydrodynamical simulations is a fruitful direction for future research.

We used the Mira–Titan hypercube of DMO simulations to calibrate a Gaussian process emulator to *directly* emulate the cosmology dependence of the aperture mass function given the simulated number counts and their likelihood, i.e. without assuming an underlying, dimensionality-reducing model for the simulation data. This is possible thanks to advances in Gaussian process modelling, allowing for the efficient optimization of large datasets and non-Gaussian likelihoods. We argued that this gives an advantage over usual emulators since the high-mass tail of the emulator will only depend on the simulation data and the assumed likelihood, *not* on the assumed mass dependence for the assumed data model. We showed that the emulator can accurately reproduce most of the simulations to within 2 per cent or within the bootstrapped variance at high-aperture masses (Fig. 4.15).

Isolating the influence of structure formation on the halo abundance, we found that, compared to the 3D halo mass function, the aperture mass function is similarly sensitive to changes in  $\sigma_8$  and  $n_s$ , and more sensitive to changes in  $\Omega_m$ ,  $h$ ,  $w_0$  and  $w_a$  (Fig. 4.13). Even  $\pm 1$  per cent changes in  $\Omega_m$ ,  $\sigma_8$ , and  $h$  result in  $> 10$  per cent changes in the expected halo number density at fixed redshift (Fig. 4.11). Including the cosmology dependence of the volume probed by the past lightcone, we found that, compared to the 3D halo mass function, the aperture mass function is more sensitive to changes in  $\Omega_m$  and  $w_a$ , similarly sensitive to changes in  $\sigma_8$  and  $w_0$  and slightly less sensitive to changes in  $h$  (Fig. 4.14). We stress that a detailed comparison between the performance of the aperture mass function compared to the 3D halo mass function also needs to take into account

the survey observable. Importantly, since emulators can easily be calibrated for multiple apertures, the consistency of the inferred cosmology for an analysis using different apertures can provide useful insights into possible biases in the cosmological analysis.

In the future, it will be possible to emulate cluster surveys using lightcones output from hydrodynamical simulations, mimicking the observable measurement and selection directly while skipping the mass calibration step (given that one can trust the simulation predictions at the accuracy required for future surveys, or marginalize over the simulation uncertainty). To validate the fidelity of such simulations, aperture masses provide the best choice to test the simulated mass–observable relations. Since no such simulations are currently available, however, we argue that our approach provides a valuable intermediate step. Emulators of the aperture mass function, which is closer to the data than the 3D halo mass function, can already be trained, minimizing the impact of uncertain modelling assumptions on cluster cosmology analyses.

## Acknowledgements

We would like to thank the referee for a clear report that helped clarify the aim of our work. This work is part of the research programme Athena with project number 184.034.002 and Vici grants 639.043.409 and 639.043.512, which are financed by the Dutch Research Council (NWO). Argonne National Laboratory’s work was supported under the U.S. Department of Energy contract DE-AC02-06CH11357. This research was supported in part by DOE HEP’s Computational HEP program. This research used resources of the Argonne Leadership Computing Facility at the Argonne National Laboratory, which is supported by the Office of Science of the U.S. Department of Energy under Contract No. DE-AC02-06CH11357. This work also used resources of the Oak Ridge Leadership Computing Facility, which is a DOE Office of Science User Facility supported under Contract DE-AC05-00OR22725.

## Data availability

The data used in this paper is available upon request to the first author.

## 4.A Weak lensing measurements of the aperture mass

In this appendix we show how aperture mass measurements from weak lensing observations relate directly to aperture masses measured from simulations. Overdensities in the mass distribution modify the light propagation from background galaxies depending on the projected distance from the overdensity, distorting the galaxy shapes. By measuring the average shape distortion of a large sample of background galaxies within some annular region, we can derive the total mass contained within that annulus without making any assumptions about the mass distribution.

In general, weak lensing-derived aperture masses are filtered measurements of the surface mass density centred on a position  $\boldsymbol{\theta}_0$ , with a filter function  $U(\boldsymbol{\theta} - \boldsymbol{\theta}_0)$ . We follow the notation of [Bartelmann & Schneider \(2001\)](#) and write

$$M_{\text{ap}}(\boldsymbol{\theta}_0) = \int d^2\boldsymbol{\theta} U(\boldsymbol{\theta} - \boldsymbol{\theta}_0)\kappa(\boldsymbol{\theta}). \quad (4.13)$$

We have introduced the convergence

$$\kappa(\boldsymbol{\theta}) = \frac{\Sigma(\boldsymbol{\theta})}{\Sigma_c}, \quad (4.14)$$

where the critical surface mass density  $\Sigma_c$ , which sets the magnitude of the lensing, is a physical constant given by

$$\Sigma_c = \frac{c^2}{4\pi G} \frac{1}{\beta D_l}, \quad (4.15)$$

which depends on the angular diameter distance to the lens,  $D_l$ , and the lensing efficiency,  $\beta = \max(0, D_{ls}/D_s)$ , for a source at angular diameter distance  $D_s$  from the observer and  $D_{ls}$  from the lens. There is no lensing signal ( $\beta = 0$ ) when the source is in front of the lens, i.e.  $D_{ls} < 0$ .

For a radial, compensated filter obeying the relation

$$\int d\theta \theta U(\theta) = 0, \quad (4.16)$$

Eq. (4.13) can be rewritten in terms of the tangential shear as

$$M_{\text{ap}}(\boldsymbol{\theta}_0) = \int d^2\boldsymbol{\theta} Q(|\boldsymbol{\theta} - \boldsymbol{\theta}_0|)\gamma_T(\boldsymbol{\theta}|\boldsymbol{\theta}_0), \quad (4.17)$$

where the tangential shear is defined as

$$\gamma_T(\boldsymbol{\theta}) = \frac{\bar{\Sigma}(\leq \boldsymbol{\theta}) - \Sigma(\boldsymbol{\theta})}{\Sigma_c}, \quad (4.18)$$

and the new filter function  $Q(\theta)$  is related to the surface mass density filter  $U(\theta)$  as

$$Q(\theta) = \frac{2}{\theta^2} \int_0^\theta d\theta' \theta' U(\theta') - U(\theta). \quad (4.19)$$

Choosing filters  $U(\theta)$  that are constant within some small inner aperture  $\theta_1$  will result in  $Q(\theta) = 0$  for  $\theta < \theta_1$ . Similarly, compensated filters with  $U(\theta) = 0$  outside  $\theta_m$  give  $Q(\theta) = 0$  for  $\theta > \theta_m$ . Hence, aperture masses can be measured from the tangential shear within some finite region  $\theta_1 < \theta < \theta_m$  for carefully chosen filters  $U$ . The region can be chosen with  $\theta_1$  large enough to avoid the contamination from the densely populated cluster core and, importantly, to ensure measurements within the weak lensing regime. Generally, gravitational lensing does not measure the tangential shear directly, but is instead sensitive to the reduced shear

$$g_T(\theta) = \frac{\gamma_T(\theta)}{1 - \kappa(\theta)}. \quad (4.20)$$

However, if  $\theta_1$  is chosen large enough, then  $\kappa(\theta) \ll 1$  and the weak lensing assumption  $g_T \approx \gamma_T$  holds.

Since galaxy ellipticities are an unbiased estimator of the local shear field in the weak lensing regime, the aperture mass can be estimated directly by summing over the observed galaxy ellipticities (Schneider, 1996). Assuming the mean number density of lensed background galaxies,  $\bar{n}_{\text{gal}}$ , we get

$$M_{\text{ap}}(\boldsymbol{\theta}_0) = \frac{1}{\bar{n}_{\text{gal}}} \sum_i Q(|\boldsymbol{\theta}_i - \boldsymbol{\theta}_0|) \gamma_T(\boldsymbol{\theta}_i). \quad (4.21)$$

The uncertainty in this aperture mass measurement depends only on the shape noise due to the finite number of galaxies sampling the shear field. For an average uncertainty  $\sigma_{\text{gal}}$  in the shear measurement  $\gamma_T$  of an individual galaxy, and a background galaxy number density  $\bar{n}_{\text{gal}}$ , the uncertainty in  $M_{\text{ap}}$  is

$$\sigma_{M_{\text{ap}}(\boldsymbol{\theta}_0)}^2 = \frac{\sigma_{\text{gal}}^2}{\bar{n}_{\text{gal}}} \sum_i Q^2(|\boldsymbol{\theta}_i - \boldsymbol{\theta}_0|). \quad (4.22)$$

The aperture masses that we have used in this paper are directly related to the  $\zeta_c$ -statistic, introduced by Clowe et al. (1998), which can be measured from the tangential shear as

$$\zeta_c(\theta_1) = 2 \int_{\theta_1}^{\theta_2} d \ln \theta \langle \gamma_T \rangle + \frac{2}{1 - \theta_2^2/\theta_m^2} \int_{\theta_2}^{\theta_m} d \ln \theta \langle \gamma_T \rangle. \quad (4.23)$$

We have introduced the tangentially averaged tangential shear,  $\langle \gamma_T \rangle$ , defined as

$$\langle \gamma_T \rangle(\theta) = \frac{1}{2\pi} \oint d\phi \gamma_T(\theta, \phi). \quad (4.24)$$

Eq. (4.23) implies a filter function

$$Q_{\zeta_c}(\theta) = \begin{cases} \frac{1}{\pi\theta^2} & \text{for } \theta_1 < \theta \leq \theta_2 \\ \frac{1}{\pi\theta^2} \frac{\theta_m^2}{\theta_m^2 - \theta^2} & \text{for } \theta_2 < \theta \leq \theta_m \\ 0 & \text{elsewhere.} \end{cases} \quad (4.25)$$

We can readily obtain  $\Delta M$  from  $\zeta_c$  as

$$\Delta M(< \theta_1 | \theta_2, \theta_m) = \Sigma_c \zeta_c(< \theta_1) \pi \theta_1^2. \quad (4.26)$$

## 4.B Scalable Gaussian processes for non-Gaussian likelihoods

We start by introducing our notation. For each of the 100 cosmologies,  $\Omega_i$ , simulated in Mira–Titan, we have calculated the aperture mass function  $n(\Delta M, \Omega_i)$  on a log-spaced grid of 50 points with  $\log_{10} \Delta M / M_\odot \in [13.5, 15.5]$  for redshifts  $z \in \{0.1, 0.24, 0.43, 0.66, 1.0, 1.6, 2.0\}$ . For a set of input locations and observations  $\{(\mathbf{x}_i, N_i) | i = 1, \dots, n\}$ , with  $n = 100 \times 50$  (100 cosmologies with 50 mass bins each), we group the  $1 \times d$ -dimensional input vectors  $\mathbf{x}_i^T$  containing the cosmological parameters and the mass bin, into the rows of the  $n \times d$  matrix  $\mathbf{X}$ , i.e.  $\mathbf{X}_i = \mathbf{x}_i^T$ , and the measured number counts for each redshift  $z_j$  into the  $n$ -dimensional vector  $\mathbf{N}_j$ . We will drop the subscript  $j$  in what follows, since the procedure will be the same for each redshift with only the input measurements differing.

Given the large dynamic range and the peaked nature of the aperture mass function, we do not model the number counts directly. Instead, we predict the number density normalized to the mean value over all cosmologies in the grid

$$f(\mathbf{x}_i) = \log n(\mathbf{x}_i) - \log \langle n(\Delta M_l) \rangle_\Omega, \quad (4.27)$$

with  $\mathbf{x}_i^T = (\Omega_k^T, \Delta M_l)$ , a vector containing the aperture mass for different cosmologies. We stress that a single cosmology,  $\Omega_k$ , has 50 mass bins,  $\Delta M_l$ , and we normalize the aperture mass function with the mean over all cosmologies for each mass bin. This normalization reduces the dynamic range of the latent function  $f(\mathbf{x}_i)$  to values approximately between -1 and 1. We can easily recover the predicted number counts from  $f(\mathbf{x}_i)$  by converting it to  $n(\mathbf{x}_i)$  using Eq. (4.27), and multiplying by the volume element and the bin-spacing in  $\Delta M$ . As long as the mean number density  $\langle n(M_l) \rangle_\Omega > 0$  in Eq. (4.27), the high-mass tail of cosmological models with no observed clusters can be fit consistently with the correct likelihood and without assuming any functional form for the aperture mass function.

To fit this model to the simulated mass functions, we need to assume the likelihood of the simulated data. Since the number counts are discrete observations with exponential cosmology sensitivity in the low-number count, high-mass tail, we cannot assume a Gaussian likelihood that does not accurately describe low number counts. We cannot assume a Poisson likelihood either, since, as shown in Fig. 4.10, the dispersion of the aperture mass function exceeds the Poisson value. Hence, we assume a negative binomial likelihood for the data  $N_i$  given the model  $f(\mathbf{x}_i)$ . The probability density function of the negative binomial distribution can be written in terms of the mean,  $\mu$ , and the variance,  $\alpha\mu$ , where  $\alpha > 1$  captures the overdispersion compared to the Poisson distribution. In our case, we write the likelihood of the simulated number counts,  $N_i$ , given the model,  $f(\mathbf{x}_i)$ , as

$$p(N_i | f(\mathbf{x}_i)) = \mathcal{NB}(N_i | N(\mathbf{x}_i), \alpha_i), \quad (4.28)$$

where  $N(\mathbf{x}_i)$  is the number of haloes inferred from  $f(\mathbf{x}_i)$ , and  $\alpha_i$  is calculated as the ratio between the bootstrapped variance and the observed number of haloes in the mass bin. Standard Gaussian processes cannot be solved analytically for data with non-Gaussian

likelihoods, so we will use the approximate, variational inference Gaussian process method from Hensman et al. (2014) and implemented in `GPyTorch`<sup>3</sup> (Gardner et al., 2021).

The Gaussian process assumption models the latent function in Eq. (4.27) as (following the notation of Rasmussen & Williams, 2006)

$$f(\mathbf{x}) \sim \mathcal{GP}(\mu, k(\mathbf{x}, \mathbf{x}'|\theta)), \quad (4.29)$$

which is shorthand for

$$\mathbb{E}[f(\mathbf{x})] = \mu, \quad (4.30)$$

$$\text{Var}[f(\mathbf{x}), f(\mathbf{x}')] = k(\mathbf{x}, \mathbf{x}'|\theta), \quad (4.31)$$

and means that the values of  $f$  are fully determined by the mean,  $\mu$ , and the covariance function  $k(\mathbf{x}, \mathbf{x}'|\theta)$  between different inputs  $\mathbf{x}$  and  $\mathbf{x}'$ . We will be using the radial basis function (or squared exponential) kernel for  $k$ :

$$k(\mathbf{x}, \mathbf{x}'|\theta) = \sigma^2 \prod_{i=0}^d \exp\left(-\frac{((\mathbf{x})_i - (\mathbf{x}')_i)^2}{2\ell_i^2}\right), \quad (4.32)$$

where  $i$  runs over the  $d = 9$  dimensions of  $\mathbf{x}$  and each dimension has its own covariance lengthscale  $\ell_i$ , resulting in hyperparameter  $\theta = (\mu, \sigma^2, \ell)$ .

4

The power of Gaussian process regression stems from the conditioning property of Gaussian distributions. In what follows, we assume  $\mu = 0$  for simplicity. Given the assumed joint Gaussian distribution between function values at  $\mathbf{X}$  and  $\mathbf{X}^*$ ,  $p(\mathbf{f}, \mathbf{f}^*)$ , which we can write as

$$p(\mathbf{f}, \mathbf{f}^*) = p\left(\begin{bmatrix} \mathbf{f} \\ \mathbf{f}^* \end{bmatrix}\right) = \mathcal{N}\left(\begin{bmatrix} \mathbf{0} \\ \mathbf{0} \end{bmatrix}, \begin{bmatrix} K_{\mathbf{XX}} & K_{\mathbf{XX}^*} \\ K_{\mathbf{X}^*\mathbf{X}} & K_{\mathbf{X}^*\mathbf{X}^*} \end{bmatrix}\right), \quad (4.33)$$

the conditional distribution  $p(\mathbf{f}^*|\mathbf{f})$  is a new Gaussian distribution given by

$$p(\mathbf{f}^*|\mathbf{f}, \theta) = \mathcal{N}(K_{\mathbf{X}^*\mathbf{X}} K_{\mathbf{XX}}^{-1} \mathbf{f}, K_{\mathbf{X}^*\mathbf{X}^*} - K_{\mathbf{X}^*\mathbf{X}} K_{\mathbf{XX}}^{-1} K_{\mathbf{X}^*\mathbf{X}}). \quad (4.34)$$

Here we have introduced the  $n \times n$  covariance matrix  $K_{\mathbf{XX}}$ , with  $(K_{\mathbf{XX}})_{ij} = k(\mathbf{x}_i, \mathbf{x}_j)$  and  $k$  given by Eq. (4.32), containing the covariance between different input points in  $\mathbf{X}$ . Importantly, the probability distribution of  $\mathbf{f}^*$  for an arbitrary input location  $\mathbf{X}^*$  depends solely on the finite set of *measured* inputs  $\mathbf{X}$ . Clearly, the accuracy of the prediction  $f(\mathbf{x}^*)$  depends on the distance to the nearest measured input  $\mathbf{x}$  in  $\mathbf{X}$  and the lengthscale hyperparameter  $\ell$ , with the function values  $f^*$  regressing to the mean 0 and prior uncertainty  $k(\mathbf{x}^*, \mathbf{x}^*)$  for  $K_{\mathbf{X}^*\mathbf{X}} \rightarrow \mathbf{0}^T$ . We can use  $p(\mathbf{f}^*|\mathbf{f}, \theta)$  to predict  $\mathbf{N}(\mathbf{X}^*)$ .

The optimal hyperparameters,  $\theta$ , for the simulated data,  $\mathbf{N}$ , are found by maximizing

$$p(\theta|\mathbf{N}) = \frac{p(\theta)p(\mathbf{N}|\theta)}{p(\mathbf{N})}. \quad (4.35)$$

---

<sup>3</sup><https://github.com/cornellius-gp/gpytorch>

where we introduced the marginal likelihood

$$p(\mathbf{N}|\theta) = \int p(\mathbf{N}|\mathbf{f})p(\mathbf{f}|\theta)d\mathbf{f}, \quad (4.36)$$

which cannot be solved analytically in the case of a negative binomial likelihood.

This standard Gaussian process encounters two major difficulties. First, the  $K_{XX}^{-1}$ -term in Eq. (4.34) becomes computationally expensive for datasets with large  $n$ . Second, non-Gaussian likelihoods require approximations to optimize Eq. (4.35), since no closed-form analytical solution exists. Both of these problems have been solved by the sparse method using inducing variables and the variational free energy as introduced by Titsias (2009) and applied to non-Gaussian likelihoods by Hensman et al. (2014) and formalized by Matthews et al. (2016). We will briefly introduce the necessary ingredients for this method.

The idea behind the method of Titsias (2009) is to introduce both an extra set of  $m \ll n$  inducing (or pseudo) inputs  $Z$  of the Gaussian process such that  $\mathbf{f}(Z) \equiv \mathbf{u}$  and an approximate distribution over these function values,  $q_\psi(\mathbf{u})$ . The inducing point locations  $Z$  and the parameters  $\psi$  of the approximate distribution family will be chosen in such a way that they optimally capture the true posterior probability of the Gaussian process, i.e.  $q_\psi(\mathbf{f}) \simeq p(\mathbf{f}|\mathbf{N})$ . Assuming a Gaussian distribution for  $q(\mathbf{u})$  with

$$q_\psi(\mathbf{u}) = \mathcal{N}(\mathbf{m}, \mathbf{S}), \quad (4.37)$$

we get  $\psi = (\mathbf{m}, \mathbf{S})$  and we calculate the full approximate distribution as

$$q_\psi(\mathbf{f}, \mathbf{u}) = p(\mathbf{f}|\mathbf{u})q_\psi(\mathbf{u}). \quad (4.38)$$

The optimization of  $(Z, \mathbf{m}, \mathbf{S})$  now needs to ensure that

$$\begin{aligned} p(\mathbf{f}|\mathbf{N}) &\simeq \int p(\mathbf{f}|\mathbf{u})q(\mathbf{u})d\mathbf{u} \\ &\Updownarrow p(\mathbf{f}|\mathbf{u}) = \mathcal{N}(K_{XZ}K_{ZZ}^{-1}\mathbf{u}, D_{XX}) \\ &= \mathcal{N}(K_{XZ}K_{ZZ}^{-1}\mathbf{m}, D_{XX} + K_{XZ}K_{ZZ}^{-1}\mathbf{S}K_{ZZ}^{-1}K_{ZX}), \end{aligned} \quad (4.39)$$

with  $D_{XX} = K_{XX} - K_{XZ}K_{ZZ}^{-1}K_{ZX}$ , due to the conditioning property of Eq. (4.34) (see Chapter 4.3 of Matthews, 2017 for detailed explanations). Evaluating this expression only requires the inverted  $m \times m$  matrix  $K_{ZZ}^{-1}$ , significantly reducing the computational cost of making model predictions.

To determine the optimal values  $(Z, \mathbf{m}, \mathbf{S})$ , we minimize the difference between the approximate distribution  $q_\psi(\mathbf{f}, \mathbf{u})$  and the model posterior  $p(\mathbf{f}, \mathbf{u}|\mathbf{N})$  through the Kullback-Leibler (KL) divergence

$$\mathcal{KL}[q(\mathbf{f}, \mathbf{u})||p(\mathbf{f}, \mathbf{u}|\mathbf{N})] = - \int q(\mathbf{f}, \mathbf{u}) \log \left( \frac{p(\mathbf{f}, \mathbf{u}|\mathbf{N})}{q(\mathbf{f}, \mathbf{u})} \right) d\mathbf{f}d\mathbf{u}. \quad (4.40)$$

Defining this equation as  $\mathcal{K}$ , we use Bayes' theorem to rewrite

$$p(\mathbf{f}, \mathbf{u}|\mathbf{N}) = \frac{p(\mathbf{N}|\mathbf{f})p(\mathbf{f}|\mathbf{u})p(\mathbf{u})}{p(\mathbf{N}|\theta)}, \quad (4.41)$$

making use of the fact that the observations are only conditionally dependent on their corresponding function values  $\mathbf{f}$ . Also filling in Eq. (4.38), we then find

$$\begin{aligned}\mathcal{K} &= - \int p(\mathbf{f}|\mathbf{u})q(\mathbf{u}) \log \left( \frac{p(\mathbf{N}|\mathbf{f})p(\mathbf{u})}{p(\mathbf{N}|\theta)q(\mathbf{u})} \right) d\mathbf{f}d\mathbf{u} \\ &= - \int q(\mathbf{f}) \log p(\mathbf{N}|\mathbf{f}) d\mathbf{f} + \int p(\mathbf{f}|\mathbf{u})q(\mathbf{u}) \log p(\mathbf{N}|\theta) d\mathbf{f}d\mathbf{u} \\ &\quad + \int p(\mathbf{f}|\mathbf{u})q(\mathbf{u}) \log \left( \frac{q(\mathbf{u})}{p(\mathbf{u})} \right) d\mathbf{f}d\mathbf{u} \\ \mathcal{K} &= \log p(\mathbf{N}|\theta) - \mathbb{E}_{q(\mathbf{f})} [\log p(\mathbf{N}|\mathbf{f})] + \mathcal{KL}[q(\mathbf{u})||p(\mathbf{u})].\end{aligned}\quad (4.42)$$

We can rearrange terms in this expression and use the fact that the KL divergence is strictly positive to arrive at the variational evidence lower bound (ELBO), which provides a lower bound on the marginal likelihood—also called the model evidence—as the name suggests

$$\log p(\mathbf{N}|\theta) \geq \mathcal{L}_{\text{ELBO}} = \mathbb{E}_{q(\mathbf{f})} [\log p(\mathbf{N}|\mathbf{f})] - \mathcal{KL}[q(\mathbf{u})||p(\mathbf{u})]. \quad (4.43)$$

Equality for this equation holds exactly when Eq. (4.40) equals zero, which is the case when  $q(\mathbf{f}, \mathbf{u}) = p(\mathbf{f}, \mathbf{u}|\mathbf{N})$ . Assuming no covariance between  $f_i$  and  $N_{j \neq i}$ , the likelihood factors and we have

$$\mathcal{L}_{\text{ELBO}} = \sum_{i=1}^n \mathbb{E}_{q(f_i)} [\log p(N_i|f_i)] - \mathcal{KL}[q(\mathbf{u})||p(\mathbf{u})], \quad (4.44)$$

where the first term consists of a sum of one dimensional integrals which can be computed easily using Gauss-Hermite quadrature, and the second term is the KL divergence between two multivariate Gaussian distributions, since  $p(\mathbf{u}) = \mathcal{N}(\mathbf{0}, K_{ZZ})$  due to the Gaussian process assumption. Optimizing the ELBO is equivalent to maximizing the marginal log-likelihood in Eq. (4.36).

We use the ApproximateGP<sup>4</sup> implementation of GPyTorch to model and optimize  $f(\mathbf{x}_i)$  with a custom implementation of the negative binomial likelihood between  $N(\mathbf{x}_i)$  and the measurements number counts from the simulations,  $N_i$ .

## 4.C Emulator performance

The approximate Gaussian process does not sample the simulation inputs, but instead optimizes the inducing point locations to accurately reproduce the posterior of the full Gaussian process, i.e. Eq. (4.40). Hence, we will not trivially reproduce the simulation aperture mass function. In our set-up, we first normalize the input parameters,  $\mathbf{X}$ , so that all parameters lie between 0 and 1. We use 500 inducing points in the ApproximateGP variational distribution and minimize the marginal likelihood, approximated by the `gpytorch.mlls.VariationalELBO`, with the Adam optimizer

<sup>4</sup>[https://docs.gpytorch.ai/en/latest/examples/04\\_Variational\\_and\\_Approximate\\_GPs/Non\\_Gaussian\\_Likelihoods.html](https://docs.gpytorch.ai/en/latest/examples/04_Variational_and_Approximate_GPs/Non_Gaussian_Likelihoods.html)

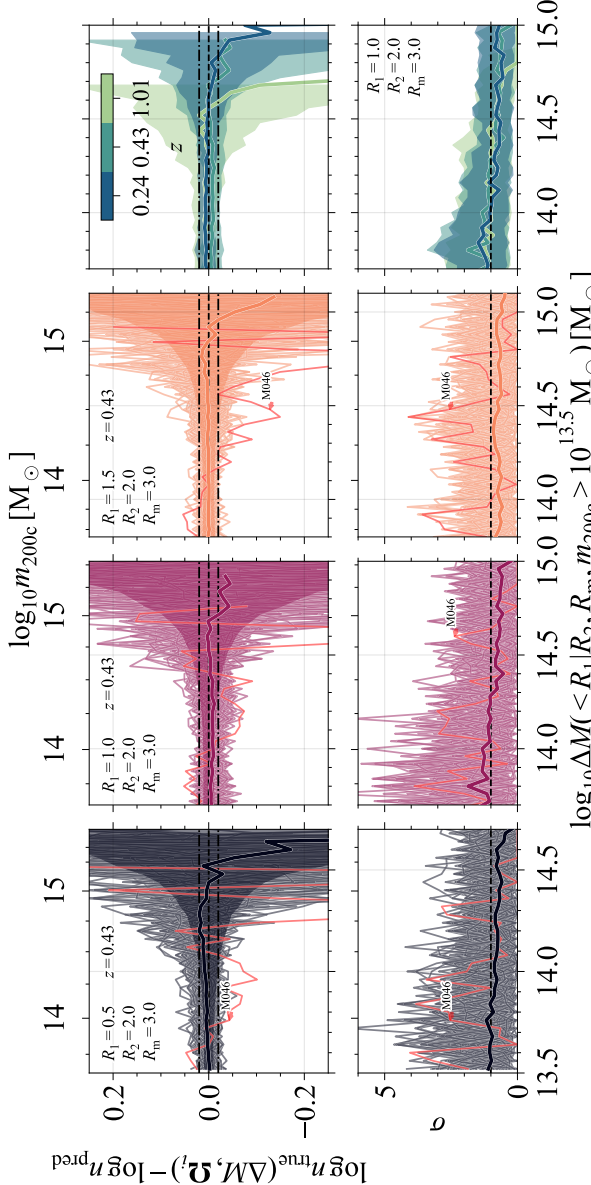


Figure 4.15: *Top row:* The residuals between the best-fit emulator and the individual simulations in the hypercube for different apertures at fixed redshift  $z = 0.43$  (*first three columns*) and at different redshifts for a fixed aperture  $(R_1, R_2, R_m) = (1, 2, 3)$  cMpc (*rightmost column*). All halo samples were selected with  $m_{200c} > 10^{13.5} M_\odot$ . For the aperture variations, we show the individual simulations and for the redshift variations the 16th to 84th percentile scatter to avoid clutter. The thick, coloured line indicates the median emulator residual and the shaded regions in the aperture plots indicate the median of the bootstrapped simulation uncertainties. The black, dashed dotted lines indicate the  $\pm 2$  per cent deviation. The median emulator residual is within the simulation uncertainty, and unbiased for low aperture masses and  $R_1 = 0.5, 1.5$  cMpc, while biased low at the  $\approx 1$  per cent level for  $R_1 = 1.0$  cMpc. For abundant, low-aperture mass haloes the emulator reaches an accuracy of  $\approx 2$  per cent for the bulk of the simulations, rarely exceeding the 5 per cent level. The most significant outlier, M046, which was run with a smaller box size, is indicated with a red line in the different panels. *Bottom row:* The Gaussian-equivalent significance of the likelihood ratio between the simulated data and the emulator. The median significance is mostly  $\approx 1\sigma$ . The significance for the individual simulations can vary wildly, but, as the top row shows, the fractional uncertainty remains reasonable.

with a learning rate of 0.01 and mini-batches of 512 observations each. These settings resulted in the fastest loss function minimization in a coarse, manual search for the optimal parameter settings. We resample the initial hyperparameters 5 times from their uniform priors to avoid local minima in the optimization. The emulator parameters are specified by the inducing point locations,  $\mathbf{u}$ , from Eq. (4.37) in Appendix 4.B, the Gaussian process mean,  $\mu$ , from Eq. (4.30), and the kernel lengthscales and normalization,  $\ell$  and  $\sigma$ , respectively, from Eq. (4.32). We choose uniform priors  $\mathbf{u} \sim \mathcal{U}(0, 1)$ ,  $\mu \sim \mathcal{U}(-1, 1)$ ,  $\ell \sim \mathcal{U}(0.05, 2.0)$ , and  $\sigma^2 \sim \mathcal{U}(0.05, 2.0)$ .

In the top row of Fig. 4.15, we show the resulting absolute deviation between the emulated latent function, Eq. (4.27), and the normalized number density from the simulation for different apertures and all cosmologies. The first three columns correspond to the different aperture sizes at  $z = 0.43$ , and the final column shows the median and 16th to 84th percentile scatter for the emulator at different redshifts. For low aperture masses, the emulator error rarely exceeds the 5 per cent difference level, and the bulk of the simulations have residuals within  $\pm 2$  per cent for the high abundance aperture mass regime. The median deviation is biased slightly low for  $R_1 = 1.0$  cMpc, but it is within  $\pm 2$  per cent for all aperture sizes and all but the most massive haloes. The bulk of the simulations lack haloes at the highest aperture masses resulting in the noticeable downturn. While the fractional deviation becomes large, it is still within the variance of the simulations, which is shown as the shaded region.

## 4

To quantify the quality of the fit in the high-mass tail, we show the equivalent Gaussian significance of the deviation between the simulated data and the emulator. We compute the significance by calculating the difference between the log-likelihood of the measured number counts in the simulation given the predicted aperture mass function of the emulator,  $\ln \mathcal{L}(N_{\text{true}}|N_{\text{pred}})$ , and the log-likelihood of the emulated number counts,  $\ln \mathcal{L}(N_{\text{pred}}|N_{\text{pred}})$ , and converting this probability ratio into the equivalent Gaussian confidence interval  $n\sigma$  around the mean expectation,  $\mu$ , given by  $\ln P(\mu + n\sigma) - \ln P(\mu)$ . We show the significance of the deviation between the emulator and the simulation data in the bottom row of Fig. 4.15. Individual simulations behave erratically for low aperture masses, rapidly oscillating between large and small significance, but rarely exceeding  $3\sigma$ . The median significance of all cosmologies, on the other hand, is consistently  $\approx 1\sigma$ . For the high-aperture mass tail, with large fractional deviations between the emulator and the simulations, the significance of the deviation  $\lesssim 1\sigma$ , indicating that the emulator captures the trends in the data to within the shot-noise.

Finally, we also perform a leave-one-out test on all simulations that are not at the edge of the parameter space for any of the cosmological parameters. In Fig. 4.16, we show how accurately the emulator predicts the aperture mass function for all left-out simulations. We colour the lines for simulations with cosmological parameters that are within the first or the last decile of the hypercube with different shades of blue and red, respectively, with darker shades indicating more significant outliers. The emulator can predict the outcome of most simulations to within  $\approx 5$  per cent up to the tail of the mass function. The most significant deviations are found for simulations that are close to the edge of the cosmological parameter space in one or more dimensions. The accuracy achieved by the emulator in the leave-one-out test indicates that the emulator generalizes well beyond the trained simulation inputs.

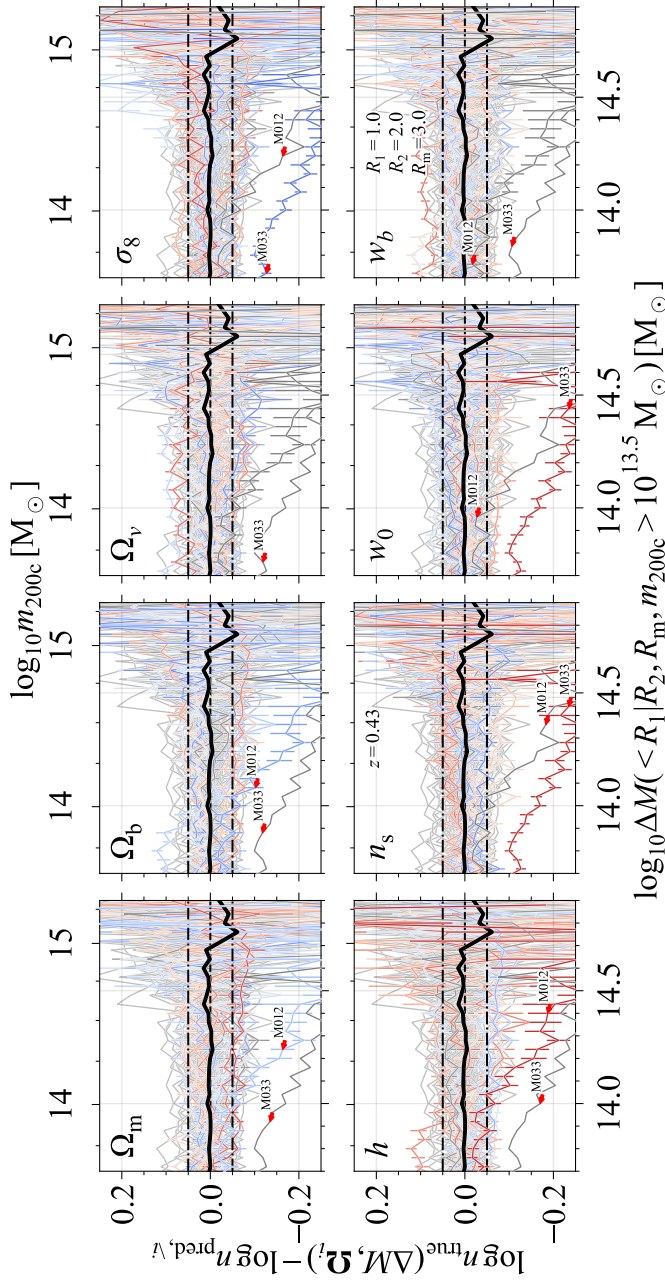


Figure 4.16: The residuals between the leave-one-out emulator and its held out simulation for all simulations that are not at the edge of the parameter space. The cosmological parameters are indicated in the top-left corner of each panel. All emulators have apertures of the form  $(R_1, R_2, R_m) = (1, 2, 3)$  cMpc and have been calibrated at  $z = 0.43$ . All halo samples were selected with  $m_{200c} > 10^{13.5} \text{ M}_\odot$ . Coloured lines indicate the simulations that are within the first (blue shades) or last (red shades) decile for the plotted cosmological parameter, with the saturation indicating the ordering. The black line indicates the median result for all simulations and the shaded region the 16th to 84th percentile scatter. The black, dash-dotted lines indicate the  $\pm 5$  per cent region. Most emulators are able to reproduce the held out simulation prediction within  $\approx 5$  per cent. The most significant outliers, M012 and M033, are indicated with red arrows and are simulations that are close to the edge of the parameter space for several cosmological parameters.

## Bibliography

- Aguena M., Lima M., 2018, *Phys. Rev. D*, 98, 123529 → p. 159
- Allen S. W., Evrard A. E., Mantz A. B., 2011, *Annu. Rev. Astron. Astrophys.*, 49, 409 → p. 128, 159
- Andreon S., Congdon P., 2014, *A&A*, 568, A23 → p. 144
- Angulo R. E., Springel V., White S. D. M., Jenkins A., Baugh C. M., Frenk C. S., 2012, *Mon. Not. R. Astron. Soc.*, 426, 2046 → p. 145
- Applegate D. E., et al., 2014, *Mon. Not. R. Astron. Soc.*, 439, 48 → p. 133
- Bahcall N. A., Kulier A., 2014, *Monthly Notices of the Royal Astronomical Society*, 439, 2505 → p. 144
- Bahé Y. M., McCarthy I. G., King L. J., 2012, *Mon. Not. R. Astron. Soc.*, 421, 1073 → p. 130, 138, 142, 143, 144
- Bartelmann M., Schneider P., 2001, *Physics Reports*, 340, 291 → p. 130, 165
- Becker M. R., Kravtsov A. V., 2011, *Astrophys. J.*, 740 → p. 130, 142, 143
- Bhattacharya S., Heitmann K., White M., Lukic Z., Wagner C., Habib S., 2011, *Astrophys. J.*, 732, 122 → p. 129
- Bleem L. E., et al., 2020, *Astrophys. J. Suppl. Ser.*, 247, 25 → p. 136, 160
- Bocquet S., Heitmann K., Habib S., Lawrence E., Uram T., Frontiere N., Pope A., Finkel H., 2020, *Astrophys. J.*, 901, 5 → p. 129, 131, 132, 150
- Bond J. R., Cole S., Efstathiou G., Kaiser N., 1991, *Astrophys. J.*, 379, 440 → p. 129
- Budzynski J. M., Koposov S. E., McCarthy I. G., Belokurov V., 2014, *Mon. Not. R. Astron. Soc.*, 437, 1362 → p. 144
- Chon G., Böhringer H., 2017, *Astron. Astrophys.*, 606, L4 → p. 160
- Clowe D., Luppino G. A., Kaiser N., Henry J. P., Gioia I. M., 1998, *Astrophys. J.*, 497, L61 → p. 166
- Crocce M., Fosalba P., Castander F. J., Gaztañaga E., 2010, *Monthly Notices of the Royal Astronomical Society*, 403, 1353 → p. 149
- Cromer D., Battaglia N., Miyatake H., Simet M., 2021, arXiv:2104.06925 [astro-ph] → p. 161
- DES Collaboration et al., 2020, *Phys. Rev. D*, 102, 023509 → p. 129
- Debackere S. N. B., Schaye J., Hoekstra H., 2021, *Monthly Notices of the Royal Astronomical Society*, 505, 593 → p. 130, 161
- Debackere S. N. B., Hoekstra H., Schaye J., 2022, *Monthly Notices of the Royal Astronomical Society*, p. stac2077 → p. 131, 161
- Despali G., Giocoli C., Angulo R. E., Tormen G., Sheth R. K., Baso G., Moscardini L., 2016, *Mon. Not. R. Astron. Soc.*, 456, 2486 → p. 129
- Diemer B., 2020, *ApJ*, 903, 87 → p. 129
- Dietrich J. P., Hartlap J., 2010, *Mon. Not. R. Astron. Soc.*, 402, 1049 → p. 161
- Dietrich J. P., et al., 2019, *Mon. Not. R. Astron. Soc.*, 483, 2871 → p. 162
- Erickson B. M. S., Cunha C. E., Evrard A. E., 2011, *Phys. Rev. D*, 84, 103506 → p. 159
- Gardner J. R., Pleiss G., Bindel D., Weinberger K. Q., Wilson A. G., 2021, arXiv:1809.11165 [cs, stat] → p. 168
- Grandis S., Bocquet S., Mohr J. J., Klein M., Dolag K., 2021, *Monthly Notices of the Royal Astronomical Society*, 507, 5671 → p. 161
- Habib S., et al., 2016, *New Astronomy*, 42, 49 → p. 131
- Haiman Z., Mohr J. J., Holder G. P., 2001, *Astrophys. J.*, 553, 545 → p. 128
- Hallman E. J., O’Shea B. W., Burns J. O., Norman M. L., Harkness R., Wagner R., 2007, *ApJ*, 671, 27 → p. 159

- Hamana T., Sakurai J., Koike M., Miller L., 2015, *Publications of the Astronomical Society of Japan*, 67, 34 → p. 130, 162
- Heitmann K., et al., 2016, *Astrophys. J.*, 820, 108 → p. 131, 132
- Heitmann K., et al., 2019, *ApJS*, 244, 17 → p. 131
- Hennawi J. F., Spergel D. N., 2005, *Astrophys. J.*, 624, 59 → p. 130, 159, 162
- Hensman J., Matthews A., Ghahramani Z., 2014, arXiv:1411.2005 [stat] → p. 150, 151, 168, 169
- Henson M. A., Barnes D. J., Kay S. T., McCarthy I. G., Schaye J., 2017, *Mon. Not. R. Astron. Soc.*, 465, 3361 → p. 130
- Hoekstra H., 2001, *Astron. Astrophys.*, 370, 743 → p. 135, 143
- Hoekstra H., 2003, *Mon. Not. R. Astron. Soc.*, 339, 1155 → p. 143
- Hoekstra H., Mahdavi A., Babul A., Bildfell C., 2012, *Monthly Notices of the Royal Astronomical Society*, 427, 1298 → p. 136
- Hoekstra H., Bartelmann M., Dahle H., Israel H., Limousin M., Meneghetti M., 2013, *Space Sci. Rev.*, 177, 75 → p. 128
- Hoekstra H., Herbonnet R., Muzzin A., Babul A., Mahdavi A., Viola M., Cacciato M., 2015, *Monthly Notices of the Royal Astronomical Society*, 449, 685 → p. 133, 136, 160
- Köhlinger F., Hoekstra H., Eriksen M., 2015, *Mon. Not. R. Astron. Soc.*, 453, 3107 → p. 128, 142
- Kratochvil J. M., Haiman Z., May M., 2010, *Physical Review D*, 81, 043519 → p. 161
- Lawrence E., et al., 2017, *Astrophys. J.*, 847, 50 → p. 131
- Le Brun A. M. C., McCarthy I. G., Melin J. B., 2015, *Mon. Not. R. Astron. Soc.*, 451, 3868 → p. 145
- Mandelbaum R., Seljak U., Baldauf T., Smith R. E., 2010, *Monthly Notices of the Royal Astronomical Society*, 405, 2078 → p. 134, 160
- Mantz A. B., 2019, *Mon. Not. R. Astron. Soc.*, 485, 4863 → p. 129, 159
- Mantz A., Allen S. W., Ebeling H., Rapetti D., Drlica-Wagner A., 2010a, *Monthly Notices of the Royal Astronomical Society*, 406, 1773 → p. 162
- Mantz A., Allen S. W., Rapetti D., Ebeling H., 2010b, *Mon. Not. R. Astron. Soc.*, 406, 1759 → p. 162
- Marian L., Smith R. E., Bernstein G. M., 2009, *Astrophys. J.*, 698, 33 → p. 151, 161
- Marian L., Smith R. E., Bernstein G. M., 2010, *Astrophys. J.*, 709, 286 → p. 130, 131, 133, 151, 161
- Martinet N., et al., 2018, *Monthly Notices of the Royal Astronomical Society*, 474, 712 → p. 130, 162
- Matthews A. G. d. G., 2017, Thesis, University of Cambridge, doi:10.17863/CAM.25348 → p. 169
- Matthews A. G. d. G., Hensman J., Turner R., Ghahramani Z., 2016, in Proceedings of the 19th International Conference on Artificial Intelligence and Statistics. PMLR, pp 231–239 → p. 169
- McClintock T., et al., 2019, *Astrophys. J.*, 872, 53 → p. 129, 150
- Nishimichi T., et al., 2019, *Astrophys. J.*, 884, 29 → p. 129
- Oguri M., Hamana T., 2011, *Mon. Not. R. Astron. Soc.*, 414, 1851 → p. 130
- Planck Collaboration et al., 2020, *Astron. Astrophys.*, 641, A6 → p. 152, 153, 154, 155, 157
- Pratt G. W., Arnaud M., Biviano A., Eckert D., Ettori S., Nagai D., Okabe N., Reiprich T. H., 2019, *Space Science Reviews*, 215, 25 → p. 128
- Press W. H., Schechter P., 1974, *Astrophys. J.*, 187, 425 → p. 129
- Rasmussen C. E., Williams C. K. I., 2006, Gaussian Processes for Machine Learning. Adaptive Computation and Machine Learning, MIT Press, Cambridge, Mass → p. 168
- Reblinsky K., Bartelmann M., 1999, *Astron. Astrophys.*, 345, 1 → p.
- Saro A., et al., 2015, *Monthly Notices of the Royal Astronomical Society*, 454, 2305 → p. 136, 160
- Sartoris B., et al., 2016, *Mon. Not. R. Astron. Soc.*, 459, 1764 → p. 128

- Schneider P., 1996, *Mon. Not. R. Astron. Soc.*, 283, 837 → p. 130, 134, 142, 166
- Schneider P., Van Waerbeke L., Jain B., Kruse G., 1998, *Mon. Not. R. Astron. Soc.*, 296, 873 → p. 135
- Shan H., et al., 2018, *Monthly Notices of the Royal Astronomical Society*, 474, 1116 → p. 130, 162
- Shirasaki M., Nagai D., Lau E. T., 2016, *Monthly Notices of the Royal Astronomical Society*, 460, 3913 → p. 160
- Smith R. E., Marian L., 2011, *Monthly Notices of the Royal Astronomical Society*, 418, 729 → p. 149
- Tinker J., Kravtsov A. V., Klypin A., Abazajian K., Warren M., Yepes G., Gottlöber S., Holz D. E., 2008, *Astrophys. J.*, 688, 709 → p. 129
- Titsias M., 2009, in Proceedings of the Twelfth International Conference on Artificial Intelligence and Statistics. PMLR, pp 567–574 → p. 150, 151, 169
- Upadhye A., Biswas R., Pope A., Heitmann K., Habib S., Finkel H., Frontiere N., 2014, *Phys. Rev. D*, 89, 103515 → p. 132
- Velliscig M., van Daalen M. P., Schaye J., McCarthy I. G., Cacciato M., Le Brun A. M., Vecchia C. D., 2014, *Mon. Not. R. Astron. Soc.*, 442, 2641 → p. 130, 161
- Voit G. M., Evrard A. E., Bryan G. L., 2001, *ApJ*, 548, L123 → p. 160
- Von der Linden A., et al., 2014, *Mon. Not. R. Astron. Soc.*, 439, 2 → p. 136, 160
- Wang S., Haiman Z., May M., 2009, *The Astrophysical Journal*, 691, 547 → p. 161
- Wang C., et al., 2018, *Monthly Notices of the Royal Astronomical Society*, 475, 4020 → p. 144
- Yang X., Kratochvil J. M., Wang S., Lim E. A., Haiman Z., May M., 2011, *Phys. Rev. D*, 84, 043529 → p. 162
- Zhang Y., Annis J., 2022, *Monthly Notices of the Royal Astronomical Society: Letters*, 511, L30 → p. 160
- Zu Y., Mandelbaum R., 2015, *Mon. Not. R. Astron. Soc.*, 454, 1161 → p. 144
- van Haarlem M. P., Frenk C. S., White S. D. M., 1997, *Monthly Notices of the Royal Astronomical Society*, 287, 817 → p. 159

# 5 | Galaxy cluster aperture masses are more robust to baryonic effects than 3D halo masses

Based on

Stijn N. B. Debackere, Henk Hoekstra, Joop Schaye

*Monthly Notices of the Royal Astronomical Society, Volume 515, Issue 4,  
p. 6023-6031 (2022)*

Systematic uncertainties in the mass measurement of galaxy clusters limit the cosmological constraining power of future surveys that will detect more than  $10^5$  clusters. Previously, we argued that aperture masses can be inferred more accurately and precisely than 3D masses without loss of cosmological constraining power. Here, we use the Baryons and Haloes of Massive Systems (BAHAMAS) cosmological, hydrodynamical simulations to show that aperture masses are also less sensitive to changes in mass caused by galaxy formation processes. For haloes with  $m_{200m,dmo} > 10^{14} h^{-1} M_\odot$ , binned by their 3D halo mass, baryonic physics affects aperture masses and 3D halo masses similarly when measured within apertures similar to the halo virial radius, reaching a maximum reduction of  $\approx 3$  per cent. For lower-mass haloes,  $10^{13.5} < m_{200m,dmo}/h^{-1} M_\odot < 10^{14}$ , and aperture sizes  $\sim 1 h^{-1} \text{cMpc}$ , representative of weak lensing observations, the aperture mass is consistently reduced less ( $\lesssim 5$  per cent) than the 3D halo mass ( $\lesssim 10$  per cent for  $m_{200m}$ ). The halo mass reduction evolves only slightly, by up to 2 per centage points, between redshift 0.25 and 1 for both the aperture mass and  $m_{200m}$ . Varying the simulated feedback strength so the mean simulated hot gas fraction covers the observed scatter inferred from X-ray observations, we find that the aperture mass is consistently less biased than the 3D halo mass, by up to 2 per centage points at  $m_{200m,dmo} = 10^{14} h^{-1} M_\odot$ . Therefore, aperture mass calibrations provide a fruitful path to reduce the sensitivity of future cluster surveys to systematic uncertainties.

## 5.1 Introduction

Future large-scale surveys such as *Euclid*<sup>1</sup> and the Rubin Observatory Legacy Survey of Space and Time (LSST)<sup>2</sup> will study the competition between the growth of structure from the gravitational collapse of matter, and the accelerated expansion of the Universe due to dark energy or modified gravity (e.g. LSST Science Collaboration et al., 2009; Amendola et al., 2018). Galaxy clusters probe this effect particularly well because they are still actively forming due to the hierarchical growth of structure. Hence, the cluster abundance as a function of mass and time is sensitive to the amount of matter and the cosmological expansion history (e.g. Haiman et al., 2001; Allen et al., 2011).

The statistical power of current cluster surveys is still limited by their modest sample sizes. However, the recently released Atacama Cosmology Telescope (ACT) cluster sample already contains  $> 4000$  objects (Hilton et al., 2021) and for *Euclid* and the LSST sample sizes of  $> 10^5$  objects are expected (e.g. Tyson et al., 2003; Sartoris et al., 2016), ushering in the era of cluster surveys that will be limited by systematic uncertainties (Köhllinger et al., 2015).

Currently, building a cluster sample for a cosmology analysis requires three steps. First, clusters need to be detected in the data by identifying large matter overdensities either through the clustering of galaxies in space and redshift in optical images or through peaks in the X-ray emission, the Sunyaev-Zel'dovich effect or the weak lensing shear. Second, measures of cluster masses are calibrated, usually, by measuring the mass–observable relation that links the survey detection observable to the cluster mass derived from weak lensing observations. Third, by modelling the cluster selection through the survey observable, the measured abundance can be compared to predictions based on the theoretical, cosmology-dependent halo mass function to constrain the cosmological parameters of the Universe.

The exponential sensitivity of the cluster abundance to the cluster mass means that the accuracy of the cluster mass calibration limits the cosmological constraining power of cluster surveys. In Debackere et al. (2022), hereafter Paper I, we argued that aperture mass calibrations can greatly reduce the systematic uncertainty of cluster cosmology analyses. Aperture masses can be measured directly from weak lensing observations and in simulations, which avoids the deprojection of the observations and, hence, bypasses the additional biases and uncertainties introduced by the assumed spherically symmetric density profile in the deprojection. Moreover, aperture masses can be measured within fixed angular or physical apertures, with no need to derive an overdensity radius that depends on the assumed density profile. The aperture mass measurement uncertainty depends solely on the number of background galaxies used to sample the shear field and is  $\approx 2-3$  times smaller than the uncertainty in the inferred 3D halo masses. We also showed that, compared to the 3D halo mass function, the aperture mass function is more sensitive to changes in  $\Omega_m$  and  $w_a$ , similarly sensitive to changes in  $\sigma_8$ ,  $w_0$ , and  $n_s$ , and slightly less sensitive to changes in  $h$ . Hence, the aperture mass function can also constrain the cosmological evolution of the Universe.

<sup>1</sup><https://www.euclid-ec.org>

<sup>2</sup>[https://www.lsst.org/](https://www.lsst.org)

Since the projected mass within an aperture is actually derived from the weak lensing signal of galaxies outside of the aperture, the measured aperture mass is also less sensitive to sources of systematic error near the cluster centre such as miscentring and contamination of the lensing signal due to cluster galaxies (e.g. Mandelbaum et al., 2010; Hoekstra et al., 2012). Moreover, aperture masses can be measured unambiguously, even for triaxial and disturbed systems. Hence, the aperture mass measurement is relatively robust to different sources of systematic uncertainty.

One source of systematic uncertainty that will become important for future surveys, is the impact of baryonic physics on the inferred cluster mass compared with a universe containing only dark matter. All currently available theoretical predictions of the halo abundance rely on suites of large-volume dark matter-only (DMO) simulations (e.g. Tinker et al., 2008; Nishimichi et al., 2018; McClintock et al., 2019; Bocquet et al., 2020). However, we have known for a long time that baryonic processes related to galaxy formation can significantly modify cluster masses (e.g. Rudd et al., 2008; Stanek et al., 2009; Cui et al., 2012; Martizzi et al., 2014; Velliscig et al., 2014; Bocquet et al., 2016). To ensure realistic cluster gas fractions—and to prevent overcooling—simulations with sub-grid models for radiative cooling and star formation also need to include the feedback from Active Galactic Nuclei (AGN, e.g. McCarthy et al., 2010). For clusters with masses between  $10^{14} \lesssim m_{200m}/(h^{-1} M_\odot) \lesssim 10^{14.5}$ , where  $m_{200m}$  is the mass within a radius enclosing an average overdensity of  $\langle \rho \rangle = 200\rho_m(z) = 200\Omega_m\rho_{\text{crit}}(z=0)(1+z)^3$ , AGN feedback reduces the total halo mass by 1–5 per cent with a larger impact for lower halo masses, compared to the same halo in a universe comprising only dark matter (e.g. Velliscig et al., 2014; Bocquet et al., 2016). This mass reduction will become an important systematic uncertainty due to the increased statistical power of future surveys. Since the aperture mass measures the projected mass, it should be less sensitive to baryonic processes that dominate the cluster density profile on small scales (see e.g. Henson et al., 2017; Lee et al., 2018; Debackere et al., 2021).

To include the effect of baryons in a traditional cluster cosmology analysis that relies on DMO simulations to predict the cosmology dependence of the halo mass function, we need to include a baryonic correction in the theoretical halo mass to infer unbiased cosmological parameters (e.g. Balaguera-Antolínez & Porciani, 2013; Debackere et al., 2021). Thus, to write down the full forward model of the observed cluster number counts, we need a calibrated mass–observable relation,  $P(\mathcal{O}|\mathcal{M})$ , a theoretical prediction of the cosmology-dependent halo abundance,  $n(\mathcal{M}, \Omega)$ , where  $\Omega$  indicates the cosmological parameters, and a conversion between the observed cluster mass,  $\mathcal{M}_{\text{obs}}$ , and the theoretical halo mass,  $\mathcal{M}$ . This conversion includes the baryonic mass correction if the theoretical halo abundance was predicted using DMO simulations. We can then write the number counts,  $N(\mathcal{O}_i, z_j | \Omega)$ , within the observable bin,  $\mathcal{O}_i$ , and redshift bin,  $z_j$ , for the assumed cosmology,  $\Omega$ , as

$$\begin{aligned} N(\mathcal{O}_i, z_j | \Omega) &= \Omega_{\text{sky}} \int_{\mathcal{O}_i}^{\mathcal{O}_{i+1}} d\mathcal{O} \int_{z_j}^{z_{j+1}} dz \int d\mathcal{M}_{\text{dmo}} \mathcal{M}_{\text{hydro}} d\mathcal{M}_{\text{obs}} \\ &\quad \times P(\mathcal{O}|\mathcal{M}_{\text{obs}}, z) P(\mathcal{M}_{\text{obs}}|\mathcal{M}_{\text{hydro}}, z) \\ &\quad \times P(\mathcal{M}_{\text{hydro}}|\mathcal{M}_{\text{dmo}}, z) n_\Omega(\mathcal{M}_{\text{dmo}}, z | \Omega). \end{aligned} \quad (5.1)$$

Here, the observable and the redshift are integrated over their respective bins and the different halo masses from 0 to  $\infty$ . The theoretical halo mass function,  $n_\Omega$ , is calculated per unit survey area and redshift interval. We have introduced a redshift-dependent conversion between the theoretical halo mass from DMO simulations,  $\mathcal{M}_{\text{dmo}}$ , and the mass of the same halo in a universe containing baryons,  $\mathcal{M}_{\text{hydro}}$ . Moreover, we explicitly differentiate between  $\mathcal{M}_{\text{obs}}$ , the cluster mass measured observationally, and  $\mathcal{M}_{\text{hydro}}$ , the total halo mass measured in the hydrodynamical simulation, since  $\mathcal{M}_{\text{obs}}$  is a noisy measurement of  $\mathcal{M}_{\text{hydro}}$  due to observational systematic uncertainties. We will assume perfect knowledge of the selection function, to simplify the analysis, but we refer the interested reader to Section 5.1 of [Paper I](#) for a discussion about how the selection function will impact a cosmological analysis relying on aperture mass calibrations.

One straightforward way to eliminate the systematic uncertainty in converting halo masses from the DMO to the hydrodynamical simulation, is to predict the cosmology dependence of the halo abundance directly from large-volume hydrodynamical simulations for a grid of cosmological parameters, i.e. to predict  $n_\Omega(\mathcal{M}_{\text{hydro}}, z|\Omega)$ . However, due to the computational expense and the uncertain astrophysics, such an effort has so far not been undertaken.

The relation between the measured observable and halo mass,  $P(\mathcal{O}|\mathcal{M}_{\text{obs}})$  can be measured observationally, with the caveat that the inferred 3D halo mass depends on the density profile assumed in the deprojection, thus introducing a significant modelling uncertainty. The measurement uncertainty,  $P(\mathcal{M}_{\text{obs}}|\mathcal{M}_{\text{hydro}})$ , can be calibrated using simulations for both the aperture mass and the 3D halo mass. In [Paper I](#), we emphasized that the measurement uncertainty in the aperture mass,  $P(\Delta\mathcal{M}_{\text{obs}}|\Delta M)$ , depends only on the number density of background galaxies used to reconstruct the weak lensing shear. For 3D halo masses, on the other hand, the assumption of a density profile to deproject the observations and to infer the mass within a fixed overdensity radius, introduces a model-dependent bias in the inferred halo mass due to the mismatch between the spherically symmetric density profile and the true, triaxial halo, including substructure and correlated structure. Uncorrelated structure along the line-of-sight introduces an additional uncertainty (e.g. [Hoekstra, 2001](#)).

## 5

We use the Baryons and Haloes of Massive Systems (BAHAMAS) suite of large-volume cosmological, hydrodynamical simulations ([McCarthy et al., 2017, 2018](#)) to study the effect of feedback processes related to galaxy formation on halo aperture masses, that is, the  $P(\mathcal{M}_{\text{hydro}}|\mathcal{M}_{\text{dmo}})$  term in Eq. (5.1). The BAHAMAS simulations have been calibrated to reproduce the observed galaxy stellar mass function and the cluster hot gas fractions derived from X-ray observations, and they reproduce a wide range of observed properties of massive systems, enabling realistic cosmology forecasts that include the effect of baryons. We quantify the change in the aperture mass in BAHAMAS, and examine how it depends on the strength of the implemented feedback. We compare our results to the baryonic correction to the 3D DMO halo mass.

This paper is structured as follows: in Section 5.2, we introduce the BAHAMAS simulations, describe the aperture mass measurement, and we discuss the matching between haloes in the hydrodynamical and DMO simulations. In Section 5.3, we show the relation between the aperture mass and the 3D halo mass. In Section 5.4, we compare the mean change in the halo mass when including baryons and its scatter for both aperture masses

and 3D halo masses, we study its redshift evolution and sensitivity to different baryonic physics models that bracket the observationally allowed range of cluster gas fractions derived from X-ray observations. We conclude in Section 5.5.

## 5.2 Simulations

We measured the projected aperture masses of group and cluster-sized haloes from the BAHAMAS suite of cosmological hydrodynamical simulations (McCarthy et al., 2017). This suite of simulations is well-suited for our aims for several reasons. First, due to the  $(400h^{-1} \text{ cMpc})^3$  volume, we obtain a sufficiently large sample of massive haloes with  $m_{200m} > 10^{13.5} h^{-1} M_\odot$ . Second, the subgrid model parameters for the feedback from supernovae and AGN of the fiducial simulation have been calibrated to reproduce the present-day galaxy stellar mass function (GSMF), and, crucially for our work, the hot gas mass fractions of groups and clusters of galaxies. Moreover, variations of both the cosmological model and of the non-resolved, subgrid physics model parameters are available.

### 5.2.1 Simulation set

The BAHAMAS model remains unchanged from its predecessors OWLS (Schaye et al., 2010) and cosmo-OWLS (Le Brun et al., 2014), except for the values of the subgrid model parameters, which were chosen to reproduce the observed large-scale mass distribution of the Universe. Hence, we refer the interested reader to Schaye et al. (2010) for a detailed description of the different subgrid physics models.

The BAHAMAS suite consists of simulations run with a modified version of the Lagrangian TreePM-SPH code GADGET-3 (unpublished—for GADGET-2, see Springel, 2005) in boxes with a periodic side length of  $400h^{-1} \text{ cMpc}$  with initial conditions matching the maximum-likelihood cosmological parameter values from the WMAP9 data (Hinshaw et al., 2013), i.e.

$$\{\Omega_m, \Omega_b, \Omega_\Lambda, \sigma_8, n_s, h\} = \{0.2793, 0.0463, 0.7207, 0.821, 0.972, 0.700\}. \quad (5.2)$$

The initial linear power spectrum is generated at  $z = 127$  using CAMB<sup>3</sup> (Lewis et al., 2000) and converted into particle positions using S-GenIC<sup>4</sup>, which is a modified version of NGenIC<sup>5</sup>, that includes second-order Lagrangian perturbation theory and supports massive neutrinos. The hydrodynamical and their corresponding dark matter-only (DMO) simulations contain  $(2 \times 1024)^3$  and  $1024^3$  particles, respectively. This results in dark matter and (initial) baryonic particle masses of  $\approx 3.85 \times 10^9 h^{-1} M_\odot$  and  $\approx 7.66 \times 10^8 h^{-1} M_\odot$ , respectively, for the WMAP9 cosmology (the dark matter particle mass in the DMO simulations is  $\approx 4.62 \times 10^9 h^{-1} M_\odot$ ). The gravitational softening length is set to  $4h^{-1} \text{ kpc}$  in physical (comoving) coordinates for  $z \leq (>)3$ .

<sup>3</sup><https://camb.info/>

<sup>4</sup><https://github.com/sbird/S-GenIC>

<sup>5</sup><https://www.h-its.org/2014/11/05/ngenic-code/>

Haloes are identified using the Friends-of-Friends (FoF) algorithm with a linking length of 0.2 and their spherical overdensity masses are calculated within the FoF halo, including particles that are not gravitationally bound, centred on the minimum of the gravitational potential using SUBFIND (Springel et al., 2001). The so-called subgrid models for non-resolved physical processes were taken from the preceding OWLS and cosm-OWLS projects (Schaye et al., 2010; Le Brun et al., 2014, respectively). These models include recipes for the radiative heating and cooling of the 11 dominant elements tracked in the simulations (H, He, C, N, O, Ne, Mg, Si, S, Ca, Fe), by interpolating the tabulated CLOUDY (Ferland et al., 1998) rates of Wiersma et al. (2009a) as a function of density, temperature and redshift. Star formation follows the implementation of Schaye & Dalla Vecchia (2008), fixing the unresolved cold interstellar medium (ISM) gas to an effective equation of state and a pressure-dependent star formation efficiency in order to reproduce the observed Kennicut–Schmidt star formation law. Stellar evolution and the chemical enrichment of gas due to both type Ia and type II supernovae, stellar winds, and asymptotic giant branch (AGB) stars are implemented following Wiersma et al. (2009b). Supernova feedback is implemented kinetically, following Dalla Vecchia & Schaye (2008). Finally, black hole seeding in low-mass galaxies, black hole growth through mergers and gas accretion, and the feedback from active galactic nuclei are modelled following Booth & Schaye (2009).

In Table 5.1, we list the specific simulations of the BAHAMAS suite that we use in this work. We list the DMO simulation and the hydrodynamical simulations with identical initial conditions and possible variations in the subgrid model assumptions. We will investigate the impact of variations in the strength of the AGN feedback by increasing (decreasing) the heating temperature  $\Delta T_{\text{heat}}$  by 0.2 dex relative to the calibrated, fiducial value of  $\Delta T_{\text{heat}} = 10^{7.8}$  K. This results in lower (higher) hot gas mass fractions in groups and clusters of galaxies (see McCarthy et al., 2017).

Table 5.1: A list of all the simulations (dark matter-only and the matching hydrodynamical runs) for which we computed the halo aperture masses. BAHAMAS simulation names follow the convention TYPE\_nuN\_ZZZ, with N the sum of the neutrino masses in eV and ZZZ the base cosmological model. All simulations have periodic side lengths of  $400h^{-1}$  cMpc and  $1024^3$  dark matter particles (with the same number of baryonic particles in the hydrodynamical case).

simulation	redshifts	variation
DMONLY_nu0_WMAP9	0.25, 0.5, 1	—
AGN_TUNED_nu0_WMAP9	0.25, 0.5, 1	$\Delta T_{\text{heat}} = 10^{7.8}$ K
AGN_7p6_nu0_WMAP9	0.25, 0.5, 1	$\Delta T_{\text{heat}} = 10^{7.6}$ K
AGN_8p0_nu0_WMAP9	0.25, 0.5, 1	$\Delta T_{\text{heat}} = 10^{8.0}$ K

### 5.2.2 Aperture mass measurement

We follow the literature and refer to the excess projected mass within an aperture of size  $R_1$ , defined as

$$\begin{aligned}\Delta M(< R_1 | R_2, R_m) &= \pi R_1^2 (\bar{\Sigma}(< R_1) - \bar{\Sigma}(R_2 < R < R_m)) \\ &= M(< R_1) - M_{\text{bg}}(< R_1),\end{aligned}\quad (5.3)$$

as the aperture mass (e.g. [Bartelmann & Schneider, 2001](#)). The background surface mass density within  $R_1$  is inferred from the annulus between  $R_2$  and  $R_m$ . We have introduced the mean surface mass density

$$\bar{\Sigma}(R_2 < R < R_m) = \frac{2}{(R_m^2 - R_2^2)} \int_{R_2 < R < R_m} dR R \Sigma(R). \quad (5.4)$$

In Appendix A of [Paper I](#), we showed that this definition of the aperture mass matches the  $\zeta_c$ -statistic ([Clowe et al., 1998](#)), which measures the enclosed excess surface mass density within  $R_1$  from the observed weak lensing galaxy shears between  $R_1$  and  $R_m$ .

For our analysis, we generated projected surface mass density maps from the full simulation volume for each simulation in Table 5.1. First, we projected all the particles along the three principal axes of the simulation box. Then, we binned the projected particles into a pixel grid of  $0.05 h^{-1}$  cMpc  $\times 0.05 h^{-1}$  cMpc resolution and obtained the surface mass density  $\Sigma(i, j)$  for pixel  $(i, j)$  by summing the masses for all particles with coordinates  $(x, y)$  belonging to the pixel  $(i, j)$  and dividing by the pixel area. From the surface mass density, we calculated the aperture mass using Eq. (5.3) with  $R_1 = [0.5, 1.0, 1.5] h^{-1}$  cMpc and  $(R_2, R_m) = (2, 3) h^{-1}$  cMpc, centred on the potential minimum, for all haloes with  $m_{200m, \text{dmo}} > 10^{13} h^{-1} M_\odot$ . The chosen apertures are representative of weak lensing observations (e.g. [Hoekstra et al., 2012](#); [Applegate et al., 2014](#)).

### 5.2.3 Matching haloes to their DMO counterparts

To quantify the influence of baryons on the halo aperture masses, we compare the aperture masses from haloes in the hydrodynamical simulations to those of their counterparts in a universe including only dark matter particles. (Technically, baryons are included in the transfer function used to calculate the initial conditions.) Since all BAHAMAS simulations with the same cosmological model have identical initial conditions and consistent, unique dark matter particle identification numbers, we can link haloes between the DMO and hydrodynamical simulations. We follow the linking method of [Velliscig et al. \(2014\)](#). Briefly, we identify each halo in the reference simulation to the halo in the matching simulation that contains at least half of its  $N_{\text{mb}} = 50$  most-bound particles. Only if the same haloes are also linked when swapping the reference and the matching simulation in this procedure, do we consider them genuine counterparts. Haloes with  $m_{200m, \text{dmo}} > 10^{13} h^{-1} M_\odot$  are matched with a success rate higher than 98 per cent in all simulations.

One important caveat, which is especially important for aperture mass measurements, is that the dynamical history can differ between matched haloes in the hydrodynamical and the DMO simulation. Star formation and feedback processes modify the matter distribution, even though the distribution of haloes statistically remains the same on scales larger than the halo virial radius (e.g. [van Daalen et al., 2014](#)). The median 3D offset,  $\Delta r$ , between the 3974 matched haloes with  $m_{200m,\text{hydro}} > 10^{13.5} h^{-1} M_\odot$  is  $\approx 0.1 h^{-1} \text{cMpc}$ , with 17 (151) haloes having  $\Delta r > 1 (0.2) h^{-1} \text{cMpc}$ . Upon visual inspection, the majority of the systems with large offsets are mergers where the haloes are identified as different components between the hydrodynamical and the DMO simulation, resulting in significantly different aperture mass measurements.

We exclude all haloes with 3D offsets  $\Delta r > 0.2 h^{-1} \text{cMpc}$  from our sample. Given the minimum aperture size of  $R_1 = 0.5 h^{-1} \text{cMpc}$ , this cutoff ensures that the aperture mass measurements are not significantly affected by possibly misidentified haloes. The main effect of this selection criterion is to slightly reduce the scatter in the baryonic mass correction at the high 3D halo mass end, as some of the most massive haloes in BAHAMAS are merging and do not visually match between the hydrodynamical and the DMO simulation.

### 5.3 The relation between aperture mass and 3D halo mass

In Fig. 5.1, we show the full distribution of projected masses within apertures of size  $R_1 = 1 h^{-1} \text{cMpc}$  as a function of the 3D halo mass,  $m_{200m,\text{hydro}}$ , for all haloes at  $z = 0.5$  in the AGN\_TUNED\_nu0\_WMAP9 simulation. The median aperture mass at fixed 3D halo mass is shown with different coloured lines for different apertures  $R_1$ . We indicate the halo mass for which  $r_{200m} = R_1$  with coloured diamonds. Within a fixed aperture, aperture masses are slightly higher than the 3D halo mass when  $R_1 > r_{200m}$  and lower when  $R_1 < r_{200m}$  as the halo mass represents a smaller or larger fraction of the total aperture mass, respectively. Larger apertures result in larger masses. For masses  $m_{200m,\text{hydro}} \lesssim 10^{14} h^{-1} M_\odot$  a small but non-negligible fraction of the haloes will be surrounded by more massive structures along the line-of-sight, resulting in negative aperture masses. The fraction of haloes with negative aperture mass within  $R_1 = 1 h^{-1} \text{cMpc}$  increases from 0 per cent for  $m_{200m,\text{hydro}} = 10^{14} h^{-1} M_\odot$  to  $\approx 5$  per cent for  $m_{200m,\text{hydro}} = 10^{13.5} h^{-1} M_\odot$ . The fraction of negative aperture masses increases with increasing aperture size.

From the bottom panel of Fig. 5.1, we can see that the scatter in the aperture mass at  $R_1 = 1 h^{-1} \text{cMpc}$  at fixed 3D halo mass, calculated as half the difference between the 84th and the 16th percentiles of the aperture mass at fixed 3D mass, increases from  $\sigma_{\log \Delta M} \approx 0.15$  for  $m_{200m,\text{hydro}} = 10^{14.5} h^{-1} M_\odot$  to  $\approx 0.3$  for  $10^{14} h^{-1} M_\odot$ . Smaller apertures result in smaller scatter. We discussed in [Paper I](#) that the increase in the scatter of the aperture mass measured within a fixed aperture with decreasing 3D halo mass is caused by the large variation in the correlated structure surrounding the halo, which contributes more significantly to the total aperture mass for lower-mass haloes.

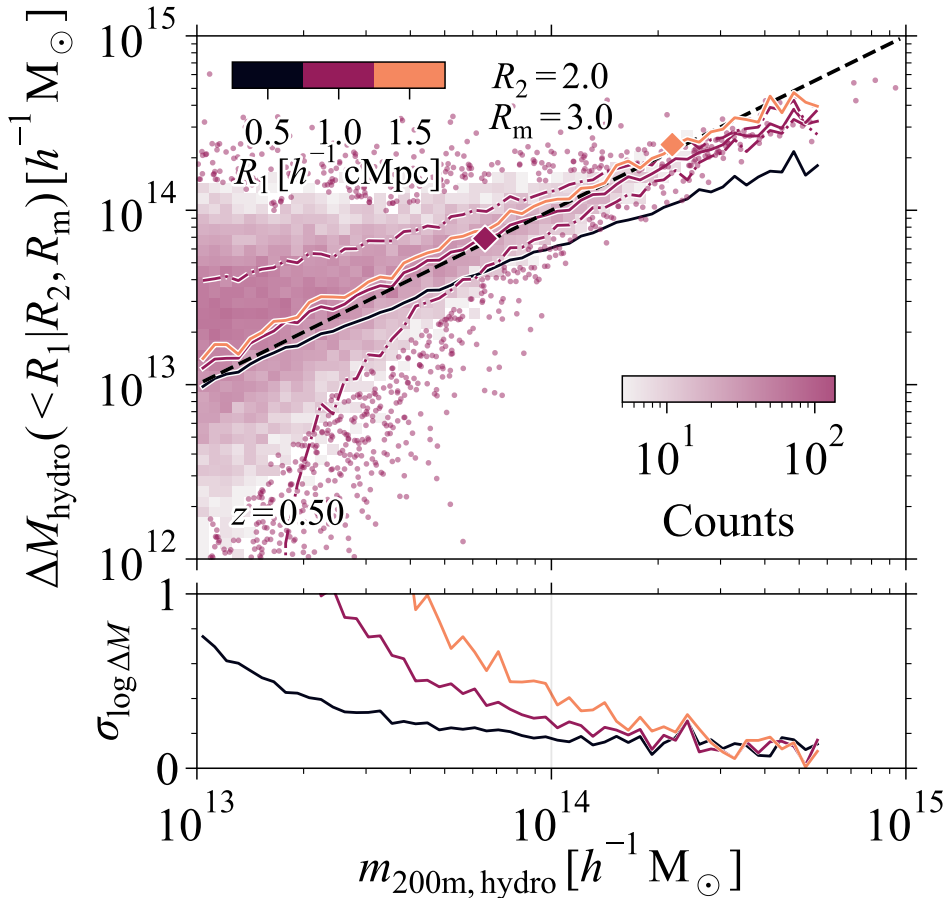


Figure 5.1: *Top panel:* The distribution of aperture masses within  $1 h^{-1} \text{cMpc}$ ,  $\Delta M_{\text{hydro}}(< R_1 | R_2 = 2 h^{-1} \text{cMpc}, R_m = 3 h^{-1} \text{cMpc})$ , as a function of the 3D halo mass,  $m_{200m, \text{hydro}}$ , at  $z = 0.5$ . The median relations for different aperture sizes are shown as coloured lines, with the dash-dotted lines indicating the 16th to 84th percentile scatter for  $R_1 = 1 h^{-1} \text{cMpc}$ . The one-to-one relation is indicated by the black, dashed line. The coloured diamonds indicate the halo mass where  $r_{200m} = R_1$ . There is a large scatter in aperture mass at fixed, low  $m_{200m, \text{hydro}}$  due to the variation in the structure along the line-of-sight to different haloes. The aperture mass tends to be slightly higher (lower) than the 3D halo mass when  $R_1 > (<)r_{200m, \text{hydro}}$ . *Bottom panel:* The logarithmic scatter in the aperture mass at fixed  $m_{200m, \text{hydro}}$ , measured as half the difference between the 84th and 16th percentiles. The scatter increases for lower 3D halo masses since matter outside the halo dominates the aperture mass. For  $m_{200m, \text{hydro}} \lesssim 10^{13.5} h^{-1} M_\odot$ , the scatter increases significantly since > 5 per cent of the haloes is surrounded by more massive structures resulting in negative aperture masses.

## 5.4 Aperture mass correction due to baryonic effects

We compare the aperture mass for matched haloes between the hydrodynamical and the DMO simulation to study the change in mass due to the inclusion of baryons and their associated galaxy formation processes. As shown by Eq. (5.1), the change in the cluster mass due to baryons can be included in the forward model of the cluster abundance when the cosmology dependence is predicted using DMO simulations. The relevant term in Eq. (5.1),  $P(\mathcal{M}_{\text{hydro}}|\mathcal{M}_{\text{dmo}}, z)$ , complicates the analysis since baryons introduce a mass and possibly redshift-dependent bias between  $\mathcal{M}_{\text{dmo}}$  and  $\mathcal{M}_{\text{hydro}}$ . Moreover, the uncertainty in  $\mathcal{M}_{\text{hydro}}$  at fixed  $\mathcal{M}_{\text{dmo}}$  needs to be accounted for correctly in order to convert the theoretical halo mass,  $\mathcal{M}_{\text{dmo}}$ , to the cluster observable,  $\mathcal{O}$ .

### 5.4.1 Binned by 3D halo mass

In a cluster cosmology analysis, baryonic effects enter as a correction in the theoretical, DMO halo mass, given by  $P(\mathcal{M}_{\text{hydro}}|\mathcal{M}_{\text{dmo}}, z)$  in Eq. (5.1). We compare the correction in the aperture mass and the 3D halo mass for the same halo sample by binning haloes according to their 3D DMO halo mass. We note that an analysis that uses the aperture mass function to model the cosmology-dependence of the cluster sample, needs to bin the halo sample by the aperture mass to model the correction, as we do in Section 5.4.2.

To calculate the mean mass correction of the halo sample binned by the 3D DMO halo mass, we compute the ratio between the mean stacked halo masses of the matched haloes in the hydrodynamical and DMO simulations, i.e.  $\langle \mathcal{M}_{\text{hydro}} \rangle / \langle \mathcal{M}_{\text{dmo}} \rangle$ . Especially for the aperture mass, it is important to use the ratio of the mean masses instead of the mean of the mass ratios of individual haloes, i.e.  $\langle \mathcal{M}_{\text{hydro}} / \mathcal{M}_{\text{dmo}} \rangle$ , because of the large scatter in the aperture mass at fixed 3D halo mass (see Fig. 5.1). Low-aperture mass haloes contribute a disproportionately large uncertainty to  $\langle \mathcal{M}_{\text{hydro}} / \mathcal{M}_{\text{dmo}} \rangle$  since a small difference in the projected mass, due to the different halo dynamical history in the hydrodynamical and the DMO simulations, causes large fluctuations in the individual mass ratios. These low-aperture mass haloes do not contribute significantly to the mean mass in the halo stack, minimizing their impact on  $\langle \mathcal{M}_{\text{hydro}} \rangle / \langle \mathcal{M}_{\text{dmo}} \rangle$ .

In the top panel of Fig. 5.2, we show the mean aperture mass in the hydrodynamical simulation relative to the DMO simulation in a stack of haloes binned by their 3D DMO halo mass,  $m_{200m,\text{dmo}}$ . The different coloured lines show the binned aperture mass changes for different aperture sizes, and the gray, dash-dotted and dashed lines for  $m_{200m}$  and  $m_{500c}$ , respectively. Since the halo baryon fraction increases with the halocentric distance, the baryonic correction decreases for larger apertures and radii enclosing a smaller overdensity. Since more massive haloes are able to retain a larger fraction of the cosmic baryons, the mass change also decreases with increasing 3D halo mass. For the most massive haloes,  $m_{200m,\text{dmo}} \gtrsim 10^{14.5} (10^{14}) h^{-1} M_\odot$ , the mass reduction is  $\lesssim 1 (5)$  per cent for all halo mass measures. For lower-mass haloes, the aperture mass is consistently less biased than the 3D halo mass.

The halo mass change due to the inclusion of baryons is caused by the heating of the intracluster gas by AGN feedback and galactic winds, transporting baryons to the halo outskirts and reducing the inner halo baryon fraction (e.g. Velliscig et al., 2014). For

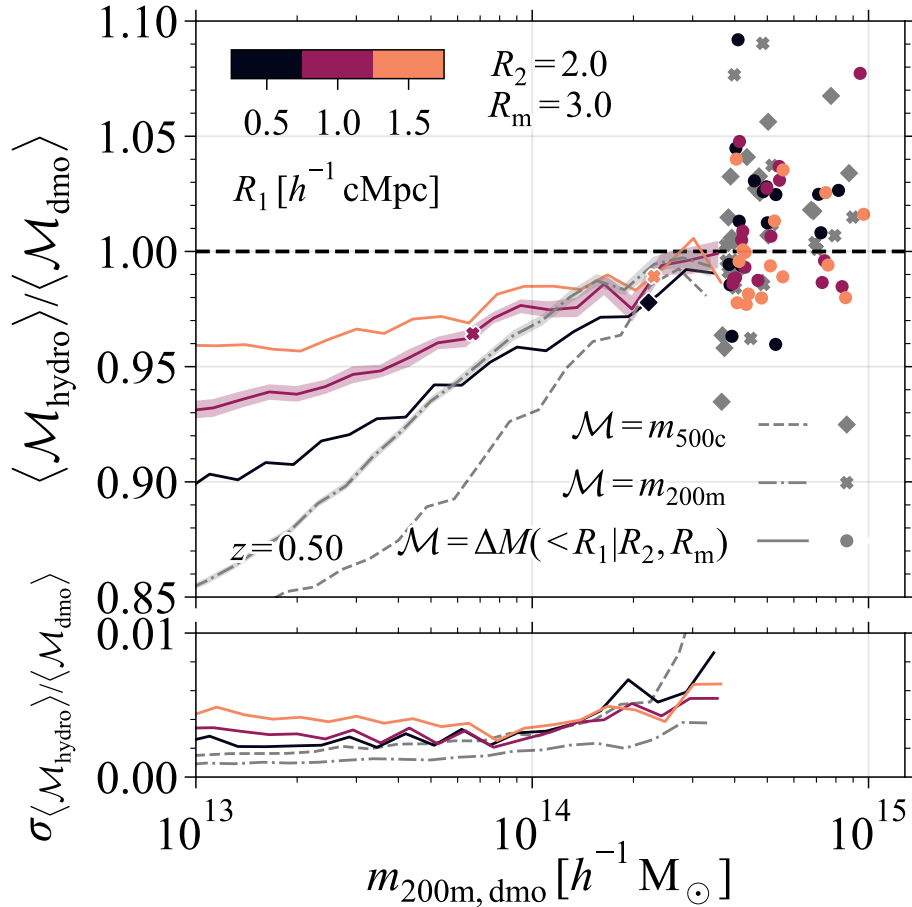


Figure 5.2: *Top panel:* The mean aperture mass of haloes in the reference hydrodynamical simulation relative to the mean mass of the matched dark matter-only simulation counterparts at  $z = 0.5$ , stacked in bins of the 3D dark matter-only halo mass. Different coloured lines show different aperture sizes  $R_1 = [0.5, 1, 1.5] h^{-1} \text{ cMpc}$ , with the background contribution calculated between  $R_2 = 2 h^{-1} \text{ cMpc}$  and  $R_m = 3 h^{-1} \text{ cMpc}$ , representative for weak lensing observations. Dash-dotted (dashed) gray lines show the change in the 3D halo mass  $\langle m_{200\text{m},\text{hydro}} \rangle / \langle m_{200\text{m},\text{dmo}} \rangle$  ( $\langle m_{500\text{c},\text{hydro}} \rangle / \langle m_{500\text{c},\text{dmo}} \rangle$ ). Shaded regions show the bootstrapped error on the ratio of the mean masses for  $m_{200\text{m}}$  and  $\Delta M(<1 h^{-1} \text{ cMpc}|R_2, R_m)$ . For bins with fewer than 10 haloes, individual measurements are shown with coloured points for the aperture mass, and gray crosses (diamonds) for the 3D halo mass,  $m_{200\text{m}}$  ( $m_{500\text{c}}$ ). Coloured crosses (diamonds) show the 3D halo mass for which  $r_{200\text{m},\text{dmo}} = R_1$  ( $r_{500\text{c},\text{dmo}} = R_1$ ). For  $m_{200\text{m},\text{dmo}} \gtrsim 10^{14} h^{-1} \text{ M}_\odot$ , the mass change is  $< 5$  per cent for all mass measures. For halo masses  $\lesssim 10^{14} h^{-1} \text{ M}_\odot$ , the aperture mass is consistently less biased than the 3D halo mass. *Bottom panel:* The  $1\sigma$  bootstrapped uncertainty in the mean mass change is  $< 1$  per cent for all mass measurements. For high-mass haloes the decrease in the number of haloes causes the larger uncertainty.

this reason, mass measurements that include more of the outer halo density profile will differ less from the DMO halo mass. We can see from Fig. 5.2 that aperture masses are less sensitive to the impact of baryons than 3D halo masses as masses measured within  $R_1 = 0.5 h^{-1} \text{ cMpc}$  are less biased than  $m_{200m}$  even when  $r_{200m,\text{dmo}} > 0.5 h^{-1} \text{ cMpc}$  because aperture masses probe scales larger than  $R_1$  along the projection axis.

In the bottom panel of Fig. 5.2, we show the bootstrapped uncertainty in the ratio between the mean halo masses measured in the hydrodynamical and DMO simulations. We obtain the bootstrapped distribution of the mean halo mass in each bin of  $m_{200m,\text{dmo}}$  by resampling the haloes 500 times with replacement. Then, we calculate the uncertainty as half the difference between the 84th and the 16th percentiles. We also show the uncertainty as the shaded region in the top panel of Fig. 5.2 for the cases  $R_1 = 1 h^{-1} \text{ cMpc}$  and  $m_{200m}$ . The uncertainty in the mean mass change is smallest for  $m_{200m}$ , being between 1.5 to 2 times smaller than the uncertainty in  $m_{500c}$  and the aperture mass measured within  $R_1 \leq 1 h^{-1} \text{ cMpc}$ . The increase in the uncertainty for higher-mass haloes is due to the limited sample size of the BAHAMAS simulation. The mass change for all mass measurements can be determined with subper cent accuracy with the BAHAMAS cluster sample of  $\approx 30$  (3800) haloes with  $m_{200m,\text{hydro}} > 10^{14.5} (10^{13.5}) h^{-1} M_\odot$ .

#### 5.4.2 Binned by aperture mass

For a cluster cosmology analysis that uses the aperture mass function to model the cosmology-dependence of the number counts, the relevant mass correction is measured in bins of the aperture mass, not the 3D halo mass. In Fig. 5.3, we show the mean aperture (solid lines) and 3D (dash-dotted lines) mass relative to the mean mass of matched haloes in the DMO simulation, binned by the DMO aperture mass measured within different apertures (different coloured lines). We only include haloes with  $m_{200m,\text{hydro}} > 10^{13.5} h^{-1} M_\odot$  to ensure a clean cluster sample. From Fig. 5.1, we can clearly see that haloes with relatively low 3D halo masses can result in aperture masses  $\Delta M \gtrsim 10^{13.5} h^{-1} M_\odot$ . However, few of these haloes would actually be identified as clusters if we had applied an observational cluster-finding algorithm instead of calculating the aperture mass for all friends-of-friends haloes identified in the simulation. For simplicity, we use the 3D halo mass in the hydrodynamical simulations as the cluster selection criterion.

To interpret the baryonic correction when binning by the aperture mass,  $\Delta M_{\text{dmo}}$ , we identify the aperture mass with the 3D halo mass bin,  $m_{200m,\text{dmo}}$ , whose haloes have the same mean aperture mass,  $\langle \Delta M_{\text{dmo}} | m_{200m,\text{dmo}} \rangle$ . Then, we see that both the 3D halo mass and the aperture mass are similarly reduced for haloes with  $R_1 \lesssim r_{200m,\text{dmo}}$  (equality is indicated with coloured crosses). For lower-mass haloes ( $R_1 > r_{200m,\text{dmo}}$ ), the aperture mass is dominated by the halo environment or structures aligned by chance along the line-of-sight, not by the 3D halo mass, resulting in a smaller reduction in the aperture mass than in the 3D halo mass.

Due to the large size of the BAHAMAS cluster sample, the bootstrapped uncertainty in the mass change, shown in the bottom panel of Fig. 5.3, is  $\lesssim 1$  per cent for all mass measurements. The sudden rise in the uncertainty towards low aperture masses for the larger aperture sizes is caused by the increased importance of matter outside of the halo, either in the halo environment or chance line-of-sight alignments. To put this

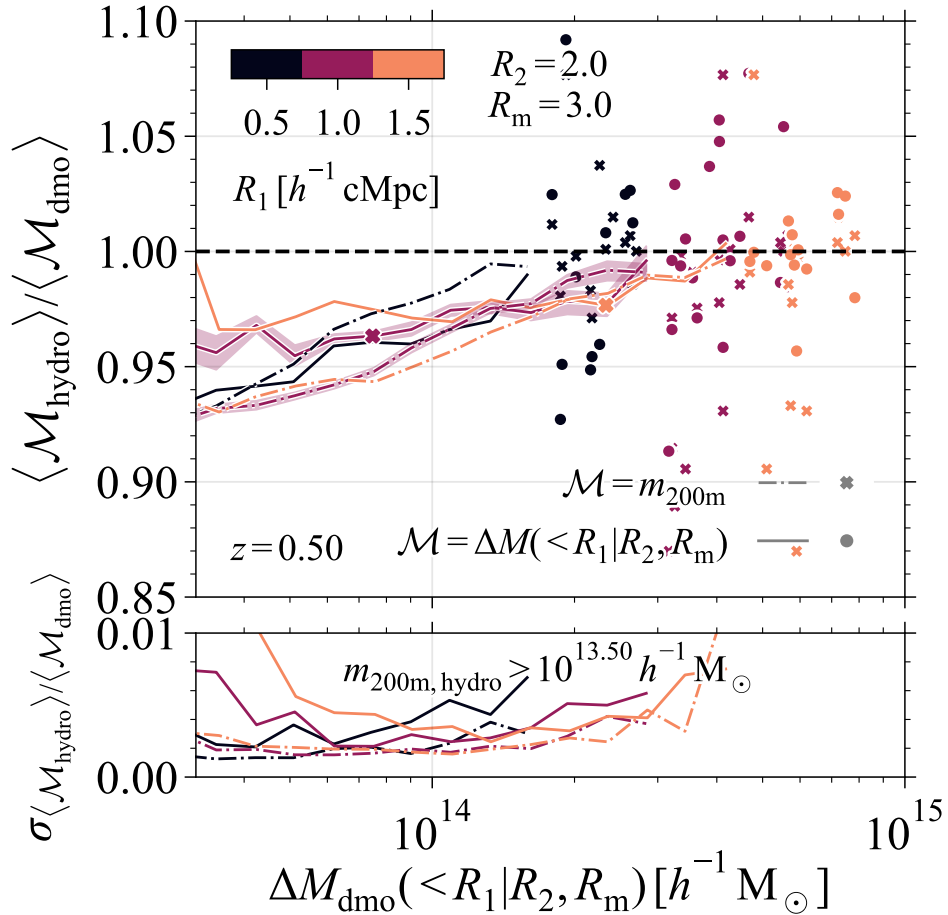


Figure 5.3: *Top panel:* The mean aperture mass of haloes, measured within different apertures (solid, coloured lines), in the reference hydrodynamical simulation relative to their matched counterparts from the dark matter-only simulation at  $z = 0.5$ , stacked in bins of the dark matter-only aperture mass for all haloes with  $m_{200m,\text{hydro}} > 10^{13.5} h^{-1} M_\odot$ . The background contribution to the aperture mass is calculated within  $R_2 = 2 h^{-1} \text{cMpc}$  and  $R_m = 3 h^{-1} \text{cMpc}$ . Coloured, dash-dotted lines show the 3D halo mass ratio,  $\langle m_{200m,\text{hydro}} \rangle / \langle m_{200m,\text{dmo}} \rangle$ , within the different aperture mass bins. Coloured crosses indicate the mean aperture mass for haloes with  $r_{200m,\text{dmo}} = R_1$ . Shaded regions show the bootstrapped error on the ratio of the mean masses for  $m_{200m}$  and  $\Delta M$  for  $R_1 = 1 h^{-1} \text{cMpc}$ . For bins with fewer than 10 haloes, individual measurements are shown with points and crosses for the aperture mass and the 3D halo mass, respectively. Aperture masses change less than (similarly to) 3D halo masses for haloes with  $r_{200m,\text{dmo}} \lesssim (\gtrsim) R_1$ . *Bottom panel:* The  $1\sigma$  bootstrapped uncertainty in the mass change for the different mass measures. The uncertainty increases for both low aperture masses with  $R_1 \gg r_{200m,\text{dmo}}$ , dominated by matter outside the halo, and high aperture masses due to their lower numbers in BAHAMAS.

in context, for aperture masses measured from weak lensing observations in apertures  $R_1 = [0.5, 1.0, 1.5] h^{-1} \text{ cMpc}$  and assuming a WMAP9 cosmology, the expected noise level due to the finite number of background galaxies with an individual galaxy shape noise of  $\sigma_{\text{gal}} = 0.3$  and a background number density of  $n_{\text{gal}} = 30 \text{ arcmin}^{-2}$ , corresponds to masses of  $\Delta M = [1.4, 3.1, 5.2] \times 10^{13} h^{-1} M_\odot$  (see Eq. A10 of Paper I), similar to the masses where the uncertainty increases. Hence, the aperture mass range with the increased uncertainty would most likely not be included in a cosmological analysis.

### 5.4.3 Scatter in the baryonic correction

Besides the bias in the mean mass of matched haloes in the hydrodynamical and DMO simulations, the scatter is also important in a cosmological analysis. If not properly accounted for, scatter in the mass of haloes in the hydrodynamical simulation at fixed DMO halo mass can significantly bias the cosmological parameter inference. We focus on the 16th to 84th percentile scatter in the  $\mathcal{M}_{\text{hydro}} - \mathcal{M}_{\text{dmo}}$  relation in Fig. 5.4. In the top panel, we repeat the mean relation for both the aperture mass measurements and the 3D halo mass,  $m_{200m}$ , each binned by their respective DMO halo mass. Hence, the aperture and 3D mass measurements cannot be compared directly since a fixed value  $\mathcal{M}_{\text{dmo}}$  does not include the same haloes. We show the scatter for  $R_1 = 1 h^{-1} \text{ cMpc}$  and  $m_{200m}$  to compare the magnitude of the scatter to the bias for the different mass measures.

In the bottom panel of Fig. 5.4, we show the  $1\sigma$  scatter for both the aperture mass and the 3D halo mass, calculated as half the difference between the 84th and 16th percentiles. For  $\mathcal{M}_{\text{dmo}} \gtrsim 10^{14} h^{-1} M_\odot$ , the scatter  $\sigma_{\log \mathcal{M}_{\text{hydro}} | \mathcal{M}_{\text{dmo}}} \lesssim 0.05$  for all the different mass measures. Towards lower halo masses, the scatter in the 3D halo mass stays below 0.04, while the scatter in the larger apertures increases to  $\approx 0.07$  and  $\approx 0.1$  for  $R_1 = 1 h^{-1} \text{ cMpc}$  and  $R_1 = 1.5 h^{-1} \text{ cMpc}$ , respectively. The aperture mass scatter is larger due to the increased contribution of matter outside of the halo.

5

In conclusion, aperture masses are, on average, slightly less sensitive to the changes in the cluster mass due to baryons because they measure the projected density, which includes contributions from larger radii. However, this also results in a slightly larger scatter. A detailed comparison of a cosmology analysis using either the aperture mass or the 3D halo mass would also need to include the additional effect of the survey observable and its scatter at fixed aperture mass or 3D halo mass.

### 5.4.4 Redshift evolution

Since future surveys will probe clusters with high completeness and purity up to high redshifts of  $z \approx 2$  (e.g. Adam et al., 2019), we need to study how the impact of the inclusion of baryons on the cluster mass changes with redshift. In Fig. 5.5, we show the redshift evolution of the change in the aperture mass,  $\Delta M(< 1 h^{-1} \text{ cMpc} | R_2 = 2 h^{-1} \text{ cMpc}, R_m = 3 h^{-1} \text{ cMpc})$ , and the 3D halo mass,  $m_{200m}$ , in bins of the 3D DMO halo mass,  $m_{200m,\text{dmo}}$ , between  $z = 0.25$  and  $z = 1$  where most of the clusters will be detected. Both the aperture mass and the 3D halo mass bias decrease slightly with increasing redshift, with the aperture mass always being less suppressed for low-mass haloes than

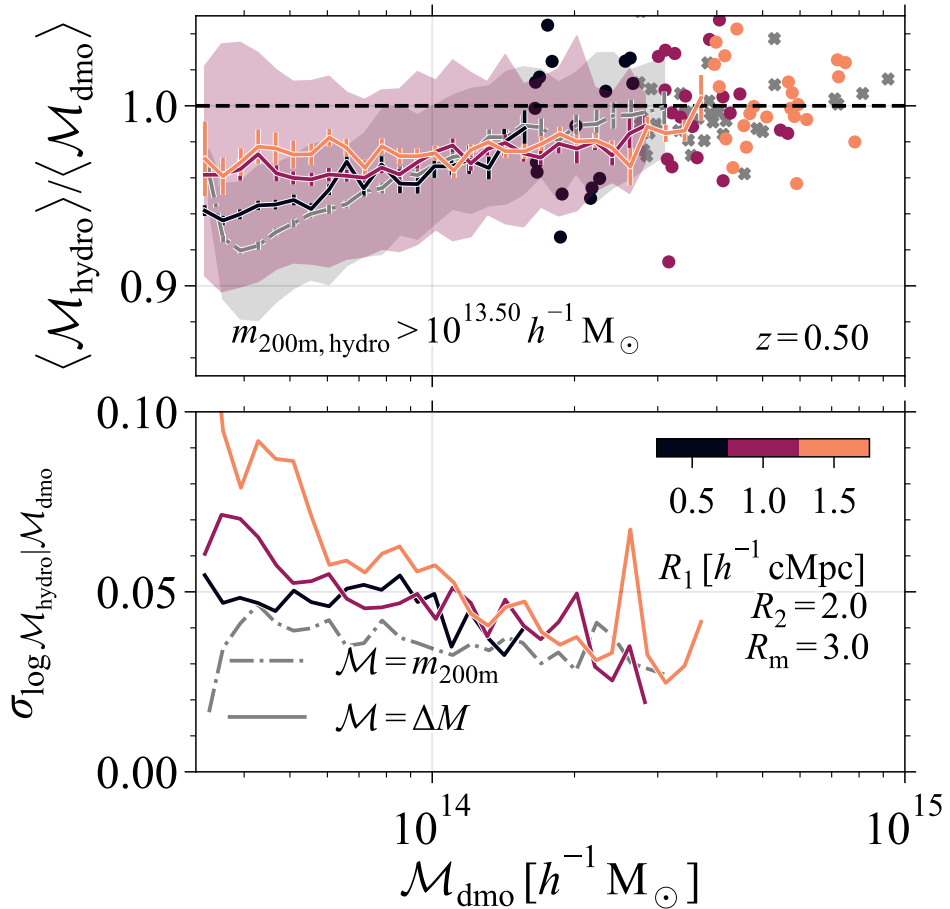


Figure 5.4: *Top panel:* The mean bias for the aperture mass (solid lines) and the 3D halo mass (dash-dotted lines) as a function of the corresponding mass of the matching dark matter-only halo at  $z = 0.5$  for all haloes with  $m_{200m, \text{hydro}} > 10^{13.5} h^{-1} M_\odot$ . Shaded regions show the  $1\sigma$  scatter for  $R_1 = 1 h^{-1} \text{cMpc}$  and  $m_{200m}$ . Error bars show the bootstrapped uncertainty on the mean mass bias. Coloured lines show the different aperture sizes  $R_1 = [0.5, 1, 1.5] h^{-1} \text{cMpc}$ , with the background contribution calculated within  $R_2 = 2 h^{-1} \text{cMpc}$  and  $R_m = 3 h^{-1} \text{cMpc}$ . Bins with fewer than 10 haloes show the individual results. Results for aperture and 3D mass measurements are not directly comparable since a fixed  $\mathcal{M}_{\text{dmo}}$  corresponds to different haloes. *Bottom panel:* The  $1\sigma$  scatter in  $\mathcal{M}_{\text{hydro}}$  at fixed  $\mathcal{M}_{\text{dmo}}$  at  $z = 0.5$ . For all mass measures, the scatter is smaller than  $\approx 5$  per cent for  $\mathcal{M}_{\text{dmo}} \gtrsim 10^{14} h^{-1} M_\odot$ . For lower masses, the aperture mass scatter increases more than the 3D halo mass scatter due to the contribution of matter outside haloes.

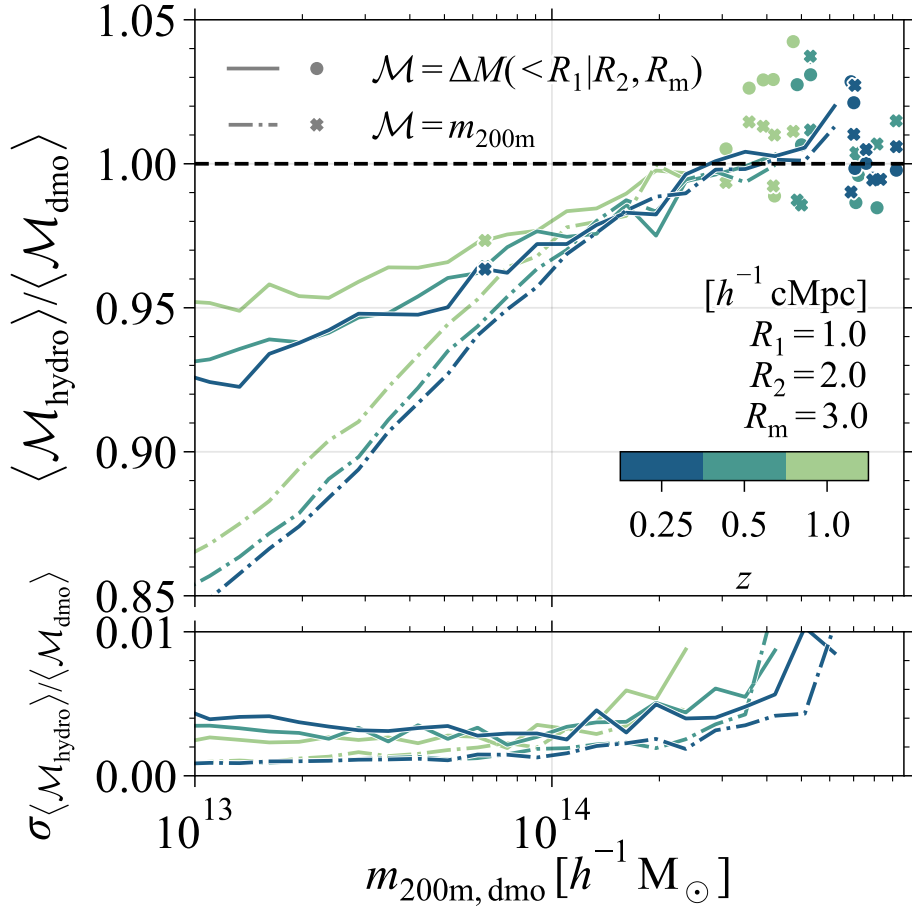


Figure 5.5: *Top panel:* The redshift dependence of the change in the aperture mass,  $\Delta M_{\text{hydro}}(< 1 h^{-1} \text{cMpc} | R_2, R_m)$  (solid lines), and the 3D halo mass,  $m_{200m}$  (dash-dotted lines), stacked in bins of the 3D dark matter-only halo mass. All background correction annuli span the region between  $R_2 = 2 h^{-1} \text{cMpc}$  and  $R_m = 3 h^{-1} \text{cMpc}$ . Coloured lines show the different redshifts and crosses the halo mass for which  $r_{200m, \text{dmo}} = R_1$ . Bins with fewer than 5 haloes show the individual results. The mass reduction decreases with increasing redshift at fixed 3D halo mass. At all redshifts, the aperture mass changes less than the 3D halo mass for  $m_{200m, \text{dmo}} \lesssim 10^{14} h^{-1} M_\odot$ . *Bottom panel:* The  $1\sigma$  bootstrapped uncertainty in the mass change of hydrodynamical haloes compared to their matched DMO counterparts for the different mass measurements. The uncertainty in the mass reduction only increases for the rarest, high-mass haloes at higher redshift.

the 3D halo mass. In the bottom panel of Fig. 5.5, we show that the bootstrapped  $1\sigma$  uncertainty in the mean mass suppression does not evolve appreciably.

#### 5.4.5 Dependence on feedback strength

Finally, we study the impact of varying the strength of the simulated AGN feedback on the cluster masses. Simulated black holes accrete from their surrounding gas until the accumulated rest-mass energy reservoir is sufficiently large to heat  $n_{\text{heat}} = 20$  randomly chosen neighbours to a minimum temperature  $\Delta T_{\text{heat}}$ . The fiducial subgrid parameter  $\Delta T_{\text{heat}} = 10^{7.8}$  K is varied to  $10^{7.6}$  K and  $10^{8.0}$  K, to have the mean simulated cluster hot gas fractions cover the scatter inferred from X-ray observations (McCarthy et al., 2017) while also reproducing the galaxy stellar mass function. We point out that these variations result in mean gas fractions that are significantly higher and lower than the mean observed X-ray gas fractions.

In Fig. 5.6, we show how the feedback strength affects the simulated cluster mass for haloes binned by the 3D halo mass,  $m_{200m,\text{dmo}}$ . We label the simulation variations with the true median cluster gas fraction relative to the cosmic baryon fraction,  $f_{\text{gas},500c}/(\Omega_b/\Omega_m)$ , in haloes of  $m_{500c,\text{hydro}} = 10^{14} h^{-1} M_\odot$  instead of the subgrid parameter,  $\Delta T_{\text{heat}}$ , since the gas fraction can be inferred observationally. We have not applied any post-processing to the simulation data to include the effects of hydrostatic bias on the cluster gas fractions inferred from observations. A higher (lower) AGN heating temperature, shown as red (blue) lines, results in stronger (weaker) feedback and lower (higher) cluster gas fractions. For low-mass clusters with  $m_{200m,\text{dmo}} \lesssim 10^{14} h^{-1} M_\odot$ , the aperture mass is consistently affected less by the inclusion of baryons than the 3D halo mass, while for higher-mass clusters, the suppression is similar.

In conclusion, we have compared how the mass of clusters matched between hydrodynamical and DMO simulations changes due to galaxy formation processes. In particular, we showed that aperture masses are consistently less sensitive to baryonic effects than 3D halo masses. This property and the fact that aperture masses can be measured directly in both simulations and observations, make the aperture mass an excellent mass calibration tool for future cluster surveys.

### 5.5 Conclusions

Future cosmological constraints from cluster surveys will be limited by our understanding of the systematic uncertainty in the measured cluster masses (e.g. Köhlinger et al., 2015). Since the current standard analysis relies on theoretical predictions of the cluster abundance based on dark matter-only simulations (e.g. Bocquet et al., 2019; DES Collaboration et al., 2020), the modification of the halo mass due to galaxy formation processes is one of the systematic uncertainties that we need to take into account (e.g. Balaguera-Antolínez & Porciani, 2013; Debackere et al., 2021). We have used the Baryons and Haloes of Massive Systems (BAHAMAS) suite of cosmological, hydrodynamical simulations, which have been shown to reproduce a wide range of the observed properties of massive systems, to study how galaxy formation processes modify the aperture mass of

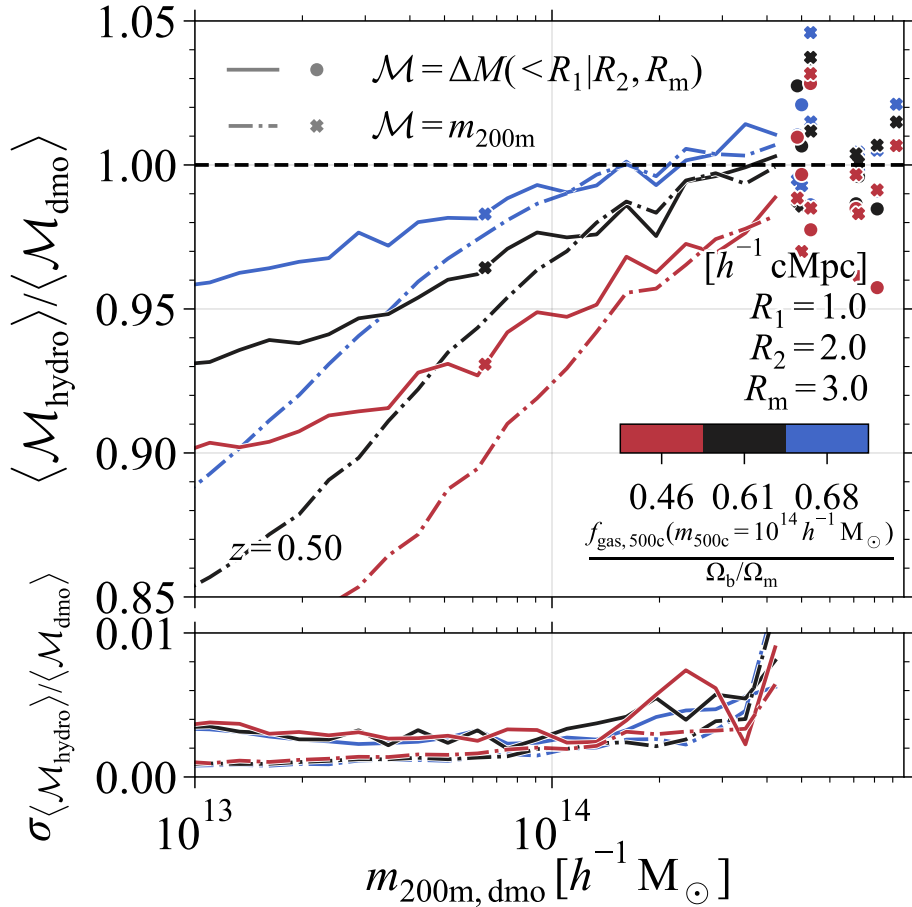


Figure 5.6: *Top panel:* The dependence of the suppression in the aperture mass,  $\Delta M_{\text{hydro}}(< 1h^{-1} \text{ cMpc}|R_2, R_m)$  (solid lines), and the 3D halo mass,  $m_{200m}$  (dash-dotted lines) on the halo gas fraction,  $f_{500c, \text{gas}}(m_{500c} = 10^{14} h^{-1} M_\odot)$ , relative to the cosmic baryon fraction,  $\Omega_b/\Omega_m$ , stacked in bins of the 3D dark matter-only halo mass. All background correction annuli span the region between  $R_2 = 2 h^{-1} \text{ cMpc}$  and  $R_m = 3 h^{-1} \text{ cMpc}$ . Red (blue) lines show higher (lower) AGN heating temperatures in the simulation, resulting in lower (higher) gas fractions. Crosses indicate the halo mass for which  $r_{200m, \text{dmo}} = R_1$ . Bins with fewer than 5 haloes show the individual suppression ratios. The mass suppression increases with increasing feedback strength and decreasing cluster gas fractions. Aperture masses are consistently suppressed less than the 3D halo mass for  $m_{200m, \text{dmo}} \lesssim 10^{14} h^{-1} M_\odot$ . *Bottom panel:* The 1 $\sigma$  bootstrapped uncertainty in the mass suppression of hydrodynamical haloes compared to their matched DMO counterparts for the different mass measurements. The uncertainty in the mass suppression only changes slightly for the most massive haloes when changing the simulated AGN feedback.

clusters compared to their matched haloes in a simulation that includes only dark matter particles.

In agreement with [Debackere et al. \(2021\)](#), who studied the sensitivity of the aperture mass to baryonic effects for idealized cluster density profiles that reproduce the cluster hot gas fractions inferred from X-ray observations, we find that aperture masses are less sensitive to baryonic effects than the 3D halo mass when measured within apertures larger than the halo virial radius. For haloes selected based on their 3D halo mass, aperture masses measured within annuli between  $1 - 3 h^{-1}$  cMpc, which is representative of weak lensing observations, are consistently less suppressed by baryonic effects than the 3D halo masses are ( $\lesssim 5$  per cent vs.  $\lesssim 10$  per cent) for all haloes with  $m_{200m} > 10^{13.5} h^{-1} M_\odot$  (Fig. 5.2). Similar conclusions hold when selecting haloes based on their aperture mass and ensuring that only genuine clusters are included by using an additional lower limit on the 3D halo mass (Fig. 5.3).

While for high-mass objects ( $m_{200m} \gtrsim 10^{14} h^{-1} M_\odot$ ) the mass suppression due to baryons is similar for aperture and 3D masses, we expect baryonic effects to pose a greater challenge for 3D halo mass determinations. This is because a functional density profile needs to be assumed to derive a 3D halo mass from observational data and we expect this profile to be affected by baryons (e.g. [Yellscig et al., 2014](#)). The smaller suppression of the mass of group-sized haloes ( $10^{13} \lesssim m_{200m}/h^{-1} M_\odot \lesssim 10^{14}$ ) and the fact that no density profile needs to be assumed to derive aperture masses, will enable robust mass estimates and, consequently, stronger constraints on galaxy formation processes in haloes at fixed mass.

Due to the sensitivity of the aperture mass to the halo environment, we find that the scatter in the aperture mass in the hydrodynamical simulation within fixed bins of the DMO aperture mass can be up to  $\approx 2$  times larger, depending on the aperture size, than the typical scatter in the 3D halo mass (Fig. 5.4). However, the scatter stays below 10 per cent for all halo masses relevant for cluster cosmology. Hence, this is by no means a limiting factor in the cosmological analysis. The slightly reduced sensitivity to baryonic effects in the cluster mass range,  $m_{200m} > 10^{14} h^{-1} M_\odot$ , combined with the significantly reduced systematic uncertainties in the aperture mass measurement compared to the 3D halo mass inference, and the high cosmological sensitivity of the aperture mass function ([Debackere et al., 2022](#)), give the aperture mass a significant advantage as it reduces the absolute bias due to mass calibration uncertainties in cluster cosmology analyses.

We find only a small redshift evolution of  $\lesssim 2$  per centage points in both the aperture mass and the 3D halo mass suppression between  $z = 0.25$  and 1 (Fig. 5.5). Finally, we find that for extreme variations in the simulation AGN feedback strength that result in simulated *mean* hot gas fractions covering the *scatter* inferred from X-ray observations of individual clusters, the aperture mass is consistently up to 2 per centage points less biased than the 3D halo mass, never exceeding a suppression of 5 per cent for  $m_{200m,\text{dmo}} > 10^{14} h^{-1} M_\odot$  (Fig. 5.6).

Looking towards the future, calibrations of the halo mass difference between hydrodynamical and DMO simulations can be bypassed when large-volume cosmological, hydrodynamical simulations run for a large grid of cosmological parameters become available. Such simulations can be used to measure the abundance of clusters directly as a function of any observable, avoiding the conversion between the theoretical prediction calibrated

on DMO simulations, and the true halo mass, including the effects of baryons. Importantly, such simulations would need to withstand thorough tests of the realism of their cluster population. As long as such simulations are not available, however, accounting for the effects of galaxy formation on the cluster mass is a necessary step for any cluster cosmology survey limited in its constraining power only by systematic uncertainties.

## Acknowledgements

This work is part of the research programme Athena with project number 184.034.002 and Vici grants 639.043.409 and 639.043.512, which are financed by the Dutch Research Council (NWO).

## Data availability

The data used in this paper can be requested from the first author.

## Bibliography

- Adam R., et al., 2019, *Astron. Astrophys.*, 627, A23 → p. 190
- Allen S. W., Evrard A. E., Mantz A. B., 2011, *Annu. Rev. Astron. Astrophys.*, 49, 409 → p. 178
- Amendola L., et al., 2018, *Living Reviews in Relativity*, 21, 2 → p. 178
- Applegate D. E., et al., 2014, *Mon. Not. R. Astron. Soc.*, 439, 48 → p. 183
- Balaguera-Antolínez A., Porciani C., 2013, *J. Cosmol. Astropart. Phys.*, 2013 → p. 179, 193
- Bartelmann M., Schneider P., 2001, *Physics Reports*, 340, 291 → p. 183
- Bocquet S., Saro A., Dolag K., Mohr J. J., 2016, *Mon. Not. R. Astron. Soc.*, 456, 2361 → p. 179
- Bocquet S., et al., 2019, *Astrophys. J.*, 878, 55 → p. 193
- Bocquet S., Heitmann K., Habib S., Lawrence E., Uram T., Frontiere N., Pope A., Finkel H., 2020, *Astrophys. J.*, 901, 5 → p. 179
- Booth C. M., Schaye J., 2009, *Mon. Not. R. Astron. Soc.*, 398, 53 → p. 182
- Clowe D., Luppino G. A., Kaiser N., Henry J. P., Gioia I. M., 1998, *Astrophys. J.*, 497, L61 → p. 183
- Cui W., Borgani S., Dolag K., Murante G., Tornatore L., 2012, *Mon. Not. R. Astron. Soc.*, 423, 2279 → p. 179
- DES Collaboration et al., 2020, *Phys. Rev. D*, 102, 023509 → p. 193
- Dalla Vecchia C., Schaye J., 2008, *Mon. Not. R. Astron. Soc.*, 387, 1431 → p. 182
- Debackere S. N. B., Schaye J., Hoekstra H., 2021, *Monthly Notices of the Royal Astronomical Society*, 505, 593 → p. 179, 193, 195
- Debackere S. N. B., Hoekstra H., Schaye J., Heitmann K., Habib S., 2022, *Monthly Notices of the Royal Astronomical Society*, p. stac1687 → p. 178, 180, 183, 184, 190, 195
- Ferland G. J., Korista K. T., Verner D. A., Ferguson J. W., Kingdon J. B., Verner E. M., 1998, *Publications of the Astronomical Society of the Pacific*, 110, 761 → p. 182
- Haiman Z., Mohr J. J., Holder G. P., 2001, *Astrophys. J.*, 553, 545 → p. 178
- Henson M. A., Barnes D. J., Kay S. T., McCarthy I. G., Schaye J., 2017, *Mon. Not. R. Astron. Soc.*, 465, 3361 → p. 179
- Hilton M., et al., 2021, *ApJS*, 253, 3 → p. 178
- Hinshaw G., et al., 2013, *Astrophys. J. Suppl. Ser.*, 208, 19 → p. 181
- Hoekstra H., 2001, *Astron. Astrophys.*, 370, 743 → p. 180
- Hoekstra H., Mahdavi A., Babul A., Bildfell C., 2012, *Monthly Notices of the Royal Astronomical Society*, 427, 1298 → p. 179, 183
- Köhlinger F., Hoekstra H., Eriksen M., 2015, *Mon. Not. R. Astron. Soc.*, 453, 3107 → p. 178, 193
- LSST Science Collaboration et al., 2009, arXiv e-prints, p. arXiv:0912.0201 → p. 178
- Le Brun A. M., McCarthy I. G., Schaye J., Ponman T. J., 2014, *Mon. Not. R. Astron. Soc.*, 441, 1270 → p. 181, 182
- Lee B. E., Le Brun A. M. C., Haq M. E., Deering N. J., King L. J., Applegate D., McCarthy I. G., 2018, *Mon. Not. R. Astron. Soc.*, 479, 890 → p. 179
- Lewis A., Challinor A., Lasenby A., 2000, *Astrophys. J.*, 538, 473 → p. 181
- Mandelbaum R., Seljak U., Baldauf T., Smith R. E., 2010, *Monthly Notices of the Royal Astronomical Society*, 405, 2078 → p. 179
- Martizzi D., Mohammed I., Teyssier R., Moore B., 2014, *Mon. Not. R. Astron. Soc.*, 440, 2290 → p. 179
- McCarthy I. G., et al., 2010, *Monthly Notices of the Royal Astronomical Society*, pp 822–839 → p. 179
- McCarthy I. G., Schaye J., Bird S., Le Brun A. M., 2017, *Mon. Not. R. Astron. Soc.*, 465, 2936 → p. 180, 181, 182, 193

- McCarthy I. G., Bird S., Schaye J., Harnois-Deraps J., Font A. S., van Waerbeke L., 2018, *Mon. Not. R. Astron. Soc.*, 476, 2999 → p. 180
- McClintock T., et al., 2019, *Astrophys. J.*, 872, 53 → p. 179
- Nishimichi T., et al., 2018 → p. 179
- Rudd D. H., Zentner A. R., Kravtsov A. V., 2008, *Astrophys. J.*, 672, 19 → p. 179
- Sartoris B., et al., 2016, *Mon. Not. R. Astron. Soc.*, 459, 1764 → p. 178
- Schaye J., Dalla Vecchia C., 2008, *Mon. Not. R. Astron. Soc.*, 383, 1210 → p. 182
- Schaye J., et al., 2010, *Mon. Not. R. Astron. Soc.*, 402, 1536 → p. 181, 182
- Springel V., 2005, *Mon. Not. R. Astron. Soc.*, 364, 1105 → p. 181
- Springel V., White S. D. M., Tormen G., Kau G., 2001, *Mon. Not. R. Astron. Soc.*, 328, 726 → p. 182
- Stanek R., Rudd D., Evrard A. E., 2009, *Mon. Not. R. Astron. Soc. Lett.*, 394, L11 → p. 179
- Tinker J., Kravtsov A. V., Klypin A., Abazajian K., Warren M., Yepes G., Gottlöber S., Holz D. E., 2008, *Astrophys. J.*, 688, 709 → p. 179
- Tyson J. A., Wittman D. M., Hennawi J. F., Spergel D. N., 2003, *Nuclear Physics B - Proceedings Supplements*, 124, 21 → p. 178
- Velliscig M., van Daalen M. P., Schaye J., McCarthy I. G., Cacciato M., Le Brun A. M., Vecchia C. D., 2014, *Mon. Not. R. Astron. Soc.*, 442, 2641 → p. 179, 183, 186, 195
- Wiersma R. P. C., Schaye J., Smith B. D., 2009a, *Mon. Not. R. Astron. Soc.*, 393, 99 → p. 182
- Wiersma R. P. C., Schaye J., Theuns T., Dalla Vecchia C., Tornatore L., 2009b, *Mon. Not. R. Astron. Soc.*, 399, 574 → p. 182
- van Daalen M. P., Schaye J., McCarthy I. G., Booth C. M., Vecchia C. D., 2014, *Mon. Not. R. Astron. Soc.*, 440, 2997 → p. 184

# Nederlandstalige samenvatting

In de Griekse mythologie is de kosmos ( $\chi\omega\mu\omega\zeta$ ) een geordende toestand die ontstaat uit de chaos ( $\chi\alpha\omega\zeta$ ), de leegte<sup>6</sup>. De kosmologie als onderzoeksgebied probeert op een gelijkaardige manier de metaforische leegte in ons begrip van het universum op te vullen: waar kwam het vandaan en hoe zal het evolueren? Slechts in de laatste eeuw is de kosmologie geëvolueerd van een voornamelijk filosofisch tijdverdrijf naar een volwaardig wetenschappelijk vakgebied. De bouw van grote telescopen met spectrografen opende een nieuwe kijk op ons heelal: de verschuiving van atomaire emissielijnen van verafgelegen objecten, veroorzaakt door hun beweging ten opzichte van de Aarde, toonde aan dat de sommige van de wazige nevels, waarvan er al duizenden ontdekt waren, in werkelijkheid gigantische opeenhopingen van sterren zijn die aan “ongeëvenaarde snelheden” van ons wegsnellen. Deze hypothese bleek initieel controversieel en leidde tot het “Grote Debat” tussen Shapley en Curtis in 1921 over de grootte van het heelal. Het definitieve antwoord kwam in 1925 via Edwin Hubble die individuele variabele Cepheïdersterren ontdekte in de nabije Andromeda- en Driehoeknevels en de relatie tussen hun periodieke helderhedsvariaties en hun lichtkracht gebruikte om aan te tonen dat deze nevels daadwerkelijk sterrenstelsels zijn die zich op miljoenen lichtjaren van ons bevinden. Georges Lemaître was de eerste die de waarnemingen van de hoge snelheden van verafgelegen sterrenstelsels in 1927 interpreteerde in de optiek van een uitdijend heelal zoals de vergelijkingen van Einsteins algemene relativiteitstheorie voorspellen. Hubble toonde in 1929 direct aan dat verder afgelegen sterrenstelsels met hogere snelheden van ons wegsnellen, precies zoals verwacht voor een uitdijend universum. Deze doorbraak luidde het begin van het tijdperk van de *observationele* kosmologie in.

Sinds de ontdekking van de uitdijing van het heelal, nu bijna een eeuw geleden, heeft een overvloed aan afzonderlijke observaties de verdeling van materie op kosmologische schalen van miljoenen tot miljarden lichtjaren verhelderd. Het consistente plaatje is dat van een uitdijend heelal dat structuur bevat op verschillende lengteschalen: sterrenstelsels hopen zich op in groepen van enkele melkwegstelsels tot clusters die er honderden tot duizenden bevatten. De groepen bevinden zich in een filamentaire structuur met de clusters in de knooppunten: een uitgebreid netwerk van overdichthes, het kosmisch web genoemd. De ruggengraat van dit netwerk bestaat uit donkere materie, een vorm van materie die enkel zwaartekracht voelt en die ongeveer 25 % van de totale energiedichtheid van het heelal beslaat. De normale materie, waar wij mee bekend zijn, bevindt zich in gaswolken, sterren, planeten en hun bewoners, maar draagt amper 5 % bij aan het energiebudget. De overige 70 % van de rekening gaat naar de mysterieuze donkere energie, een onbekende vorm van energie die de zwaartekracht tegenwerkt en het heelal in een toestand van een ogenschijnlijk oneindige versnelde uitdijing drijft.

## Kosmologie in de toekomst

Een rist telescopen zal het komende decennium hun eerste licht waarnemen met als doel de eigenschappen van deze donkere energie te verhelderen. Met behulp van de miljarden

---

<sup>6</sup>Hesiodus, *Theogonia*, 110

sterrenstelsels die ze zullen ontdekken, zullen ze de evolutie van de verdeling van de totale materie, zowel donker als normaal, over de afgelopen 10 miljard jaren in kaart brengen. De ware doorbraak zal liggen in hun vermogen om direct het tijdperk waar te nemen wanneer het heelal voldoende was uitgedijd zodat donkere energie het energiebudget begon te domineren over de zwaartekracht van de materie, ongeveer 3.6 miljard jaren geleden. De versnelde uitdijing van het heelal werkt de aantrekking van de zwaartekracht tegen, wat de vorming van structuur vertraagt en een duidelijke afdruk nalaat in de verdeling van sterrenstelsels. De uitdaging zal hem liggen in het afleiden van de verdeling van alle materie uit de observaties van enkel de sterrenstelsels.

Het is mogelijk om de totale verdeling van materie waar te nemen, zij het indirect, aangezien massa de onderliggende ruimtetijd vervormt, zoals ook het oppervlak van een trampoline, wat gevolgen heeft voor het pad dat licht aflegt op weg naar onze telescopen. De differentiële kromming van de ruimtetijd fungeert als een lens die achterliggende sterrenstelsels uitvergroot en hun afbeelding vervormt. Een extreem voorbeeld van een sterke zwaartekrachtslens is te zien in Fig. 1.5 in Hoofdstuk 1, waar een cluster van sterrenstelsels omringd is door uitgerekte bogen van sterk vervormde achterliggende melkwegstelsels. Dit effect vindt ook subtieler plaats voor sterrenstelsels die zich in projectie verder van het centrum van de cluster bevinden, zoals schematisch getoond in Fig. 1.6 in Hoofdstuk 1. Aangezien sterrenstelsels *a priori* geen voorkeursoriëntatie vertonen, kunnen we de massa van een object bepalen door statistisch de oriëntatie van vele sterrenstelsels te meten. De aanwezigheid van een grote massa zal leiden tot een preferentiële oriëntatie tangentieel aan de grote cirkels gecentreerd op de massaverdeling (zoals duidelijk te zien in de bogen in Fig. 1.5), waar de grootte van het signaal afhangt van de massa van het object. Aangezien de afbeeldingen bij de statistische methode minder vervormd zijn, spreken we in dit geval over een zwakke zwaartekrachtslens.

Door de correlaties tussen de vervorming van sterrenstelsels in het zwakke regime op verschillende afstanden van ons en op verschillende plekken aan de hemel te correleren, kunnen we de statistische verdeling van materie in het heelal bepalen. Daarnaast kunnen we met zwakke zwaartekrachtslenzen ook de massa van individuele objecten, zoals clusters van sterrenstelsels, bepalen. Clusters zijn zeldzame objecten: ze zijn extreem massief, waardoor het een lange tijd duurt vooraleer ze vormen. De evolutie in het aantal clusters hangt dus nauw af van de hoeveelheid materie en haar verdeling alsook van de geschiedenis van donkere energie.

Deze thesis focust op de interpretatie van het zwakke zwaartekrachtslenssignaal zodanig dat we de correcte massa kunnen bepalen. Dit is een ingewikkeld probleem aangezien we moeten weten hoe de normale materie zich gedraagt ten opzichte van de donkere materie. Beide soorten materie voelen de zwaartekracht, maar slechts de normale materie interageert ook door middel van de elektromagnetische kracht. Deze interacties zorgen voor fundamenteel verschillend gedrag op de relatief kleinere schalen van sterrenstelsels. Eigenlijk kunnen melkwegstelsels enkel ontstaan *dankzij* deze elektromagnetische interacties. Paradoxaal genoeg is niet alle normale materie zichtbaar voor onze telescopen aangezien een aanzienlijke fractie zich bevindt in gas van lage dichtheid en hoge temperatuur waarvoor de gevoeligheid van onze huidige Röntgenstralingtelescopen te laag is om het direct waar te nemen. Bijgevolg moeten we een manier vinden om de ongekende bijdrage van de normale materie te ontarren van het totale waargenomen lenssignaal.

## Uitdagingen

In het prille begin, ongeveer 20 000 jaren na de oerknal, is het heelal genoeg afgekoeld zodat materie en niet straling het energiebudget van het heelal domineert. Op dat moment beginnen kleine fluctuaties in de dichtheid van donkere materie te groeien onder de invloed van de zwaartekracht terwijl de overvloedige elektromagnetische straling in de vorm van fotonen nog steeds sterk gekoppeld is aan de normale materie en voorkomt dat deze meegroeit. Ongeveer 380 000 jaren na de oerknal is het heelal genoeg uitgedijd en de koppeling met de straling danig afgenomen zodat de normale materie eindelijk instort onder invloed van de zwaartekracht van de reeds sterk gegroeide donkere materie-overdichtheseden.

De elektromagnetische interacties tussen normale materie zorgen ervoor dat atomen, elektronen en ionen met elkaar kunnen botsen, wat resulteert in een druk die de instorting vanwege de zwaartekracht kan tegengaan. Bijgevolg vormt zich in de ingestorte donkere materiestructuren, een gasachtige halo met een evenwichtstemperatuur zodanig dat de druk van het gas de zwaartekracht balanceert. Dit is echter niet het volledige verhaal: eenmaal de dichtheid en de temperatuur van het gas hoog genoeg zijn, zal het gas geïoniseerd worden en zullen vrije elektronen in botsingen de atomen exciteren of ioniseren, wat gepaard gaat met de emissie van fotonen, waardoor de elektronen energie verliezen en het gas afkoelt. De meeste atomaire transities komen overeen met temperaturen tussen  $10^4 - 10^6$  K en gas met deze temperatuur zal dus efficiënt kunnen afkoelen wat leidt tot fragmentatie en stervorming in halo's met massa's van  $10^{10} - 10^{12}$  M<sub>⊙</sub>, waar M<sub>⊙</sub> een zonnemassa is. Tijdens het afkoelen zal het gas instorten naar het centrum van de halo terwijl het hoekmoment behouden blijft, wat resulteert in de vorming van sterrenschijven zoals waargenomen in spiraalstelsels. De halo's en hun sterrenstelsels groeien door de continue instroom van meer materie en door samensmeltingen met andere halo's waarin de sterrenschijven verstoord worden en de spiraalstelsels omvormen tot elliptische sterrenstelsels. Meer massieve halo's groeien hiërarchisch door de ophoping van verschillende kleinere halo's als een satellietpopulatie.

De vorming en de groei van sterrenstelsels gaat gepaard met hevige zogenaamde “feedbackprocessen”. Sterren genereren stellaire winden die het gas in hun omgeving verrijken en massieve sterren kunnen exploderen als supernovae na enkele tientallen miljoenen jaren. Deze explosies verdrijven en verhitten het naburige gas wat stervorming kan stopzetten in sterrenstelsels met lage massa. Massieve sterrenstelsels herbergen een centraal supermassief zwarte gat dat gevoed wordt door de instroom van gas. Materiaal dat de accretieschijf bereikt wordt daar versneld en voedt winden en “jets” die gas op de schaal van het hele sterrenstelsel kunnen verhitten en ontbinden wat leidt tot de injectie van verrijkt materiaal in de halo. De feedback van deze actieve galactische nucleus (AGN) stopt de stervorming in massieve stelsels en kan bovendien de verdere instroom van koel gas verhinderen. Deze heftige processen zijn moeilijk te voorspellen aangezien ze plaatsvinden op relatief kleine schalen, maar ze hebben een belangrijke impact op de totale verdeling van materie in het heelal.

Computersimulaties kunnen heel precies voorspellen hoe de gravitationele instorting van donkere materie resulteert in een kosmisch web door miljarden deeltjes onder de invloed van de zwaartekracht te laten evolueren in een volume van miljoenen lichtjaren. Het

is echter moeilijker om de normale materie mee te nemen in deze berekeningen, aangezien de feedbackprocessen plaatsvinden op schalen van enkele lichtjaren die niet gelijktijdig gesimuleerd kunnen worden in de gigantische volumes vanwege de beperkte beschikbare rekenkracht. Deze processen kunnen enkel worden meegenomen als versimpelde recepten onder de resolutielimiet van de simulaties. Bijgevolg kunnen simulaties niet van de grondbeginselen de verdeling van materie voorspellen.

## Dit proefschrift

In dit proefschrift bestuderen we hoe onze gebrekkige kennis van de vorming van sterrenstelsels en hun impact op de totale verdeling van materie, de interpretatie van toekomstige kosmologische analyses beïnvloedt. Winden op de schaal van sterrenstelsels gegenereerd door supernova-ontploffingen en verhitte bellen geblazen door de supermassieve zwarte gaten in het centrum van sterrenstelsels, hebben een sterke invloed op de verdeling van materie wanneer we deze vergelijken met een simpeler heelal dat enkel materie bevat die instort onder de invloed van de zwaartekracht. Dit bemoeilijkt de kosmologische analyse van toekomstige missies aanzienlijk, aangezien deze processen nog steeds niet goed begrepen zijn.

In **Hoofdstuk 2** verhelderen we de onzekerheid in de verdeling van alle materie voor grootschalige zwakke zwaartekrachtlensanalyses. We gebruiken een fenomenologisch halo model dat observationele data reproduceert om de totale verdeling van materie statistisch te modelleren. Dit model heeft genoeg vrijheid om de invloed van de niet waargenomen normale materie op het uiteindelijke antwoord te kwantificeren. We tonen aan dat de verdeling van het hete gas in groepen en clusters van sterrenstelsels van cruciaal belang is omdat deze objecten het totale signaal domineren op de schalen die de correlaties in de oriëntaties van sterrenstelsels bepalen. We benadrukken ook dat feedbackprocessen vooral de massa van halo's verlagen ten opzichte van een heelal dat enkel donkere materie bevat: de verdeling van de halo's zelf verandert niet veel.

In **Hoofdstuk 3** schakelen we over naar clusters als een sonde voor de evolutie van het heelal, geïnspireerd door hoe succesvol het simpele model in Hoofdstuk 2 de impact van de normale materie op de totale materieverdeling zoals voorspeld in simulaties kan reproduceren, hoewel het enkel observationele data gebruikt. We gebruiken Röntgenstralingobservaties van het hete gas in clusters om hun totale dichtheidsprofiel, inclusief donkere materie, te bepalen. We verbinden waargenomen halo's met gesimuleerde halo's in een heelal dat enkel donkere materie bevat, waardoor we theoretisch hun aantal kunnen voorspellen als functie van hun driedimensionale massa. Vervolgens simuleren we zwakke zwaartekrachtlensobservaties van onze modelclusters om te kwantificeren wat de impact is van een foute aanname voor hun dichtheidsprofiel op de afgeleide driedimensionale massa. We tonen aan dat de clusteranalyses van toekomstige missies significant verkeerde waarden zouden afleiden voor zowel de afgeleide hoeveelheid materie en haar verdeling als voor de evolutie van donkere energie, indien ze geen rekening houden met de verschillende verdeling van normale materie ten opzichte van donkere materie.

In **Hoofdstuk 4** pakken we het probleem van de massakalibratie van clusters op een andere manier aan. We constateren dat er momenteel een oneerlijke last ligt bij de zwakke zwaartekrachtlenswaarnemingen om de driedimensionale massa af te leiden aangezien

die gemakkelijk te bepalen is in simulaties. Deze stap vereist echter kennis van het gede-projecteerde dichtheidsprofiel van de cluster dat observationeel moeilijk te bepalen is. Wij stellen voor het aantal waargenomen clusters theoretisch te kalibreren als een functie van hun excessieve geprojecteerde massa die direct te meten is in zwakte zwaartekrachtlens-observaties én simulaties. We tonen aan dat deze geprojecteerde massa's met een beduidend lagere observationele fout kunnen afgeleid worden dan de driedimensionale massa. Bovendien blijkt uit grote collecties van simulaties die enkel donkere materie evolueren dat het aantal clusters als functie van de geprojecteerde massa minstens even gevoelig is voor veranderingen in de kosmologie als het aantal als functie van de driedimensionale massa. Bijgevolg kunnen geprojecteerde massakalibraties leiden tot een grote reductie in de systematische onzekerheid van kosmologische studies die het aantal clusters meten.

Tot slot gebruiken we in **Hoofdstuk 5** kosmologische hydrodynamische simulaties om het effect van normale materie op de geprojecteerde massa van clusters te kwantificeren door de verandering in de massa te vergelijken voor halo's in gesimuleerde universa met en zonder normale materie. Geprojecteerde massa's blijken enigszins minder gevoelig te zijn voor de feedbackprocessen dan de driedimensionale massa's aangezien normale materie en donkere materie aan de rand van de cluster gelijkaardig verdeeld zijn en de rand van de cluster ook bijdraagt aan de geprojecteerde massa. De gevoeligheid neemt niet dramatisch af, maar, in samenspel met de reductie in de systematische onzekerheid in de massakalibratie, is het een ander voordeel van geprojecteerde massakalibraties voor kosmologie met clusters.



# List of publications

## Refereed publications

1. *Galaxy cluster aperture masses are more robust to baryonic effects than 3D halo masses*  
Debackere, S. N. B., Hoekstra, H., Schaye, J.  
Monthly Notices of the Royal Astronomical Society, 515, 6023 (2022)
2. *Why are we still using 3D masses for cluster cosmology?*  
Debackere, S. N. B., Hoekstra, H., Schaye, J., et al.  
Monthly Notices of the Royal Astronomical Society, 515, 3383 (2022)
3. *How baryons can significantly bias cluster count cosmology*  
Debackere, S. N. B., Schaye, J., Hoekstra, H.  
Monthly Notices of the Royal Astronomical Society, 505, 593 (2021)
4. *The impact of the observed baryon distribution in haloes on the total matter power spectrum*  
Debackere, S. N. B., Schaye, J., Hoekstra, H.  
Monthly Notices of the Royal Astronomical Society, 492, 2285 (2020)

## Non-astronomy publications

1. *An evaluation of behaviours considered indicative of skill in handaxe manufacture*  
Hutchence, L., Debackere, S.  
Lithics—The Journal of the Lithic Studies Society, 36 (2019)



# Curriculum vitae

I was born on April 27th 1993 in Gent, Belgium, but moved to Leuven at four years of age. There, I attended the Sint-Albertuscollege studying Classical Languages and taking the Greek-Mathematics 8 specialization in the final two years. In my fifth year of secondary school, I took part in the astronomy summer school organized by the Flemish Astronomy Society. I had been fascinated by astronomy ever since my brother Tom received a small refractor telescope for his birthday. In my final year of secondary school, I won the Flemish Astronomy Olympiad with a proposal to determine whether the anomalous X-ray Pulsar 4U 0142+61 is a magnetar by observing polarized luminosity variations due to the lensing effect caused by its strong magnetic field.

Intending to study aerospace engineering in Delft, I encountered the astronomy programme in Leiden and was immediately sold. Eleven years later, I have completed my double Bachelor's degrees in Astronomy and Physics, culminating with a research project on the instrumental polarization of the Extremely Large Telescope with Dr. Frans Snik (*cum laude*, 2014) and obtained a Master's degree in Physics, specializing in cosmology, with a thesis supervised by professor Joop Schaye on modelling baryonic effects in hydro-dynamical simulations with a phenomenological halo model (*summa cum laude*, 2016), all at Leiden University. After a year at the University of Cambridge, where I completed the Master of Advanced Studies in Applied Mathematics (2017), I returned to Leiden as a de Sitter PhD fellow to work with professors Joop Schaye and Henk Hoekstra on studying the impact of baryonic effects on the cosmological analysis of future surveys like Euclid.

During my studies, I was able to present my research at Euclid meetings in Milan (2018), Barcelona (2019), and Paris (February 2020), the last physical meeting before the pandemic. Additionally, I have tutored first year Bachelor's students (2013-2016), taught examples classes for courses on Electromagnetic Fields (2016), Quantum Mechanics (2016), and Large-Scale Structure and Galaxy Formation (2018-2020), and supervised Joshiwa van Marrewijk's Master's project. Finally, I was consulted by secondary school students on their graduation project and I presented an introduction to dark matter to a group of Dutch and German fifteen-year-olds. From 2019 to 2022, I also served as an editor for the Dutch Journal of Physics.

In September 2022, I will be moving to México to start a new career outside of academia.



# Acknowledgments

Completing a PhD is not a solo effort, even though a lot of time is spent reading, thinking, coding and debugging on your own. Many people have helped to make my time in Leiden a memorable one. First of all, I would like to thank my supervisors, Joop and Henk, for their continuous guidance and in-depth discussions about my work, which could get lively at times. Joop, you care deeply for all of your students and wish for them to succeed. This clearly shows in the thorough comments you provide on our drafts, the dissection of papers during the preprint meetings, and your shared insights into the sociological aspects of the academic world. I have learned a lot from you. Henk, thank you for always being able to drop by your office to discuss strange results or to talk about the clearest and most concise way to get my points across. I sincerely enjoyed our discussions about education and research, and our shared appreciation for Demeyere pants. Collaborating with you has been a real pleasure.

Being part of two research groups provides twice the learning opportunities. To all the people in the cosmological simulations and weak lensing groups: thank you for the interesting meetings and for keeping me informed about a broad range of topics during times when my own projects were very singularly focussed.

The observatory is full of lively students whom I want to thank for creating a homely atmosphere. Alex, Kirsty, David, Dilovan, Steven, Leon, Leindert: thank you for the fun times both inside and outside of the observatory and the wide-ranging topics up for discussion (when we veered away from instrumentation).

Bavo, David, Kasper, Leindert, Leon en Steven: we begonnen samen aan deze reis, zo'n slordige 11 jaren geleden en nu mag ik dit hoofdstuk afsluiten. Bedankt voor alle goede tijden: de filmavonden, terrasjes, diners en de reizen. Dat er nog vele mogen volgen! David, jou wil ik in het bijzonder bedanken voor je bezorgdheid en om te verzekeren dat ik ook af en toe het daglicht zag tijdens het afronden van de thesis. Kasper, bedankt voor het aangename gezelschap, de fijne avonden met interessante discussies en af en toe een decadent diner. Leindert, bedankt voor jouw nuchtere kijk op de dingen: naast jouw inzichten in de astronomie heb ik ook genoten van onze filosofische overpeinzingen. I also sincerely want to thank Laurie: our video chats during the pandemic were remarkably effective at keeping my spirits up. Stay candid and sincere and keep those recommendations of comedians and shows coming.

Bovenal wil ik mijn ouders bedanken om mij letterlijk alles te geven. Mamaatje en papaatje, jullie continue zorgzaamheid, bezorgdheid en vertrouwen zijn altijd een betrouwbare steun geweest. Koentje en Sofie, ook bedankt voor de goede zorgen en de aangename bezoeken in Leuven met levendige discussies en schattige nichtjes, Julie en Anna. Lieve Tom, jij weet wat je voor mij betekend hebt en altijd zal betekenen. Vanuit het diepste van mijn hart: bedankt.

También quiero agradecerles a mis suegros, René y Laura, por recibirnos en su casa en los últimos momentos del doctorado. Muchísimas gracias por su cariño y su apoyo, por llevarnos a lugares tan bonitos y asegurarse que saliéramos de la casa. Discúlpennme por no ser la mejor compañía durante estos dos meses trabajando. Los invitaremos a celebrar cuando regresaremos.

Finalmente, quiero decirle a Ana Laura, mi esposa maravillosa: gracias por todo. No hay espacio para escribir todo lo que vivimos juntos. No es fácil terminar dos doctorados en diferentes países y, además, en tiempos de Corona, pero lo logramos. Muchísimas gracias por siempre ser mi apoyo, mi refugio y mi compañerita de vida.